



**Fabrication and Nano-scale Characterisation  
of Ferroelectric Thin Films**

by

Nikhil Ponon

Doctor of Philosophy

A thesis submitted in fulfilment for the degree of  
Doctor of Philosophy in the School of Electrical and Electronic Engineering

July 2014

# Abstract

This thesis focuses on the fabrication and characterisation of BaTiO<sub>3</sub> thin films. One of the aims is to deposit amorphous BaTiO<sub>3</sub> films on conductive thin films through sputtering at temperatures compatible with semiconductor manufacturing, followed by post deposition annealing to crystallise these films. However, rapid thermal processing (RTP) is known to create pinholes and cracks due to thermal mismatches between the electrode and insulator, causing degradation of the film quality. Initial focus was to develop thin film electrodes which can withstand process temperatures above 800 °C. Deposition conditions, including the nitrogen flow rate relative to that of argon during deposition were optimised to obtain TiN<sub>x</sub> with least resistivity and excellent material properties through reactive sputtering. TiN<sub>x</sub> films deposited at various nitrogen flow rates were then annealed in a non-oxidising condition and their properties were thoroughly studied. Films deposited at the highest nitrogen flow rate (95%) showed least variation in resistivity and showed excellent material properties even after a high temperature anneal.

BaTiO<sub>3</sub> films of varying thicknesses were deposited on TiN<sub>x</sub> using RF-sputtering and subjected to RTP at various temperatures. It was found that there exists a critical thickness for each RTP temperature below which BaTiO<sub>3</sub> films are pinhole free. A process was then developed by depositing and annealing multiple layers of BaTiO<sub>3</sub> films, with the thickness of each deposition less than the critical thickness. It was observed that the multi-layered films are stable and pinhole free with a smooth surface while the single layers of equivalent thicknesses showed cracked surfaces. Current-atomic force microscopy studies showed leakage current through large pinholes in single-layered films, whereas the pinholes were not the leakage path for multi-layered films. Metal-insulator-metal capacitor structures were also fabricated using BaTiO<sub>3</sub> with TiN<sub>x</sub> top and bottom electrodes and the fringing effects in leakage characteristics were studied.

Finally, the polarisation reversal mechanism in BaTiO<sub>3</sub> was investigated using

---

piezoresponse force spectroscopy (PFS). It was experimentally demonstrated that the polarisation reversal in these materials is a two-step process, which involves polarisation rotation and switching when the applied electric field is not parallel to the crystallographic orientation of the grain. However, it is a single step switching when the polarisation and the electric field are parallel, as widely perceived. The two step polarisation reversal was found to help [101] and [111] oriented grains to switch at a lower electric field compared to [001] grains.

# Acknowledgements

I would like to express my sincerest gratitude to my supervisor, Prof. Anthony O'Neill for his guidance, support and advice throughout my PhD. I would also like to thank my second supervisor Dr. Kelvin Kwa who supported me alongside Prof. Anthony O'Neill during my studies. I feel privileged to have been able to work under their supervision and I truly acknowledge their priceless help and encouragement.

Further obligations are gratefully remembered to Engineering and Physical Sciences Research Council (EPSRC), UK and Intel Ireland for providing the financial support to carry out this research. Special thanks to Dr. Jonathan Goss, Dr. Peter King and Bernie Capraro (Intel Ireland) for their mentoring support, numerous fruitful discussions and feedback. I am thankful to Gary Potts for his support in the clean room and for the great friendship we shared. During my PhD I was privileged to work with exceptional colleagues in the research group. In particular, I would like to thank Daniel Appleby, Srinivas Ganti, Dr. Erhan Erac, Sami Ramdan and Dr. Zhiyong Zhou for the constructive discussions, feedbacks and above all, for their valuable comradeship.

I will take this opportunity to thank our project collaborators from Imperial College, especially Dr. Ullrich Hannemann and Prof. Neil Alford for sharing their knowledge and for providing the PLD samples used for this study. Thanks to Maggie White for XRD, Dr. Anders Barlow and Prof. Peter Cumpson for XPS and Dr. Budhika Mendis and Leon Bowen (Durham University) for TEM analysis. I would also like to thank all my dear friends who made my PhD journey a pleasant one.

I would like to thank my brother Nidhin, sister in law Rupa and nephew Siddhanth, for their continuous support during my PhD. I would also like to thank my fiancée Arathi, for her love and constant encouragement while writing-up this thesis. Last but not the least, I would like to thank my beloved parents for their never-fading love and support. I owe everything in my life to them.

# Contents

<b>Abstract</b>	<b>i</b>
<b>Acknowledgements</b>	<b>iii</b>
<b>Contents</b>	<b>iv</b>
<b>Journals and Conferences</b>	<b>viii</b>
<b>List of Figures</b>	<b>x</b>
<b>List of Tables</b>	<b>xxiii</b>
<b>Abbreviations</b>	<b>xxiv</b>
<b>1 Introduction</b>	<b>1</b>
1.1 Research Objectives . . . . .	8
1.2 Research Hypothesis and Questions . . . . .	9
1.3 Thesis Outline . . . . .	10
<b>2 Background</b>	<b>12</b>
2.1 Introduction . . . . .	12
2.2 Ferroelectric Phase Transition . . . . .	14
2.3 Ferroelectric Switching . . . . .	15
2.3.1 Macro-scale domain reversal . . . . .	16
2.4 Piezoelectricity . . . . .	16
2.5 Field Induced Phase Transition . . . . .	17
2.6 Crystallisation Kinetics . . . . .	18

---

2.6.1	Miller indices . . . . .	20
2.7	Thermal Budget of Silicon Technology . . . . .	21
2.8	Thin Film Failure Modes . . . . .	23
2.9	Titanium Nitride . . . . .	25
2.10	Summary . . . . .	25
<b>3</b>	<b>Fabrication and Characterisation of Thin Films</b>	<b>27</b>
3.1	Thin Film Deposition and Post Deposition Processing . . . . .	27
3.1.1	Sample preparation . . . . .	27
3.1.2	Thin film deposition . . . . .	29
3.1.2.1	Sputter deposition . . . . .	29
3.1.2.2	Pulsed laser deposition (PLD) . . . . .	35
3.1.2.3	Electron beam evaporation . . . . .	35
3.1.3	Rapid thermal processing (RTP) . . . . .	36
3.1.4	Optical lithography . . . . .	36
3.1.5	Reactive ion etching (RIE) . . . . .	37
3.2	Metrology Challenges and Techniques for Emerging Materials . . . . .	38
3.2.1	Scanning probe microscopy . . . . .	39
3.2.1.1	Atomic force microscopy (AFM) . . . . .	40
3.2.2	Nano-scale electrical analysis modes in SPM . . . . .	45
3.2.2.1	Current AFM . . . . .	45
3.2.2.2	Electrostatic force microscopy . . . . .	49
3.2.2.3	Piezoresponse force microscopy and spectroscopy . . . . .	50
3.2.3	X-ray diffraction (XRD) . . . . .	56
3.2.4	X-ray photoelectron spectroscopy (XPS) . . . . .	57
3.2.5	Raman spectroscopy . . . . .	59
3.2.6	Transmission electron microscopy (TEM) . . . . .	60
3.2.7	Sheet resistance . . . . .	60
3.2.7.1	Dual configuration technique . . . . .	61
3.2.8	I-V characterisation . . . . .	63

---

3.3	Summary . . . . .	63
<b>4</b>	<b>Electrode Technology</b>	<b>65</b>
4.1	Introduction . . . . .	65
4.2	Experimental Details . . . . .	68
4.3	Process Development . . . . .	70
4.3.1	Target conditioning . . . . .	70
4.3.2	Deposition conditions . . . . .	72
4.4	Process Optimisation . . . . .	73
4.4.1	Oxidation resistance . . . . .	76
4.5	Post Deposition Annealing . . . . .	77
4.5.1	Variations in resistivity . . . . .	77
4.5.2	Variations in orientation . . . . .	78
4.5.3	Variations in vacancies . . . . .	82
4.5.4	Variations in stoichiometry . . . . .	83
4.5.5	Variations in surface morphology . . . . .	88
4.5.6	Discussion . . . . .	89
4.6	TiN <sub>x</sub> Dry Etching . . . . .	92
4.7	Summary and Conclusions . . . . .	93
<b>5</b>	<b>Thin Film Deposition and Post Deposition Anneal of BaTiO<sub>3</sub></b>	<b>96</b>
5.1	Introduction . . . . .	96
5.2	Experimental Setup . . . . .	99
5.3	Material Characterisation . . . . .	101
5.4	Peripheral Leakage Effects . . . . .	103
5.4.1	Discussion . . . . .	107
5.5	Post Deposition Anneal of BaTiO <sub>3</sub> Thin Films . . . . .	110
5.6	Multi-layered BaTiO <sub>3</sub> . . . . .	115
5.6.1	Leakage current study . . . . .	119
5.6.2	Discussion . . . . .	126

---

5.7	Summary and Conclusions . . . . .	128
<b>6</b>	<b>Polarisation Reversal Mechanisms in BaTiO<sub>3</sub></b>	<b>130</b>
6.1	Introduction . . . . .	130
6.2	Experimental Details . . . . .	133
6.3	Material Characterisation . . . . .	134
6.4	Polarisation Reversal Mechanism . . . . .	139
6.4.1	Discussion . . . . .	143
6.5	Impact of Polarisation Rotation on the Switching Field . . . . .	147
6.5.1	Dependence of crystalline orientation on switching field . . . . .	153
6.6	Summary and Conclusions . . . . .	154
<b>7</b>	<b>Summary and Conclusions</b>	<b>156</b>
7.1	Future Work . . . . .	160
	<b>References</b>	<b>163</b>

# Journals and Conferences

- **N. K. Ponon**, D. J. R. Appleby, Erhan Arac, P. J. King, K. S. K. Kwa, and A. O'Neill, "Effect of deposition conditions and post deposition anneal on reactively sputtered titanium nitride thin films," *Journal of Applied Physics* -Submitted.
- D. J. R. Appleby, **N. K. Ponon**, K. S. K. Kwa, U. Hannemann, P. K. Petrov, N. M. Alford, and A. O'Neill, "Ferroelectric properties in thin film barium titanate grown using pulsed laser deposition," *Journal of Applied Physics* -Submitted.
- D. J. R. Appleby, **N. K. Ponon**, K. S. K. Kwa, B. Zou, P. K. Petrov, T. Wang, N. M. Alford, and A. O'Neill, "Experimental observation of negative capacitance in ferroelectrics at room temperature," *Nano Letters* -Article ASAP.
- **N. K. Ponon**, D. J. R. Appleby, Erhan Arac, K. S. K. Kwa, J. P. Goss, U. Hannemann, P. K. Petrov, N. M. Alford and A. O'Neill, "Impact of Crystalline Orientation on the Switching Field in Barium Titanate Using Piezoresponse Force Spectroscopy," in *Advances in Scanning Probe Microscopy, MRS Proceedings*, 1652, 2014.
- D. J. R. Appleby, **N. K. Ponon**, S. A. Mojarad, J. P. Goss, Z. Zhou, U. Hannemann, P. K. Petrov, K. S. K. Kwa, N. M. Alford, and A. O'Neill, "Low temperature fabrication of STO capacitors for integration with silicon," *E-MRS Spring Meeting*, 27-31 May 2013, Strasbourg, France.
- S. A. Mojarad, J. P. Goss, K. S. K. Kwa, Z. Zhou, R. A. S. Al-Hamadany, D. J. R. Appleby, **N. K. Ponon** and A. O'Neill, "Leakage current asymmetry and resistive switching behaviour of SrTiO<sub>3</sub>," *Applied Physics Letters*, 101, 173507 (2012).

- **N. K. Ponon**, D. J. R. Appleby, S. A. Mojarad, K. Kwa, and A. O'Neill, "Ferroelectric for nanoelectronics," *Intel European Research and Innovation Conference*, 3-4 October 2012, Dublin, Ireland.
- S. A. Mojarad, K. S. K. Kwa, J. P. Goss, Z. Zhou, **N. K. Ponon**, D. J. R. Appleby, R. A. S. Al-Hamadany, and A. O'Neill, "A comprehensive study on the leakage current mechanisms of Pt/SrTiO<sub>3</sub>/Pt capacitor," *Journal of Applied Physics*, vol. 111, no. 1, p. 014503, 2012.
- **N. K. Ponon**, D. J. R. Appleby, Z. Zhou, K. S. K. Kwa, and A. O'Neill, "Ferroelectric for nanoelectronics," *Intel European Research and Innovation Conference*, 13-14 October 2011, Dublin, Ireland.

# List of Figures

1.1	Plot of polarisation (P) against external electric field (E) for (a) dielectric, (b) paraelectric and (c) ferroelectric materials. . . . .	2
1.2	Series capacitance model showing a ferroelectric negative capacitor in series with a non ferroelectric capacitor showing an overall positive capacitance. . . . .	4
2.1	Illustration of (a) unit cell of tetragonal BaTiO <sub>3</sub> . The Ti <sup>4+</sup> ion is displaced from the centre (schematically represented by the arrow) in the tetragonal structure leading to spontaneous polarisation. Also shown is the c-axis of the lattice. (b) Ferroelectric hysteresis loop. E <sub>c</sub> is coercive electric field and P <sub>R</sub> is remnant polarisation. . . . .	13
2.2	Schematic illustration of the temperature dependent ferroelectric phase transitions in BaTiO <sub>3</sub> . In the figure, a, b, c are the lattice parameters and α, β, and γ are angles between each side. Arrows indicate the direction of spontaneous polarisation for each phase. . . . .	14
2.3	Showing the (a) ‘upward’ and (b) ‘downward’ states of polarisation in tetragonal BaTiO <sub>3</sub> . . . . .	15
2.4	Cohen’s cube showing the sequence of field induced phase transition. T is tetragonal, O is orthorhombic, R is rhombohedral, M <sub>A</sub> , M <sub>B</sub> , M <sub>C</sub> are the monoclinic phases. Arrows indicate the direction of spontaneous polarisation for each phase. . . . .	18
2.5	‘S’ shaped curve showing the relationship between fraction of phase transformation and time for a specific annealing temperature. . . . .	19
2.6	Illustration of crystallographic directions and planes in a crystal lattice. . . .	21

---

2.7	Schematic illustration of the cross-section of a classic CMOS with FEOL separated from BEOL, after [51]. . . . .	21
2.8	Schematic illustration of failure mechanisms in thin films, showing (a) cracking, (b) de-lamination, (c) pinholes and (d) hillock formation. . . .	24
3.1	Illustration of a DC sputter deposition system. . . . .	30
3.2	Showing (a) Oxford Plasma400 sputter chamber with three different targets assembled, (b) warped titanium target due to insufficient cooling and (c) BaTiO <sub>3</sub> target bonded to a copper backing plate . . . . .	32
3.3	Thornton's zone structure model showing the influence of the deposition conditions on the structure and topography of a sputtered coating, after [69]. In the figure T is the substrate temperature and $T_m$ is the melting point of the depositing material. . . . .	34
3.4	(a) Schematic representation of Park Systems XE 150 AFM setup, (b) shows the scanning electron microscopy image of CDT-NCHR AFM tip, (c) the attractive force experienced between tip and the sample surface when operated in non contact mode and (d) three dimensional topography scan of BaTiO <sub>3</sub> surface using non contact mode. . . . .	41
3.5	Plot of force experienced by the tip as a function of tip distance from the sample. . . . .	42
3.6	Illustrating the shift in non contact AFM tip resonance curve due to surface interactions. . . . .	43
3.7	Showing (a) schematic illustration of I-AFM measurement setup used for this research and (b) leakage current map of SrTiO <sub>3</sub> on platinum bottom electrode [78] measured using the XE 150 AFM used for this research. . . .	46

3.8	Additional setup required for External I-AFM measurement using XE-150 AFM from park systems. Shows the AFM head with head extension which is connected to the current amplifier. Output of the current amplifier is connected to the AFM through frame module. Inset shows the modified AFM head with the mounted I-AFM tip which has a wire connected to the cantilever to detect the current. . . . .	47
3.9	I-AFM components mounted on the AFM. AFM is placed inside an isolation box to avoid effects from the environment. . . . .	47
3.10	Variation in average leakage current through a $1 \mu\text{m} \times 1 \mu\text{m}$ area for different values of contact force. . . . .	48
3.11	Expansion and contraction of a ferroelectric domain on the application of an external field. Domain expansion causes the cantilever to deflect more and contraction will reduce the bending compared to the initial state. . . . .	51
3.12	Illustrating contraction and expansion of the ferroelectric domain due to AC biasing of the tip and deflection of the laser due to deformations. Showing (a) PFS scanning of a domain with downward polarisation and (b) PFS scanning of a domain with upward polarisation. The amplitude of oscillation depends on the longitudinal piezoresponse and the phase depends on the direction of ferroelectric polarisation. Amplitude and phase are then detected using a lock-in technique. . . . .	52
3.13	Illustrating (a) setup for PFM and PFS measurements, (b) Connections for PFM measurement using XE 150 and SR830 and (c) a typical PFS amplitude and phase measurement [82] . . . . .	55
3.14	Illustrating the operating principle of XRD . . . . .	56
3.15	Showing (a) illustration of an XPS instrument setup and (b) XPS survey spectrum of $\text{BaTiO}_3$ . CPS is counts per seconds . . . . .	58
3.16	Illustration of four-point probe measurement technique . . . . .	60
3.17	Three possible four-probe measurement configuration for a dual configuration technique [86] . . . . .	61

3.18	Sheet resistances of three different samples measured using three different inter-probe spacing using the dual configuration technique after [87]. Inset defines the inter-probe spacing $d_1$ , $d_2$ and $d_3$ . Sheet resistance measurements for this research were all carried out on the same system. . . .	62
4.1	Variation in the potential drop between the electrodes at different power levels for a fixed deposition time of 4 minutes. Initially, when the applied power was 100 W, the variation in the voltage between the start and end of the process is high, indicating the presence and the removal of the surface layer. In the following steps the variation is minimal indicating that the surface layer has been removed and the target is pure titanium. . . . .	71
4.2	Oxygen content variation in the $TiN_x$ films deposited at different vacuum levels measured by XPS. The sample deposited at improved vacuum has lower oxygen contamination in the film compared to the one deposited at $1 \times 10^{-6}$ Torr. . . . .	72
4.3	Variation in resistivity and rate of deposition with increase in nitrogen flow rate for fixed deposition time of 10 minutes, power of 800 W and substrate temperature of 250 °C. . . . .	73
4.4	Variation in resistivity with (a) power and (b) substrate temperature for samples deposited with 95% nitrogen content. . . . .	74
4.5	Resistivity vs annealing temperature for low temperature furnace annealing in air for $TiN_x$ deposited with 95% nitrogen flow rate. $TiN_x$ showed good oxidation resistance below 500 °C and was completely oxidised at 550 °C. The film annealed at 550 °C showed insulating properties and the measured current was below the detection of the measurement system. Hence, the data point is not shown in the plot. . . . .	76
4.6	Variation of $TiN_x$ resistivity with annealing temperature for a fixed annealing time of 1 minute, showing the decrease in resistivity with annealing temperature. . . . .	77

4.7	Variation in $\text{TiN}_x$ resistivity with annealing time for a fixed annealing temperature of 700 °C. Resistivity is inversely proportional to annealing time. . . . .	78
4.8	Variation in resistivity with variation in nitrogen content, annealing time and temperature. The as-deposited samples are presented at temperature 25 °C and time 0 minutes. Resistivity is inversely proportional to nitrogen flow rate, annealing temperature and annealing time. Highest resistivity was observed on as-deposited 20% sample and the lowest resistivity was observed on 95% sample annealed at 900°C for 20 minutes. . . . .	79
4.9	XRD spectra showing primarily two preferred orientations for $\text{TiN}_x$ 20% and 95% samples as-deposited, and annealed at 700 °C for 1 minute and 10 minutes. . . . .	80
4.10	Grain sizes calculated using Scherrer equation for $\text{TiN}_x$ deposited at various nitrogen flow rates. . . . .	81
4.11	Relative intensity of [111] peak to [200] peaks of TiN in XRD spectra against variation in nitrogen flow rate. . . . .	81
4.12	Raman spectra of as-deposited and annealed (700 °C, 10 minutes) $\text{TiN}_x$ deposited at 20% and 95% nitrogen flow rate. . . . .	82
4.13	High resolution XPS spectra of Ti 2 <i>p</i> of as-deposited and annealed (900 °C, 20 min) samples deposited at 20% and 95% nitrogen content. . . . .	84
4.14	High resolution XPS spectra of N 1 <i>s</i> of as-deposited and annealed (900 °C, 20 minutes) samples deposited at 20% and 95% nitrogen content. . . . .	85
4.15	High resolution XPS spectra of O 1 <i>s</i> of as-deposited and annealed (900 °C, 20 min) samples deposited at 20% and 95% nitrogen content. . . . .	86
4.16	Variations in nitrogen, oxygen and titanium concentration before and after anneal for $\text{TiN}_x$ deposited at various gas flow rates. . . . .	87

4.17	XPS depth profile of $\text{TiN}_x$ deposited at 95% nitrogen and annealed at 700 °C for 10 minutes. Results demonstrate the stability of $\text{TiN}_x$ films at high temperature processing against silicon or oxygen diffusion from the $\text{SiO}_2$ layer underneath. . . . .	87
4.18	Surface roughness of as-deposited and annealed (900 °C, 20 minutes) against various gas flow rates. Surface roughness increases for nitrogen content samples compared to high nitrogen content samples, indicating good stability against annealing. . . . .	88
4.19	AFM topography scan of as-deposited film deposited with (a) 20% and (b) 95% nitrogen flow. The surface irregularities on the 20% sample are much larger than the one deposited at 95% nitrogen flow. . . . .	89
4.20	AFM surface scan of $\text{TiN}_x$ deposited with 95% nitrogen flow rate and annealed at 900 °C. The surface is found to be smooth and free of any protrusions or de-lamination, showing good stability against high temperature processing. . . . .	89
4.21	Etching of 70 nm $\text{TiN}_x$ deposited on $\text{BaTiO}_3$ . There is no more increase in the step height once the $\text{TiN}_x$ is completely etched, showing good selectivity of the etchant against $\text{BaTiO}_3$ . . . . .	93
4.22	Optical microscopy image of $\text{TiN}_x$ top electrodes for $\text{BaTiO}_3$ based MIM capacitors patterned by reactive ion etching using $\text{SF}_6/\text{Ar}$ . . . . .	93
5.1	XPS survey scan of sputter deposited $\text{BaTiO}_3$ . Surface layer was etched in the XPS chamber in order to avoid contribution from surface contamination. Results show the presence of barium, titanium and oxygen. CPS is counts per second. . . . .	101
5.2	High resolution XPS spectra of (a) Ba 3 <i>d</i> , (b) Ti 2 <i>p</i> and (c) O 1 <i>s</i> . Binding energies of the corresponding XPS peaks indicate a stoichiometric $\text{BaTiO}_3$ as described in the text. . . . .	102

5.3	Showing (a) $1\ \mu\text{m} \times 1\ \mu\text{m}$ and (b) $10\ \mu\text{m} \times 10\ \mu\text{m}$ AFM topography scan of as-deposited $\text{BaTiO}_3$ on $\text{TiN}_x$ . As-deposited films are found to be smooth and without any pinholes or cracks on the surface. . . . .	103
5.4	Schematic illustration of electric field lines passing through the insulator of a MIM capacitor. . . . .	103
5.5	Leakage current per unit area for $\text{TiN}/\text{BaTiO}_3/\text{TiN}$ MIM capacitor with circular top electrodes. Leakage current density expressed in $\text{A}/\text{cm}^2$ increases with decrease in electrode area, indicating that this form of representation still depends on the geometry of the electrodes. For electric field lower than $100\ \text{kV}/\text{cm}$ , the leakage current is very low resulting in a very low signal to noise ratio. . . . .	104
5.6	Plot of leakage current density (in $\text{A}/\text{cm}^2$ ) against perimeter to area ratio for an electric field strength of $600\ \text{kV}/\text{cm}$ , based on equation 5.3. . . . .	106
5.7	Areal current density and peripheral current density extracted from equation 5.3 for $d$ ranging from $50\ \mu\text{m}$ to $300\ \mu\text{m}$ at various values of electric fields. . . . .	106
5.8	Showing the peripheral leakage current, areal leakage current, total current and measured current for a device with $50\ \mu\text{m}$ electrode. Results imply that the peripheral leakage is a major contribution towards the total leakage for small electrodes. . . . .	107
5.9	Showing (a) peripheral leakage current, areal leakage current and total current against electrode diameter and (b) ratio of perimeter to area against electrode diameter. Illustrates that the peripheral leakage makes a significant contribution towards the total leakage. This is down to the high perimeter to area ratio as the electrode size becomes smaller. . . . .	109
5.10	Optical microscopy images of $100\ \text{nm}$ thick amorphous $\text{BaTiO}_3$ deposited on (a) platinum electrode, (b) $\text{TiN}_x$ electrode and annealed, (c) nickel electrode and annealed and (d) platinum electrode and annealed. RTP was done at $750\ ^\circ\text{C}$ for $60\ \text{s}$ in forming gas ( $\text{N}_2/\text{H}_2$ ). . . . .	110

- 5.11 Showing optical microscopy image of 80 nm thick BaTiO<sub>3</sub> deposited on TiN<sub>x</sub> and annealed at 750 °C for 60 s, with a ramp up rate of 75 °C/minute and ramp down rate of 25 °C/minute. Numerous small dots seen on the surface are either pinholes or hillocks. . . . . 112
- 5.12 Surface roughness against thickness for BaTiO<sub>3</sub> films deposited on TiN<sub>x</sub> annealed at different temperatures and a fixed time of 60 s. A large increase in the roughness implies presence of pinholes or de-lamination. A critical roughness of 2 nm was observed for the formation of pinholes. Demonstrates that pinhole formation is dependent on both annealing temperature and film thickness. . . . . 112
- 5.13 AFM topography scan of (a) 30 nm and (b) 50 nm thick BaTiO<sub>3</sub> deposited on TiN<sub>x</sub> and annealed at 750 °C in forming gas. Figures show the dependence of film stability on thickness, after annealing. . . . . 113
- 5.14 Effect of thickness and RTP temperature on the pinhole formation in BaTiO<sub>3</sub> deposited on TiN<sub>x</sub>. Maximum thickness of BaTiO<sub>3</sub>, in order to obtain a pinhole free film after a post deposition anneal decreases with increase in RTP temperature. Data points indicate the onset of pinhole formation. Shaded region provides the parameter space for producing pinhole free films. . . . . 114
- 5.15 Process flow for the deposition and RTP of multi-layered BaTiO<sub>3</sub> on TiN<sub>x</sub>. . 116
- 5.16 Optical microscopy images of (a) multi-layered and (b) single layered BaTiO<sub>3</sub> having a thickness of 80 nm. Films were deposited on TiN<sub>x</sub> and the RTP was at 800 °C in forming gas for 60 s. Multi-layered films are pinhole free compared to single layered films which shows pinholes. . . . . 116
- 5.17 AFM topography of multi-layered (left column) and single layered (right column) BaTiO<sub>3</sub> on TiN<sub>x</sub> after post deposition RTP. . . . . 118

- 5.18 Showing the RMS surface roughness measured using AFM topography scans on multi-layered and single layered films with thicknesses varying from 20 nm to 80 nm. Demonstrates that the surface roughness of the multi-layered films do not increase with thickness compared to single layered films after the post deposition RTP at 800 °C. . . . . 119
- 5.19 Shows (a) AFM topography scan and (b) I-AFM scan of 80 nm thick single layered BaTiO<sub>3</sub> on TiN<sub>x</sub> annealed at 800 °C for 60 s. Areas which showed very high leakage in (b) corresponds to pinholes in (a). (i), (ii), (iii) and (iv) show the topography variation and leakage current across a horizontal line in the AFM image. The results illustrate that the pinholes are major source of leakage in single layered films of 80 nm thickness. . . . . 120
- 5.20 Shows (a) AFM topography scan and (b) I-AFM scan of 80 nm thick multi-layered BaTiO<sub>3</sub> on TiN<sub>x</sub> annealed at 800 °C for 60 s. (i), (ii), (iii) and (iv) show the topography variation and leakage current across a horizontal line in the AFM image. The results illustrate that the leakage current is not through pinholes in multi-layered films. . . . . 122
- 5.21 Shows the RMS leakage current measured from I-AFM scans on multi-layered film of various thicknesses. The RMS leakage current decreases with increase in number of layers or layer thickness. . . . . 123
- 5.22 XPS survey spectrum of 20 nm thick BaTiO<sub>3</sub> deposited on TiN<sub>x</sub> and undergone an RTP at 800 °C for 60 s. . . . . 123
- 5.23 High resolution XPS spectra of (a) Ba 3*d*, (b) Ti 2*p* and (c) O 1*s* of 20 nm thick BaTiO<sub>3</sub> deposited on TiN<sub>x</sub> and undergone an RTP at 800 °C for 60 s. Binding energies of the corresponding XPS peaks indicate a stoichiometric BaTiO<sub>3</sub> even after the RTP. . . . . 124
- 5.24 AFM topography of (a) as-deposited and (b) annealed multi-layer BaTiO<sub>3</sub> having a thickness of 80 nm. In the multi-layer deposition process, RTP were done at 800 °C for 60 s. . . . . 125

- 5.25 Showing EFM scan of  $8 \mu\text{m} \times 8 \mu\text{m}$  region on an 80 nm thick multi-layered BaTiO<sub>3</sub> (a) prior to an electrical loading and (b) after loading a  $4 \mu\text{m} \times 4 \mu\text{m}$  region inside the  $8 \mu\text{m} \times 8 \mu\text{m}$  region. Stripe pattern was obtained by reversing the polarity of applied bias while loading. Figure confirms the ferroelectric property of the multi-layered BaTiO<sub>3</sub>. . . . . 126
- 6.1 XRD of BaTiO<sub>3</sub> showing the polycrystalline nature of the film deposited on Pt. BaTiO<sub>3</sub> shows three preferred orientations including [001], [101] and [111]. . . . . 135
- 6.2 XRD spectrum of BaTiO<sub>3</sub> reference sample deposited on epitaxially grown SrRuO<sub>3</sub> on SrTiO<sub>3</sub> single crystal substrate. BaTiO<sub>3</sub> is grown in the same crystal orientation as that of the substrate. . . . . 135
- 6.3 XPS survey scan of BaTiO<sub>3</sub> film. Measurements were taken after etching away the surface layer in the XPS chamber in order to avoid any contribution from surface contamination. Results indicate presence of barium, titanium and oxygen and do not show any contamination or diffusion. Argon is believed to have originated from the ion source during XPS etching. O KLL and Ba MNN are the Auger peaks. . . . . 136
- 6.4 High resolution XPS spectra of (a) Ba 3*d*, (b) Ti 2*p* and (c) O 1*s*. Binding energies of the corresponding peaks indicate a stoichiometric BaTiO<sub>3</sub> as described in the text. . . . . 136
- 6.5 AFM topography of 160 nm BaTiO<sub>3</sub> deposited on Pt/Ti/SiO<sub>2</sub>/Si. AFM surface scan illustrates an average grain size of 30 nm. . . . . 137
- 6.6 EFM scan of (a)  $8 \mu\text{m} \times 8 \mu\text{m}$  area which covers a previously polarised  $4 \mu\text{m} \times 4 \mu\text{m}$  area. The ability of the film to retain the polarisation after removal of electric field indicates the ferroelectric nature of the film. (b) PFM scan of  $1.5 \mu\text{m} \times 1.5 \mu\text{m}$  from the previously polarised region. Ferroelectric domains are identifiable with their contrasting colours. Ferroelectric domains are more than 200 nm in diameter and are much larger than grain sizes shown in Fig. 6.5. . . . . 138

- 6.7 TEM images of (a) cross section of BaTiO<sub>3</sub> sandwiched between platinum electrodes and (b) high resolution TEM highlighting individual columns. Regions showing non overlapping crystals are demarcated by dotted lines. Orientation of the column is shown by red lines in region (1). A Similar orientation runs through other regions, indicating that the same orientation is present throughout the column. . . . . 139
- 6.8 Dependence of longitudinal piezoelectric coefficient,  $d_{zz}$  on direction of polarisation in BaTiO<sub>3</sub> calculated based on equation. 6.1. The maximum of piezoresponse occurs when the polarisation is oriented at 49° with measurement direction. . . . . 140
- 6.9 Amplitude (a) and phase (b) of reference BaTiO<sub>3</sub> sample epitaxially grown on [001] oriented single crystal substrate. Arrows indicate direction of electric field sweeping. There is no enhanced piezoresponse in the amplitude signal and polarisation rotation is not apparent from the phase signal implying a one-step direct switching. The forward and reverse sweeps were taken as two different measurements with a 2 s hold between the measurements resulting in a noncontinuous spectra. The DC bias was set to 0 V between measurements. This was done since a continuous sweep always resulted in a pseudo-enhanced piezoresponse between the forward and reverse seeps. . . . . 141
- 6.10 (a) amplitude and (b) phase of piezoresponse as a function of applied electric field. The units of amplitude and phase are arbitrary, as explained in the text. The arrows indicate the direction of electric field sweeping. . . . 142

- 6.11 Direction the polarisation vector makes with longitudinal axis at different electric fields for the forward sweep (-500 kV/cm to +500 kV/cm) and reverse sweep (-500 kV/cm to +500 kV/cm). Red and blue colours indicate the up and down orientation of the polarisation respectively. Figure indicates that the polarisation reversal is a two step mechanism which includes both polarisation rotation and switching. Polarisation rotation is indicated as same coloured arrows and the switching happens when the colour of the arrows changes. Inset shows the direction of polarisation and tetragonal phase of the BaTiO<sub>3</sub> at zero field. . . . . 145
- 6.12 PFS spectra taken at three different domains. Arrows indicate the spectra for forward and reverse sweeping of the electric field. The coercive field (indicated by dotted lines) decreases as the c-axis of the tetragonal lattice moves away from the perpendicular direction. The domains are predicted as (a) [001], (b) [101] (or [011]) and (c) [111] as explained in the text. . . . 147
- 6.13 Schematic illustration of polarisation reversal in ferroelectric domains of spectrum in Fig. 6.12 (a) during a forward sweep showing; (a) orientation of the polarisation at high negative fields (point (1)), (b) the direction of polarisation at zero field (point (2)) and (c) the switching of direction of polarisation at coercive field (point (3)). Point (1), (2) and (3) are marked on Fig. 6.12 (a). . . . . 149
- 6.14 Schematic illustration of polarisation reversal in ferroelectric domains of spectrum shown in Fig. 6.12 (b) during a forward sweep showing; (a) approximate orientation of the polarisation at high negative fields (point (1)), (b) orientation of polarisation at zero field (point (2)); along the c-axis of the tetragonal lattice and (c) approximate orientation of the polarisation during enhanced piezoresponse (point (3)). Point (1), (2) and (3) are marked on Fig.6.12 (b). . . . . 150

- 
- 6.15 Schematic illustration of polarisation reversal of spectrum shown in Fig. 6.12 (c) during a forward sweep showing; (a) approximate orientation of the polarisation at high negative fields (point (1)), (b) approximate orientation of the polarisation during enhanced piezoresponse (point (2)), (c) orientation of polarisation at zero field (point (3)); along the c-axis of the tetragonal lattice. Point (1), (2) and (3) are marked on Fig.6.12 (c). . . . 152
- 6.16 Variations in the switching field with variations in orientation based on five domains of each orientation for BaTiO<sub>3</sub>. Shows that polarisation rotation helps the ferroelectric domains to switch at lower fields. Coercive field reduces as the c-axis orientation of the tetragonal lattice move away from the longitudinal axis. . . . . 153
- 7.1 Schematic illustration of ferroelectric integration into the gate stack of a MOSFET in order to achieve a steep sub-threshold slope. . . . . 161

# List of Tables

3.1	Summary of thin film properties and sputtering parameters . . . . .	34
4.1	Summary of the optimised recipe for $\text{TiN}_x$ deposition. . . . .	75
4.2	$\text{TiN}_x$ dry etching recipe . . . . .	92

# Abbreviations

AFM	Atomic Force Microscopy
B.E	Binding Energy
BEOL	Back-End-Of-Line
CMOS	Complementary Metal-Oxide-Semiconductor
CPS	Counts per Seconds
DC	Direct Current
DI	De-Ionized
DRAM	Dynamic Random Access Memory
EFM	Electrostatic Force Microscopy
FEOL	Front-End-Of-Line
I-AFM	Current AFM
IC	Integrated Circuit
ICSD	Inorganic Crystal Structure Database
IPA	Isopropyl Alcohol
ITRS	International Technology Roadmap for Semiconductors

---

K.E	Kinetic Energy
MIM	Metal-Insulator-Metal
MOSFET	Metal-Oxide-Semiconductor Field Effect Transistor
NMP	N-Methylpyrrolidone
PFM	Piezoresponse Force Microscopy
PFS	Piezoresponse Force Spectroscopy
PLD	Pulsed Laser Deposition
PLL	Phase-Locked-Loop
PSD	Phase Sensitive Detector
PSPD	Position Sensitive Photo Detector
PVD	Physical Vapour Deposition
RCA	Radio Corporation of America
RF	Radio Frequency
RIE	Reactive Ion Etching
RMS	Root Mean Square
RTP	Rapid Thermal Processing
SC-1	Standard Clean-1
SPM	Scanning Probe Microscopy
SRAM	Static Random Access Memory
STM	Scanning Tunneling Microscopy
TEM	Transmission Electron Microscopy

ULSI	Ultra Large Scale Integration
UV	Ultra Violet
XPS	X-ray Photoelectron Spectroscopy
XRD	X-ray diffraction

## Introduction

An ever increasing demand for devices with higher packing density, faster circuit speed and lower power consumption has resulted in continued functional and dimensional scaling of complementary metal-oxide-semiconductor (CMOS) technology. The density of transistors on integrated circuits (ICs) has doubled every 18-24 months, keeping up with Moore's law, predicted in 1965 [1]. The rapid down-scaling of traditional CMOS would require new and innovative levels of miniaturisation to further develop advanced CMOS technologies, which falls in the 'more Moore' domain of the semiconductor technology roadmap. Complimenting the digital part of the integrated system is a 'more than Moore' approach which allows non digital functionalities, which may not scale with Moore's law to be incorporated in ICs, providing additional functionalities. The ever increasing need for miniaturisation and diversification of applications has brought a fierce competition for incorporating novel materials in semiconductor device fabrication. Among them, ferroelectrics are one of the closely monitored materials and they have the potential to impact on future technologies in the semiconductor industry [2–4].

Materials with a stable electrical dipole moment at zero electric field whose direction can be reversed by an external applied electric field are known as ferroelectric. When an external electric field is applied to an insulator, a polarisation is induced. For most of the materials, including SiO<sub>2</sub>, the induced polarisation is proportional to electric field as shown in Fig.1.1 (a). This is known as dielectric polarisation. Electric

permittivity, which is the slope of the polarisation-electric field curve, is a constant for these materials. For some materials, polarisation shows a nonlinear characteristic with an applied electric field and is known as paraelectric (eg.  $\text{SrTiO}_3$ ). The behaviour of paraelectric polarisation, depicted in Fig. 1.1 (b) allows these materials to show a permittivity which is dependent on the electric field. Ferroelectric materials, in addition to being nonlinear, demonstrate a remnant polarisation at zero electric field. The polarisation can be reversed by an external electric field of suitable strength, giving rise to a hysteresis loop as shown in Fig. 1.1 (c). Few examples of ferroelectric materials

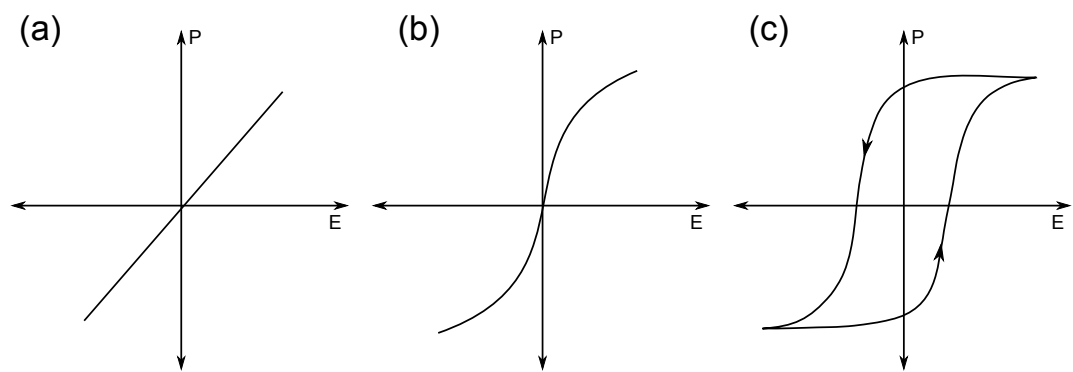


**Figure 1.1:** Plot of polarisation (P) against external electric field (E) for (a) dielectric, (b) paraelectric and (c) ferroelectric materials.

include  $\text{BaTiO}_3$ ,  $\text{PbTiO}_3$ ,  $\text{Pb}_x\text{Zr}_{1-x}\text{TiO}_3$  (PZT), polyvinylidene fluoride (PVDF) and triglycine sulfate.

Since ferroelectricity was discovered back in 1921 [5], its potential application in realising memory and logic circuits had been conceptualised due to the two stable polarisation states it can offer [6]. The advances in integrated silicon devices and thin film processing in the late 1960s and early 1970s triggered a further development of ferroelectric thin film based non-volatile memories [7, 8]. Further research into this field led to the demonstration of a ferroelectric memory integrated with silicon CMOS in 1988 [9]. Research had already started towards the integration of ferroelectric based micro-sensors and micro electro mechanical systems (MEMS) by then. An increased interest in these materials among the scientific community led to further understanding of the material and the physics, which in turn resulted in their usage in a plethora of applications. Among these applications, some are commercially available, and others

were demonstrated in research labs around the globe.

In recent years, ferroelectric research is spreading out in several directions [3]. Ferroelectric materials are used in a variety of applications, not only because of their polarisation switching properties, but also due to their excellent dielectric, piezoelectric, pyroelectric and optical properties. In the past 20 years there has been a surge in literatures based on the applications of ferroelectric materials which includes ferroelectric memories capable of switching at a standard logic level voltage (5 V) for silicon transistors [10], micro-sensors and actuators, microwave electronic components, electrically controlled tunnel junction [11], electrocaloric cooling devices [12], resistive random access memories (RRAMS) [13] and photovoltaics [14].

An important aspect of the thin films produced out of these materials is that their properties can be varied by controlling the deposition conditions. For example, the ferroelectric properties of  $\text{BaTiO}_3$  can be varied by incorporating strontium [15]. The composition of barium and strontium in  $\text{Ba}_x\text{Sr}_{1-x}\text{TiO}_3$  can be varied such that films are paraelectric at specific temperatures which show a very high non-linear dielectric response to an applied electric field. Tuneable capacitors thus formed have attracted interest in integrated circuits for communication devices as elements for dynamic impedance matching circuits or in power amplifier circuits. Capacitors are amongst the largest elements in integrated circuits. Hence, the integration of ferroelectric based tuneable capacitors in the back-end-of-line (BEOL) metallisation of radio frequency (RF) CMOS would reduce the size per unit capacitance of next generation communication devices. Integration of ferroelectric tuneable capacitors in the BEOL falls in the ‘more than Moore’ agenda of increased IC functionality by integrating new materials. These high- $\kappa$  films can also be used as capacitor elements in dynamic random access memory (DRAM) cells in order to increase the packing density.

More interestingly, recent experimental evidence [16–18] of ferroelectric materials showing effective negative capacitance has led to the speculation that it can reduce the required change in gate potential below 60 mV for a decade change in the current (known as the sub-threshold swing) of a metal-oxide-semiconductor field effect

transistor (MOSFET) [19, 20]. This could potentially break the fundamental lower limit on the operating voltage [21] and hence reduce the power dissipation in CMOS IC.

Since a negative capacitance correspond with a negative energy density, it must be incorporated into a device with overall positive capacitance and hence positive energy density. The total capacitance ( $C_T$ ) in a series capacitor model is given by;

$$\frac{1}{C_T} = \frac{1}{C_D} + \frac{1}{C_F} \quad (1.1)$$

where  $C_D$  is the capacitance of the dielectric and  $C_F$  is the capacitance of the ferroelectric material which is negative. The series capacitance model is given in Fig. 1.2. Equation 1.1 implies that for certain values of  $C_D$  and  $C_F$ ,  $C_T$  can be positive,

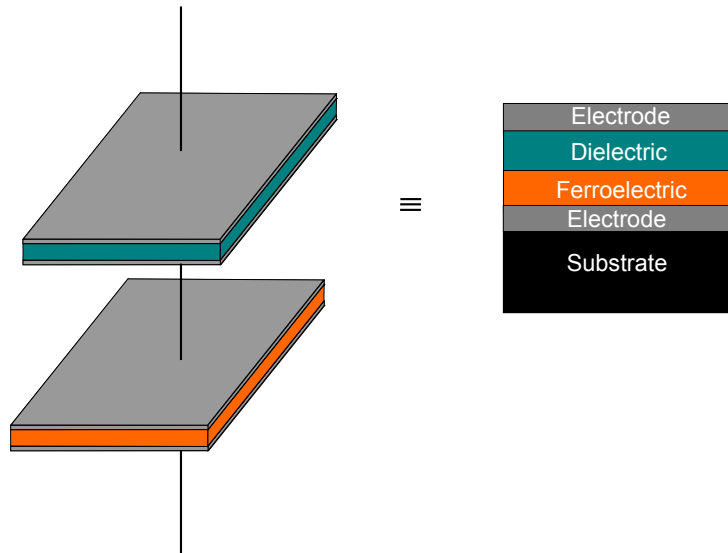


**Figure 1.2:** Series capacitance model showing a ferroelectric negative capacitor in series with a non ferroelectric capacitor showing an overall positive capacitance.

providing a stable overall capacitance. It has been demonstrated experimentally that a metal-insulator-metal (MIM) capacitor stack consisting of a ferroelectric thin film ( $\text{BaTiO}_3$ ) in series with a non ferroelectric film ( $\text{SrTiO}_3$ ) can show an increase in overall capacitance at room temperature [18]. The inclusion of a ferroelectric film in the series capacitor model was shown to introduce a negative capacitance which increased the overall capacitance, which would have been lower than the individual capacitances otherwise.

The ferroelectric effect is a collective phenomenon which arises from a positive

---

feedback where an applied external field increase the internal electric field. This increase in the internal field further increases the polarisation, which again increases the internal field [22]. The internal positive feedback effect provided by the negative capacitance of the ferroelectric capacitor which is in series with the gate dielectric acts as a step-up voltage transformer that will amplify the gate voltage thus reducing the sub-threshold swing of a MOSFET below 60 mV/dec [19]. Incorporation of ferroelectric materials in the gate stack of a MOSFET in the front-end-of-line (FEOL) may reduce the sub-threshold slope and thereby reduce power consumption, enabling the advancement of the ‘more Moore’ agenda of CMOS IC scaling. Utilisation of ferroelectric materials in CMOS integrated circuits is not just limited to tuneable capacitors, DRAM and the gate stack. The hysteresis effect arises due to the ability to switch a permanent electric dipole moment by the application of an electric field, which can be used to realise ‘universal memories’ that can be packed more densely than DRAM, as fast as a flash memory, and have the retention power of static random access memory (SRAM) [3, 23].

It is imperative to understand and produce high quality ferroelectric thin films for each of these applications. The negative capacitance models discussed earlier were demonstrated on lattice matched substrates such as SrTiO<sub>3</sub>. However a major challenge in using ferroelectric thin films in integrated circuits is their integration on silicon [24]. The International technology roadmap for semiconductors (ITRS) has recognised the potential of ferroelectric materials as an emerging research material, even though their integration with existing CMOS processing has been identified as a significant challenge [25]. One of the major problems associated with silicon integration is that, most of the ferroelectric materials have a crystallisation temperature above 500 °C. Ferroelectricity is a collective phenomenon as described in the previous section, hence a crystalline phase is required. Even though organic ferroelectrics (eg. PVDF) have a lower crystallisation temperature, ferroelectric oxides are preferred for silicon integration due to their sharp and well-behaved hysteresis and better dynamic response [25]. A leading ferroelectric oxide candidate for the integration with CMOS

is BaTiO<sub>3</sub>. Although Pb<sub>x</sub>Zr<sub>1-x</sub>TiO<sub>3</sub> (PZT) is a well known ferroelectric/piezoelectric material which is used in a variety of commercially available applications, an increasing environmental concern and legislation against lead-based materials pushes for alternatives.

BaTiO<sub>3</sub> is a lead-free perovskite material which shows ferroelectric properties at room temperature [26] and has found a wide range of potential applications. It shows an intrinsic coercive field value close to 250 kV/cm in an unstrained state [27] and a remnant polarisation of 15  $\mu\text{C}/\text{cm}^2$  [28]. BaTiO<sub>3</sub> has gained a lot of attention recently due to the experimental evidence of ferroelectric BaTiO<sub>3</sub> showing effective negative permittivity [18, 29]. Moreover, its properties can be optimised during deposition for its application in ferroelectric memories, tuneable capacitors or in DRAM cells. They can also be directly integrated to mature silicon technology with existing, process compatible deposition techniques. However, their integration also poses challenges. Hence, research should be focused to address those fabrication issues before they can be integrated into CMOS for realising various applications.

Like most of the other ferroelectric oxides, BaTiO<sub>3</sub> also requires a very high crystallisation temperature, which is generally above 700 °C [30]. These elevated crystallisation temperatures are expected to cause issues for silicon integration. An elevated substrate temperature is not compatible for CMOS manufacturing mainly due to inter-diffusion of materials. Hence, rapid thermal processing (RTP) which involves rapid ramp-up and ramp-down of annealing temperatures is essential for crystallisation of these materials. An RTP process could affect the stability of the deposited thin film when there is a mismatch between the thermal coefficients of expansion between the film and the silicon substrate. However, this needs to be verified in the case of BaTiO<sub>3</sub> thin films and methods should be developed to evade this if it is an issue. Moreover, the fabricated films should also be characterised in order to confirm their quality.

The fundamental role of ferroelectric materials in the electronics industry is as the insulating layer of a capacitor. Hence, the properties of electrode or buffer layer used to deposit BaTiO<sub>3</sub> is also significant. Moreover, thin films of these electrodes

should also be able to withstand the high temperature processing which the BaTiO<sub>3</sub> film will be undergoing. Since most metals are prone to diffusion and oxidation at high annealing temperatures, thin films of conductive oxides or nitrides are used as the electrodes [30, 31] for ferroelectric films. TiN<sub>x</sub> is a refractory metal nitride which is widely used in CMOS processing as an adhesion layer, gate electrode, capacitor electrode and diffusion barrier [25]. Their properties can also be optimised by varying the deposition conditions. If it is possible to optimise the TiN<sub>x</sub> such that it can withstand a high temperature anneal without deteriorating its electrical properties, they can act as a cheap alternative for a number of applications including ferroelectric integration. However, their properties need to be well understood and optimised to match the process conditions required for BaTiO<sub>3</sub>. Electrical characteristics exhibited by these devices can be influenced by parasitic effects. Such effects will be more prominent as the device sizes become smaller. Hence, understanding the parasitic effects will also be crucial before they are integrated to a CMOS.

For memory applications, the coercive electric field required to switch ferroelectric polarisation should be compatible with the operating voltage of modern CMOS. Recent theoretical studies have suggested that the coercive field of BaTiO<sub>3</sub> can depend on the orientation of the film [32]. This is found to be due to an effect called ‘polarisation rotation’. Classical understanding of polarisation switching in ferroelectric materials is a single-step switching at the coercive field. However, polarisation in BaTiO<sub>3</sub> is predicted to rotate before it actually switches if the applied electric field is not oriented with the crystallographic orientation of the film [32, 33], and this warrants further study. Such findings and their experimental demonstration will be crucial for the functional diversification of the integrated circuits and falls in the ‘more than Moore’ agenda of CMOS IC scaling.

Scanning probe microscopy techniques provide unique information about film properties at nano-scale resolution which conventional macro-scale techniques cannot offer. Such techniques can be effectively utilised for the nano-scale analysis of the deposited film and more importantly, to experimentally demonstrate new properties

which have theoretical validity. This non destructive technique can also be improvised for understanding the properties at the domain level which would benefit in the design and characterisation of future nano-scale ferroelectric devices. The fact that the coercive field of BaTiO<sub>3</sub> can be reduced by the crystalline orientation itself could lead to realisation of lead-free ferroelectric memories.

## 1.1 Research Objectives

The overall goals of this research are to investigate the realisation and understanding of BaTiO<sub>3</sub> based ferroelectric thin films. This thesis aims to address challenges in fabricating BaTiO<sub>3</sub> thin films and elucidate the underpinning mechanisms in polarisation reversal. The context of this research is in line with the negative capacitance work carried out by Appleby et al [18], and focuses on the silicon integration issues of BaTiO<sub>3</sub>. Hence, both researches combined together will provide future directions for fabricating BaTiO<sub>3</sub> based MOSFETs which show steep sub-threshold slope. The deposition conditions will be optimised to achieve the thermal budget constraints set by the silicon technology industry. This research is timely as it tries to address fabrication issues and aims to demonstrate properties which may directly assist in achieving the ‘more Moore’ and ‘more than Moore’ concepts of the semiconductor technology roadmap. The specific objectives of this research are;

- Thin film deposition and post deposition annealing of TiN<sub>x</sub> based electrodes on silicon substrates through reactive sputtering.
- Sputter deposition and post deposition annealing of BaTiO<sub>3</sub> on silicon substrates.
- Developing methods to deposit thin film BaTiO<sub>3</sub> on silicon substrates which can withstand high temperature post deposition annealing.
- Optimisation of deposition conditions such that the processing temperature is silicon process compatible.

- Characterisation and analysis of material and electrical properties of  $\text{BaTiO}_3$  and  $\text{TiN}_x$ .
- Experimental demonstration of polarisation reversal mechanisms in  $\text{BaTiO}_3$  at the domain level using scanning probe microscopy.

## 1.2 Research Hypothesis and Questions

The following hypotheses will be tested and the underlying physics will be understood during the course of this thesis:

**Effect of deposition conditions and post deposition annealing on reactively sputtered  $\text{TiN}_x$  thin films:-**  $\text{TiN}_x$  will be deposited using reactive sputtering at temperatures below  $500^\circ\text{C}$ . The initial hypothesis tested will be whether the process parameters, especially the nitrogen flow during deposition can be varied to modify the film resistivity.  $\text{TiN}_x$  would then undergo a post deposition anneal and its effect on resistivity will be tested. The question here will be whether the films can withstand the post deposition anneal without deteriorating its resistivity. Material characterisation techniques will be used to identify the reasons behind any variations in resistivity.

**Effect of film thickness on post deposition annealed  $\text{BaTiO}_3$  deposited on a silicon substrate:-**  $\text{BaTiO}_3$  will be deposited on a silicon substrate coated with a  $\text{TiN}_x$  electrode at a silicon process compatible temperature. Amorphous films thus produced will be post deposition annealed for the purpose of crystallisation. Initially, the film stability after RTP needs to be tested. The hypothesis to be tested here is whether there exist a critical thickness corresponding to each RTP temperature, below which films are stable and pinhole free.

**Identification of multi-layered thin films as a method of fabricating high quality ferroelectric thin films which can withstand high temperature processing:-** If a critical thickness can be identified for producing a stable  $\text{BaTiO}_3$  film after an anneal, the next question is whether a thicker film can be produced by repeating the process of deposition of thin films below its critical thickness followed by an RTP. The film's

electrical as well as material properties, including the ferroelectric effect will be tested and compared with their single layered counterparts.

**Study the effect of fringing electric fields in leakage current characteristics of micro-scale MIM capacitors.** Leakage current in a MIM capacitor depends on device dimensions. It can be hypothesised that a fringing electric field can contribute significantly towards the total leakage current in a MIM capacitor, especially when the device dimensions are a few tens of microns. Simple mathematical equations will be used to extract the leakage current due to the fringing field from the total current in order to test this hypothesis.

**Investigation of polarisation reversal mechanism in ferroelectric domains:-** It has been theoretically predicted that polarisation reversal involves complex mechanisms when the applied electric field is not parallel with the tetragonal axis (c-axis) of BaTiO<sub>3</sub>. This property will be tested at a domain level using a SPM technique by utilising the piezoresponse property shown by BaTiO<sub>3</sub>. Another hypothesis to be tested here is whether the electric field strength required to reverse the polarisation can be influenced by the orientation of the applied electric field with the c-axis of the domain.

## 1.3 Thesis Outline

Chapter 2 discusses the background of this study. This section introduces ferroelectric materials and their properties. The classical concepts related to polarisation switching and ferroelectric domain reversal are discussed along with the concept of piezoelectricity. Also given is the temperature dependent ferroelectric phase transition and field induced ferroelectric phase transition. This chapter also describes the crystallisation kinetics associated with the phase transition from an amorphous state to a crystalline state. Later in the chapter a brief discussion on TiN<sub>x</sub> is also given along with a discussion on temperature constraints due to the silicon technology processing.

In chapter 3, fabrication and characterisation techniques used to address the research hypotheses are described. The aim of this chapter is also to give a clear description of specific steps that were followed in order to carry out the research. Process parameters

used for fabrication of thin films are presented along with a brief introduction about the technique. Also given is the setup used for characterising the deposited films.

The effect of deposition conditions and post deposition annealing on reactively sputtered  $\text{TiN}_x$  thin films is given in chapter 4. This chapter commences with discussions on developing a recipe for sputter deposited  $\text{TiN}_x$  from a titanium target. Nitrogen flow rate during deposition was varied and its effect on film properties was studied. Films were then annealed and their properties are compared with the as-deposited films. The reasons for variation in the film's electrical resistivity with deposition conditions were elucidated by analysing their material properties. Also given in this chapter is a reactive ion etching recipe for selectively etching  $\text{TiN}_x$  which is deposited on  $\text{BaTiO}_3$ .

Chapter 5 discusses sputter deposition and post deposition annealing of  $\text{BaTiO}_3$  on a silicon substrate coated with  $\text{TiN}_x$  as a bottom electrode. Post deposition anneals at a temperature above  $500\text{ }^\circ\text{C}$  typically resulted in films with pinholes or de-lamination from the substrate. The study also involves finding the critical thickness below which the films are pinhole free. Later in this chapter, a multi-layer approach has been shown which was found to avoid the pinhole occurrence. Nano-scale leakage current analysis of single layered films and multi-layered films is also presented along with material characterisation of annealed  $\text{BaTiO}_3$ .

The Polarisation reversal mechanism in  $\text{BaTiO}_3$  is analysed using piezoresponse force microscopy in chapter 6. A two-step mechanism in polarisation reversal, which involves a rotation of the polarisation followed by switching has been demonstrated. Also shown in this chapter is the effect of crystalline orientation on the electric field strength that is required to reverse the polarisation. A summary of the study is presented in chapter 7 along with conclusions. Finally, directions toward future work that can be carried out based on the findings of this study are also given.

# Background

## 2.1 Introduction

This chapter provides a brief introduction to some of the concepts related to ferroelectric materials, particularly  $\text{BaTiO}_3$ . The focus of this chapter is to give adequate information which might be useful for understanding later chapters of this thesis.

Materials with a stable electric polarisation state, referred to as ‘remnant polarisation’ at zero applied bias, whose direction of polarisation can be changed by the application of an external electric field are known as ferroelectric. The concept of electric polarisation for a finite system can be defined as the average dipole moment obtained from the charge density divided by the system volume. A comprehensive understanding of ferroelectric systems is given in text books such as [34–37] and their properties and applications are reviewed thoroughly in [3, 38].

Among ferroelectric materials, perovskite oxides are of particular interest. Material which exists in the form of  $\text{ABO}_3$ , where A and B are cations and O is the oxygen anion are perovskites. A ions reside at the eight corners of the unit cell, B ion at the centre and oxygen at the face centres.  $\text{BaTiO}_3$  is an archetypical example of a ferroelectric perovskite. Fig. 2.1 (a) shows the crystal structure of  $\text{BaTiO}_3$  at room temperature. At room temperature  $\text{BaTiO}_3$  typically shows a tetragonal symmetry [26]. The positive and negative ions are displaced against each other in the tetragonal lattice which leads to a spontaneous polarisation [39] in the direction of the tetragonal axis.  $\text{BaTiO}_3$  shows

a permittivity well above 1000 when it is in the tetragonal phase [26, 38]. The ability of these materials to exhibit spontaneous polarisation originates from asymmetry in the lattice structure. However, it is the re-orientability of this spontaneous polarisation under the application of an external electric field which makes them ferroelectric.

The characteristic property of ferroelectric materials is the *hysteresis loop* occurring during a polarisation reversal, under the application of an external electric field. Fig.2.1 (b) displays typical hysteresis of the polarisation (P) as a function of the electric field (E). During an initial electrical loading, polarisation increases from  $P = 0$  with

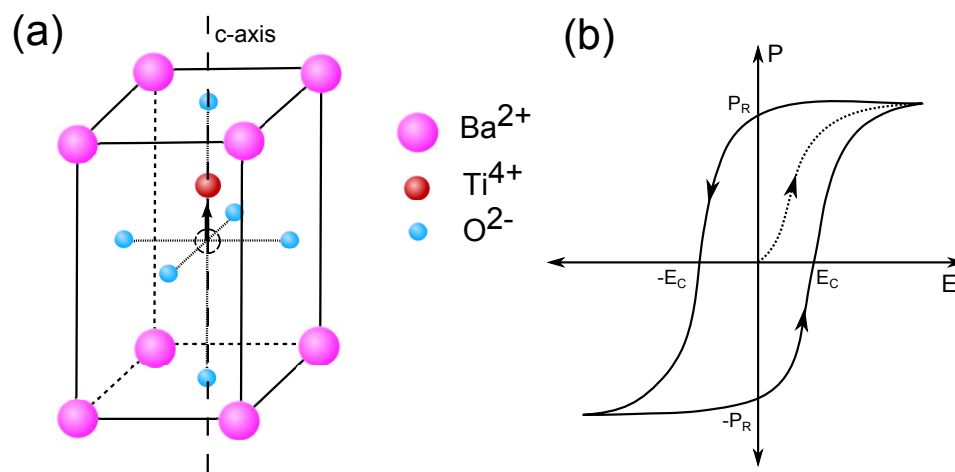


**Figure 2.1:** Illustration of (a) unit cell of tetragonal BaTiO<sub>3</sub>. The Ti<sup>4+</sup> ion is displaced from the centre (schematically represented by the arrow) in the tetragonal structure leading to spontaneous polarisation. Also shown is the c-axis of the lattice. (b) Ferroelectric hysteresis loop.  $E_c$  is coercive electric field and  $P_R$  is remnant polarisation.

an increase in the electric field until it saturates, represented by the dotted line in Fig. 2.1 (b). Upon reduction of electric field from the saturation polarisation, it reaches a remnant polarisation  $P_R$  at  $E = 0$ . For an increase in the electric field in the negative direction, the polarisation switches at a threshold negative electric field referred to as the coercive field  $E_c$ , before it saturates at higher negative fields. During the reverse sweep of the electric field (from negative to positive), polarisation follows the similar hysteresis behaviour but in a reverse sense. However, the ferroelectric property is dependent on the operating temperature and this is discussed in the next section.

## 2.2 Ferroelectric Phase Transition

Upon heating from room temperature, tetragonal  $\text{BaTiO}_3$  transforms into a cubic lattice and the positive and negative ions deform into a symmetric structure. Due to this symmetry in the cubic high temperature phase,  $\text{BaTiO}_3$  does not display any spontaneous polarisation or ferroelectricity and is paraelectric. The temperature at which ferroelectric materials transform into a paraelectric phase is called the Curie temperature.  $\text{BaTiO}_3$  has a Curie temperature around  $130^\circ\text{C}$  [26]. Fig. 2.2 depicts the temperature dependent phase transition observed in  $\text{BaTiO}_3$  which is discussed in this section. Upon cooling from room temperature, tetragonal  $\text{BaTiO}_3$  transforms into

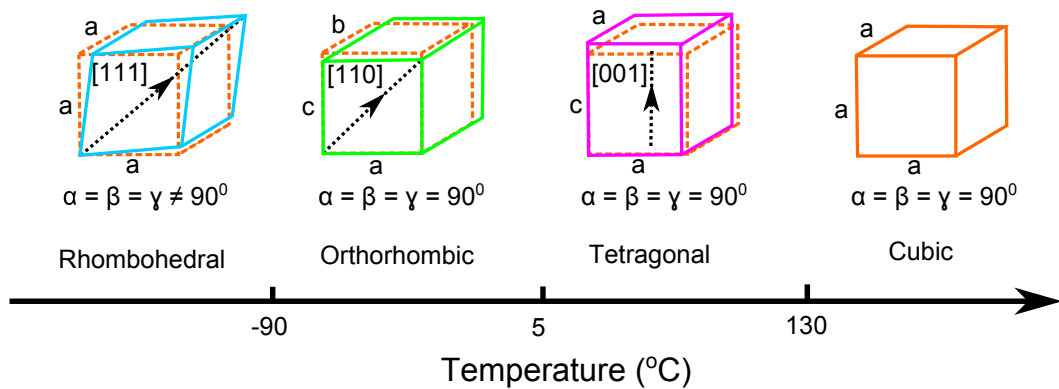


**Figure 2.2:** Schematic illustration of the temperature dependent ferroelectric phase transitions in  $\text{BaTiO}_3$ . In the figure,  $a$ ,  $b$ ,  $c$  are the lattice parameters and  $\alpha$ ,  $\beta$ , and  $\gamma$  are angles between each side. Arrows indicate the direction of spontaneous polarisation for each phase.

an orthorhombic structure. In this case the direction of spontaneous polarisation is diagonally across the face whereas it is along the tetragonal axis for a tetragonal phase as described in the last section. For a further reduction in temperature, around  $-90^\circ\text{C}$  a further transformation takes place from the orthorhombic phase to a rhombohedral phase. Here, the spontaneous polarisation is facilitated by the displacement of the central positive ion along the diagonally opposite corner. Ferroelectric materials undergo phase transitions in order to minimise the free energy. A detailed description of the thermodynamics of the field induced phase transition can be obtained from [38].

## 2.3 Ferroelectric Switching

Polarisation switching is a fundamental characteristic of a ferroelectric material and it attracts keen interest due to its role in various applications. In tetragonal  $\text{BaTiO}_3$  the central  $\text{Ti}^{4+}$  ion can move towards any of the oxygen ions along the elongated c-axis to generate spontaneous polarisation. Hence, the  $\text{Ti}^{4+}$  ion can be either in an ‘up’ or ‘down’ state along the c-axis. The notation used for the state of the  $\text{Ti}^{4+}$  ion is also the direction of polarisation. Fig. 2.3 shows the upward and downward orientation of polarisation in  $\text{BaTiO}_3$ . Considering a scenario where the c-axis is

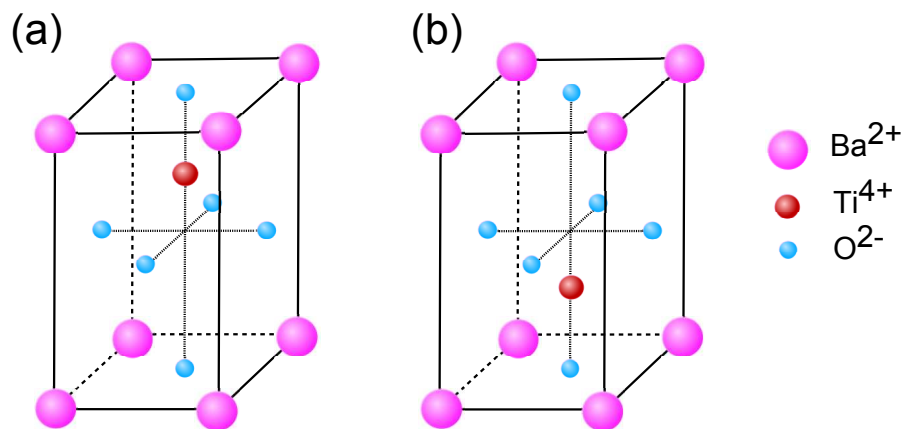


**Figure 2.3:** Showing the (a) ‘upward’ and (b) ‘downward’ states of polarisation in tetragonal  $\text{BaTiO}_3$ .

along the out-of-plane direction, and if the polarisation is pointing upwards, under the application of a positive coercive electric field along the out-of-plane axis the  $\text{Ti}^{4+}$  ion switches downwards. The polarisation switches back at a negative coercive field. The thermodynamics of a ferroelectric phase transition and polarisation switching in simple ferroelectric thin films can be explained in terms of Landau-Devonshire theory which is described well in various text books [6, 38, 40]. However, the mechanisms and kinetics of polarisation reversal is still not well understood in complex scenarios and is an area of interest [4, 32]. For example, the polarisation reversal is not straightforward direct switching if the electric field direction and direction of the c-axis are not in the same direction [32] (neither parallel nor anti-parallel). Polarisation reversal in such scenarios is explained in detail in chapter 6 of this thesis. One of the key objectives of

this thesis is the demonstration of the polarisation reversal mechanism in BaTiO<sub>3</sub> with different crystallographic orientations in the nano-scale. However, at a macroscopic level, there are additional entities to be considered and these are introduced briefly in the next section, since this understanding might be helpful in drawing an overall picture about ferroelectric switching.

### 2.3.1 Macro-scale domain reversal

A domain is a region with a uniform direction for its spontaneous polarisation. Domains are formed in ferroelectric materials in order to minimise the free energy of the system. The allowed domain directions are determined by the crystallographic orientation of the system with two possible states (up or down) for each orientation. The boundary between these domains, where an abrupt change in polarisation direction occurs, is referred to as a domain wall.

At a macroscopic scale, the classic switching scenario involves domain nucleation and domain wall movement [41] under the application of an external electric field. Lateral motion of the domain wall occurs by a nucleation step on the domain wall, which would then rapidly grow along the length of the wall, increasing the size of the favourably oriented domain. A review of different but closely related macroscopic level domain reversal mechanisms in ferroelectric materials can be obtained from [4].

## 2.4 Piezoelectricity

The piezoelectric effect is the ability of certain materials to accumulate electric charge in response to an applied mechanical stress. An important characteristic of the piezoelectric effect is that it is reversible. The converse piezoelectric effect, where the application of an electric field results in stress generation, therefore causes deformation in these materials. The converse piezoelectric effect has been utilised to detect the field induced phase transition and polarisation rotation in this research. Since any mechanical stress results in a strain in the material, all polar crystals such as ferroelectrics show piezoelectricity due to their elastic properties. In addition, this strain

will affect the polarisation in ferroelectric materials since the polarisation is caused by the displacement of charged ions.

Given below are the relationships between polarisation (P), stress (T), strain (S) and electric field (E,) defining the piezoelectric effect in materials. The relationship between the polarisation and stress is given as;

$$P = d.T \quad (2.1)$$

where d is the piezoelectric coefficient. The relationship between the strain and the applied electric field in the converse effect is given as;

$$S = d.E \quad (2.2)$$

The piezoelectric coefficient d is a rank three tensor and has only three components in ferroelectric ceramics [38] which are  $d_{33}$  (parallel component),  $d_{31}$  (perpendicular component) and  $d_{15}$  (shear component).

## 2.5 Field Induced Phase Transition

As well as the temperature dependent phase transition, the structural properties of ferroelectric materials can be influenced by an external electric field. The piezoelectric properties of these materials were found to be dependent on the initial phase of the material and the direction of applied electric field [42, 43]. An extra-ordinary piezoresponse was observed along directions other than the directions of the spontaneous polarisation [44, 45]. Experimental evidence on an enhanced piezoresponse shown by ferroelectric materials along non polar directions led to a conclusion that this is due to an effect called field induced phase transition [42]. For instance, based on calculations performed on a rhombohedral  $\text{BaTiO}_3$  which has a [111] polar direction, it was proposed that applying an electric field along the [001] direction induces a phase transition along the rhombohedral-tetragonal path through an intermediate monoclinic phase [33]. Furthermore, an orthorhombic crystal

with its polarisation along the [101] axis would undergo an orthorhombic-tetragonal transformation based on the direction and intensity of the electric field. These phase transitions occur through an intermediate monoclinic phase. It is the existence of this metastable monoclinic phase which is found to be the reason for the enhanced piezoresponse shown by them. A simple way to understand the path of a phase transition is through a ‘Cohen’s cube’ [33] shown in Fig. 2.4. Phase transition can occur along all closed paths in the cube, based on the direction and intensity of the electric field. However, a phase transition would be absent if the electric field direction is same as the direction of spontaneous polarisation.

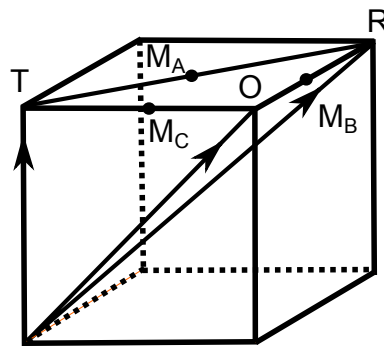


**Figure 2.4:** Cohen’s cube showing the sequence of field induced phase transition. T is tetragonal, O is orthorhombic, R is rhombohedral,  $M_A$ ,  $M_B$ ,  $M_C$  are the monoclinic phases. Arrows indicate the direction of spontaneous polarisation for each phase.

The concept of polarisation rotation originates from the field induced transition. The direction of spontaneous polarisation depends on the phase of the crystal as discussed in section 2.2. Since the phase of the system undergoes a transition under the application of an external electric field, the direction of polarisation also changes. This change in the direction of polarisation which occurs during a field induced phase transitions is termed polarisation rotation.

## 2.6 Crystallisation Kinetics

Ferroelectricity is a collective phenomenon. Hence, a long range order among the unit cells is necessary in order to demonstrate the properties described in earlier sections. Solids that display long-rang, repeating units are crystalline. They are formed when the constituting atoms, molecules or ions have an opportunity to arrange themselves into

an ordered arrangement, known as lattices. Materials that do not possess a long-range order and periodicity are best classified as amorphous. However, amorphous materials might display short-range order over distances of 1 nm - 10 nm or so [46]. Formation of an amorphous phase is favoured over a crystalline phase in kinetically bound processes even though a crystalline phase is the thermodynamically stable state [47]. Hence, sufficient energy needs to be applied to the atoms in an amorphous state in order to arrange themselves and acquire a crystalline phase.

Phase transformation involves redistribution of atoms via diffusion. The process of phase transformation from an amorphous state to a crystalline state involves two stages: nucleation and growth. Formation of stable, small particles known as nuclei occurs at the nucleation phase. They are often formed at grain boundaries or defects. The second stage involves growth of a new phase at the expense of the initial phase, stemming from the nuclei. Phase transformations generally follow a characteristic ‘S’ shaped profile where the rate is low at the nucleation phase, rapid in the middle before it saturates at the end. Fig. 2.5 shows the ‘S’ shaped, two-step crystallisation mechanism. The

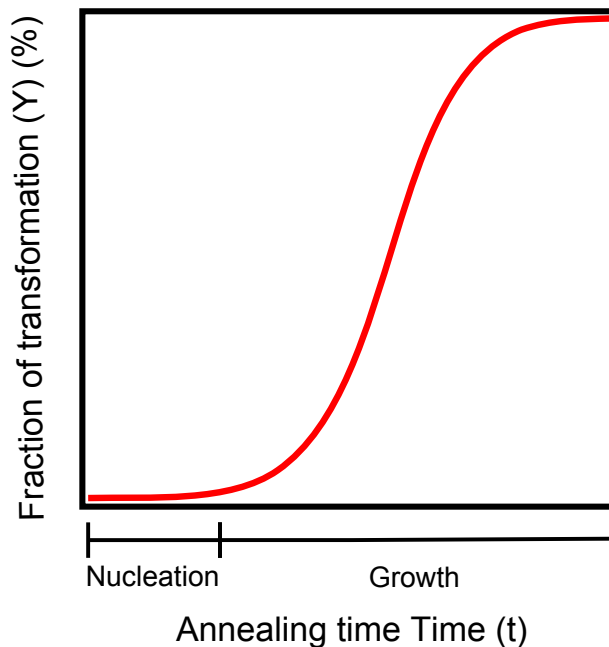


**Figure 2.5:** ‘S’ shaped curve showing the relationship between fraction of phase transformation and time for a specific annealing temperature.

fraction of transformed material for a specific time, in a homogeneous system, is given

by the Johnson-Mehl-Avrami-Kolmogorov equation [48–50], expressed as;

$$Y = 1 - e^{-(Kt)^n} \quad (2.3)$$

where  $Y$  is the fraction of transformation,  $t$  is the annealing time,  $n$  is an integer representing the nature of transformation and  $K$  is the effective reaction rate constant.

$K$  has an Arrhenian temperature dependence such that:

$$K = K_0 e^{\left(-\frac{E_a}{RT}\right)} \quad (2.4)$$

where  $E_a$  is the activation energy,  $R$  is the universal gas constant and  $K_0$  is a pre-exponential factor. The key concept here is that transformation from an amorphous state to a crystalline state is an activation energy mediated mechanism. Materials with a high activation energy require a higher annealing temperature for phase transformation. Moreover, the temperature of annealing has more impact on the amount of transformation than the annealing time. Hence, rapid thermal processing at a relatively higher temperature for a shorter period can crystallise more volume of material than annealing for a longer period at a lower temperature.

### 2.6.1 Miller indices

Miller indices are a notation system for crystallographic directions and planes in a crystal lattice used to identify the orientation of a surface or crystal plane. The crystallographic direction is a fictitious line linking nodes (atoms, molecules or ions). Similarly, crystallographic planes are fictitious planes connecting nodes. Lattice planes and directions are described using a set of three integers known as Miller indices. The orientation of a plane can be represented using Miller indices by considering how it intersects with the main crystallographic axis. Fig. 2.6 shows three examples of crystal planes based on its intersection with the axis. Similarly, Miller indices for crystal directions can be denoted by identifying the vector connecting the nodes as shown in Fig. 2.6.

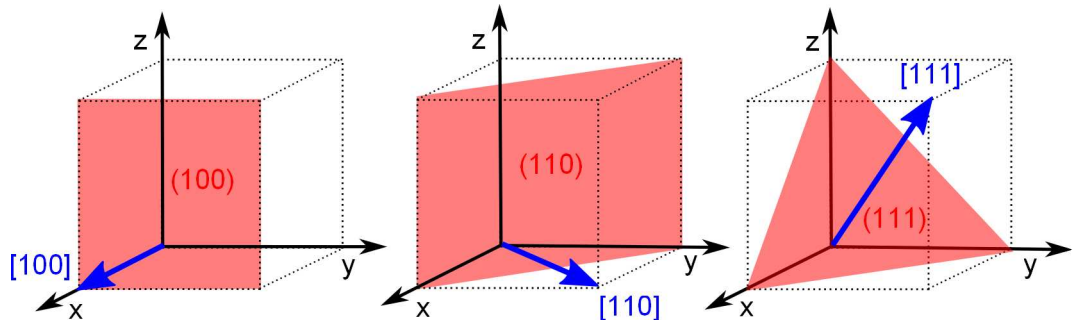


**Figure 2.6:** Illustration of crystallographic directions and planes in a crystal lattice.

It is apparent that sufficient thermal energy is necessary for the crystallisation of the films. However, the silicon technology imposes some constraints on high temperature processing during fabrication, some of which are described in the next section.

## 2.7 Thermal Budget of Silicon Technology

The concept of thermal budget in CMOS processing is central to front-end process. Fig. 2.7 is a schematic illustration of a classical CMOS separating the front-end-of-line (FEOL) and back-end-of-line (BEOL) stacks. A thermal budget

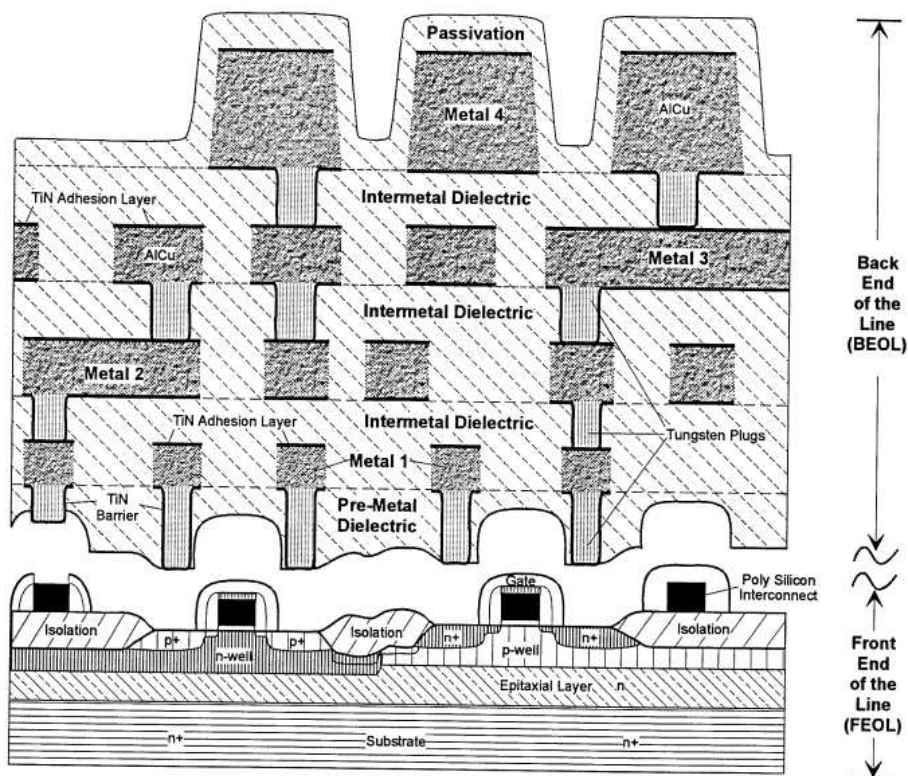


**Figure 2.7:** Schematic illustration of the cross-section of a classic CMOS with FEOL separated from BEOL, after [51].

puts a limit on the allowed total time of high temperature processes during CMOS fabrication. There are many process steps in CMOS fabrication which involves high temperature treatment. This covers source-drain implant anneal, dopant activation, gate oxide growth, high- $\kappa$  gate dielectric formation and contact and interconnect formation (silicidation). Inter-diffusion of materials, especially diffusion of dopant distribution becomes more and more problematic and leads to a continuous lowering of thermal budget along with the miniaturisation of devices [52]. However, the need to form high quality films and to minimise defects, demands that high temperature processes are often required. Hence, the thermal budget in modern CMOS fabrication is realised through a rapid thermal processing (RTP) which provides a better time-temperature control and gas ambient control. All high temperature deposition/growth processes have been replaced with low temperature processes in advanced CMOS fabrication [53]. Furthermore, furnace oxidation of silicon has been replaced with a time controlled, high temperature rapid thermal oxidation in order to control the diffusion of channel implants during gate oxidation. A rapid thermal oxidation also results in films with lower interface stress, smoother surface, reduced leakage, reduced trapped charges and interface states [53–55] compared to furnace annealed films. A better control over thermal budget is also key for strain engineering in the front-end, a key issue in advanced CMOS nodes.

In the BEOL, an important constrain on the thermal budget arises during silicide formation, used for realising low resistance contacts and inter-connects. In advanced CMOS nodes, NiSi is used as a low resistance inter-connect for connecting the terminals (source, drain). Silicides of nickel are formed by deposition and annealing of nickel on silicon. However, a strict thermal budget is necessary to obtain the desired low resistance NiSi. An RTP at temperature between 400 °C - 500 °C is required to obtain NiSi. Thermal stability of NiSi deteriorates above this temperature and a highly resistive NiSi<sub>2</sub> phase is formed around 650 °C [56, 57]. Hence, for BEOL processes the maximum allowable temperature is around 500 °C. It is a strict requirement that introduction of new materials must not compromise the thermal budget of the

CMOS process chain. Hence, a low substrate temperature is always preferred during deposition. Even though there is no strict definition for ‘high’ and ‘low’ temperature in CMOS processing, temperature above 500 °C is generally considered as ‘high’ and below 500 °C is considered as ‘low’. Moreover, the thermal processing can lead to failure of deposited films. Different modes of failures in thin film are discussed in the next section.

## 2.8 Thin Film Failure Modes

Efficient and stable growth of ferroelectric thin films will enhance the possibilities of fabricating high density non-volatile memories, among other applications. However, these films deposited on a substrate are subjected to different kinds of stresses. These stresses result in strain within the film. Stresses which exceed the elastic limit of the thin film can lead to failure of the film. Stresses in thin films have three primary origins: intrinsic, thermal and mechanical [58]. Out of these, intrinsic and thermal stresses are commonly referred to as residual stress. Intrinsic stresses arise during the deposition process and depend on the deposition temperature. Reasons for intrinsic stress include grain growth, defects, lattice mismatch between the thin film layer and the substrate, phase transition or evaporation of a solvent. Most of the mechanisms leading to intrinsic stress are the result of a change in volume, which then produces stress due to the mechanical constraints from the substrate. Intrinsic stresses differ from thermal stress in that intrinsic stress arises due to the deposition temperature whereas thermal stress arises when the thin film and the substrate have different thermal expansion coefficients. Thermal stress can be generated during the cooling stage if the thin film is deposited at a high substrate temperature or during a post deposition anneal. As the name indicates mechanical stresses originate when the film is subjected to an external force.

There are many modes of failures in thin films, which arise from stresses that are too large. Cracking or de-lamination of a film can occur due to stresses that are tensile [59]. Fig. 2.8 (a) and (b) represent schematic illustrations of cracking and de-lamination of thin films respectively. A compressive stress can cause pinhole (Fig. 2.8 (c)), or

hillock (Fig. 2.8 (d)) formation [60, 61]. A compressive stress is found to generate hillocks on the surface at the beginning, which would then lead to formation of pinholes. Both compressive and/or tensile stresses could force the thin film to peel off due to de-bonding from the interface depending on the adhesion between the film and the substrate.

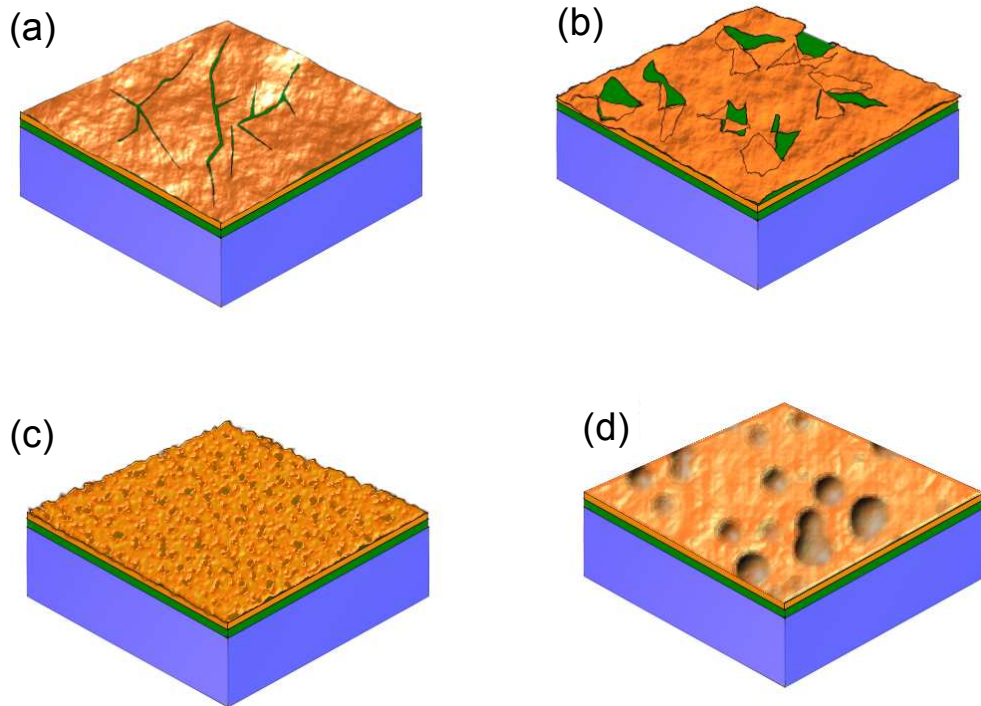


**Figure 2.8:** Schematic illustration of failure mechanisms in thin films, showing (a) cracking, (b) de-lamination, (c) pinholes and (d) hillock formation.

The failure due to residual stress is related to thickness of the film ( $h$ ) [59, 62] such that;

$$h = \left( \frac{K}{\sigma\Omega} \right)^2 \quad (2.5)$$

where  $K$  is the fracture resistance,  $\sigma$  is the stress and  $\Omega$  is a non-dimensional parameter referred to as de-cohesion number. Critical values of  $\Omega$  and  $K$  depend on the sign of the residual stress (compressive or tensile), ductility and modulus of elasticity of film and the substrate. From equation 2.5 it can be observed that the critical thickness for a failure is inversely proportional to the residual stress. Hence, for a particular thin film-substrate combination prepared by a specific deposition method, there exists a critical thickness corresponding to each value of residual stresses below which films

are stable and free from any failure mechanisms.

## 2.9 Titanium Nitride

Nitrides are compounds of nitrogen bonded with an element of equal or lower electronegativity.  $\text{TiN}_x$  is a refractory interstitial nitride where nitrogen atoms reside at the interstices of the titanium lattice. Here, ' $x$ ' is the ratio of nitrogen to the titanium content.  $\text{TiN}_x$  can exist in various phases, such as stoichiometric TiN or  $\text{Ti}_2\text{N}$  based on the nitrogen content in the interstitial sites [63]. Bonding between atoms is primarily metallic in stoichiometric TiN with some covalent and ionic contributions as well [63]. The metallic characteristic of TiN is the reason for its high thermal as well as electrical conductivity. Stoichiometric  $\text{TiN}_x$  exists in a rocksalt structure where nitrogen atoms occupy the octahedral sites of an fcc titanium sub-lattice. Properties of the  $\text{TiN}_x$  film vary with crystal structure, which depends on the amount of incorporated nitrogen. Hence, it is possible to obtain  $\text{TiN}_x$  films with desirable properties by optimising the deposition conditions.

## 2.10 Summary

Some of the key concepts which will be used in this thesis were introduced in this chapter. To summarise, ferroelectricity arises from an asymmetry in the crystal structure. These materials show this asymmetry in order to be in a lowest possible energy state. The phase of the crystal and hence the ferroelectric property shown by  $\text{BaTiO}_3$  is dependent on temperature. However, the phase can also depend on the applied electric field and its direction with respect to the polar direction of the crystal. The polar nature of ferroelectric materials makes them piezoelectric as well. However, these materials require a crystalline phase and a long range order in order to exhibit these properties. A crystalline phase is normally achieved through a high temperature anneal. However, a high temperature anneal could lead to failure of the thin film due to thermal stress. The failure of the film during annealing can be avoided by controlling

---

the thickness of the film. The next chapter discusses fabrication and characterisation techniques and their setup employed to address research questions.

# Fabrication and Characterisation of Thin Films

## 3.1 Thin Film Deposition and Post Deposition Processing

Many of the technological advances in ultra large scale integration (ULSI) integrated circuits are traced to advances in thin film processing. Thin film deposition is any technique for depositing a thin film on a substrate and which allows layer thickness to be controlled within a few tens of nanometers. However, defects and contamination greatly influence the material properties when the film dimensions are at sub-micron level. It is important to carry out the processing steps in a clean room environment and to follow standard procedures used for semiconductor fabrication. The key objective of this thesis is the deposition and characterisation of  $\text{BaTiO}_3$  thin films and  $\text{TiN}_x$  electrodes and to understand their properties. This section of the chapter introduces the fabrication process modules used for this research, and discusses the process steps that are involved. Discussions about the characterisation techniques used are given in a later section.

### 3.1.1 Sample preparation

In this research, single crystal silicon was used as a substrate for depositing thin films. A  $\langle 100 \rangle$  oriented silicon substrate was cleaved into smaller pieces of size  $2 \times 2$  cm and were then thoroughly cleaned. Initially samples were immersed in N-Methylpyrrolidone (NMP) and refluxed in a tank of the ultrasonic bath at  $80^\circ\text{C}$

for 2 minutes. Samples underwent the same treatment in a reflux bath of Isopropyl Alcohol (IPA) and were then rinsed in de-ionized (DI) water. Solvents such as NMP and IPA would dissolve organic contaminants from the sample surface. This process was followed by general cleaning in a 'Piranha' solution. The Piranha solution was prepared by heating  $\text{H}_2\text{SO}_4$  at  $85\text{ }^\circ\text{C}$  and adding an equal volume of  $\text{H}_2\text{O}_2$ . Samples were then immersed in the bubbling Piranha solution which was placed in an ultrasonic bath for 5 minutes. Cleaning in Piranha is especially useful for removing hardened photoresist. Subsequently, samples underwent a series of three cleaning processes collectively known as RCA (developed in Radio Corporation of America) cleaning. The first step, which is also known as Standard Clean-1 (SC-1), was prepared by mixing five parts of DI water, one part of aqueous  $\text{NH}_4\text{OH}$  and two parts of aqueous  $\text{H}_2\text{O}_2$ . The SC-1 solution was heated to  $80\text{ }^\circ\text{C}$  and the immersed samples were treated in an ultrasonic bath for 5 minutes. This base-peroxide mixture is effective in removing particles, organic residues and some metallic contaminants from the surface. However, this process results in the formation of a thin layer of  $\text{SiO}_2$  on the silicon surface, which will be removed in the following step. Silicon dioxide on the surface was stripped by dipping the samples in a buffered oxide ( $\text{NH}_4\text{F}/\text{HF}/\text{H}_2\text{O}$ ) etch solution. The final step in the RCA process is SC-2 cleaning which is used for removing remaining traces of metallic contaminants, some of which might be introduced during the previous cleaning steps. DI water, HCL and aqueous  $\text{H}_2\text{O}_2$  were mixed in a 5:1:1 ratio to prepare the SC-2 solution. Samples were immersed in the SC-2 solution, which was kept at  $70\text{ }^\circ\text{C}$ , and were again subject to an ultrasonic treatment for 5 minutes. Samples were immersed in DI water in between processing steps in order to prevent the exposure of the samples to any atmospheric contamination. The cleaned samples were then rinsed in DI water and blow dried using a nitrogen gun.

An 80 nm thick  $\text{SiO}_2$  layer was grown on the cleaned silicon substrates using furnace oxidation. This oxide layer acts as an electrically insulating layer between the deposited thin films and the silicon substrate. A thick layer of  $\text{SiO}_2$  will also prevent diffusion of silicon into the upper layers during an annealing process.

### 3.1.2 Thin film deposition

This section introduces some of the thin film physical vapour deposition (PVD) techniques used in this thesis.

#### 3.1.2.1 Sputter deposition

Sputtering is a term used to describe the mechanism in which atoms are ejected from the surface of a solid material when they are struck by particles of sufficient energy. The sputtering system consists of a pair of electrodes; a cathode and an anode within an isolated chamber. The cathode assembly consists of an electrode and a 'target'. The target is made out of materials which are to be deposited. Substrates are placed on the anode. The process involves creation of a plasma using inert gases such as argon at a high electric field. The positive charged ions from the plasma are accelerated towards the cathode and strike the negative electrode with sufficient force to eject atoms out of the target. The dislodged atoms from the face of the target will condense on surfaces that are placed in proximity to the cathode. Conductive materials can be deposited by using a DC power supply and insulators are deposited using an RF power supply. Fig. 3.1 shows a schematic of a DC sputter deposition system.

**Magnetron sputtering:** The cathode assembly often employs magnetrons which control both electric and magnetic fields to confine electrons near the surface of the target. Electrons follow a helical path around magnetic field lines of the magnetron causing more collisions with the gaseous neutrals near the target surface than in the case of a conventional DC cathode. These collisions enhance the efficiency of an initial ionisation process and allows plasma to be generated at gas pressures as low as  $1 \times 10^{-5}$  Torr [64] but more typically  $1 \times 10^{-3}$  Torr. Sputtering at a low gas pressure reduces incorporation of background gas in the growing film and also reduces the energy loss of sputtered atoms. The confinement of electrons near the target surface helps in self-sustainment of plasma even at low gas pressures. In magnetron sputtering, the magnetic field increases plasma density which increases the ion current density. An increase in current density at the cathode would in turn increase the sputtering discharge

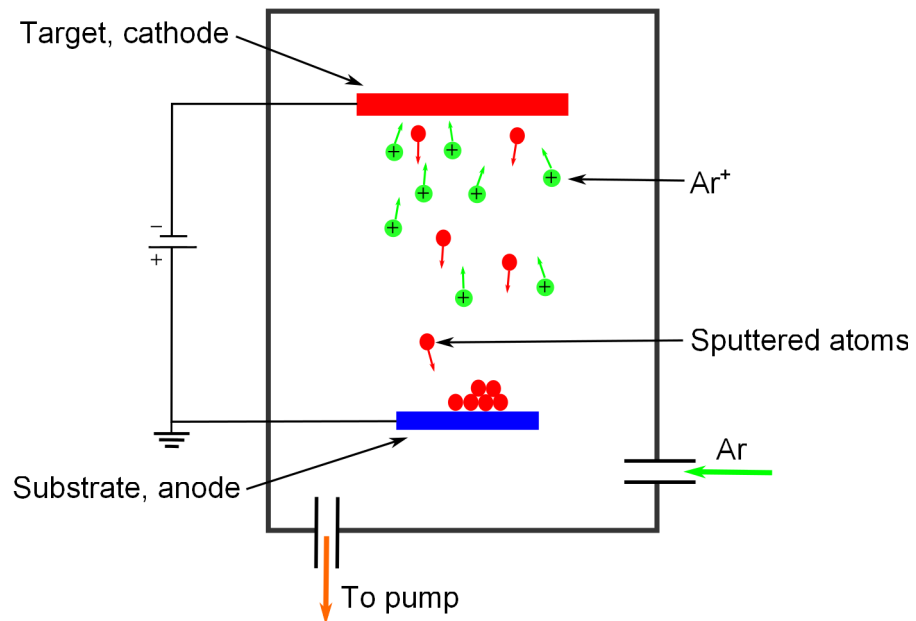


**Figure 3.1:** Illustration of a DC sputter deposition system.

at the target. Due to the low chamber pressure, sputtered particles traverse the discharge space without collision which results in a high deposition rate. Magnetron sputtering can be done using both DC and RF power supplies.

**Reactive sputtering:** The conditions in the sputter chamber can be modified to include reactive gases such as nitrogen or oxygen along with the inert gas to form compound thin films such as TiN, SiO<sub>2</sub>, SiN<sub>x</sub> and AlN. The deposited film is formed by a chemical reaction between the target material and the reactive gas. Film composition can be controlled by varying the relative pressures of the reactive gas and the inert gas. It is anticipated that the reactions happen on the surface of the substrate. However, the reactive gas could react with the sputter target also and this phenomenon is known as ‘target poisoning’. Target poisoning can happen due to chemisorption, diffusion or ion implantation [65, 66]. Target poisoning can severely affect the process stability and film quality, especially if the reaction forms an insulating layer on a metal target. This can lead to a significant drop in the deposition rate and can also result in arcing effects due to the charge build up at the target surface.

The consequences of target poisoning are not severe if the reaction forms a

conductive film on a metallic target. Moreover, intensive erosion of the target due to sputtering avoids a complete poisoning of the target in the case of conducting films. Target poisoning can be reduced by careful design of the chamber, pumping system, magnetron and gas delivery. Target voltage, which is a function of discharge impedance between the electrodes, can be used to monitor the condition of the target during sputtering. A large variation in the target voltage for a given deposition condition is an indication of target poisoning.  $\text{TiN}_x$  thin films produced during research were developed using reactive sputtering of a titanium target in an ambient of nitrogen and argon. Development and optimisation of the reactive sputtering process for depositing  $\text{TiN}_x$  is discussed in chapter 4.

**RF sputtering:** The sputtering discharge cannot be sustained in the case of insulating targets due to the immediate build up of positive ions on the front side of the insulator from the  $\text{Ar}^+$  ion bombardment. In RF sputtering an RF voltage is capacitively coupled through the insulating target in order to create and sustain the glow discharge. Due to the high mobility of electrons compared to heavier positive ions, electrons are collected at both electrodes during the first few complete cycles of the RF voltage. The DC isolation of the insulating target results in a potential build up at the cathode. The negative potential aids the transport of positive ions in the plasma towards the cathode. Thus the induced negative biasing of the target allows continuous sputtering even using an alternating voltage. RF sputtering traditionally uses a frequency of 13.56 MHz which is high enough to maintain the plasma. Insulating oxides including  $\text{BaTiO}_3$  require RF energy for sputter deposition. Chapter 5 of this thesis discusses the deposition of  $\text{BaTiO}_3$  thin films from a  $\text{BaTiO}_3$  target through RF sputtering.

### **Sputter system setup**

An Oxford Instruments PlasmaPro System400 PVD was used to deposit  $\text{TiN}_x$  and  $\text{BaTiO}_3$  films. The sputter system is fitted with two DC magnetrons for depositing metals and an RF magnetron for depositing insulators. It allows simultaneous loading of four 150 mm wafers. Design of the system is such that the target is on top and the wafer

table is at the bottom and the distance between the target and the substrate is 10 cm. The wafer table can be operated in static mode or it can be rotated to enhance uniformity or to achieve extremely low thickness for the deposited film. A typical uniformity of  $\pm 5\%$  is achievable on a 150 mm wafer when operated in rotating mode. The wafer table can be operated from room temperature up to 390 °C. The process chamber is divided into four sub-chambers isolating the target sources from each other to minimise cross contamination. The system also allows deposition of multiple materials in one chamber in a single process. A base pressure of  $1 \times 10^{-6}$  Torr is achievable with the help of a turbo molecular pumping system. The working pressure can vary from 1 mTorr to 60 mTorr.

The DC magnetrons can be loaded with 8" metallic targets and the RF magnetron can be loaded with 4" targets. Fig. 3.2 (a) shows the Plasma400 system connected with two metallic targets (aluminium and titanium) and an oxide ( $\text{BaTiO}_3$ ) target. During the sputtering process a shutter is used to cover the unused targets. The shutter is not present in Fig. 3.2 (a). Sputtering is a momentum transfer process where high energy ions

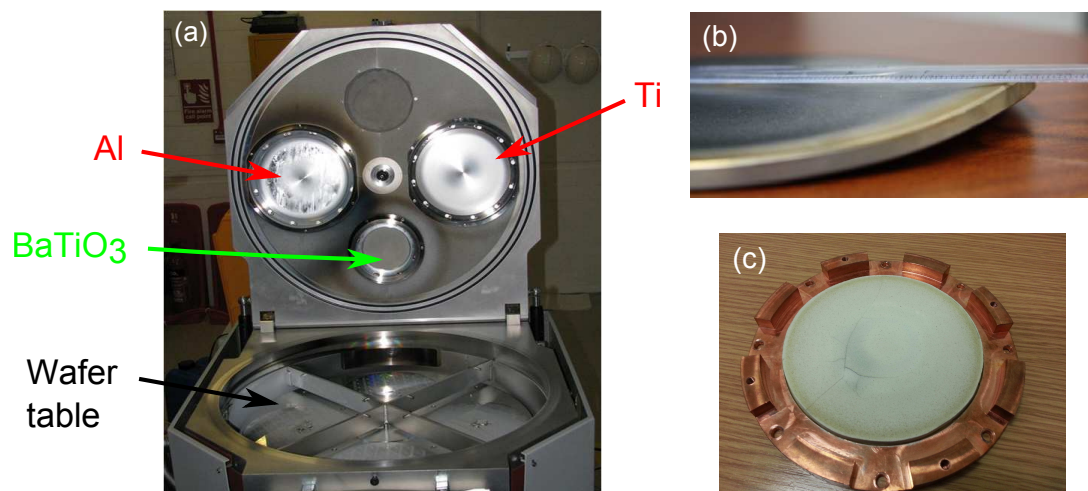


**Figure 3.2:** Showing (a) Oxford Plasma400 sputter chamber with three different targets assembled, (b) warped titanium target due to insufficient cooling and (c)  $\text{BaTiO}_3$  target bonded to a copper backing plate

collide with the target to eject target atoms. However, a portion of the kinetic energy will also be converted to heat. The heat generated on the surface of the target should be effectively carried away. Target cooling is generally achieved through water cooling of the magnetron. The heat experienced on the target surface depends on the target

material, power used, sputtering gas, gas pressure, efficiency of cooling and the thermal conductivity of the target. Materials like titanium with a lower thermal conductivity ( $20 \text{ Wm}^{-1}\text{K}^{-1}$  [67]) would require a more efficient cooling than materials with a higher thermal conductivity like aluminium ( $200 \text{ Wm}^{-1}\text{K}^{-1}$  [67]). Lack of adequate cooling can cause excessive heat accumulation at the target which would then lead to target warping (for metals) or shattering (for ceramics, silicon). Fig. 3.2 (b) shows a titanium target which is warped due to inefficient target cooling. Generally, targets are bonded to a copper backing plate to improve the heat conduction from the target to the magnetron, which is water cooled. Copper discs of 3 mm thickness have been used as a backing plate for the titanium target and  $\text{BaTiO}_3$  target. The Targets were bonded in-house using a thermally conductive silver filled epoxy adhesive KL-325L from Kurt J. Lesker Company. Fig. 3.2 (c) shows the  $\text{BaTiO}_3$  target bonded with a copper backing plate. A reusable conductive elastomeric disk procured from Kurt J. Lesker was placed in between the backing plate and the magnetron to further enhance thermal conductivity. The elastomeric disk was made using silicone rubber and contained silver-coated copper powder for thermal as well as electrical conductivity.

### Process development

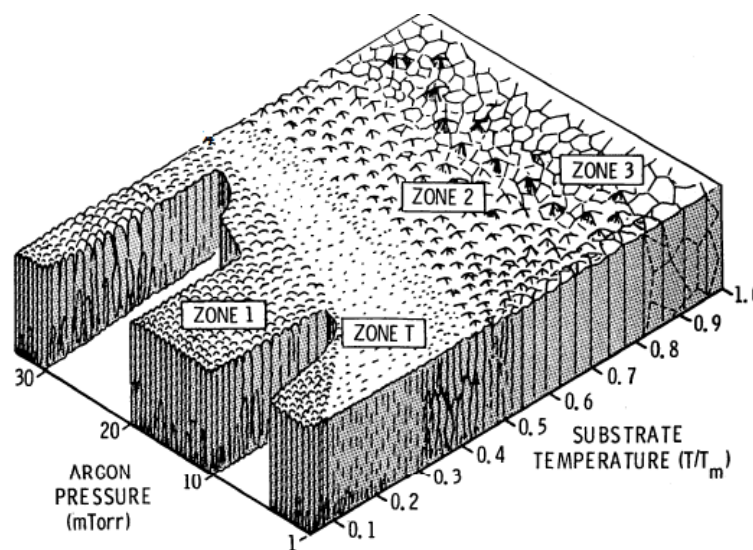
A number of different parameters can be manipulated in the sputter process to obtain films of different quality. The deposition rate depends on sputtering yield. Sputter yield is the number of sputtered atoms per number of incident ions. It depends on parameters such as target type, binding energy of target atoms, relative mass of target atoms and inert gas ions, incident ion energy and angle of incidence of ions. Incident ion energy and thereby the sputter yield can be varied by changing process parameters such as gas pressure and power [68]. Apart from controlling the deposition rate, process parameters can also be optimised to manipulate the film stoichiometry, crystallinity, phase, microstructure, stress and defects [64]. Table.3.1 summarises the thin film properties and key sputtering parameters [64].

Fig. 3.3 shows the zone structure model depicting the influence of sputter

**Table 3.1:** Summary of thin film properties and sputtering parameters

<i>Film Properties</i>	<i>Key Sputtering Parameters</i>
Composition	Target composition Reactive gas
Crystal phase	Deposition rate (sputtering power, spacing)
Microstructure	Deposition temperature
film	Post deposition anneal temperature
surface	Sputtering atmosphere (total pressure, partial pressure)
interface	Substrate materials
Defects	Substrate position, base pressure, Post deposition cooling rate, cooling atmosphere

pressure and substrate temperature on structure and topography of the deposited films. According to this model, the microstructure of the deposited film can be divided into four different zones based on the deposition conditions. The model explains the role of substrate temperature on obtaining a coarse granular structure. An increase in grain size and complete crystallisation was observed only for an elevated substrate temperature. However, sputter deposition of thin films at temperatures compatible for semiconductor processing is one of the objectives of this thesis. Hence, it is apparent that a post



**Figure 3.3:** Thornton's zone structure model showing the influence of the deposition conditions on the structure and topography of a sputtered coating, after [69]. In the figure T is the substrate temperature and  $T_m$  is the melting point of the depositing material.

deposition anneal would be necessary to obtain crystallisation of the thin films.

A newly procured target will have a contaminated surface. It is also possible for the target surface to have a different composition due to the reaction of the target with atmospheric gases (eg.  $\text{TiO}_2$  on a titanium target). Hence, the target is cleaned by sputtering using inert gas at a low power (eg. 100 W) and high pressure (eg. 20 mTorr). This is to avoid any chance of excessive heat formation on the target. The target voltage gives feedback information about the target condition. Once a stable target voltage is achieved, process parameters are optimised to develop a recipe.

### 3.1.2.2 Pulsed laser deposition (PLD)

Pulsed laser deposition (PLD) is a thin film physical vapour deposition technique which uses intense laser pulses of short duration to evaporate materials from the target. In this thesis, the PLD technique was also used to deposit  $\text{BaTiO}_3$  thin films. In PLD, the laser beam is generated outside the chamber and is directed towards the target of the material to be deposited using a focusing lens. The high energy laser vaporises the material from the target and the ablated particles deposit as a thin film on the substrate. The target is rotated for uniform coverage. The PLD process can be done in high vacuum or in the presence of an ambient gas such as oxygen. The substrate can be heated to enhance the growth kinetics of the deposited film. PLD can be used to deposit a large variety of materials, especially oxides [70]. However, small coverage area and lack of uniformity makes the technique not favourable for industrial applications.

### 3.1.2.3 Electron beam evaporation

Evaporation is also a physical vapour deposition technique in which a target is bombarded with a high energy electron beam under high vacuum. The electron beam causes atoms from the target to transform into gaseous phase which then precipitates on the substrate as a thin solid film. Platinum bottom electrodes used for this research were deposited by the electron beam evaporation technique using a BOC-Edwards e-beam evaporator. Prior to platinum deposition, a 10 nm titanium adhesion layer

was evaporated on the SiO<sub>2</sub>/Si stack. 100 nm platinum was then evaporated at a base pressure of  $3 \times 10^{-6}$  Torr.

### 3.1.3 Rapid thermal processing (RTP)

Rapid thermal processing (RTP) is a semiconductor manufacturing process which uses an array of lamps to heat a wafer to desired temperatures (up to 1300 °C) at a very rapid heating and cooling rate. RTP systems are used for dopant activation, thermal oxidation, re-crystallisation, crystal growth, ohmic contact formation, junction formation or for modifying the properties of thin films. Short annealing times and its relative simplicity are advantages of this method when compared to conventional furnace annealing. The RTP can be done using different gas ambients or in vacuum. In this research, the RTP was used to anneal BaTiO<sub>3</sub> and TiN<sub>x</sub> thin films and to study their stability during high temperature processing. A Jetfirst 200 bench top RTP system was used to anneal the samples at temperatures up to 900 °C in forming gas (N<sub>2</sub>/H<sub>2</sub>). A ramp up rate of 30 °C was used while the ramp down was through natural cooling.

### 3.1.4 Optical lithography

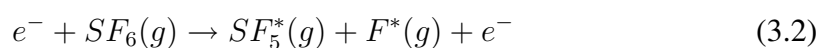
In order to fabricate top electrodes for a metal-insulator-metal (MIM) capacitor structure used as part of this research, the sample surface was patterned using optical lithography. Optical lithography is a process of transferring a pattern onto the wafer by selectively exposing and developing a light-sensitive chemical known as photoresist [71]. Here, light is used as a medium to transfer the pattern from a photo-mask to the photoresist. For this research, positive resist AZ-5214 E has been used. A positive resist allows the exposed regions to be soluble in a developing solution.

Initially, the sample surface was covered with the photoresist using a spinner. The recipe was optimised to obtain a photoresist thickness of 1.5 μm. Prior to exposure, the sample was pre-baked in an oven at 90 °C for 15 minutes. The pre-baking process increases the sensitivity of the photoresist to light by removing its solvent component. The sample was then exposed by a Karl Suss MJB-3 aligner which uses a mercury lamp

as an ultra violet (UV) source. The exposure intensity was set at  $6.4 \text{ mW/cm}^2$  and the exposure time was 20 s. AZ-326 MIF was used to develop the photoresist leaving only the unexposed regions of the photoresist on the sample. The patterned resist consisted of circular and square structures of variable sizes. Diameters of the circular structures and the length of each side of the square structures ranged from  $50 \text{ }\mu\text{m}$  to  $300 \text{ }\mu\text{m}$ . Regions which are not covered by the photoresist were etched away using a reactive ion etching process as explained in the next section.

### 3.1.5 Reactive ion etching (RIE)

Top electrodes were fabricated by etching away  $\text{TiN}_x$  from regions which were not covered by the photoresist using a reactive ion etching (RIE) process. Etching of  $\text{TiN}_x$  which is not covered by the photoresist was preferred over a lift-off process which involves deposition of metals onto the developed photoresist. This was done to avoid damage of the photoresist due to the high energy involved in the sputtering process ( $2 \text{ eV} - 7 \text{ eV}$ ). RIE is a dry etch process which uses chemically reactive plasma to etch deposited materials on wafers. Initially, the chamber is filled with reactive gases such as  $\text{SF}_6$  or  $\text{CF}_4$  and inert gas such as Ar. Plasma is generated by applying a strong radio frequency field to the wafer platter causing ionisation of gas molecules. In each cycle of the electric field, electrons move up and down in the chamber and the collisions with the gas molecules trigger further ionisation. Electrons will also collide with the chamber wall and wafer platter. However, electrons hitting the wafer platter cause a negative charge build up due to its DC isolation. This results in the positive charged ions accelerating towards the wafer platter. A plasma discharge contains ions and excited neutrals (free radicals). Given below is an example of the ionisation process occurring in the chamber;



Free radicals such as  $SF_5^*(g)$  are very reactive and enable chemical reaction at the surface whereas ions such as  $Ar^+$  enhances the reaction rate by providing additional energy. Due to the vertical delivery of reactive ions, the RIE process can produce an anisotropic etch profile.

## **3.2 Metrology Challenges and Techniques for Emerging Materials**

Bulk property measurements once provided accurate information for material processing in the electronics industry. However, with recent technological advance, material characterisation at the macro-scale no longer adequately meets the requirements. This is especially true in the case of the nanoelectronics industry where device dimensions continue to decrease every year. In this regard it is necessary to measure and analyse nano-scale material properties. Since the contact size of the scanning probe microscopy (SPM) cantilever tip can be as small as a few nanometers, local topographical, electrical, mechanical as well as electromechanical properties can be accurately measured using AFM in samples with nanometer-scale features. Rapid development of electronic devices based on ferroelectric materials has necessitated the nano-scale analysis of ferroelectric thin films and their properties.

SPM techniques have revolutionised the understanding of ferroelectricity. It provided, for the first time, an opportunity for non-destructive visualisation of ferroelectric domain structures at the nano-scale [72]. It can provide crucial information related to ferroelectric materials such as electromechanical (inverse piezoelectric) response, surface potential and nonlinear dielectric constant with unprecedented spatial resolution [73] of just few nanometres. Furthermore, the SPM technique can be used to analyse nano-scale cracks and pinholes in thin films through leakage current analysis and surface mapping. Stability and uniformity of the deposited thin film is crucial for devices in the nanoelectronic era. SPM is the characterisation technique of choice for studying the surface roughness, topography mapping, step height measurement and

nano-scale leakage current analysis. Mapping of surface/domain properties or local domain level spectroscopic measurements in SPM are mainly limited by the tip size which is only a few nanometres, making it a high resolution characterisation technique. The following sections discuss the operating principles and measurement setup of some of the modes in SPM, which are used for topographical, electrical as well as electromechanical analysis of deposited ferroelectric thin films and electrodes in this research.

Properties such as crystallinity, phase, composition and resistivity along with the growth mechanism and defects in the film are crucial for the detection and quantification of deposited films. Commonly used material characterisation techniques such as x-ray diffraction (XRD), x-ray photoelectron spectroscopy (XPS) and Raman spectroscopy have been used for analysing crystallinity, phase, stoichiometry and defects in the deposited film. These non-destructive techniques provide insight into material properties of the film. Transmission electron microscopy (TEM) provides a significantly higher resolution visual image of these films when compared to a conventional optical microscope and can be used for studying the film structure. Resistivity is another quick way of characterising conducting thin films and is derived through a sheet resistance measurement. An introduction and measurement setup of the above mentioned techniques are briefly discussed in later sections of this chapter.

### **3.2.1 Scanning probe microscopy**

SPM as the name suggests, is the common name given to a family of surface imaging and characterisation techniques operating on the principle of near-field probe scanning and imaging. In SPM, a sharp cantilever tip scans across the surface of interest to produce a two or three dimensional image of the surface. Such techniques have high lateral and vertical resolutions and are generally non-destructive. Scanning tunnelling microscopy (STM) was one of the early adaptations of SPM [74]. STM uses a sharp conductive tip having a radius of curvature of few tens of nanometres to scan the surface of the sample. Its operation is based on the tunnelling current between the

probe and the sample. However, its use is limited only to conductive samples. Atomic force microscopy (AFM), which is capable of imaging insulating surfaces [75], has revolutionised the SPM technique. Over the years, AFM has evolved into a highly useful surface analysis technique capable of providing atomic resolution. Nowadays, AFM is extensively used for surface analysis in the fields of semiconductors, surface science, biology and electro-chemistry.

### **3.2.1.1 Atomic force microscopy (AFM)**

AFM is one of the foremost tools for imaging, measuring and manipulating matter at the nano-scale. It uses a cantilever with a sharp tip (probe) at the end of it to scan the specimen surface. The cantilever is typically made of silicon and the tip has a radius of curvature of a few nanometres as shown in Fig. 3.4 (a). When the tip is brought into close proximity of the sample surface, atomic forces between the tip and the sample surface lead to a deflection of the cantilever. When this distance is very short, the interactive force is repulsive due to electrostatic repulsion. For relatively larger distances, the interactive force becomes attractive in nature due to long range van der Waals forces. AFM operates by interpreting the attractive or repulsive force between the tip and the sample.

A schematic representation of the XE 150 AFM from Park Systems, used for this research is shown in Fig. 3.4 (b). A position sensitive photo detector (PSPD) and a laser are used to detect the bending of the cantilever under the influence of interactive forces. This system also has two scanners responsible for the movement in all three directions. The X-Y scanner shown in the schematic is a piezoelectric scanner used for the movement of the sample in the x-y direction. The information from the PSPD and the information about the location from the scanner are used by the control system to generate the topography map of the sample surface. The PSPD also forms a feedback loop which controls the vertical movement of the scanner. The Z-scanner is used to move the cantilever in the z-direction in order to keep the cantilever under the influence of the interactive force between the tip and the sample irrespective of the steep variations

in topography.

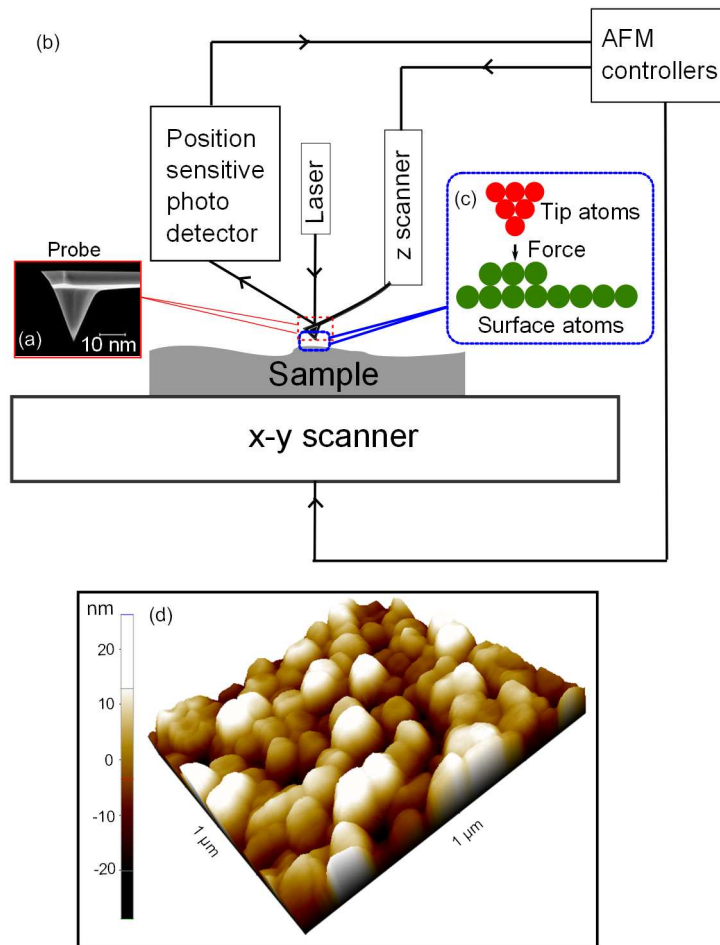


**Figure 3.4:** (a) Schematic representation of Park Systems XE 150 AFM setup, (b) shows the scanning electron microscopy image of CDT-NCHR AFM tip, (c) the attractive force experienced between tip and the sample surface when operated in non contact mode and (d) three dimensional topography scan of BaTiO<sub>3</sub> surface using non contact mode.

### AFM imaging modes

Interactive forces experienced by tip relative to its distance from the region under study are given in Fig. 3.5. Based on the interactive forces between the tip and the sample, AFM can be operated in multiple modes which are;

- *Contact mode:* This mode utilises the repulsive force between the tip and the sample to acquire the topography. Here, the tip makes a soft ‘physical contact’ with the surface of the sample for the entire duration of the scan. Depending on the curvature of the region under study, the tip will bend up or down. This

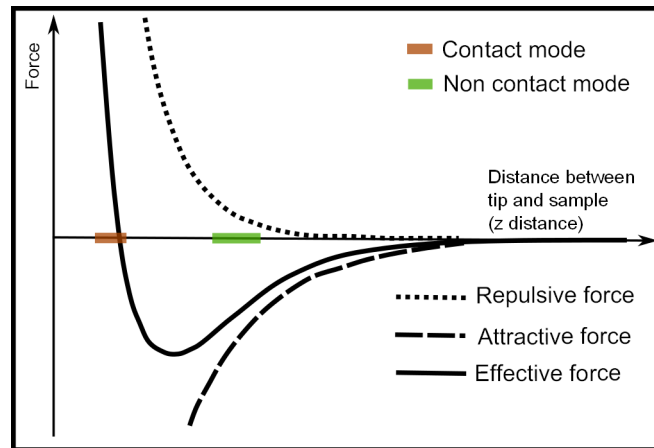


**Figure 3.5:** Plot of force experienced by the tip as a function of tip distance from the sample.

bending of the cantilever deflects the laser from the back of the cantilever. The laser deflection causes a change in the location at which the laser falls on a PSPD as shown in Fig. 3.4. The variation in the topography and thereby the cantilever deflection is quantified by the position of the laser on the PSPD. In contact mode, even nanometre scale changes in the topography can be detected due to the sufficiently small spring constant of the tip. This mode is mainly used to scan hard (for eg. silicon) surfaces. However, the sample and the tip are prone to contamination due to the soft contact the tip makes with the sample.

- *Non contact mode:* Non contact mode [76] utilises the attractive van der Waals forces for recording the topography. In this mode, the cantilever is mechanically oscillated using a bimorph<sup>1</sup> with very small amplitude at a fixed frequency near the resonant frequency of the cantilever. When the tip comes under the influence of van der Waals forces, the attraction between the tip and the sample causes changes in both amplitude and phase of the cantilever vibration. This change in amplitude indicates the change in the distance between the probe and the sample due to surface topography.

A non contact cantilever has a resonance frequency between 200 kHz and 300 kHz. The interactive forces between the tip and the sample cause a change in the spring constant ( $k_0$ ) of the cantilever vibrating near the sample surface. The

<sup>1</sup>A bimorph is an assembly of two piezoelectric crystals such that application of an electric field will result in one to expand and the other to contract.

resulting effective spring constant ( $k_{eff}$ ) is given as;

$$k_{eff} = k_0 - F' \quad (3.3)$$

where  $F'$  is the force gradient [77]. The relationship between the resonant frequency and spring constant is given as;

$$f_0 = \sqrt{\frac{k_0}{m}} \quad (3.4)$$

where  $m$  is the mass of the cantilever. The value of  $k_{eff}$  reduces with increasing interaction, i.e. reduced tip-sample distance. The resonant frequency of the cantilever also shifts from  $f_0$  to  $f_{eff}$  as shown in Fig. 3.6. The cantilever is

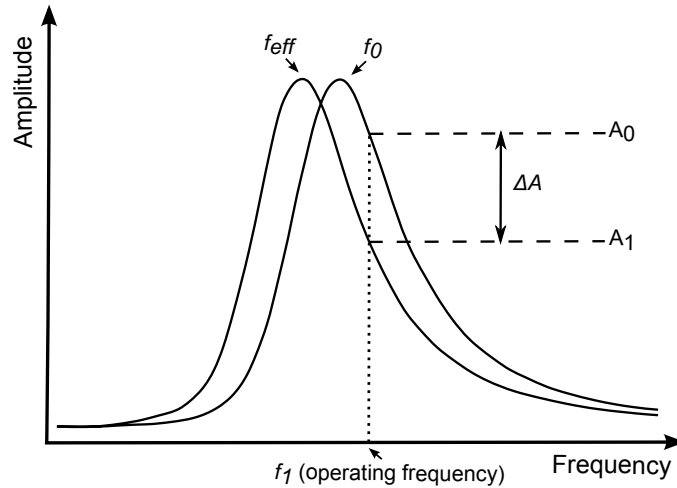


**Figure 3.6:** Illustrating the shift in non contact AFM tip resonance curve due to surface interactions.

vibrated at a frequency,  $f_1$  where a steep slope is observed in the amplitude vs. frequency plot in Fig. 3.6. Even a very small change in the resonant frequency results in a very large change in amplitude ( $\Delta A$ ). Hence, the change in amplitude or change in resonance frequency is a measure of the variation in topography. These changes are monitored by the z-scanner feedback system to control the sample distance. Non contact mode maintains constant amplitude and tip-sample distance to map the surface topography without making physical contact with the surface. This mode is highly useful for imaging materials with soft surfaces and to avoid tip damage.

- *Tapping mode:* Tapping mode combines both the contact mode and the non contact mode. Similar to the non contact mode, the cantilever is driven to oscillate, but with a greater amplitude than in the non contact mode. The cantilever tip makes contact with the surface on each oscillation cycle and detaches from the surface due to the large amplitude of oscillation. In this way the tapping mode avoids lateral frictional force. The variations in the oscillation amplitude are detected and the feedback loop ensures that the amplitude remains constant. The changes in the oscillation amplitudes are used to construct the surface map. This mode is generally used for samples that are easily damaged or loosely hold to the substrate as it can avoid problems due to friction or adhesion.

The XE 150 system used for this research uses two independent closed loop x-y and z scanners for the sample and the tip. The system has an x-y scan range of  $100 \mu\text{m} \times 100 \mu\text{m}$  and z-scanner range of  $25 \mu\text{m}$  providing accurate height and topography images. Topography images used in this study were obtained using True Non Contact Mode™ in XE 150 and were processed using an XEI software package from Park Systems. Surface roughness from topography maps were calculated from their root mean squared values of surface roughness profile. Root mean square (RMS) roughness ( $R_q$ ) is defined as;

$$R_q = \sqrt{\frac{1}{L} \int_0^L |Z^2(x)| dx} \quad (3.5)$$

where  $Z(x)$  is the function that describes the surface profile where  $Z$  is the height and  $x$  is the position.  $L$  is the evaluation length. RMS roughness was preferred over average roughness values while reporting the surface roughness, as it is more sensitive to peaks and valleys due to the squaring of the height term in its calculation.

### 3.2.2 Nano-scale electrical analysis modes in SPM

#### 3.2.2.1 Current AFM

Conductive AFM (I-AFM) provides a non destructive way to measure microscopic leakage through thin films. The topographical image is obtained by scanning the surface in contact mode. Simultaneously, the constant voltage applied between the conductive tip and the bottom electrode is used to measure the leakage current through the thin film. Therefore, I-AFM can produce a true mapping of leakage current with reference to the topography of the insulator by providing both current and topographical images. The external I-AFM mode in the XE 150 AFM from Park Systems was used in this thesis to detect pinholes and cracks in thin film BaTiO<sub>3</sub> after a post deposition anneal.

The I-AFM mode requires an additional setup to the normal contact mode AFM setup, in order to measure the current between the tip and the sample. Fig. 3.7 shows the setup needed for I-AFM. Components marked using red colour are those that need additional setup steps for current measurement. In insulators, the current flowing between the tip and the sample has a very small magnitude and needs to be amplified before it is processed into an image. The measurable current range of the I-AFM is determined by the gain of the amplifier used. For this research a DLCPA-200 variable gain low noise current amplifier was used externally, hence the mode used is 'External I-AFM'. With the help of the variable gain amplifier, the measurable current with the External I-AFM can range from 1 pA to 10 mA. A diamond coated slightly doped CDT-NCHR 10M.T conductive tip with a radius of approximately 100 nm has been used for I-AFM measurements. The DC bias for the measurements was applied through the bottom electrode. The diamond tip has a high mechanical Q-factor for high sensitivity. The detector side of the cantilever has a 30 nm thick aluminium coating which improves the reflectivity of the laser by a factor of 2.5. Fig. 3.8 shows the additional components required for the leakage current measurement. The inset figure shows the I-AFM cantilever mounted on the modified AFM head. The I-AFM head consists of an additional head extension module which is connected to the variable gain

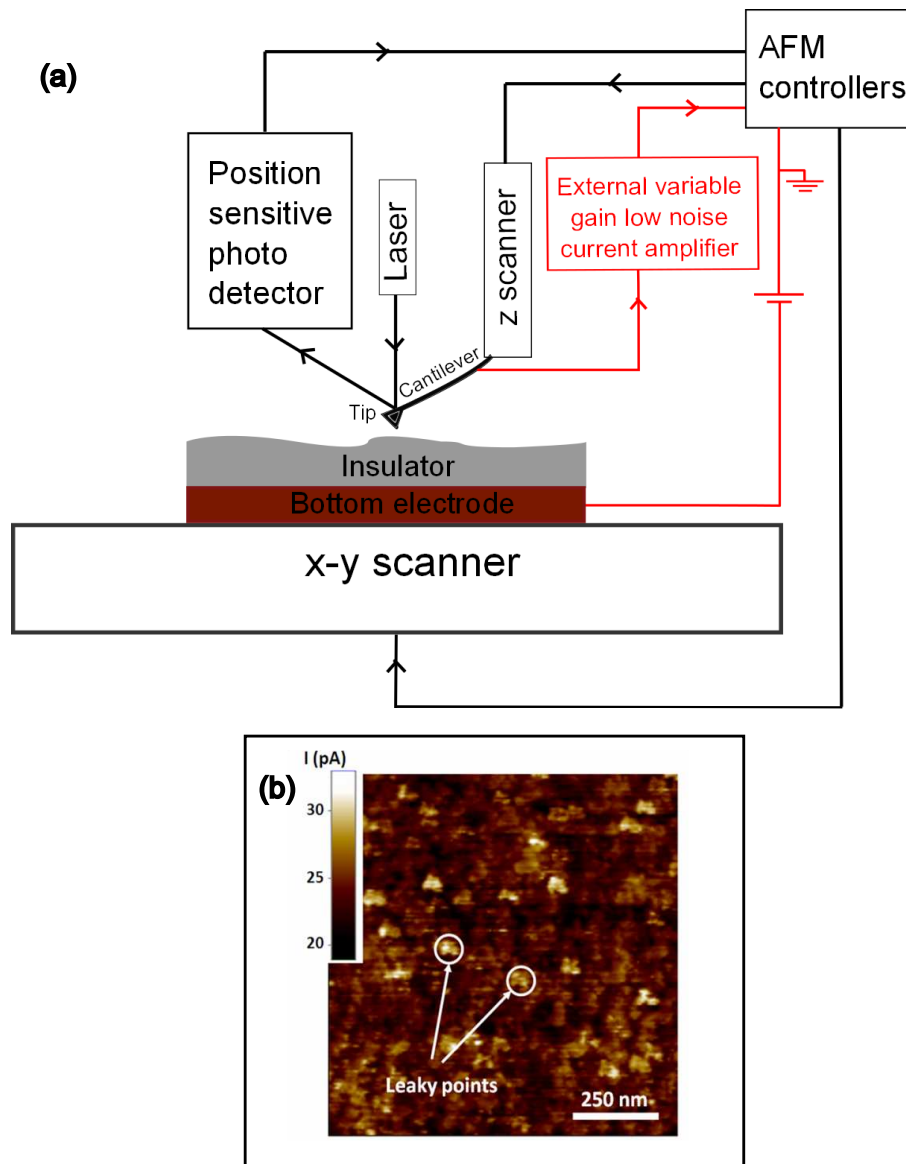


**Figure 3.7:** Showing (a) schematic illustration of I-AFM measurement setup used for this research and (b) leakage current map of SrTiO<sub>3</sub> on platinum bottom electrode [78] measured using the XE 150 AFM used for this research.

current amplifier. The conductive cantilever is connected to the head extension module via a lead wire as shown in the inset image. The amplified output is fed to the AFM through a frame module. Fig. 3.9 shows the I-AFM setup mounted on the XE 150 AFM.

I-AFM has been used to measure the leakage current through sputter deposited BaTiO<sub>3</sub> thin films in this thesis. Prior to the measurement, the force of contact between the tip and the dielectric has to be optimised [79]. Scanning a soft material like BaTiO<sub>3</sub> using a relatively harder diamond coated tip requires optimisation of the force applied

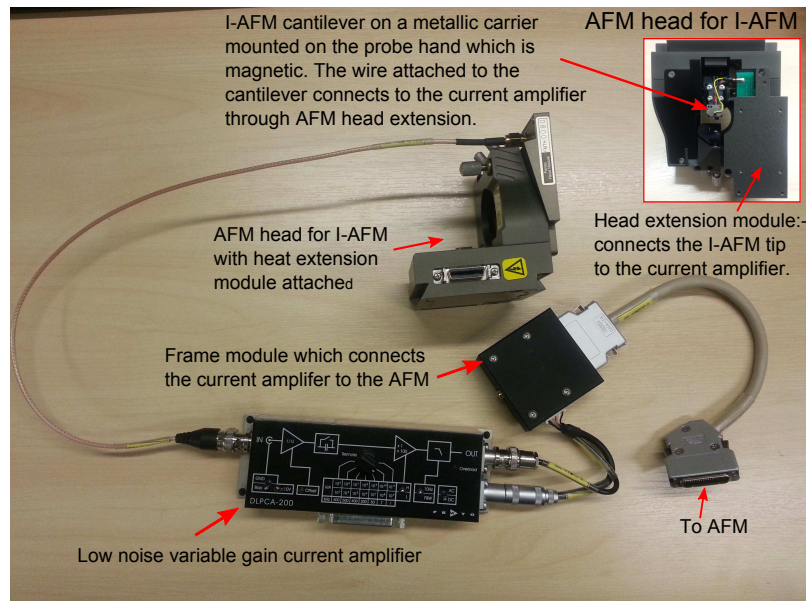


**Figure 3.8:** Additional setup required for External I-AFM measurement using XE-150 AFM from park systems. Shows the AFM head with head extension which is connected to the current amplifier. Output of the current amplifier is connected to the AFM through frame module. Inset shows the modified AFM head with the mounted I-AFM tip which has a wire connected to the cantilever to detect the current.

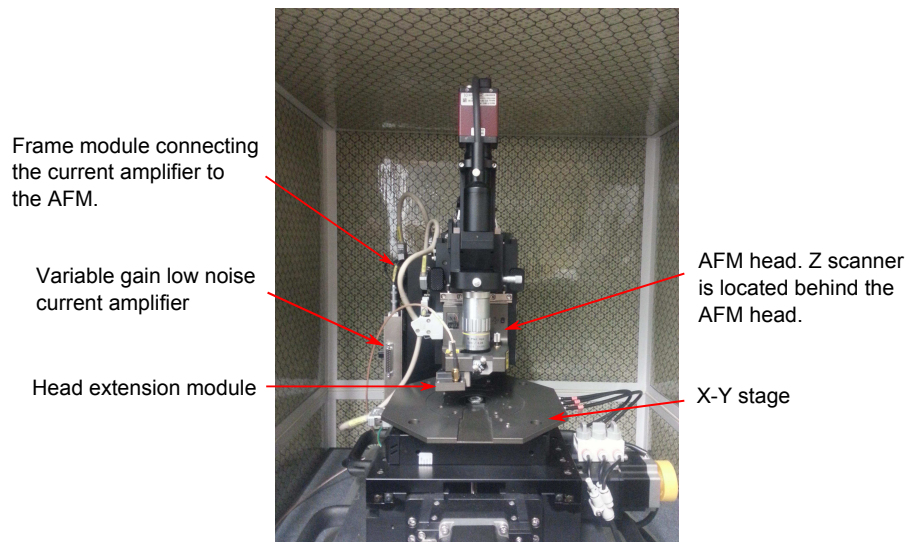


**Figure 3.9:** I-AFM components mounted on the AFM. AFM is placed inside an isolation box to avoid effects from the environment.

on the material to avoid any physical or electrical damage of the sample. It was shown in previous studies that the dielectric is prone to an early breakdown for high values of force of contact. The cantilever tip does not make sufficient physical contact with the sample surface for low values of contact force. Hence a contact force has to be selected where the average leakage current stays constant among a range of contact force values [79]. An optimised value can be any value in this range. BaTiO<sub>3</sub> deposited on a TiN<sub>x</sub> electrode on a silicon substrate was used to optimise the force of contact for this research. The force of contact was varied from 100 nN to 700 nN for each scan keeping the region under study the same. The applied voltage was kept at 2 V to find the range of values where the average leakage current stays constant. The variation in average leakage current through the same 1  $\mu\text{m} \times 1 \mu\text{m}$  region for different values of force of contact is given in Fig. 3.10. The leakage current saturates for contact forces

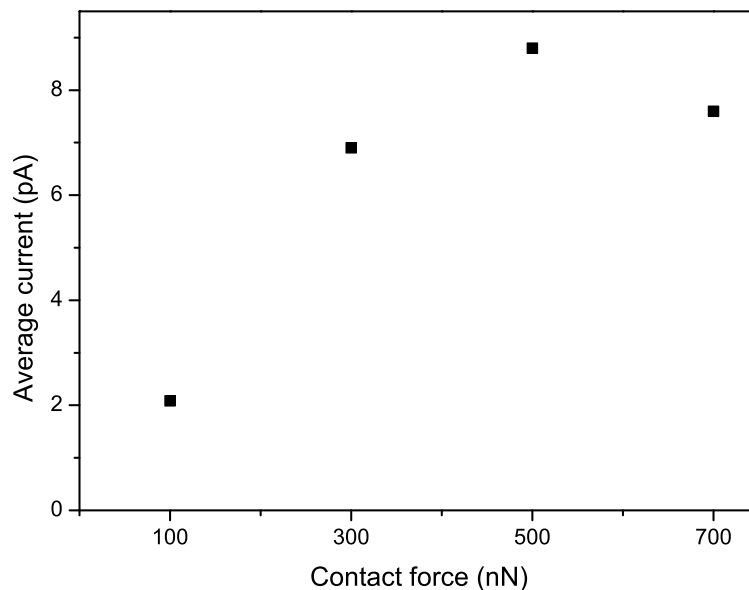


**Figure 3.10:** Variation in average leakage current through a 1  $\mu\text{m} \times 1 \mu\text{m}$  area for different values of contact force.

between 300 nN and 700 nN. Hence an optimised value of 600 nN was used as the set point for contact force for this research. Results showing the leakage current maps of sputter deposited BaTiO<sub>3</sub> are discussed in chapter 5 section 5.6.1.

### 3.2.2.2 Electrostatic force microscopy

In electrostatic force microscopy (EFM), the electrostatic force between the surface and a biased cantilever tip is measured in order to map the electric properties of the sample. A bias is applied between the tip and the sample while the cantilever scans the surface without touching it. The cantilever deflects when it scans over static charges. Hence, EFM is an effective technique to map charged domains locally. In EFM, the van der Waals force between the tip and the sample is used to measure the topography while the electrical properties are mapped by making use of electrostatic forces.

EFM was used to map the domain polarisation of BaTiO<sub>3</sub> in chapter 6 of this thesis. Enhanced EFM mode in XE 150 AFM uses an external lock-in amplifier. The purpose of the lock-in amplifier is to apply an AC bias of frequency  $\omega$  in addition to the DC bias applied by the controller and to separate the frequency component  $\omega$  from the output signal. The frequency of this AC bias is around 20 kHz which is much lower than the vibration frequency of the cantilever (200 kHz - 300 kHz). The sinusoidal wave frequency is much lower than the cantilever's vibration frequency and can be easily extracted by the lock-in amplifier without any interference. The voltage between the tip and the surface can be expressed as;

$$V(t) = V_{DC} - V_s + V_{AC} \sin(\omega t) \quad (3.6)$$

where  $V_{DC}$  is the DC offset applied to the cantilever and  $V_s$  is the surface potential on the sample.  $V_{AC}$  and  $\omega$  are the amplitude and frequency of the applied AC bias generated by the external lock-in amplifier. The electrostatic force ( $F$ ) between the tip and the sample can be calculated by considering them as two parallel plates of a capacitor [80], and can be represented as;

$$F = -\frac{\delta C}{\delta d} \times (V^2/2) \quad (3.7)$$

here,  $d$  is tip to sample distance,  $V$  is electric potential and  $C$  is capacitance. Then,

$$\begin{aligned}
 F = & -\frac{1}{2} \frac{\delta C}{\delta d} \times [(V_{DC}) - V_s]^2 + \frac{1}{2} V_{AC}^2 \\
 & - \frac{\delta C}{\delta d} \times (V_{DC} - V_s) \times V_{AC} \sin(\omega t) \\
 & + \frac{1}{4} \frac{\delta C}{\delta d} V_{AC}^2 \cos(2\omega t)
 \end{aligned} \tag{3.8}$$

The lock-in amplifier detects signals containing  $\omega$  and  $2\omega$ . The  $2\omega$  term which contains the gradient of surface capacitance between the tip and the sample is used to normalise the  $\omega$  signal. Finally, the  $\omega$  signal is used to derive  $V_s$  and thereby map the surface charge distribution.

The direction of domain polarisation in ferroelectric materials causes a variation in the electrostatic interaction between the tip and the sample. Due to its high spatial resolution (limited by the tip diameter), EFM is a non invasive and effective technique to map ferroelectric domains. Generally, the domains are electrically loaded initially by scanning an area in contact mode while applying a DC bias between the tip and the sample. The polarised region is then scanned using EFM mode, which is a non contact mode, in order to obtain a ferroelectric domain map of the previously polarised area.

### 3.2.2.3 Piezoresponse force microscopy and spectroscopy

The operating principle of piezoresponse force microscopy (PFM) is based on the detection of the inverse piezoelectric effect shown by ferroelectric materials. The conductive cantilever is biased with a pre-set voltage establishing an external field within the sample. The sample area which is under the tip would undergo deformation in the form of elongation or contraction due to the inverse piezoelectric effect. These deformations would depend on the initial polarisation direction of the domain under study. For example, if the initial polarisation is parallel to the applied field (perpendicular to the sample surface), the domain would undergo a vertical expansion due to the inverse piezoelectric effect. However, when the applied field and the direction of polarisation are in opposite directions, the domain will contract. The expansion would increase the cantilever deflection and the contraction would decrease

the deflection as shown in Fig. 3.11. The amount of cantilever deflection is directly related to the expansion or contraction and hence proportional to the applied field.

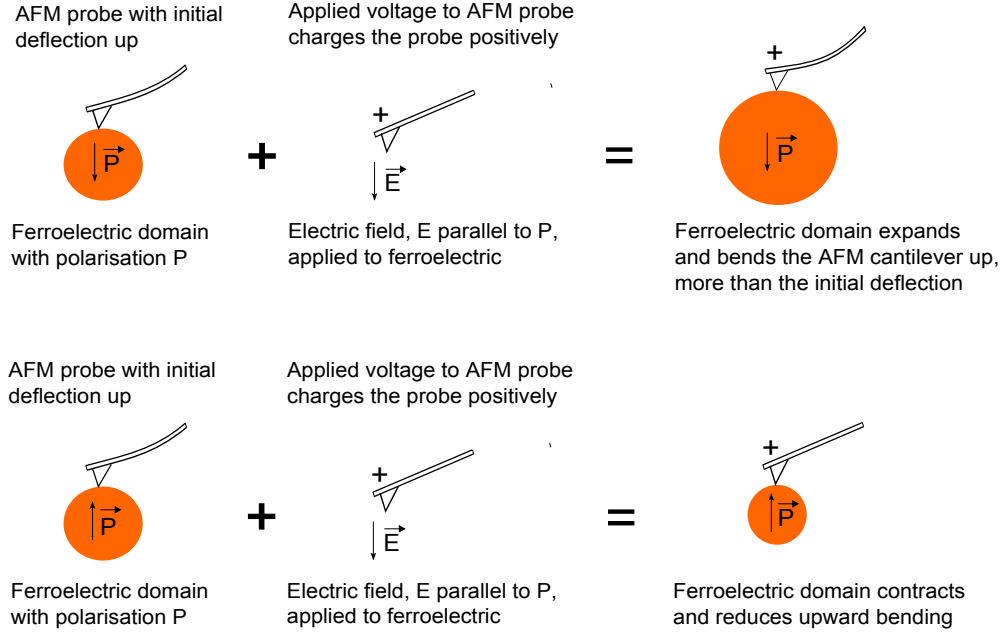


**Figure 3.11:** Expansion and contraction of a ferroelectric domain on the application of an external field. Domain expansion causes the cantilever to deflect more and contraction will reduce the bending compared to the initial state.

If the applied bias contains a small AC component, the sample surface will oscillate with the same frequency as the applied signal due to the inverse piezoelectric effect. Under the AC modulation voltage  $V = V_0 \sin(\omega t)$ , the sample surface would also oscillate with the form  $\Delta Z = \Delta Z_0 \sin(\omega t + \phi)$  where  $\Delta Z_0$  is the vibration amplitude and  $\phi$  is the phase difference between sample domain orientation and applied electric field [72, 81]. When the polarisation is pointing downward, the ferroelectric domain expands for the positive half cycle of the sinusoidal wave and it contracts for the negative half cycle as shown in Fig. 3.12 (a). Hence, the phase difference between the AC bias and domain oscillation will be  $0^\circ$ . However, the phase difference  $\phi$  will be  $180^\circ$  when the polarisation is pointing outwards as shown in Fig. 3.12 (b). This is due to the contraction of the domain in the positive half cycle and expansion in the negative half cycle. The vibration amplitude  $\Delta Z_0$  is given as;

$$\Delta Z_0 = d_{zz} V_0 = [(d_{31} + d_{15}) \sin^2 \theta \cos \theta + d_{33} \cos^3 \theta] V_0 \quad (3.9)$$

where  $d_{zz}$  is the longitudinal piezoresponse,  $d_{31}$ ,  $d_{15}$  and  $d_{33}$  are the piezoelectric tensors of the material under study and  $\theta$  is the angle between the lab coordinate system and crystal coordinate system of the sample. Since the probe is in direct contact with the sample, the sample oscillation would be directly reflected in the amplitude and phase of the AFM probe and can be read out using a lock-in amplifier. Thus, domain mapping can be obtained by scanning the surface while detecting the oscillation of the cantilever. The amplitude of cantilever oscillation would depend on the amplitude of the vertical piezoresponse and the phase would depend on the direction of domain polarisation. Signal detection using a lock-in amplifier is discussed in a later section.

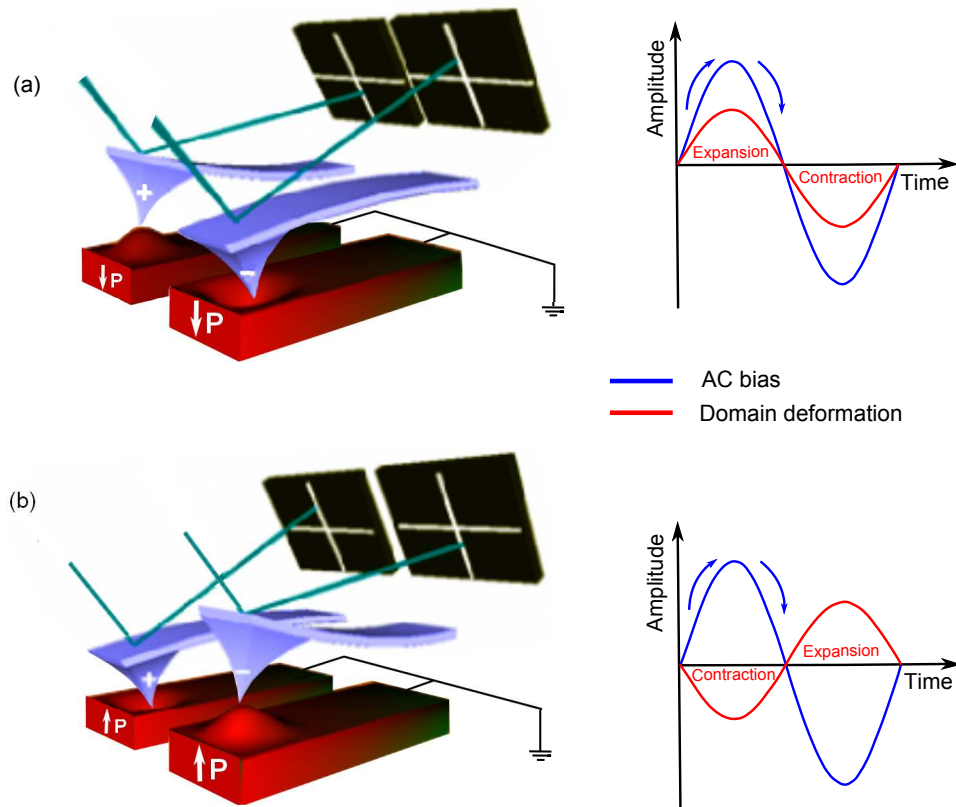


**Figure 3.12:** Illustrating contraction and expansion of the ferroelectric domain due to AC biasing of the tip and deflection of the laser due to deformations. Showing (a) PFS scanning of a domain with downward polarisation and (b) PFS scanning of a domain with upward polarisation. The amplitude of oscillation depends on the longitudinal piezoresponse and the phase depends on the direction of ferroelectric polarisation. Amplitude and phase are then detected using a lock-in technique.

In PFM imaging, the amplitude of the applied AC bias is set to be much lower than the coercive field of the sample to avoid alteration of the domain. However, a DC bias could also be swept along with the AC bias in order to generate local hysteresis loops

in ferroelectric materials, and is referred to as piezoresponse force spectroscopy (PFS). Hence, PFS can provide valuable information about polarisation switching behaviour of individual domains on the nano-scale as a function of DC bias. In chapter 6 of this thesis, the PFS technique was used to detect the polarisation reversal mechanism in BaTiO<sub>3</sub> at the domain level. Mapping of the domain structure was carried out using PFM.

### Signal detection using lock-in amplifier

This section discusses the signal detection using an SR830 lock-in amplifier. Lock-in amplifiers can detect very small AC signals of amplitude down to a few nanovolts. They are used to make accurate measurements even when the signal is obscured by noise sources many thousands of times larger. Lock-in amplifiers use a phase sensitive detection to single out signals at a specific reference frequency and phase. Lock-in requires a reference frequency,  $\omega_r$ , which is normally an external reference signal. If the signal from the experiment is of the form,  $V_{sig} \sin(\omega_r t + \theta_{sig})$ , where  $V_{sig}$  is the signal amplitude and  $\theta_{sig}$  is the phase difference between the reference and signal, lock-in generates another reference of the form  $V_L \sin(\omega_L t + \theta_{ref})$ . Lock-in amplifiers use a phase-locked-loop (PLL) to generate the reference signal. The PLL locks-in the internal reference oscillator with the external reference resulting in a lock-in reference signal of frequency  $\omega_r = \omega_L$  and a fixed phase shift of  $\theta_{ref}$ .

The amplified experimental signal is then multiplied by the lock-in reference using a phase sensitive detector (PSD). The output of the PSD is given as;

$$\begin{aligned} V_{psd} &= V_{sig} V_L \sin(\omega_r t + \theta_{sig}) \sin(\omega_L t + \theta_{ref}) \\ &= 1/2 V_{sig} V_L \cos([\omega_r - \omega_L]t + \theta_{sig} - \theta_{ref}) - \\ &\quad 1/2 V_{sig} V_L \cos([\omega_r + \omega_L]t + \theta_{sig} + \theta_{ref}) \end{aligned} \quad (3.10)$$

The output of the PSD is two signals, one with differing frequency ( $\omega_r - \omega_L$ ) and the other at a summation frequency ( $\omega_r + \omega_L$ ). Since  $\omega_r = \omega_L$  as described previously, the signal with differing frequency is a DC signal. The signal containing the summed

frequency, which is an AC signal, can be filtered out. The remaining pure DC signal is given as;

$$V_{psd1} = 1/2V_{sig}V_L\cos(\theta_{sig} - \theta_{ref})$$

$$V_{psd1} \approx V_{sig}\cos\theta \quad (3.11)$$

where  $\theta = \theta_{sig} - \theta_{ref}$ . Lock-in uses a second PSD which multiplies the signal with the reference oscillator shifted by  $90^\circ$ . The lock-in reference of this PSD will be  $V_L\sin(\omega_L t + \theta_{ref} + 90^\circ)$  and the output after filtering the AC signal will be;

$$V_{psd2} = 1/2V_{sig}V_L\sin(\theta_{sig} - \theta_{ref})$$

$$V_{psd2} \approx V_{sig}\sin\theta \quad (3.12)$$

Two PSDs generate two signals of which one is proportional to  $\cos\theta$  and the other one is proportional to  $\sin\theta$ . These outputs are denoted as;

$$X = V_{sig}\cos\theta \quad (3.13)$$

$$Y = V_{sig}\sin\theta \quad (3.14)$$

From this, the signal amplitude ( $R$ ) can be calculated as;

$$R = \sqrt{(X^2 + Y^2)} = V_{sig} \quad (3.15)$$

and phase  $\theta$  is;

$$\theta = \tan^{-1}(Y/X) \quad (3.16)$$

In the case of PFM measurements, the amplitude  $R$  will be proportional to the amplitude of piezoresponse. The phase  $\theta$  will represent the phase difference between the AC bias applied to the cantilever and the cantilever oscillation due to the piezoresponse. The lock-in reference signal is used to bias the AFM cantilever.

**PFM setup**

Fig. 3.13 (a) illustrates the setup for PFM and PFS measurements. Signals between the AFM controller and the lock-in amplifier are exchanged using BNC (Bayonet Neil-Concelman) cables. Connections between the controller and the lock-in amplifier

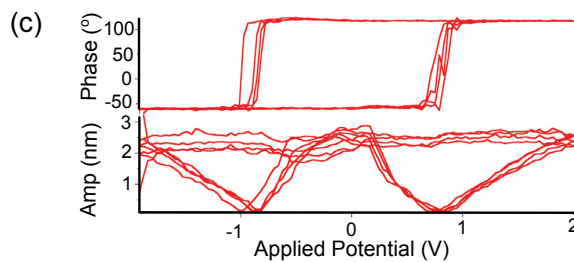
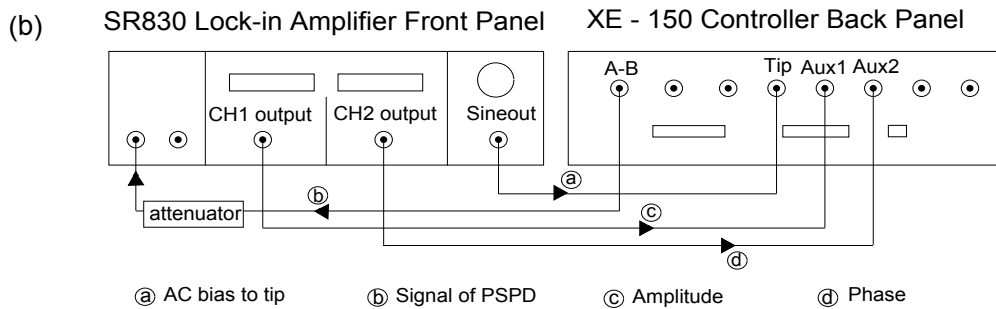
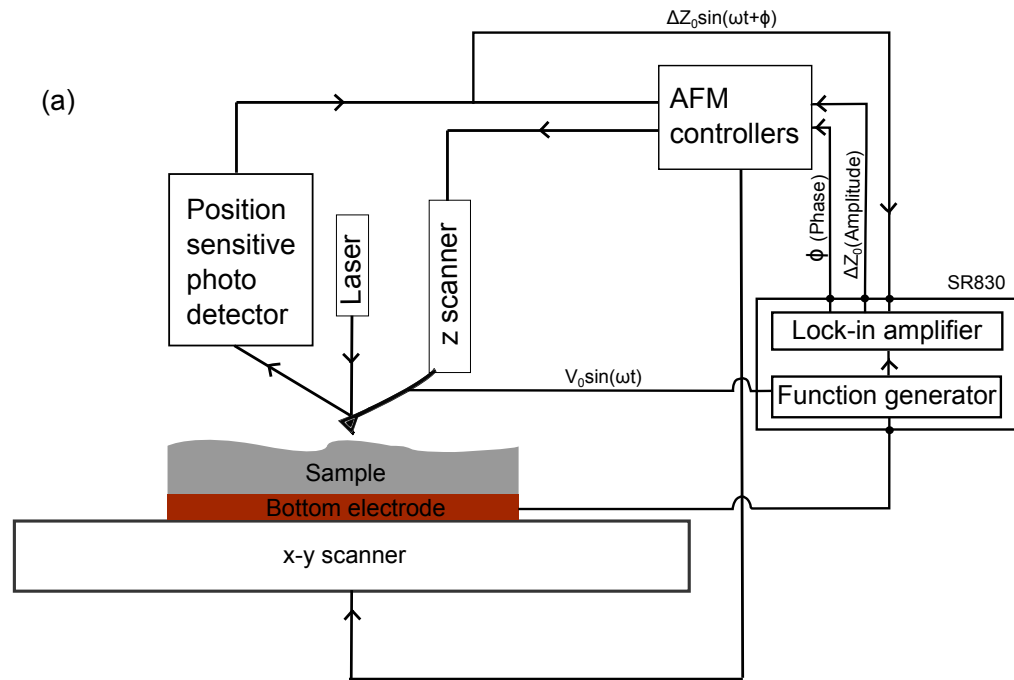


**Figure 3.13:** Illustrating (a) setup for PFM and PFS measurements, (b) Connections for PFM measurement using XE 150 and SR830 and (c) a typical PFS amplitude and phase measurement [82]

are shown in Fig. 3.13 (b). **Sine Out** carrying the lock-in reference signal is fed to the AFM cantilever through the **Ext. Tip Bias** port on the controller. **A-B**, which is the cantilever vertical oscillation signal due to sample deformation detected through the PSPD is the input signal (**A/I**) to the lock-in. The attenuator helps to reduce the amplitude of this signal to 1 V. **CH1 output** ( $R$ ) and **CH2 output** ( $\theta_{sig}$ ) feed the amplitude and phase signal to the controller through **Aux ADC1** and **Aux ADC2**. XEP software then interprets these signals to display the PFM or PFS amplitude and phase signals. Fig. 3.13 (c) shows a typical PFS amplitude and phase signal [82].

### 3.2.3 X-ray diffraction (XRD)

X-ray diffraction (XRD) is a non-destructive non-contact characterisation technique used to determine the crystallinity and phase of solids. In XRD, a monochromatic x-ray beam with wavelength  $\lambda$  is irradiated on the sample surface at an angle of  $\theta$ . X-rays are diffracted due to elastic scattering at crystal planes. A detector which is placed at an angle of  $2\theta$  with respect to the incident beam records the diffracted x-rays. Fig. 3.14 illustrates the principle of XRD. Constructive interference of diffracted x-rays occurs at

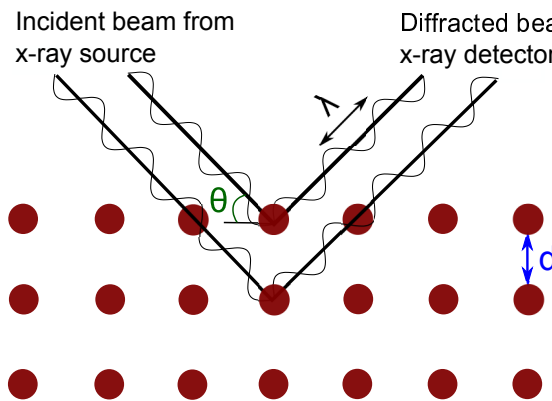


**Figure 3.14:** Illustrating the operating principle of XRD

a particular value of  $\theta$  and is defined by Bragg's law which is expressed as;

$$n\lambda = 2d\sin\theta \quad (3.17)$$

where  $n$  is an integer representing the order of diffraction and  $d$  is the distance between the crystal planes. Normally, first order diffraction is studied ( $n = 1$ ). A diffraction peak

appears for values of  $\theta$  when  $\lambda = 2d\sin\theta$  is satisfied. Therefore, a crystal structure can be determined by interpreting the angular position of the XRD peaks from the XRD spectrum.

The XRD instrument used for this research is a PANalytical X'Pert Pro Multipurpose Diffractometer powered by a Philips PW3040/60 X-ray generator and with an X'Celerator detector. X'Celerator is an ultrafast X-ray detector that uses an array of one hundred channels which can simultaneously count X-rays diffracted from a sample over a range of angles. Hence, it is able to produce high quality diffraction data in a significantly short time period. The X-ray radiation source was Cu-K $_{\alpha}$  which has a characteristic wavelength of 1.5418 Å. X-rays were generated from the Cu anode with a voltage of 40 kV and a current of 40 mA. In the following chapters, the XRD technique is used to determine the crystallinity and phase of thin film TiN $_x$  and BaTiO $_3$ . An internationally used standard database of XRD spectra, known as Inorganic Crystal Structure Database (ICSD) produced cooperatively by FIZ Karlsruhe and National Institute of Standards and Technology was used as a reference for comparing acquired spectra.

### **3.2.4 X-ray photoelectron spectroscopy (XPS)**

X-ray photoelectron spectroscopy (XPS) is a surface analysis technique used for elemental as well as chemical or electronic state identification and quantification. In XPS, the sample is irradiated with x-rays causing photoelectrons to be emitted from the top 10 nm of the sample surface. Fig. 3.15 illustrates the setup of XPS where a beam of x-rays irradiates at a particular wavelength. The photons excite electronic states from the surface of the sample. The ejected electrons pass through the hemispherical analyser which allows electrons of a given energy to reach the detector. In the detector, the kinetic energy (K.E) and the number of electrons emitted are simultaneously determined using an electron energy analyser. The electron binding energy of the emitted electrons

can be calculated by;

$$E_{binding} = E_{photon} - (E_{kinetic} + \phi) \quad (3.18)$$

where  $E_{binding}$  is the binding energy of the electron,  $E_{photon}$  is the energy of x-ray photons,  $E_{kinetic}$  is the energy of emitted electrons measured by the detector and  $\phi$  is the work function of the spectrometer. The binding energy and intensity of the

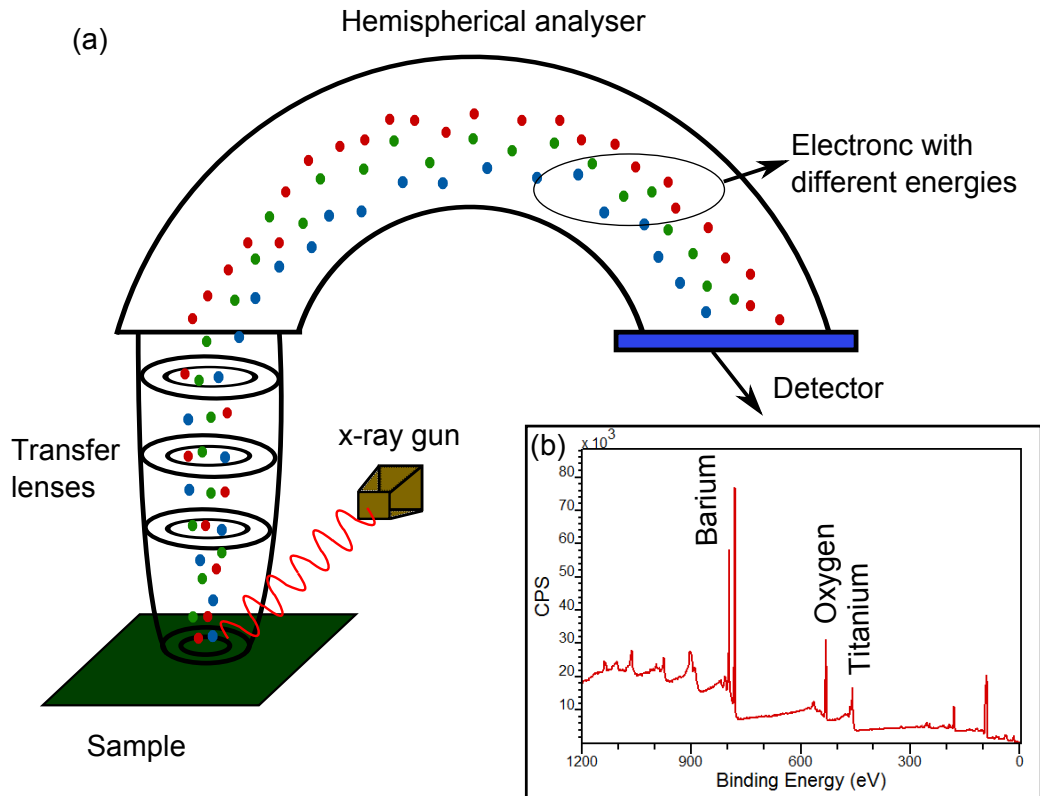


**Figure 3.15:** Showing (a) illustration of an XPS instrument setup and (b) XPS survey spectrum of BaTiO<sub>3</sub>. CPS is counts per seconds

photoelectron peak gives information about the surface layers. XPS can also be used for elemental analysis of inner layers by intentional ion beam etching of the surface layers, also known as depth profiling. A typical XPS spectrum is a plot of the number of electrons detected against binding energy of the detected electrons. Elements are identified by their characteristic set of peaks at characteristic binding energy values. The number of detected electrons is related to the amount of elements present in the sampling volume. Fig. 3.15 (b) shows a typical survey spectrum of BaTiO<sub>3</sub>.

XPS, being one of the principle methods of probing the composition and electronic

structure of surfaces has been used in this thesis to confirm the elemental composition, atomic concentration, stoichiometry and surface contamination of  $\text{TiN}_x$  and  $\text{BaTiO}_3$  thin films. XPS depth profiling has been employed to map the atomic concentration from the surface of the sample to inner layers. XPS analyses were done using a Thermo Scientific K-Alpha system which uses a micro-focused monochromated Al  $K\alpha$  source. The system provides a variable spot size between 30 - 400  $\mu\text{m}$  in 5  $\mu\text{m}$  steps. The K-Alpha system has a  $180^\circ$  hemispherical analyser and has a 128-channel detector. Depth profiling is achieved through ion milling using a monoatomic argon source. Dual beam charge neutralisation helps to acquire XPS spectra of insulating surfaces.

### **3.2.5 Raman spectroscopy**

Raman spectroscopy relies on inelastic scattering or Raman scattering of monochromatic light when it impinges on a molecule. Raman spectroscopy is used to observe vibrational or other low-frequency modes in a system. The interaction of laser light with molecular vibrations or phonons results in the energy of a very small portion (a few parts per million) of these laser photons to be shifted up or down. This weak inelastic scattering is known as Raman scattering. The shift in energy, also known as a Raman shift gives information about the vibrational modes in the system. This shift is sensitive to material properties like chemical composition, vacancies, defects, crystallinity and strain.

Typically in a Raman spectroscopy system, the sample is illuminated with a laser beam in the visible, near infrared or near ultraviolet range. Reflected light is collected with a lens and passed through a monochromator. Wavelengths close to the laser line due to Rayleigh scattering are filtered out and the rest of the scattered light is passed onto a detector via a holographic grating. Raman spectroscopy has been used in this thesis to identify the chemical composition and vacancies in sputter deposited  $\text{TiN}_x$ .

### 3.2.6 Transmission electron microscopy (TEM)

In transmission electron microscopy (TEM), a beam of electrons is passed through an ultra-thin sample and the interaction of transmitting electrons with the atoms in the sample is used to create an image. The much lower wavelength of electrons compared to light makes it possible for TEM to create images at a very high resolution. In this research, TEM images were used to study the growth mechanism of BaTiO<sub>3</sub>. A JEOL 2100F TEM fitted with a Schottky field emitter operating at 200 kV has been used to generate TEM images. The sample stage was piezo-driven for precision sample movement. High quality images were acquired using a Gatan Orius camera.

### 3.2.7 Sheet resistance

The sheet resistance of a conductive thin film is often measured using a four-point probe technique. In this method, the outer two probes are used to source the current while the inner two probes are used to measure the voltage as shown in Fig. 3.16. Since the

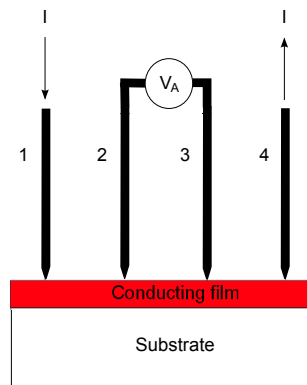


**Figure 3.16:** Illustration of four-point probe measurement technique

high impedance voltmeter draws little current, errors due to the voltage drop across the probe, spreading resistance and the contact resistance are very small. The most common way of measuring the sheet resistance is by using a four-point collinear method. When current flows through the outer probes, the voltage drop across the inner probes can be measured and the sheet resistance in this case will be,

$$R_S = G \frac{V}{I} \quad (3.19)$$

where  $R_S$  is the sheet resistance in  $\Omega/\square$ ,  $V$  is the voltage drop across the inner two probes,  $I$  is the current flow between the outer probes and  $G$  is the geometric factor which depends on the ratio of probe to wafer diameter and ratio of wafer thickness to probe separation and is a constant if the sample size is much larger than the spacing between the probes [83].

However, the above method depends on equal inter-probe spacing and hence requires additional setup. A dual configuration technique is an alternative method which can be used to measure the sheet resistance even with unequal inter-probe spacing. This method allows correction for discrepancies in probe spacing and does not require any geometric correction factors.

### 3.2.7.1 Dual configuration technique

Similar to the four-point probe technique, the dual configuration technique [84–86] also uses two probes for sourcing the current and the remaining two probes are used to measure the potential drop. Three configurations that can be used for the dual configuration technique are shown in Fig. 3.17. In this technique, after a

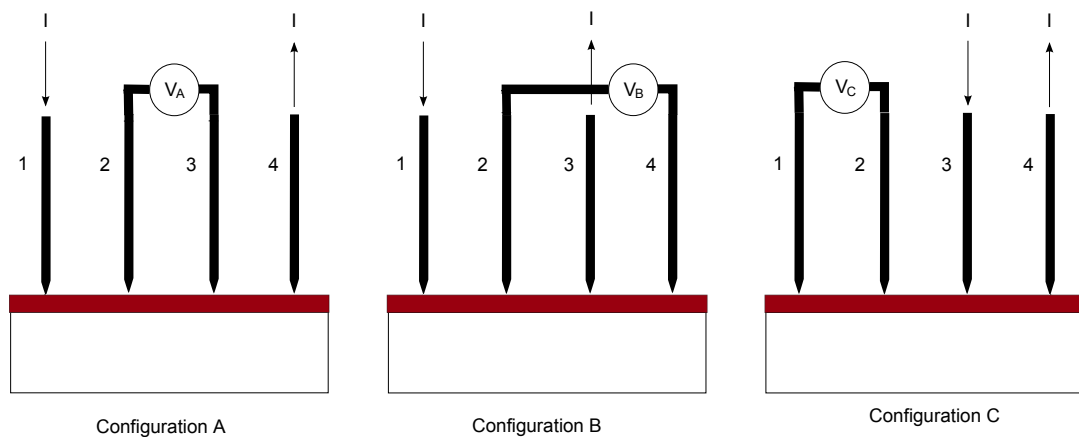


**Figure 3.17:** Three possible four-probe measurement configuration for a dual configuration technique [86]

measurement using configuration A is made, another measurement is performed using either configuration B or C. The resistances  $R_A$ ,  $R_B$  and  $R_C$  for configurations A, B and C can be calculated from the readings of current and potential drop of each configuration

as;

$$R_A = \frac{V_A}{I}; R_B = \frac{V_B}{I}; R_C = \frac{V_C}{I} \quad (3.20)$$

where  $V_A$ ,  $V_B$  and  $V_C$  are the potential drops of configurations A, B and C. The equations to calculate  $R_S$  are given as;

$$\exp\left(\frac{2\pi R_A}{R_S}\right) - \exp\left(\frac{2\pi R_B}{R_S}\right) = 1 \quad (3.21)$$

or

$$\exp\left(-\frac{2\pi R_A}{R_S}\right) + \exp\left(-\frac{2\pi R_C}{R_S}\right) = 1 \quad (3.22)$$

Using equation 3.21 or 3.21 the value of  $R_S$  can be calculated using an iteration method. Fig. 3.18 shows the sheet resistance of three different materials with different

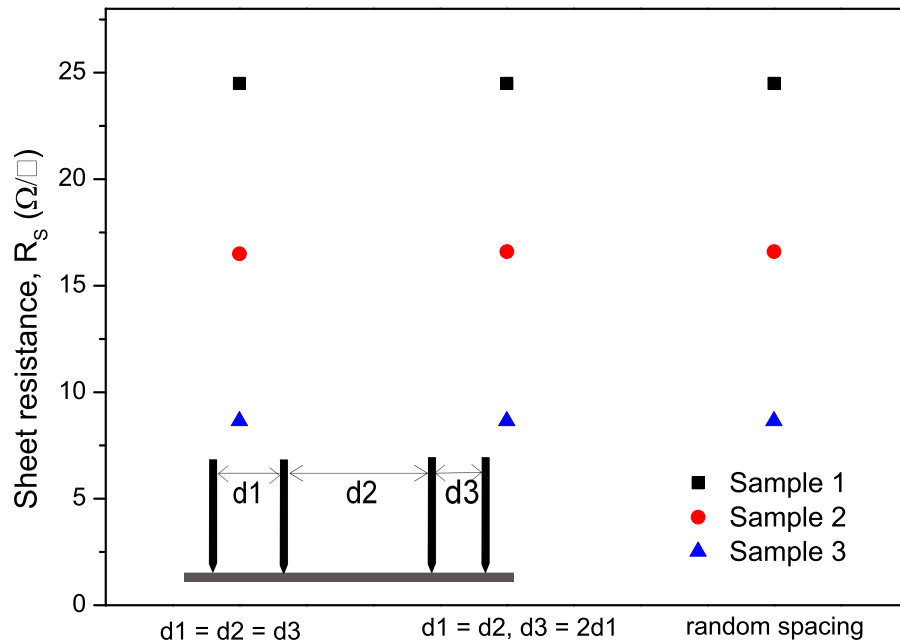


**Figure 3.18:** Sheet resistances of three different samples measured using three different inter-probe spacing using the dual configuration technique after [87]. Inset defines the inter-probe spacing  $d1$ ,  $d2$  and  $d3$ . Sheet resistance measurements for this research were all carried out on the same system.

thicknesses measured [87] using the dual configuration technique. The sheet resistances measured using different inter-probe spacings ( $d1$ ,  $d2$  and  $d3$ ) were all consistent as demonstrated in the figure. Even though the four probes are not necessarily equidistant in this technique, they still have to be collinear with each other for obtaining accurate results [86].

From the values of sheet resistance, resistivity ( $\rho$ ) can be calculated as;

$$\rho = R_s \times t \quad (3.23)$$

where  $t$  is the thickness of the layer to be measured.

In this thesis, the dual configuration technique has been used to measure the resistivity of  $\text{TiN}_x$  films which is discussed in Chapter 4. Sheet resistance measurements were done using an Agilent 4155C parameter analyzer.

### 3.2.8 I-V characterisation

The current-voltage (I-V) measurements are used in this thesis to find out the contributions from parasitic leakage effects in MIM capacitors. Electrical measurements were performed using an Agilent 4155C parameter analyzer in combination with a Cascade probe station. Fabricated devices had access to both top and bottom electrodes. Measurements were performed by sweeping the voltage on the top electrode while the bottom electrode was grounded.

## 3.3 Summary

This chapter briefly introduced most of the fabrication process modules and metrology techniques used for this research. Different tools and processing parameters employed for the deposition and characterisation of ferroelectric thin films have also been discussed. A more detailed description of the system setup and process development for the sputter deposition of thin films was given in the first section of this chapter. The importance of the SPM techniques and its different modes for the nano-scale analysis of thin films has been analysed in the later part of the chapter.

Properties of thin films and devices depend a lot on the processing steps and parameters. Hence, it is necessary to optimise the process conditions to obtain films with desired characteristics. A comprehensive utilisation of techniques like SPM, which offers insight into a film's physical structure as well as its electrical or material

properties at the resolution of few nanometres is essential for achieving the key objectives of this research. Other macro-scale electrical and material characterisation techniques should also be exploited for the qualitative and quantitative analysis of ferroelectric thin films and devices.

# Electrode Technology

## 4.1 Introduction

A key fabrication challenge for the integration of ferroelectric materials with existing silicon technology is their high crystallisation temperature [88]. In order to crystallise, these materials need substrate temperatures above 700 °C during deposition or require a post deposition anneal at even higher temperatures if they are deposited in an amorphous state. Ferroelectricity is a collective phenomenon, hence a crystalline phase is required for them to exhibit associated properties so that they can be used in integrated circuit devices. Since ferroelectric materials require high temperature processing, the electrode material used to deposit them should also be able to tolerate high temperatures without deteriorating its morphological or electrical properties. Most metals cannot withstand high temperature processing; they undergo chemical or morphological changes upon annealing at high temperatures. Being ‘noble group’ elements, platinum group metals (Ru, Pt, Ir) [89, 90], their oxides (IrO<sub>2</sub>, RuO<sub>2</sub>) [91] and alloys (Ru-Ti, Ir-Ta-O) [92] have attracted considerable interest because of their low resistivity and high chemical stability. However, high costs associated with these materials make them less favourable for semiconductor manufacturing. Refractory metal nitrides (TiN, TaN *etc.*) have been extensively studied and used in semiconductor manufacturing for processing temperatures below 500 °C. In this chapter we will discuss the electrical, chemical, material as well as morphological stability of TiN<sub>x</sub>, for

it to be used as a potential electrode for technologies which require high temperature processing.

TiN<sub>x</sub> is an extremely hard material with high thermal and chemical stability and low electrical and thermal resistivity [93]. It has found many applications in the microelectronics industry as a diffusion barrier [94], gate material [95], Schottky barrier contact [96] and adhesion layer [97]. TiN<sub>x</sub> is also used as an electrode in DRAM cells as well as back-end-of-line (BEOL) metal-insulator-metal (MIM) capacitor electrode in integrated circuits [98]. With the increased use of metal nitrides in front-end-of-line (FEOL) processes, which may undergo a post deposition anneal at temperatures well above 500 °C, the stability of these materials at process-relevant temperatures is of paramount interest. The stability of TiN<sub>x</sub> is also key for high temperature electronic circuits, as they can be used as capacitor electrodes and transistor gate electrodes in wide-gap semiconductor devices [99].

TiN<sub>x</sub> can be deposited in a variety of ways [100–103]. One such method is direct current (DC) magnetron reactive sputtering. This inexpensive technique can deposit films that have high purity and uniformity with a good control over stoichiometry. In reactive sputtering, the quality of the deposited films depends upon deposition parameters such as nitrogen content in the chamber during deposition, power, residual oxygen in the chamber, pressure, substrate temperature and substrate bias [103]. In the case of integrated circuit applications, TiN<sub>x</sub> with better electrical properties may be preferred over stoichiometric TiN.

In microelectronic applications there are constraints on the use of high substrate temperatures during deposition. This is to avoid structural and compositional changes to other materials used in device manufacture and to prevent any uncontrolled diffusion or metal extrusion [104]. However, these structures may undergo a controlled high temperature rapid thermal process (RTP) for dopant activation, dielectric crystallisation or metal-semiconductor interface activation. Hence, understanding the impact of post deposition annealing on TiN<sub>x</sub> is crucial. To date, there are currently no detailed investigations reported in the literature on the role of post deposition annealing in an

oxygen-free ambient above 500 °C on TiN<sub>x</sub> deposited with various nitrogen contents. TiN shows a bulk resistivity value between 20 μΩcm and 30 μΩcm [105, 106]. Many research groups have reported that the resistivity of sputtered TiN<sub>x</sub> increases between 100 μΩcm - 1000 μΩcm [107–109] after annealing in a non oxidising environment in the 500 °C - 800 °C range, which is claimed to be due to the oxygen impurity in the annealing ambient [110]. A drastic increase in the sheet resistance after the RTP process is not generally desirable from a semiconductor device point of view. Moreover, a sheet resistance value below 400 μΩcm is typically preferred for microelectronics applications [108, 111]. Here, we have annealed the samples in high vacuum conditions ( $1 \times 10^{-6}$  Torr) at temperatures ranging from 500 °C to 900 °C and time varying from 1 minute to 20 minutes in order to avoid the effect of oxygen impurity in the annealing process. The impact of nitrogen flow rate relative to that of argon (N<sub>2</sub>/N<sub>2</sub>+Ar) during deposition, and the post deposition thermal treatment of TiN<sub>x</sub> are the main focuses of this chapter. Results show that resistivity decreases with increase in nitrogen flow rate during deposition, annealing temperature and time. It was found that there is more than one factor which affects the resistivity of the film. Based on these results, reasons for the drop in resistivity with increase in nitrogen flow rate and with a post deposition anneal are also assessed.

In order to use TiN<sub>x</sub> as an electrode for MIM capacitors or in any other structures, the sputtered films will have to be patterned. Since the high energy sputtered atoms attack the photoresist, traditional metal lift-off process cannot be used to pattern them. Therefore, sputter deposited TiN<sub>x</sub> films require a post deposition etching in order to fabricate thin film structures. A variety of wet as well as dry etchants [112, 113] can be used for effective patterning of TiN<sub>x</sub>. Selectivity between TiN<sub>x</sub> and the underlying structure, BaTiO<sub>3</sub> in this case, will be the key parameter while choosing the right etchant. TiN<sub>x</sub> can be etched with precise time control in a solution of ammonium hydroxide (NH<sub>4</sub>OH) : hydrogen peroxide (H<sub>2</sub>O<sub>2</sub>) : deionised water (H<sub>2</sub>O) = 1 : 2 : 5 at 60 °C [112], which is also known as the RCA-1 solution. However, the RCA-1 solution also attacks the photoresist and hence requires a hard mask, resulting in additional

processing steps. TiN can be also be patterned effectively by reactive ion etching using process gases such as SF<sub>6</sub>/Ar, CF<sub>4</sub>/CHF<sub>3</sub>, C<sub>2</sub>F<sub>6</sub>/Ar. Here we have also developed a dry etching recipe using SF<sub>6</sub>/Ar gas in order to selectively etch TiN<sub>x</sub> which is deposited on BaTiO<sub>3</sub>.

This chapter discusses the TiN<sub>x</sub> process development, optimisation and also the impact of post deposition annealing at temperatures above 500 °C on sputter deposited films. Experimental details are given in section 4.2. Section 4.3 of this chapter discusses the initial process development. Target conditioning and the importance of chamber vacuum on the deposited films are also covered in this section. Section 4.4 discusses the optimisation of TiN<sub>x</sub> process parameters in order to obtain films of varying resistivity. In section 4.5, results showing the impact of deposition conditions on the post deposition thermal treatment of TiN<sub>x</sub> are presented. The results are analysed based on the material as well as electrical characteristics of the deposited films. In the final section, a dry etching recipe is also discussed for selectively etching TiN<sub>x</sub> deposited on BaTiO<sub>3</sub>.

## 4.2 Experimental Details

TiN<sub>x</sub> was sputtered in an Oxford plasma 400™DC magnetron sputtering system using an eight inch high purity (99.995%) titanium target in a mixture of argon and nitrogen gas. Prior to that, the titanium target was cleaned and conditioned in pure argon gas. For target conditioning, the power applied to the magnetron was increased from 100 W to 500 W in steps of 100 W with each step lasting 4 minutes. There was a delay of 2 minutes between each step so that the heat generated on the target during the conditioning is dissipated properly. The system was baked out at 100 °C for 12 hours which reduced the chamber pressure to  $1 \times 10^{-6}$  Torr. Further improvement in the vacuum was achieved by depositing titanium on a dummy wafer in two steps of 15 minutes each, which reduced the vacuum of the system to  $1 \times 10^{-7}$  Torr. The sputtered titanium is believed to react with the remaining oxygen in the chamber creating oxides and thereby reducing the gas pressure inside the chamber.

Initially the  $\text{TiN}_x$  recipe was optimised in order to find the least resistivity for the as-deposited samples. A series of experiments were carried out to find the impact of deposition conditions such as nitrogen flow rate, deposition power and the role of substrate temperature on the resistivity. No bias voltage was applied to the substrate and the target-to-substrate distance was fixed at 10 cm. 80 nm thick thermally oxidised silicon dioxide on  $\langle 100 \rangle$  oriented silicon was used as the substrate. The deposition time was set to 10 minutes, with the chamber pressure kept at 4 mTorr and the base pressure was  $1 \times 10^{-7}$  Torr. The flow rate of nitrogen relative to that of argon was varied from 20% to 95% in order to produce samples of varying stoichiometry. The power variation was from 500 W to 800 W and the substrate temperature was varied from room temperature up to 250 °C.

After the initial optimisation experiments, the deposition power used was 800 W for all experiments and the substrate temperature was limited to 250 °C in order to make the process compatible for both front and back end of line integration. Step height measurement using AFM after etching a thin strip of the film showed that the thickness variation was from 130 nm to 170 nm corresponding with the variation in nitrogen flow rate. In order to examine the role of high temperature processing on  $\text{TiN}_x$  thin film properties, as-deposited samples deposited in different nitrogen flow rates were annealed in high vacuum ( $1 \times 10^{-6}$  Torr). Annealing processes were carried out at 500 °C, 700 °C and 900 °C for 1, 2, 10 and 20 minutes.

A Plasma-Therm 790 series reactive ion etching system was used to dry etch the  $\text{TiN}_x$  films in order to fabricate top electrodes of MIM capacitors. Prior to etching, a pattern containing circles with diameters ranging from 50  $\mu\text{m}$  to 300  $\mu\text{m}$  was created on the  $\text{TiN}_x$  films using photolithography. A detailed description of the photolithography process is given in section 3.1.4 of chapter 3. Photoresist AZ 5214E was spun and exposed using a Karl Suss MJB-3 mask aligner. The exposed resist was subsequently developed using AZ 326 MIF. The patterned resist had circles of varying diameter which would act as a mask while reactive ion etching, so that  $\text{TiN}_x$  top electrodes of varying diameter can be realised.

Sheet resistance was measured at room temperature by a standard four point probe measurement technique. Phase composition and crystallinity was characterised by X-ray diffraction (XRD) using PANalytical X'Pert Pro. with Cu-K $\alpha$  X-ray radiation having a characteristic wavelength of 1.5418 Å. The X-rays were generated from a Cu anode supplied with 40 kV and a current of 40 mA. Instrumental broadening of the XRD spectrum was calculated using a BaTiO<sub>3</sub> powder sample of known grain size. X-ray photo-electron spectroscopy (XPS) was performed on samples using a Thermo Scientific K-alpha instrument. Argon ions with a beam current of 5 mA, an acceleration of 5 kV and a square raster of 1 mm was used to etch the sample for depth profiling. The X-ray spot size was 110  $\mu$ m for the XPS measurements. Raman spectroscopy was used to identify vacancies in the film. A 514 nm laser was used for Raman spectroscopy measurements. The acquisition time was 30 s and the confocal aperture was set to 300  $\mu$ m. Surface roughness of the deposited film was measured using a Park Systems XE 150 AFM in non contact mode. The SiO<sub>2</sub> surface has a RMS roughness of 0.3 nm. The majority of the material analysis was carried out on samples deposited at the lowest nitrogen content (20%) and highest nitrogen content (95%), in order to isolate the physical/structural origins of any observed differences in resistivity.

## 4.3 Process Development

### 4.3.1 Target conditioning

A thin layer of oxide is expected to form on the titanium target due to its high reactivity with oxygen even at room temperature. This oxide layer, along with the absorbed water vapour from the atmosphere and other particulate contamination form a non conductive layer on the surface of a newly purchased titanium target. This non conductive coating can generate substantial heat on the target if it is subjected to a high power. The heat generated on the target due to the surface layer combined with the low thermal conductivity of titanium, generates excessive heat on the target. This heat leads to undesirable effects such as target bending or warping. Moreover, the titanium target

should be free of any surface layers prior to the reactive sputtering of  $\text{TiN}_x$  so that the deposited films are not contaminated. Bias voltage, which shows the potential drop from the cathode (target, magnetron) to the anode (substrate, ground) is a good measure in order to monitor the target conditions. An electrically non conductive oxide layer on the surface of the target will cause a higher potential drop across the electrodes than a pure titanium target.

The variation in the potential drop between the electrodes at the start and at the end of the 4 minute deposition cycle for each power level is shown in Fig. 4.1. The power

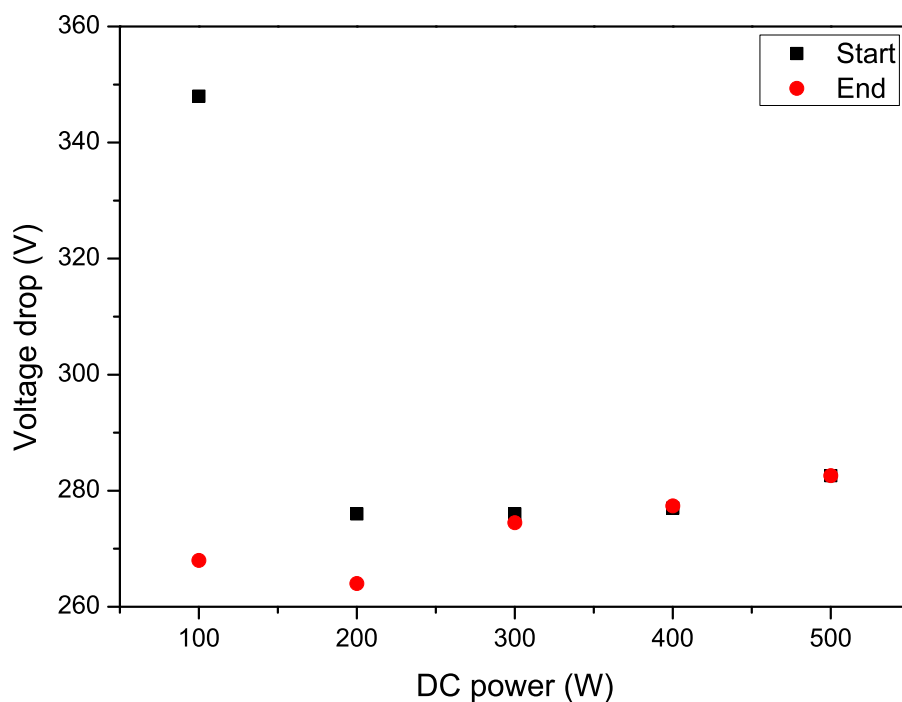


**Figure 4.1:** Variation in the potential drop between the electrodes at different power levels for a fixed deposition time of 4 minutes. Initially, when the applied power was 100 W, the variation in the voltage between the start and end of the process is high, indicating the presence and the removal of the surface layer. In the following steps the variation is minimal indicating that the surface layer has been removed and the target is pure titanium.

applied was gradually increased from 100 W to 500 W so that the heat generated was better controlled. The delay of 2 minutes between each step ensures that the generated heat is adequately dissipated. Initially, when the power applied was 100 W, the variation in the potential drop is high as shown in Fig. 4.1. This indicates the presence of a surface layer and its removal with time. For the following cycles, the variation between start and end of deposition reduces as the surface layer gets thinner. For 400 W and 500 W

cycles the potential drop from start to end remains same showing the complete removal of the surface layer. The potential drop at 500 W was also used as the reference value for a cleaned titanium target. A target cleaning step was carried out prior to each  $\text{TiN}_x$  deposition at 500 W, ensuring the reference value is achieved so that the initial target conditions remain the same for all deposition runs.

### 4.3.2 Deposition conditions

Incorporation of oxygen in the sputtered films is an undesirable characteristic of nitrides deposited at base pressure in the normally achievable high vacuum range ( $1 \times 10^{-6}$  Torr) [114, 115]. A newly created titanium thin film can absorb the residual oxygen in the chamber to create oxides which act to improve the vacuum, known as ‘gettering’. The gettering process improved the vacuum from  $1 \times 10^{-6}$  to  $1 \times 10^{-7}$  Torr. Fig. 4.2 shows XPS results confirming the variation in atomic percent of oxygen against distance from the surface in samples deposited at two different base pressure levels keeping all other deposition conditions constant. There is a higher oxygen concentration on the surface for both samples, which reduces as the etching progresses towards the bulk. The sample deposited at  $1 \times 10^{-7}$  Torr shows almost 8% lower oxygen

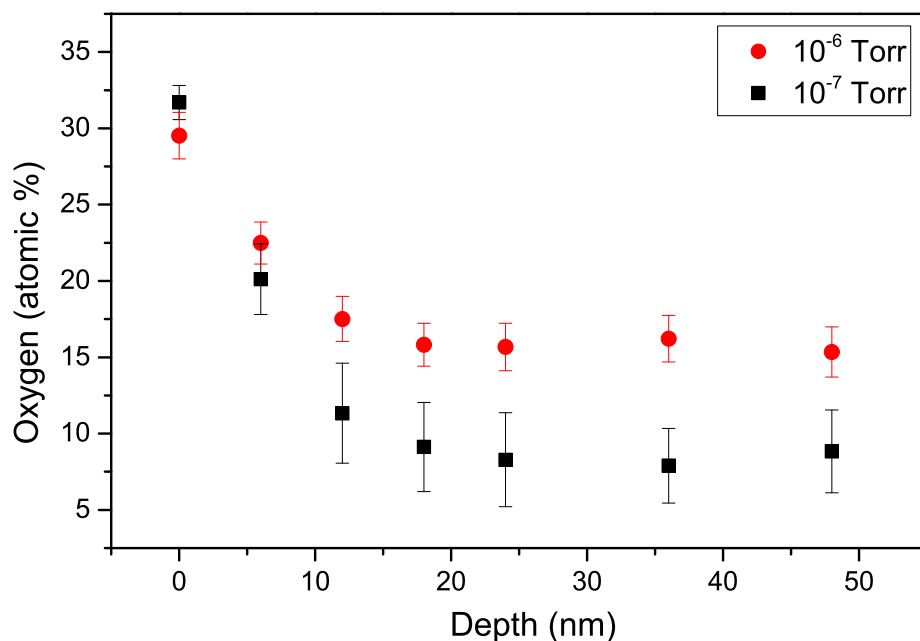


**Figure 4.2:** Oxygen content variation in the  $\text{TiN}_x$  films deposited at different vacuum levels measured by XPS. The sample deposited at improved vacuum has lower oxygen contamination in the film compared to the one deposited at  $1 \times 10^{-6}$  Torr.

concentration in the bulk compared to the one deposited at a base pressure level of  $1 \times 10^{-6}$  Torr. The small amount of oxygen still present in the film could be primarily due to the oxygen contamination in the nitrogen source [110] or due to residual oxygen still present inside the chamber. Oxygen acts as an impurity in the  $\text{TiN}_x$  films and the enhancement in vacuum results in an improvement in the resistivity of the film. The film deposited at  $1 \times 10^{-7}$  Torr showed a resistivity of  $80 \mu\Omega\text{cm}$  whereas the resistivity of the film deposited at  $1 \times 10^{-6}$  Torr was  $150 \mu\Omega\text{cm}$ . The higher oxygen concentration near the surface was thought to be due to surface oxidation of nonstoichiometric  $\text{TiN}_x$  as a result of the low oxidation threshold of titanium.

## 4.4 Process Optimisation

The resistivity of the as-deposited film showed a decreasing trend with increasing nitrogen flow rate as shown in Fig. 4.3. The resistivity of the as-deposited samples was highest when the nitrogen flow rate was lowest (20%). Resistivity reduces with an

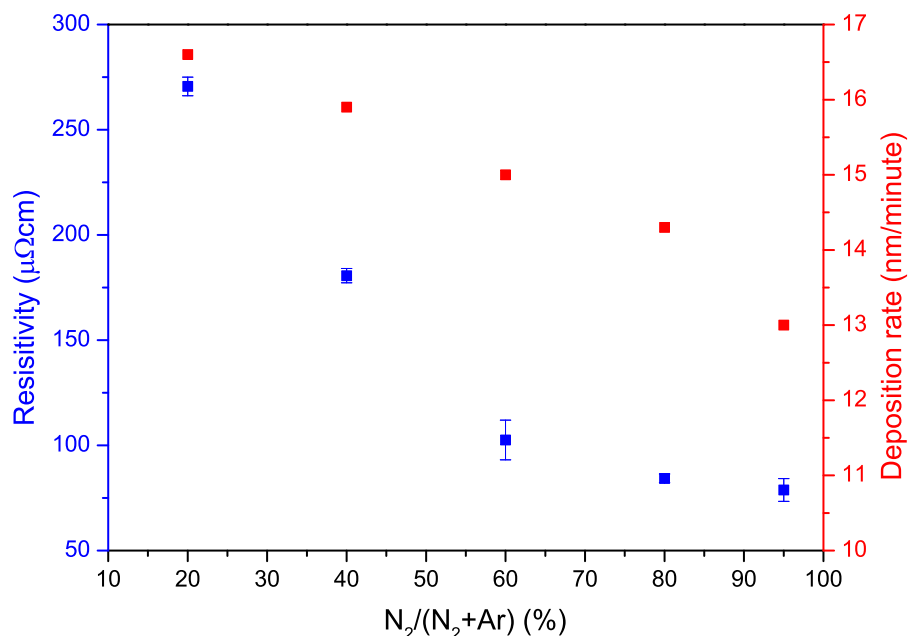


**Figure 4.3:** Variation in resistivity and rate of deposition with increase in nitrogen flow rate for fixed deposition time of 10 minutes, power of 800 W and substrate temperature of  $250^\circ\text{C}$ .

increase in nitrogen content during deposition and reaches the lowest value of  $80 \mu\Omega\text{cm}$  for the highest nitrogen content of 95%. Hence, the maximum nitrogen content used

was 95%. The deposition rate decreased from 16.5 nm/minute for the 20% sample to 13 nm/minute for the 95% sample for a power of 800 W. The density of sputtering ions ( $\text{Ar}^+$ ) in the chamber decreases with increasing nitrogen content which reduces the sputtering yield and hence a decrease in deposition rate. The reduction in the resistivity of the deposited films with the increase in nitrogen flow rate is described in the discussion part of the next section. Conditions such as sputtering power and temperature can also affect the quality of the deposited films.

Fig. 4.4 (a) shows a decrease in resistivity with an increase in sputtering power. An

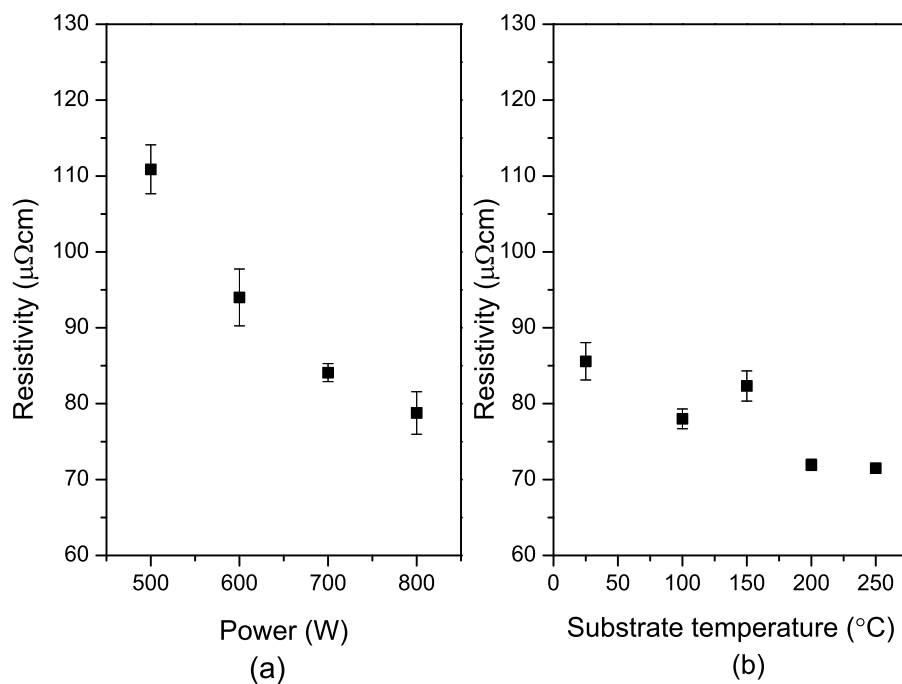


**Figure 4.4:** Variation in resistivity with (a) power and (b) substrate temperature for samples deposited with 95% nitrogen content.

increase in sputtering power will give more energy to the titanium ions to react with nitrogen, and will reduce the presence of unreacted titanium in the films. An increase in the sputter power will also increase the rate of deposition which can influence the oxygen content in the films [116] hence reducing the resistivity. Fig. 4.4 (b) shows the improvement in resistivity with increase in substrate temperature. The increase in substrate temperature facilitates the reaction between sputtered titanium and nitrogen acting to lower the resistivity. The increase in power as well as substrate temperature gives more energy to the sputtered species, this improves the reaction between the

sputtered species and reacting gas (nitrogen). The maximum sputtering power used was 800 W in order to avoid excessive heating of the target and the maximum substrate temperature used was limited to 250 °C so that the process is BEOL friendly. Results show that the resistivity of  $\text{TiN}_x$  can be varied by changing the nitrogen content during deposition, keeping all other parameters constant.

**Table 4.1:** Summary of the optimised recipe for  $\text{TiN}_x$  deposition.

<b><i>General parameters</i></b>	
Base pressure	$1 \times 10^{-7}$ Torr
Chamber pressure	4 mTorr
Substrate temperature	250 °C
Table mode	static
Target to substrate distance	10 cm
<b><i>Target cleaning</i></b>	
Ar	50 sccm
Power	500 W
Time	10 minutes
<b><i>Pre-sputter</i></b>	
$\text{N}_2/(\text{N}_2+\text{Ar})$	20% - 95%
Power	700 W
Time	5 minutes
<b><i>Deposition</i></b>	
$\text{N}_2/(\text{N}_2+\text{Ar})$	20% - 95%
Power	800 W
Time	10 minutes

Based on the above results, an optimised recipe was proposed. A summary of the optimised recipe for the development of  $\text{TiN}_x$  with varying resistivity is given in Table. 4.1. Parameters such as base pressure, chamber pressure, substrate temperature and deposition power were kept constant based on previous optimisation results. The process involves three steps; target cleaning, pre-sputtering and deposition. Initially the target is cleaned in order to remove contaminants from its surface. In the pre-sputtering

step  $\text{TiN}_x$  is deposited with the desired nitrogen flow rate so that the chamber and target conditions are initialised for the following deposition step. Variations in resistivity were obtained by varying the nitrogen flow rate.

#### 4.4.1 Oxidation resistance

Oxidation resistance is a good measure of understanding the quality of  $\text{TiN}_x$  [117]. Unreacted titanium oxidises at a temperature much lower than titanium bonded with nitrogen. Stoichiometric TiN is found to be oxidation resistant below 500 °C [117, 118]. BEOL integration of  $\text{TiN}_x$  demands annealing in an oxidising environment as they show better diffusion barrier properties when the film is oxygen rich [119].  $\text{TiN}_x$  samples were annealed from 400 °C to 550 °C in the furnace in an oxidising environment for 120 minutes and the resistivity values were obtained as shown in Fig. 4.5. There is

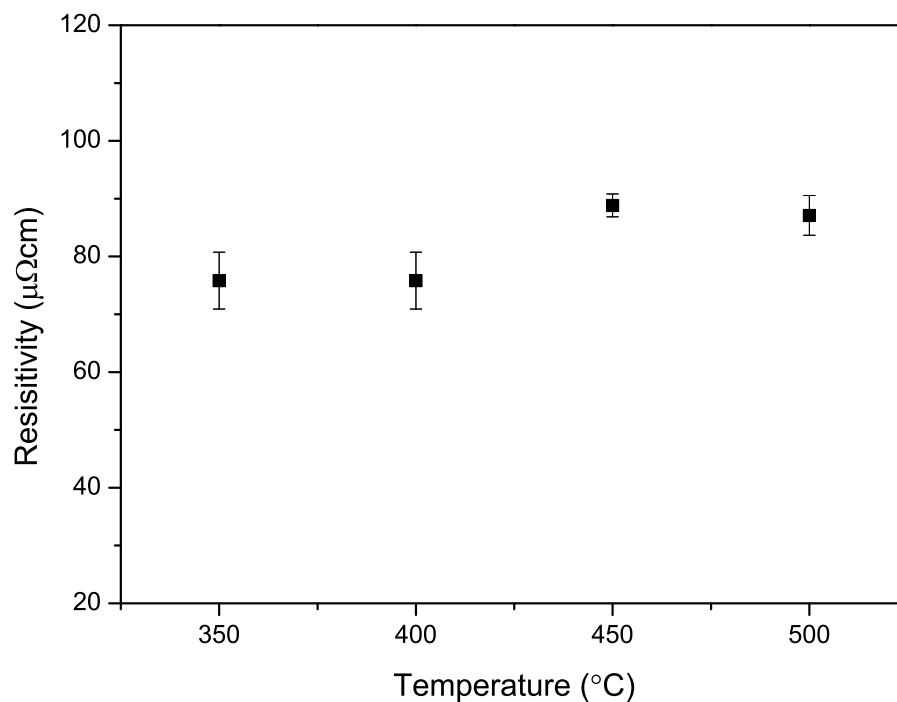


**Figure 4.5:** Resistivity vs annealing temperature for low temperature furnace annealing in air for  $\text{TiN}_x$  deposited with 95% nitrogen flow rate.  $\text{TiN}_x$  showed good oxidation resistance below 500 °C and was completely oxidised at 550 °C. The film annealed at 550 °C showed insulating properties and the measured current was below the detection of the measurement system. Hence, the data point is not shown in the plot.

a small increase in resistivity with increase in temperature up to 500 °C which could be due to slight oxidation of  $\text{TiN}_x$ . At 550 °C the sample becomes completely non

conductive indicating complete oxidation.  $\text{TiN}_x$  deposited with optimised recipe is found to be oxidation resistant below  $500\text{ }^\circ\text{C}$ . Moreover, the resistivity values for below  $500\text{ }^\circ\text{C}$  annealing are lower than  $400\text{ }\mu\Omega\text{cm}$  making the process compatible for BEOL integration.

## 4.5 Post Deposition Annealing

### 4.5.1 Variations in resistivity

Changes in resistivity as a function of nitrogen flow rate during  $\text{TiN}_x$  deposition and for different annealing temperatures for a 1 minute anneal are shown in Fig. 4.6 along with the resistivity of the as-deposited samples. The resistivity of films reduces with

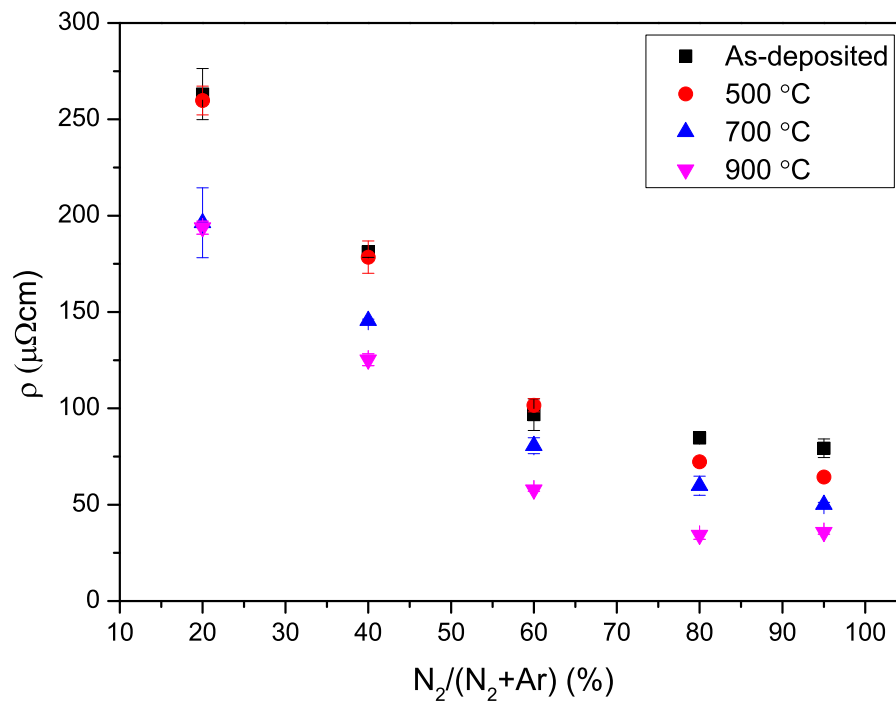


**Figure 4.6:** Variation of  $\text{TiN}_x$  resistivity with annealing temperature for a fixed annealing time of 1 minute, showing the decrease in resistivity with annealing temperature.

increasing annealing temperatures for all nitrogen contents, and falls to  $35\text{ }\mu\Omega\text{cm}$  for the sample deposited at 95% nitrogen content when annealed at  $900\text{ }^\circ\text{C}$  for 1 minute. Resistivity for different annealing times at a fixed annealing temperature of  $700\text{ }^\circ\text{C}$  is shown in Fig. 4.7. It can be seen that resistivity drops with annealing time and the lowest value of  $30\text{ }\mu\Omega\text{cm}$  was obtained when annealing the highest nitrogen content

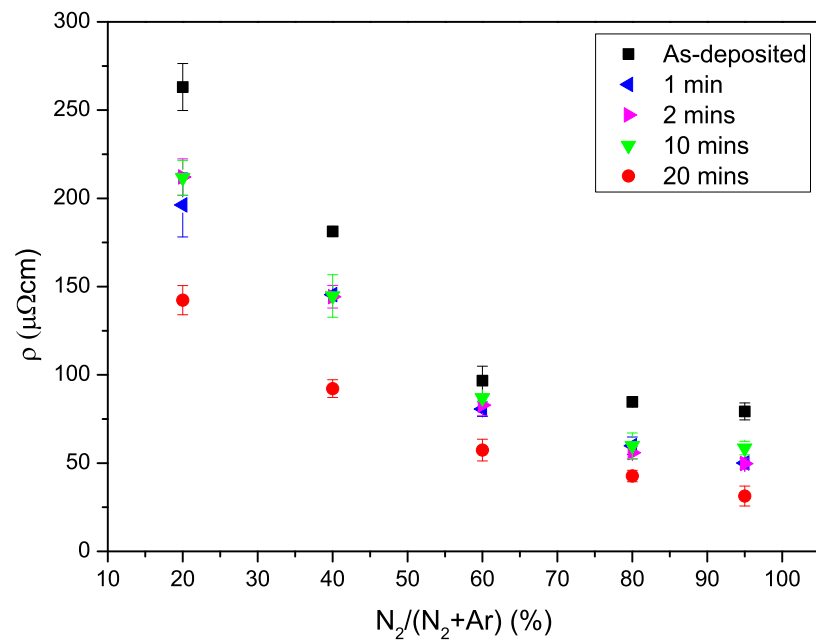


**Figure 4.7:** Variation in  $\text{TiN}_x$  resistivity with annealing time for a fixed annealing temperature of  $700\text{ }^\circ\text{C}$ . Resistivity is inversely proportional to annealing time.

sample for 20 minutes. Fig. 4.8 shows the resistivity for variations in nitrogen content, annealing temperature and annealing time. The as-deposited sample is also shown, for a temperature of  $25\text{ }^\circ\text{C}$  and time 0 minutes. It can be clearly observed that the resistivity decreases with increase in nitrogen content during deposition, annealing time and annealing temperature. The highest resistivity was present for the as-deposited samples deposited in 20% nitrogen flow. The lowest resistivity was obtained when the nitrogen flow rate was at its highest (95%) and when annealed at  $900\text{ }^\circ\text{C}$  for 20 minutes. The variation in the material properties after a post deposition anneal is discussed in the following sections and reasons for these variations are described in the discussion section.

#### 4.5.2 Variations in orientation

The XRD spectra of  $\text{TiN}_x$  deposited at 20% or 95% nitrogen flow rate and then annealed at  $700\text{ }^\circ\text{C}$  for 1 minute and 10 minutes are shown in Fig. 4.9. The 20% sample shows a main peak associated with the [111] orientation at around  $36.7^\circ$ , whereas the 95% sample shows a weaker peak for [111] orientation and a predominant peak for [200] orientation around  $42.8^\circ$ . The XRD peak positions confirm that samples deposited at

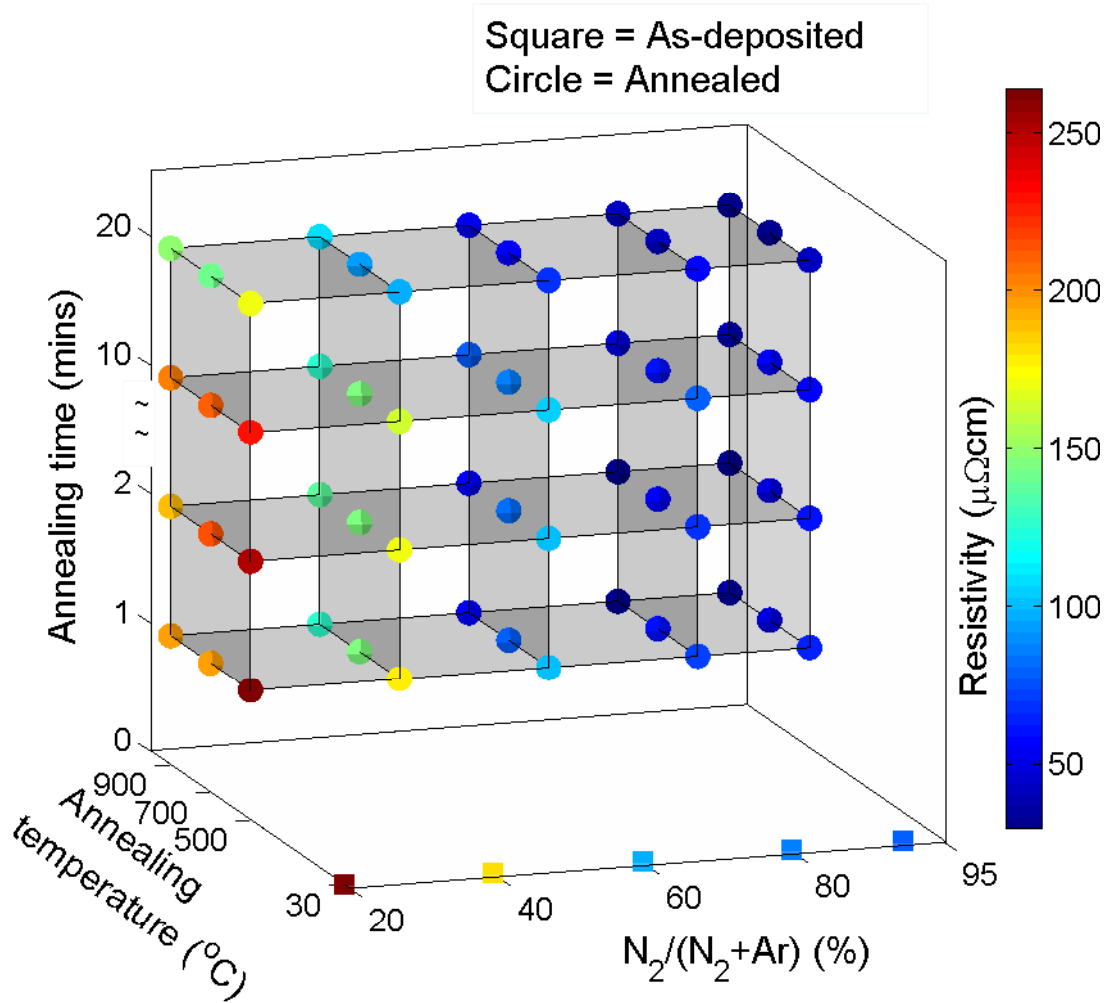


**Figure 4.8:** Variation in resistivity with variation in nitrogen content, annealing time and temperature. The as-deposited samples are presented at temperature 25 °C and time 0 minutes. Resistivity is inversely proportional to nitrogen flow rate, annealing temperature and annealing time. Highest resistivity was observed on as-deposited 20% sample and the lowest resistivity was observed on 95% sample annealed at 900°C for 20 minutes.

various nitrogen pressures are all TiN phases [120]. Grain size ( $L$ ) can be calculated from XRD spectra using Scherrer equation [121] given by;

$$L = \frac{K\lambda}{\beta \cos\theta} \quad (4.1)$$

where  $K$  is a dimension less shape factor with a value of 0.94.  $\lambda$  is the x-ray wavelength,  $\beta$  is the line broadening at half the maximum intensity after removing the instrumental line broadening and theta  $\theta$  is the Bragg angle. Fig. 4.10 shows the grain size calculated using the Scherrer equation for TiN<sub>*x*</sub> deposited at 20%, 60% and

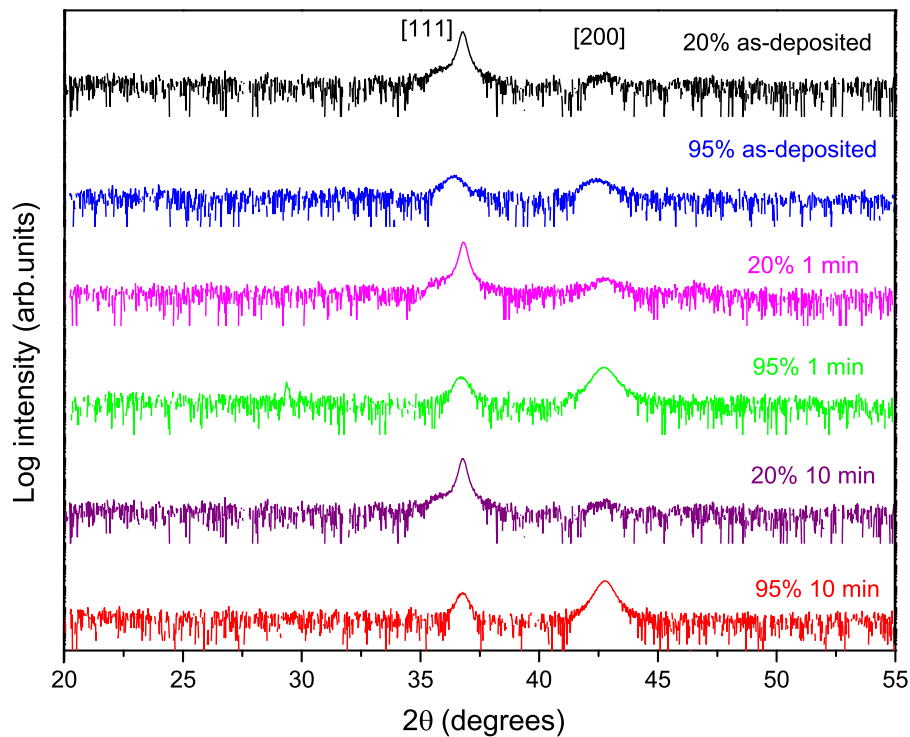


**Figure 4.9:** XRD spectra showing primarily two preferred orientations for  $\text{TiN}_x$  20% and 95% samples as-deposited, and annealed at 700 °C for 1 minute and 10 minutes.

95% nitrogen flow rates. The 20% sample has larger grains compared to the 60% and 95% ones. Moreover, the grain size is found to increase with annealing time for all the samples. The increase in grain size after an anneal is due to the re-crystallisation effects.

The relative intensity ( $I[111]/I[200]$ ) from the XRD spectra is shown in Fig. 4.11.

$\text{TiN}_x$  films with the highest  $I[111]/I[200]$  intensity in XRD spectra demonstrate the highest resistivity; these are also the films deposited at lowest nitrogen content. The  $I[111]/I[200]$  XRD peak intensity and the resistivity decrease with increasing nitrogen flow rate for the as-deposited samples. These results demonstrate that the resistivity of  $\text{TiN}_x$  depends on the phase orientation. However, after post deposition annealing, the change in  $I[111]/I[200]$  intensity was not proportional to the annealing time even though the resistivity decreased with increasing annealing time. Moreover, the  $I[111]/I[200]$  XRD peak intensity increased when compared to that of the as-deposited sample deposited in 60% nitrogen ambient. This would suggest that there is more than one factor directly influencing the resistivity of the film. These other factors affecting the resistivity of the film are investigated in the following sections. Based on these

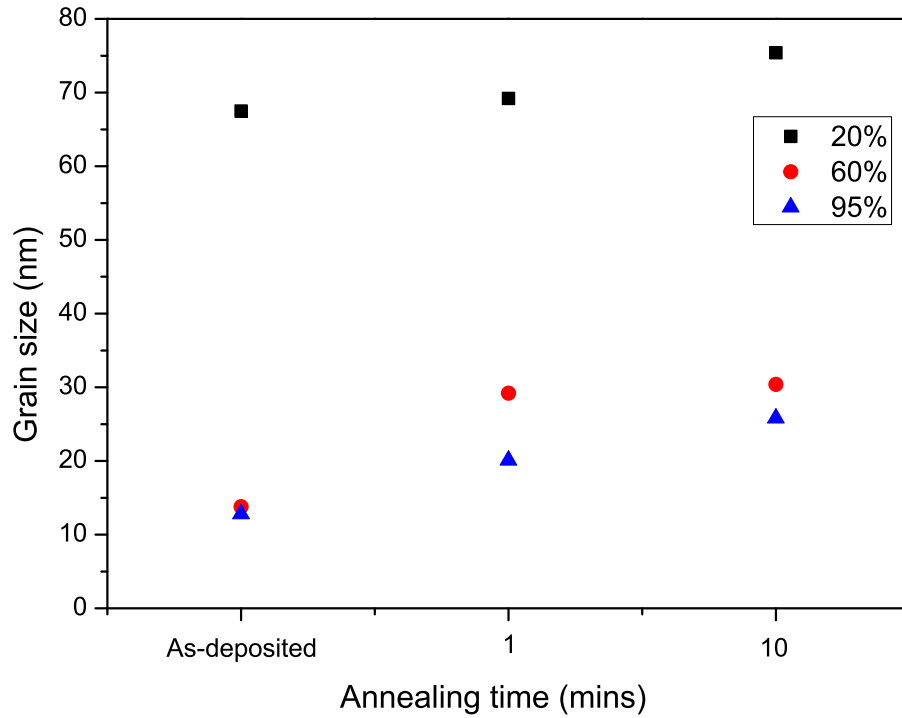


**Figure 4.10:** Grain sizes calculated using Scherrer equation for  $\text{TiN}_x$  deposited at various nitrogen flow rates.

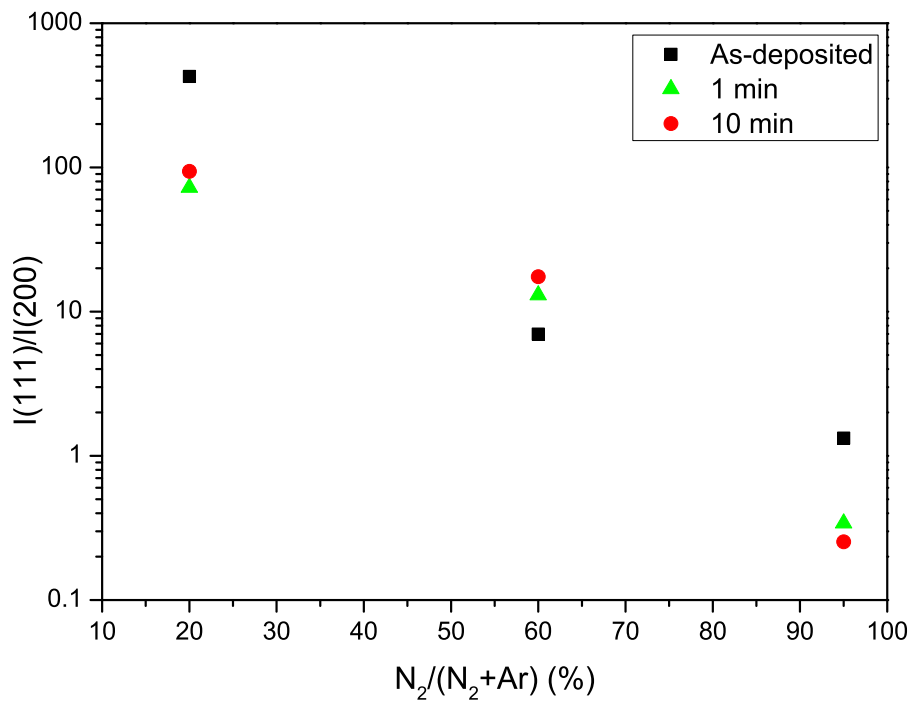


**Figure 4.11:** Relative intensity of [111] peak to [200] peaks of  $\text{TiN}$  in XRD spectra against variation in nitrogen flow rate.

results, reasons for the drop in resistivity with increase in nitrogen flow rate and with a post anneal are assessed in the discussions section.

### 4.5.3 Variations in vacancies

Raman spectra of the as-deposited and annealed samples (10 min, 700 °C) for 20% and 95% nitrogen flow rate during  $\text{TiN}_x$  deposition are shown in Fig. 4.12.  $\text{TiN}_x$  contains

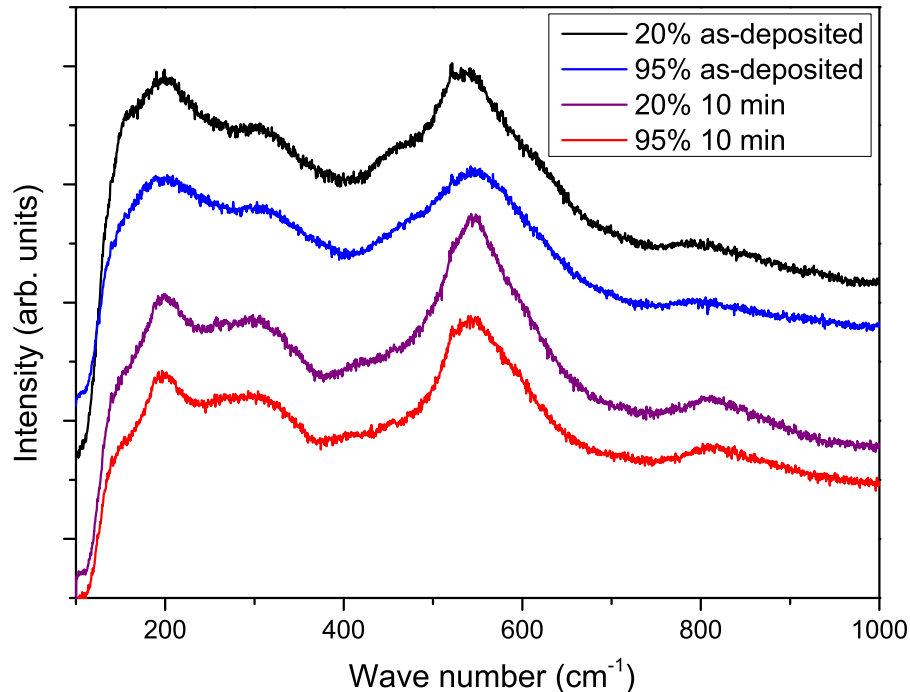


**Figure 4.12:** Raman spectra of as-deposited and annealed (700 °C, 10 minutes)  $\text{TiN}_x$  deposited at 20% and 95% nitrogen flow rate.

both titanium and nitrogen vacancies even for stoichiometric samples. Due to these vacancies, defect induced first-order Raman scattering is possible even though  $\text{TiN}$  has a symmetric cubic lattice [122]. Raman spectra for  $\text{TiN}_x$  show two broad bands in the  $150 \text{ cm}^{-1}$  -  $300 \text{ cm}^{-1}$  region and one around  $550 \text{ cm}^{-1}$ . The bands below  $300 \text{ cm}^{-1}$  (titanium mode) arise due to acoustic transitions (LA and TA) and the band around  $550 \text{ cm}^{-1}$  (nitrogen mode) is due to optic modes (LO and TO) [122, 123]. Raman scattering in the acoustic range is characterised by vibrations of the relatively heavy titanium ions, and the scattering at the optic range is due to lighter nitrogen ions. The presence of titanium modes also indicates nitrogen vacancies and the existence of nitrogen modes indicates titanium vacancies [124]. The slight variations in the peak positions in Fig. 4.12 correspond with small variations in vacancy concentrations [125]. The intensity ratio of the titanium to nitrogen mode is a semi-quantitative method to analyse the deviations in vacancy concentrations. The titanium/nitrogen peak intensity

ratio is near unity for the as-deposited samples deposited at various nitrogen levels. However, after annealing the titanium/nitrogen peak intensity decreases considerably for all the samples. An increase in the nitrogen mode intensity would indicate the creation of titanium vacancies. It is possible that the titanium slightly oxidises due to the presence of residual oxygen in the chamber, creating titanium vacancies in the  $\text{TiN}_x$  lattice. Nevertheless, the influence on resistivity from oxidation is minimal and, as such, the resistivity in the annealed films does not increase. The increase in oxygen concentration after annealing is confirmed through XPS and is discussed in detail in the next section.

#### 4.5.4 Variations in stoichiometry

The variations in stoichiometry were analyzed using XPS spectra. A top layer of  $\text{TiN}_x$  was etched away in the XPS chamber in order to remove contamination at the surface. High resolution XPS spectra of Ti  $2p$  as-deposited and annealed samples are shown in Fig. 4.13. The Ti  $2p_{3/2}$  for TiN occurs at around 455.0 eV for all nitrogen to argon flow ratios. This is consistent with literature values for stoichiometric TiN [126]. The binding energy (B.E) for Ti  $2p_{3/2}$  remains the same after annealing. The variations in binding energy between different nitrogen to argon flow rates and between as-deposited and annealed samples are less than 0.02 eV. This indicates that there is minimal variation in stoichiometry for  $\text{TiN}_x$  between these samples. The high shoulder regions in Fig. 4.13 for the Ti  $2p_{1/2}$  and the Ti  $2p_{3/2}$  peaks correspond with the nitrogen/titanium atom ratio and are found to be the highest for stoichiometric TiN [126]. However, the oxide phases and oxy-nitride phases of titanium also occur at the same binding energy. These results suggest that the presence of small amounts of oxide cannot be confirmed through XPS spectra of titanium species.

Similar to the titanium spectra, N  $1s$  spectra (Fig. 4.14) also do not vary between the samples under investigation, again confirming the consistency in stoichiometry before and after annealing for samples deposited at different gas flow rates. The N  $1s$  spectra of  $\text{TiN}_x$  is observed at 397.3 eV, consistent with previous studies for stoichiometric

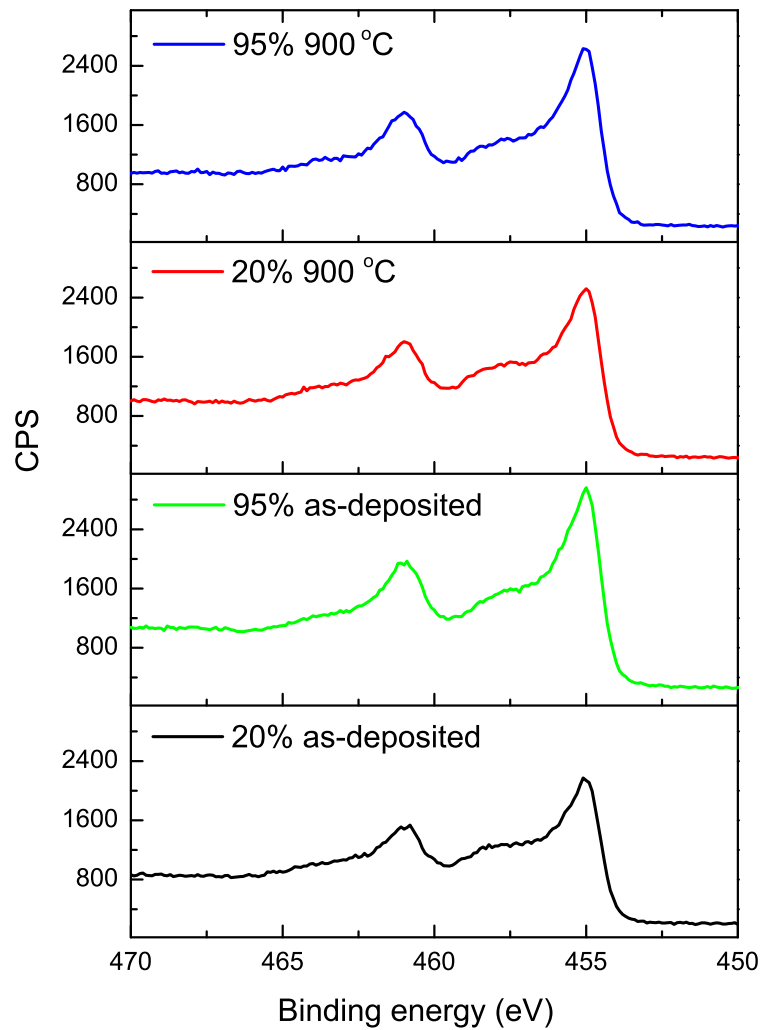


**Figure 4.13:** High resolution XPS spectra of Ti  $2p$  of as-deposited and annealed (900 °C, 20 min) samples deposited at 20% and 95% nitrogen content.

TiN [127]. The low intensity, high binding energy peak can be attributed to the oxy-nitride phases. O  $1s$  spectra (Fig. 4.15) is contributed by oxygen atoms from the oxides.

The variations in concentration of nitrogen, oxygen and titanium based on the XPS analysis are given in Fig. 4.16. The 20% as-deposited sample is nitrogen deficient and the 60% and the 95% as-deposited samples are nitrogen rich. The 20% sample contains greater concentrations of oxygen impurities compared to the nitrogen rich films, which have 13% oxygen impurity concentrations. After post deposition annealing, oxygen levels increase slightly for all samples. Oxygen may have been introduced from the remaining oxygen in the vacuum chamber, which was maintained at a pressure of  $1 \times 10^{-6}$  Torr. This oxygen would react with titanium in  $\text{TiN}_x$  to make oxides. This

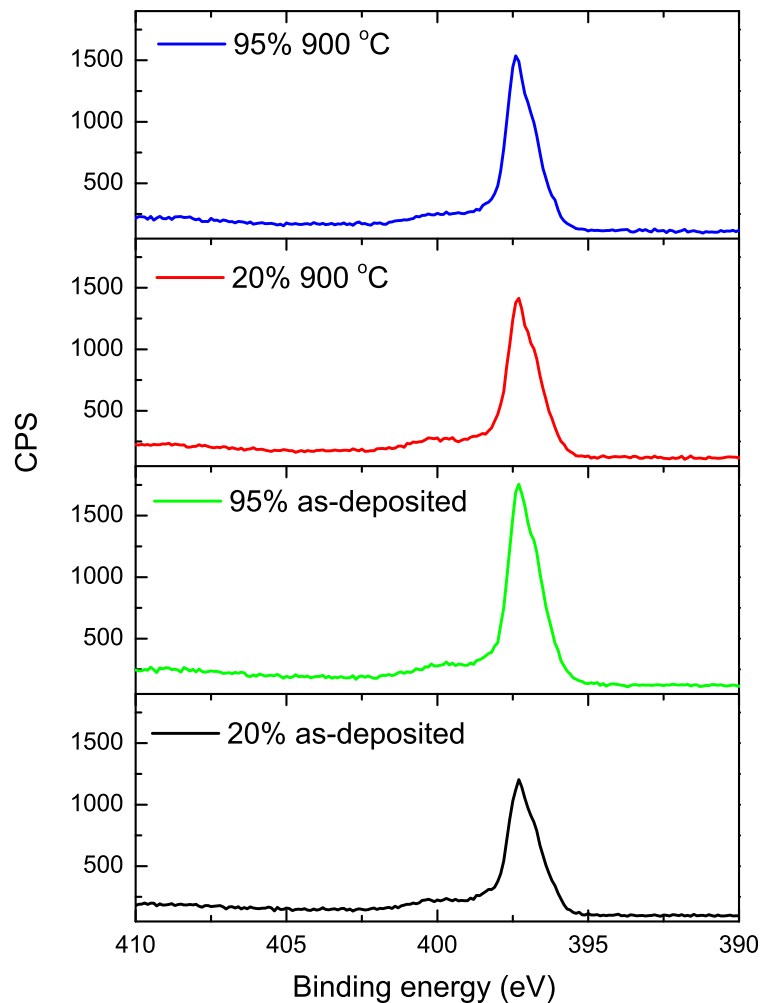


**Figure 4.14:** High resolution XPS spectra of N  $1s$  of as-deposited and annealed (900 °C, 20 minutes) samples deposited at 20% and 95% nitrogen content.

oxide formation creates titanium vacancies in the lattice, causing an increase in nitrogen mode peak intensity in the Raman spectra as discussed earlier. There is no variation in the titanium concentration after annealing, as expected. The nitrogen content also remains the same for the 20% sample after annealing. The nitrogen content for the nitrogen rich samples (60% and 95%) reduces after the annealing process. This could be due to the release of nitrogen which was precipitated at the grain boundaries [128] while annealing. However, these samples remain slightly nitrogen rich even after annealing at 900 °C for 20 minutes.

The XPS depth profile of the 95% sample annealed at 700 °C for 10 minutes is shown in Fig. 4.17. On the surface, the elemental contributions are different compared to the bulk. The sample surface has a high concentration of carbon and oxygen. This

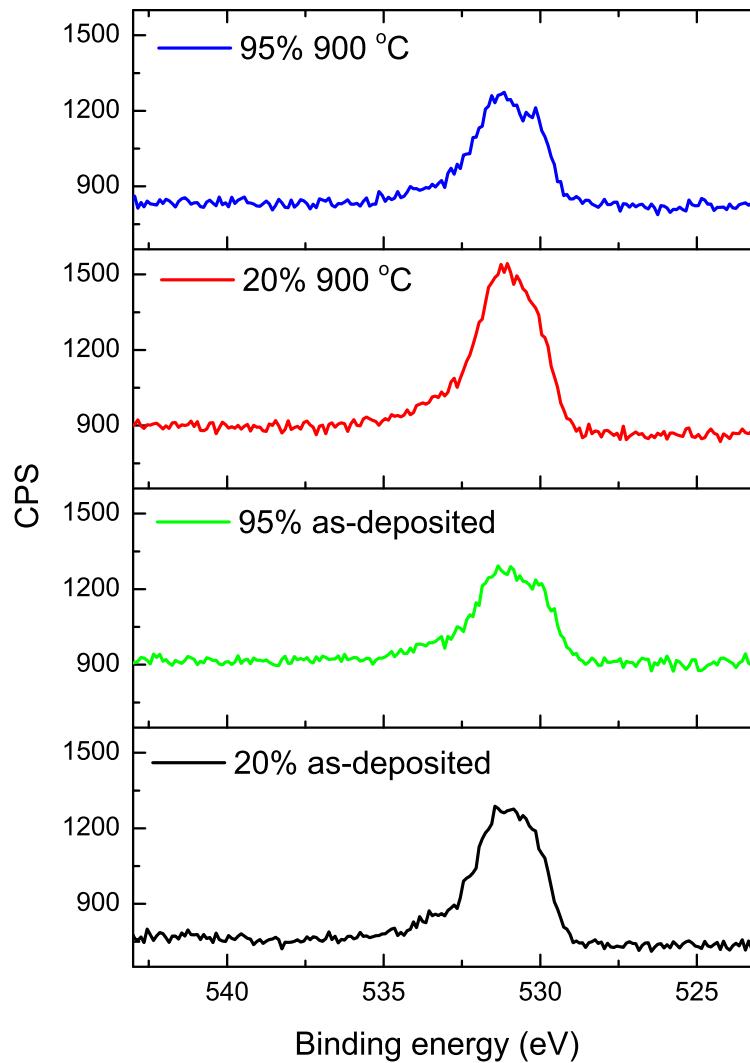


**Figure 4.15:** High resolution XPS spectra of O  $1s$  of as-deposited and annealed (900 °C, 20 min) samples deposited at 20% and 95% nitrogen content.

is due to contributions from hydrocarbons and/or surface hydration. After an initial etching cycle, these contaminants reduce. Moreover, carbon was not observed in the bulk of the film. The concentration of nitrogen is higher than that of titanium throughout the film, similar to the high resolution spectra results discussed in the last paragraph. It is also apparent that there is no diffusion of silicon from the bottom  $\text{SiO}_2$  showing good barrier properties. Diffusion of silicon dioxide into  $\text{TiN}_x$  during annealing at temperatures above 500 °C is a known issue [129]. However, here we have shown that the  $\text{TiN}_x$  deposited at high nitrogen content prevents the diffusion of  $\text{SiO}_2$ . Oxygen concentration is almost 15% throughout the film, which might have been introduced by the contamination in the nitrogen source during deposition [130].

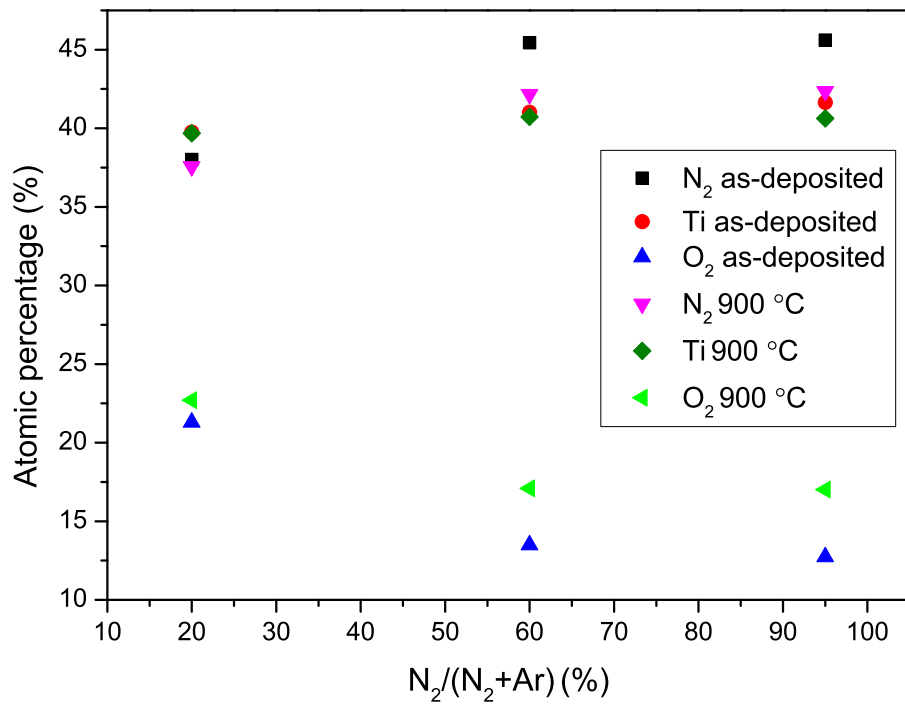


**Figure 4.16:** Variations in nitrogen, oxygen and titanium concentration before and after anneal for  $TiN_x$  deposited at various gas flow rates.

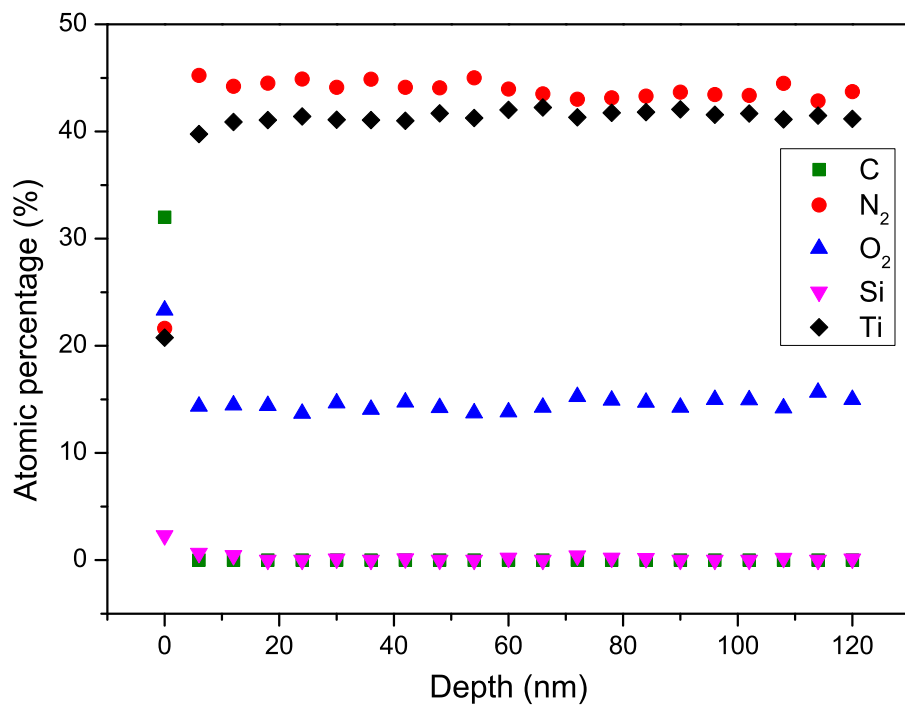


**Figure 4.17:** XPS depth profile of  $TiN_x$  deposited at 95% nitrogen and annealed at 700 °C for 10 minutes. Results demonstrate the stability of  $TiN_x$  films at high temperature processing against silicon or oxygen diffusion from the  $SiO_2$  layer underneath.

### 4.5.5 Variations in surface morphology

The variations in the surface roughness as a function of nitrogen to argon flow for the as-deposited sample and one annealed at 900 °C for 20 minutes is presented in Fig. 4.18. The root mean square (RMS) roughness decreases with increasing nitrogen

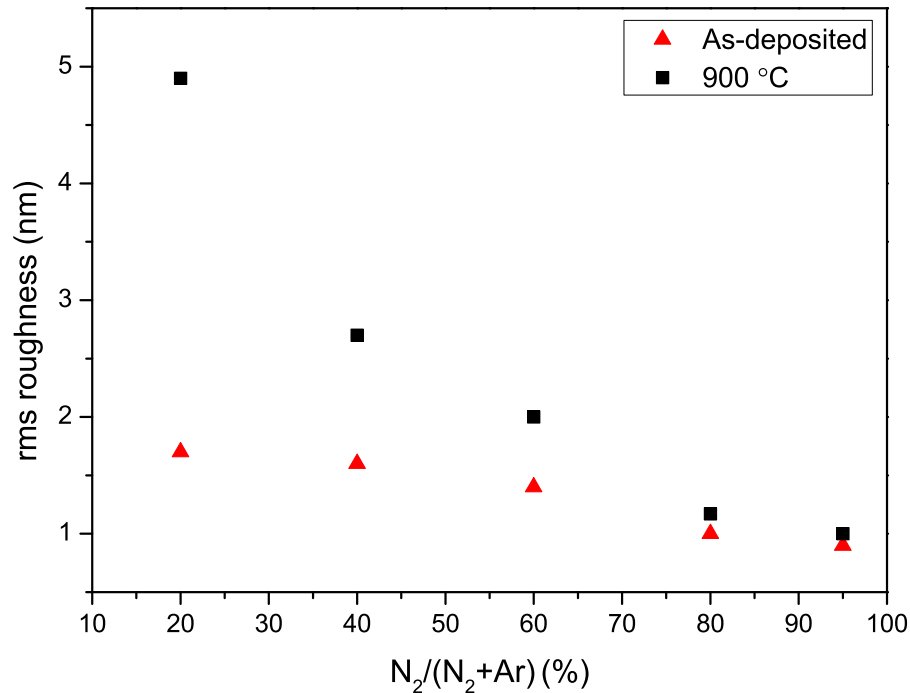


**Figure 4.18:** Surface roughness of as-deposited and annealed (900 °C, 20 minutes) against various gas flow rates. Surface roughness increases for nitrogen content samples compared to high nitrogen content samples, indicating good stability against annealing.

flow rate. After the anneal, the variation in surface roughness is more than double for lower nitrogen flow rate samples compared to the ones deposited at higher nitrogen flow. Surface roughness of  $TiN_x$  deposited at high nitrogen flow rate does not vary greatly after an anneal, showing good stability. Fig. 4.19 shows the AFM topography scan of as-deposited samples deposited at 20% and 95% nitrogen flow rates. The surface roughness on the 20% sample in Fig. 4.19 (a) is found to be much larger than the 95% sample shown in Fig. 4.19 (b). Fig. 4.20 shows the AFM scan of a  $1 \mu m \times 1 \mu m$  area carried out on  $TiN_x$  deposited at 95% nitrogen flow rate and annealed at 900 °C for 20 minutes. The surface is found to be stable and free of any protrusions, pinholes or de-lamination effects. A stable and smooth  $TiN_x$  film after a post deposition anneal is

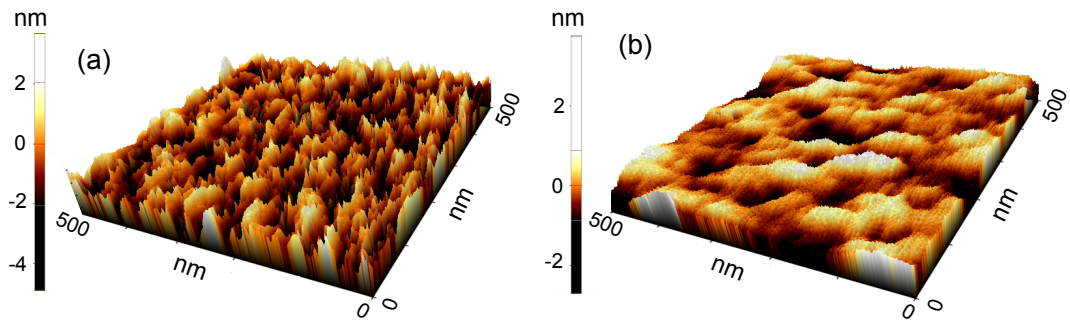


**Figure 4.19:** AFM topography scan of as-deposited film deposited with (a) 20% and (b) 95% nitrogen flow. The surface irregularities on the 20% sample are much larger than the one deposited at 95% nitrogen flow.

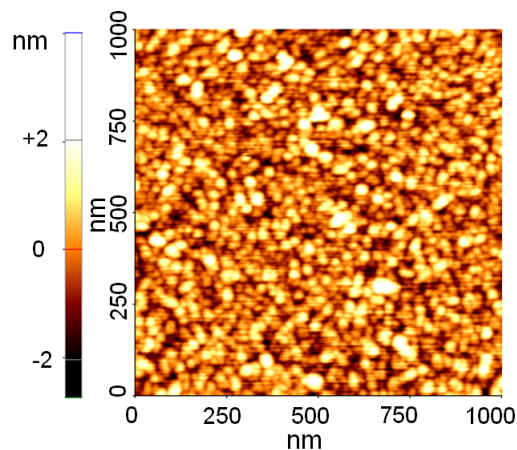


**Figure 4.20:** AFM surface scan of  $\text{TiN}_x$  deposited with 95% nitrogen flow rate and annealed at 900 °C. The surface is found to be smooth and free of any protrusions or de-lamination, showing good stability against high temperature processing.

highly desired especially for this research as it has been used as the bottom electrode for sputter deposited  $\text{BaTiO}_3$ , which is discussed in the next chapter.

#### 4.5.6 Discussion

The resistivity of any thin film is determined mainly by phase, composition, defects (impurities) and micro structure, provided the measurement temperature remains the same. The XRD peak positions and the XPS binding energy of titanium and nitrogen spectra indicate that the films deposited at various nitrogen flow rates consist of  $\text{TiN}$  phases and are all nearly stoichiometric. Based on the XPS data shown in Fig. 4.16, the ratio of titanium concentration to that of nitrogen for 20% samples is 0.96 which increases to 1.04 for 95% samples, after deducting the nitrogen which was believed to be precipitated at grain boundaries for high nitrogen content samples.

The variations in stoichiometry are very small, given the large variation in nitrogen partial pressure, which was obtained by varying the flow rate from 20% to 95%.  $\text{TiN}_x$  films deposited above 7% nitrogen flow rate were found to contain stoichiometric TiN phases [131]. However, we have shown that the variation in nitrogen flow rate and hence the nitrogen partial pressure in the chamber during deposition has a huge impact on the crystalline orientation of the film. Samples deposited at 20% nitrogen flow rate were predominantly [111] oriented compared to the 95% sample which showed a predominant [200] orientation (Fig. 4.9). This variation in the orientation is the primary cause for the observed decrease in resistivity with increase in nitrogen flow rate, indicating that  $\text{TiN}_x$  with [200] orientation is more conductive than [111]. The decrease in resistivity of the as-deposited  $\text{TiN}_x$  films with decrease in  $I[111]/I[200]$  intensity was also observed in previous studies [132, 133].

One of the main causes of resistivity variations in thin films is the scattering of conductive electrons via lattice defects. Raman spectra of as-deposited samples (Fig. 4.12) showed that the defect densities do not change with variations in nitrogen flow rates. However, there is a gradual decrease in surface roughness with increase in nitrogen flow rate as shown in Fig. 4.18.  $\text{TiN}_x$  with [111] orientation has been found to have a different surface structure compared with the [200] oriented films leading to variations in the surface roughness [133]. We have seen that the [200] phase increases with an increase in nitrogen flow rate during deposition. Therefore, the increase in [200] phase decreases the surface roughness and increasing nitrogen content contributes towards the increase in conductivity. AFM topography scans shown in Fig. 4.19 confirm the variation in the surface structure with differences in crystallographic orientation. The sample which showed predominant [200] orientation (95% nitrogen flow) is found to have a much smoother surface than the one with [111] orientation (20% nitrogen flow). A smoother surface helps in the reduction of electron scattering and improves the conductivity. The resistivity of  $\text{TiN}_x$  can be influenced by stoichiometry and the orientation of the film. Since the variation in stoichiometry is negligible, the reason for the decrease in resistivity with nitrogen flow rate for the as-deposited samples is the

variation in the crystallographic orientation.

XPS results have confirmed that  $\text{TiN}_x$  deposited at various nitrogen flow rates are all stoichiometric TiN, although there are differences in the nitrogen concentration of the film. However, the observed decrease in resistivity after annealing cannot be explained by the orientation of the film, as the variation in relative intensities after annealing shows a random behaviour (Fig. 4.11). This indicates the possibility of a secondary mechanism which is contributing towards the decrease in resistivity for all samples after annealing. A post-deposition anneal typically results in re-crystallisation and crystal growth of the as-deposited amorphous material. All the samples have shown an increase in crystallisation after annealing, as evident from the XRD spectra (Fig. 4.9). An increase in grain size would reduce the number of scattered conducting electrons at grain boundaries, in turn reducing the resistivity. An increase in the anneal temperature or duration will increase grain size, leading to a reduction in electron scattering, which can explain the annealing temperature and time dependence on resistivity as shown in this study.

The reported values for nitrogen content used for  $\text{TiN}_x$  deposition are varied in the literature, with the majority using a nitrogen content lower than 50% [103]. Higher nitrogen content having resulted in nitrogen precipitation in grain boundaries [128] and superstructure formation [134]. However, here we have shown that a nitrogen content higher than 50% is in fact beneficial to achieve low resistivity, making the films more suitable for microelectronic applications. Stoichiometrically, films deposited at various nitrogen contents are all TiN. However, these films show variations in electrical, material and morphological properties based on the nitrogen flow rate used during deposition.  $\text{TiN}_x$  deposited at high nitrogen content showed least variation in resistivity after annealing, offering better electrical stability compared to  $\text{TiN}_x$  deposited at low nitrogen content. The nitrogen rich films also prevented the diffusion of silicon during annealing, showing good thermal stability. Moreover, the films deposited at higher nitrogen content showed the lowest variation in surface roughness upon annealing, demonstrating better mechanical stability. We have also shown that the slight oxidation

of the film during annealing did not affect the resistivity adversely. The reduction in resistivity due to grain growth during annealing superseded the effects due to oxidation or the increase in surface roughness of the film.

## 4.6 TiN<sub>x</sub> Dry Etching

Since the high energy involved in the sputtering process damages photoresist, a lift-off process is not feasible for TiN<sub>x</sub> patterning, as discussed in the introduction section of this chapter. A reactive ion etching recipe using SF<sub>6</sub> as the reacting gas and argon as the carrier gas was developed in order to pattern the TiN<sub>x</sub> films deposited on BaTiO<sub>3</sub>. The SF<sub>6</sub> : Ar flow rate used was 6 : 1 and the power used was 100 W. The etch depth against etching time for the reactive ion etching process of a 70 nm thick TiN<sub>x</sub> film deposited on 45 nm BaTiO<sub>3</sub> is shown in Fig. 4.21. The etch rate is found to be approximately 60 nm/minute. Once the 70 nm TiN<sub>x</sub> film is etched, there is no more increase in the step height as evident from Fig. 4.21. This would indicate that the etching rate of BaTiO<sub>3</sub> is negligible for the process conditions. A summary of the optimised etching recipe is given in Table. 4.2. An optical microscopy image of patterned TiN<sub>x</sub> film on BaTiO<sub>3</sub> is shown in Fig. 4.22. The etching process did not damage either the BaTiO<sub>3</sub> or the remaining TiN<sub>x</sub>.

**Table 4.2:** TiN<sub>x</sub> dry etching recipe

Pressure	75 mTorr
SF <sub>6</sub>	30 sccm
Ar	5 sccm
Power	100 W
Etching rate	60 nm/minute

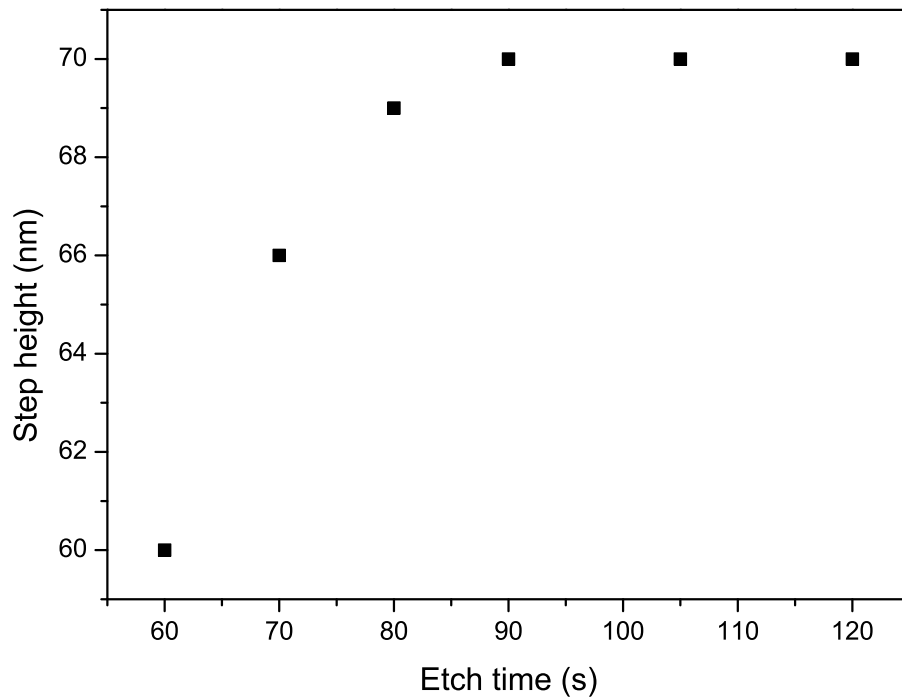


**Figure 4.21:** Etching of 70 nm  $\text{TiN}_x$  deposited on  $\text{BaTiO}_3$ . There is no more increase in the step height once the  $\text{TiN}_x$  is completely etched, showing good selectivity of the etchant against  $\text{BaTiO}_3$ .

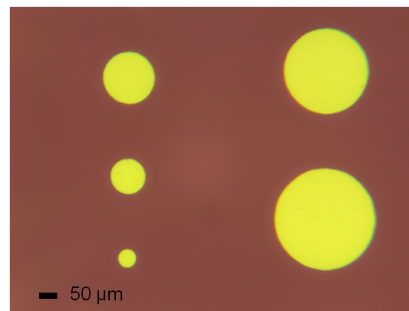


**Figure 4.22:** Optical microscopy image of  $\text{TiN}_x$  top electrodes for  $\text{BaTiO}_3$  based MIM capacitors patterned by reactive ion etching using  $\text{SF}_6/\text{Ar}$ .

## 4.7 Summary and Conclusions

In this chapter,  $\text{TiN}_x$  films which can be used as electrodes and can withstand high temperature processing were demonstrated. A newly purchased titanium target has been found to have a thin non-conducting layer on its surface. This layer was carefully removed by gradually increasing the applied power during deposition in order to avoid excessive heating of the target. It was also shown that depositing pure titanium can improve the vacuum in the chamber by an order of magnitude. Process parameters such as substrate temperature, applied power *etc.* were optimised in order to develop

the  $\text{TiN}_x$  recipe. The gas flow rates during deposition were varied in order to develop films with varying resistivity. The deposited  $\text{TiN}_x$  films were also found to be oxidation resistant up to 500 °C showing the good quality of the films.

The effect of post deposition annealing in an oxygen free environment on the material and electrical properties of reactive sputtered  $\text{TiN}_x$  was also investigated. As-deposited  $\text{TiN}_x$  resistivity showed a gradual decrease with increase in nitrogen flow rate during deposition. A lowest resistivity of 80  $\mu\Omega\text{cm}$  was obtained for nitrogen rich films. The variations in orientation and therefore the surface roughness is found to be the reason for this decrease in resistivity.  $\text{TiN}_x$  films sputtered at various nitrogen contents showed good stability and improved stoichiometry after a post deposition RTP in vacuum, without showing any silicon diffusion. Resistivity of these films decreased from the as-deposited levels upon annealing, and went down with annealing time and temperature. The re-crystallisation and grain growth led to a further reduction in resistivity. XPS results showed that films deposited at various nitrogen flow rates are all TiN phases. However, films deposited with lower nitrogen content (20%) are titanium rich compared to films deposited with higher nitrogen content which are nitrogen rich. The nitrogen rich films showed least variation in resistivity and morphology. It was also observed that small traces of oxygen do not impact the resistivity of the film. Resistivity of  $\text{TiN}_x$  is found to reduce after annealing in an oxygen free environment showing a good thermal and electrical stability. This study concludes that, though variation in the nitrogen flow rate and thereby the nitrogen partial pressure during deposition does not have a large influence on the stoichiometry of the film, the nitrogen partial pressure can influence the orientation and the morphology. Films deposited at higher nitrogen partial pressures are electrically, thermally and morphologically more stable than the ones deposited at low nitrogen content, and hence they are more suitable for microelectronic applications.

A dry etching recipe using  $\text{SF}_6/\text{Ar}$  with an estimated etching rate of 60 nm/minute was also developed in order to pattern the  $\text{TiN}_x$ . The reactive ion etching process based on the aforementioned gases showed good selectivity between  $\text{TiN}_x$  and the underlying

---

BaTiO<sub>3</sub> layer. Due to its low electrical resistivity and high thermal stability, TiN<sub>x</sub> deposited at 95% are used as electrodes for BaTiO<sub>3</sub> thin films which is discussed in the next chapter.

# Thin Film Deposition and Post Deposition Anneal of BaTiO<sub>3</sub>

## 5.1 Introduction

After developing a stable TiN<sub>x</sub> electrode which can withstand high temperature processing, focus will now shift towards optimisation of deposition and post deposition annealing parameters of BaTiO<sub>3</sub> thin films. BaTiO<sub>3</sub> thin films showing excellent electrical and material properties can be deposited in a variety of ways [30, 31, 135, 136]. However, most of them are achieved by depositing films at a substrate temperature above 500 °C which is generally not compatible with silicon technology due to undesirable inter-diffusion and chemical reaction issues. Many of them are also fabricated utilising lattice matched substrates such as MgO [137] or SrTiO<sub>3</sub> [31, 135] among many others [137] and were deposited on conductive oxides such as SrRuO<sub>3</sub>, La<sub>x</sub>Sr<sub>1-x</sub>MnO<sub>3</sub> or RuO<sub>2</sub> [30, 31, 137] as electrodes. The lattice matched substrates cannot replace mature silicon technology. Moreover, controlling the composition of conductive oxides during deposition is rather difficult and they are expensive. Certainly, buffer layers such as TiN [30, 136], LaNiO<sub>3</sub> [138], MgO [139] and CeO<sub>2</sub> [140] can be used to grow high quality epitaxial oxide films on silicon. These films can also be used as electrodes if they are conductive or can serve as a template for growing conductive electrodes. Among them TiN is an inexpensive and highly promising candidate due to its diffusion resistance, corrosion resistance, barrier properties and adhesion properties

between oxides and silicon. We have also demonstrated the stability of  $\text{TiN}_x$  towards a high temperature anneal, in the previous chapter.

$\text{BaTiO}_3$  and  $\text{BaTiO}_3/\text{SrTiO}_3$  superlattices grown on TiN which was deposited on a silicon substrate show an epitaxial growth mechanism and exhibit excellent electrical as well as materials properties [136, 141, 142]. Moreover, an abrupt interface was also observed between the insulator layer and the electrode layer [136, 142]. However, those films were also deposited at substrate temperatures above  $500\text{ }^\circ\text{C}$ , making the process incompatible for silicon process integration as discussed previously. A post deposition anneal will be necessary to crystallise these films if the films are deposited as amorphous. It is apparent that there is a gap in the literature between demonstrating these excellent properties using expensive or incompatible processes and processes which are compatible for silicon integration. This chapter discusses methods of fabricating  $\text{BaTiO}_3$  thin films on  $\text{TiN}_x$  electrodes under the constraints set by silicon technology. It also describes how effects like fringing electric field can influence the measured leakage properties of a thin film when the device dimensions are on a micro-scale.

A major difficulty in using ferroelectric materials in integrated circuits is the difficulty associated with depositing very thin ( $<300\text{ nm}$ ) yet uniform films with required electrical as well as material properties at a temperature suitable for semiconductor manufacturing [30].  $\text{BaTiO}_3$  deposited on an unheated substrate or deposited at a substrate temperature below  $500\text{ }^\circ\text{C}$  is amorphous in nature [143, 144]. Amorphous  $\text{BaTiO}_3$  thin films are non-ferroelectric materials which possess a moderate dielectric constant (around 30) compared to its bulk value of above 1000. In order to use these materials as a high permittivity dielectric or ferroelectric film, a crystalline phase is required. The transition from an as-deposited amorphous phase to a crystalline phase is normally achieved through high temperature annealing as discussed in section 2.6 of chapter 2. A post deposition anneal is also essential for crystal growth. Hence, high temperature rapid thermal processing (RTP) with a reduced annealing time is desirable in thin film manufacturing processes to crystallise these films while minimising the

inter-diffusion of materials that occur during annealing. However, a high temperature anneal could result in the formation of excessive thermal stress which can lead to cracking, de-lamination, hillock formation or buckling of the film. Excessive tensile stress often leads to cracking [59] whereas an excessive compressive stress leads to hillock, pinhole formation or buckling of the film [59, 61].

Pinhole, hillock, cracking and de-lamination have been a long-standing problem in thin film processing [58, 59]. The presence of sizable pinholes causes many undesirable characteristics such as high leakage current, high surface roughness and low break down voltage. Although smooth films could be obtained by deposition at low substrate temperatures, a post deposition anneal results in films with either pinholes or de-lamination, which causes device breakdown. Hence the objective is to develop a means of forming  $\text{BaTiO}_3$  thin films free from cracks or pinholes. The peeling or cracking that occurs after post deposition RTP is believed to be due to different coefficients of thermal expansion exhibited by the film and the substrate [58, 145]. However, there exists a critical thickness for crack propagation or growth of pinholes in thin films. Films thinner than the critical thickness are often found to be stable after thermal stressing. Factors influencing crack or pinhole formation in thin films during high temperature processing were discussed in section 2.8 of chapter 2.

A chemical solution deposition technique and other solution based deposition techniques have traditionally been done by multiple cycles of deposition and annealing [146, 147]. In such techniques, precursors are spin coated or sprayed on the substrate, followed by one or more high temperature anneals to form a thin film. The annealing processes help the precursors to react and form the desired compound and also crystallise the film. This coating-drying cycle will then be repeated to attain a desired film thickness. Films prepared by such techniques were found to be pinhole or crack free [147, 148]. The multi-layer approach used by a solution based technique is mainly employed to reduce the stress generated while the liquid phase evaporates [60], which is the primary cause of cracking in such techniques [149]. However, in films which are deposited through sputtering and are annealed afterwards, the de-lamination

arises purely from the thermal stress generated during the RTP. Here, we have employed multiple deposition-RTP cycles to sputter deposit BaTiO<sub>3</sub> film of a desired thickness on TiN<sub>x</sub> while avoiding the de-lamination effects that can occur after an RTP. The critical thickness for the formation of pinholes for annealing temperatures ranging from 500 °C to 1000 °C was also measured for BaTiO<sub>3</sub> deposited on TiN<sub>x</sub>.

Experimental details are given in section 5.2. In section 5.3 of this chapter, material properties of as-deposited BaTiO<sub>3</sub> are analysed using XPS and AFM. Section 5.4 of this chapter looks at the effects of fringing electric field on the leakage current in a MIM capacitor. Effects of a post deposition anneal on the quality of the film is discussed in section 5.5. A post deposition anneal results in the formation of pinholes or cracks in the film as expected. A multi-layer deposition approach was found to help in avoiding the formation of pinholes. Surface morphology as well as nano-scale leakage current through thin films of the same thickness deposited as a single layer and multiple layers is discussed in section 5.6. Section 5.7 contains a summary and conclusion of the results discussed in this chapter.

## 5.2 Experimental Setup

BaTiO<sub>3</sub> thin films were deposited on TiN<sub>x</sub>/SiO<sub>2</sub>/Si stacks from a BaTiO<sub>3</sub> target using an Oxford plasma 400<sup>TM</sup>RF magnetron sputtering system. A detailed description of the fabrication process modules as well as metrology techniques used for this research was given in chapter 3. 100 nm thick TiN<sub>x</sub> was reactively sputtered on 80 nm thick SiO<sub>2</sub>, which was grown on a <100> oriented silicon substrate. TiN<sub>x</sub> was sputtered using a nitrogen to argon (N<sub>2</sub>/(N<sub>2</sub>+Ar)) flow rate of 95% and at a substrate temperature of 250 °C. Optimisation of the TiN<sub>x</sub> recipe was discussed in the previous chapter. Experiments were also carried out by replacing TiN<sub>x</sub> with thin films of metallic electrodes such as platinum or nickel. Platinum or nickel having a thickness of 100 nm was evaporated using an electron beam evaporator. A 10 nm thick titanium layer was used as an adhesion layer prior to the platinum deposition whereas a chromium layer of the same thickness served as the adhesion layer for the nickel film. BaTiO<sub>3</sub>

films of different thicknesses were sputter deposited in an oxygen to argon flow rate ( $O_2/(O_2+Ar)$ ) of 40% and pressure of 5 mTorr. The presence of oxygen in the sputtering gas is found to reduce the oxygen vacancies that might have been created during the sputtering process [150]. Deposition power was kept at 150 W and the substrate temperature was 130 °C for all depositions. The deposition rate was 1.7 nm/minute. Substrate temperature during deposition was kept below 500 °C so that the process is compatible with semiconductor manufacturing processes. Samples were annealed in forming gas ( $N_2/H_2$ ). Annealing was performed in forming gas in order to avoid any oxidation of the  $TiN_x$  bottom electrode. Top electrodes were fabricated using the optimised RIE recipe which was discussed in section 4.6 of chapter 4.

The X-ray spot size used for the XPS measurements was 110  $\mu m$ . Argon ions with beam current 5 mA, an acceleration voltage of 5 kV and a square raster of 1 mm was used to clean the sample surface prior to acquiring the spectra. XPS spectra were calibrated using the C  $1s$  line of hydrocarbon on the sample surface which has a binding energy of 284.8 eV. The Ar  $2p$  line with a binding energy of 241.82 eV from implanted argon during the etching was also used to confirm the energy calibration. The RMS value of surface roughness was measured using AFM topography scans in non contact mode. A study of the origin of leakage current in single layered and multi-layered  $BaTiO_3$  after a post deposition anneal was performed using current AFM (I-AFM). The setup required for measuring current between the conductive probe and the bottom electrode was explained in section 3.2.2.1 of chapter 3. The EFM scans were carried out in non contact mode. The amplitude and phase of the cantilever oscillation was read using a Stanford Research Systems DSP lock-in amplifier, model SR830. All the measurements were taken at room temperature. For analysing the ferroelectric property, a 4  $\mu m \times 4 \mu m$  area was scanned in contact mode while applying a bias having a magnitude of 10 V to the bottom electrode. The polarity of the applied bias was reversed for each 1  $\mu m$  covered by the tip during scanning in vertical direction. This was done in order to polarise the  $BaTiO_3$  film in both directions, giving rise to stripe pattern.

## 5.3 Material Characterisation

This section mainly discusses the material properties of BaTiO<sub>3</sub> deposited through RF-sputtering. Fig. 5.1 shows an XPS survey spectrum of the BaTiO<sub>3</sub> film. Spectra were acquired after etching away the surface layer in the XPS chamber in order to remove the surface contamination. The survey spectrum shows the presence of barium, titanium and oxygen without the presence of contamination from carbon or any other sources. It also does not indicate the presence of any diffusion from the underlying substrate. The presence of argon is believed to be from the argon ion source used to etch the surface layer in the XPS chamber.

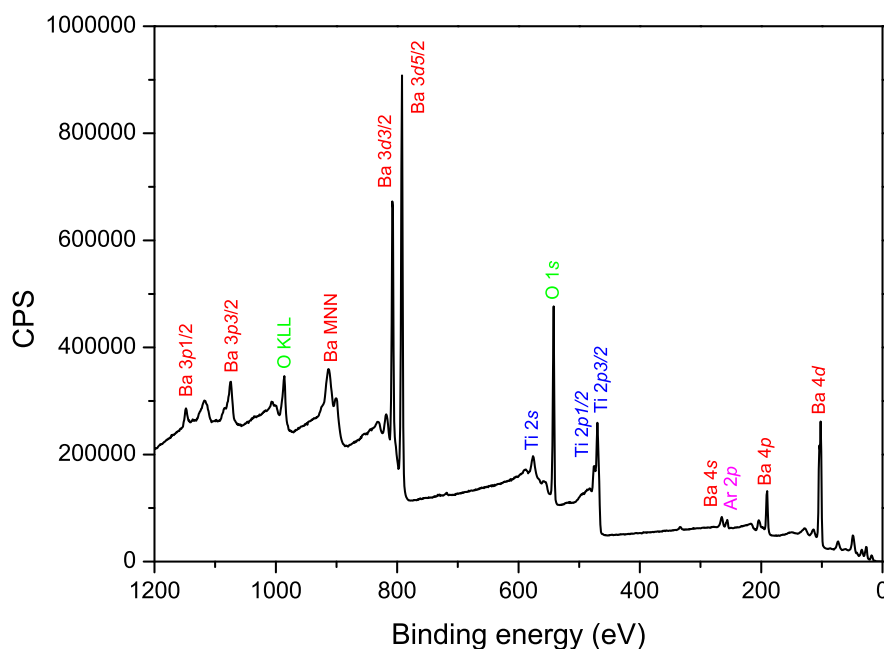


**Figure 5.1:** XPS survey scan of sputter deposited BaTiO<sub>3</sub>. Surface layer was etched in the XPS chamber in order to avoid contribution from surface contamination. Results show the presence of barium, titanium and oxygen. CPS is counts per second.

Fig. 5.2 shows the high resolution spectra of a) Ba 3*d*, (b) Ti 2*p* and (c) O 1*s*. The atomic percentage of elements calculated from the spectra are barium = 19%, titanium = 20% and oxygen = 61%. XPS peak positions were compared with literature values to investigate the stoichiometry of the film. The Ba 3*d*<sub>5/2</sub> peak centred at 779 eV shown in Fig. 5.2 (a) is in good agreement with the literature values for stoichiometric BaTiO<sub>3</sub> [151]. Similarly, the Ti 2*p*<sub>3/2</sub> peak centred at 458 eV in Fig. 5.2 is attributed

to the titanium in stoichiometric  $\text{BaTiO}_3$ .  $\text{O } 1s$  peak at 529.6 eV is contributed by the oxygen in the  $\text{BaTiO}_3$  lattice. XPS results confirm the stoichiometric nature of the sputter deposited  $\text{BaTiO}_3$ .

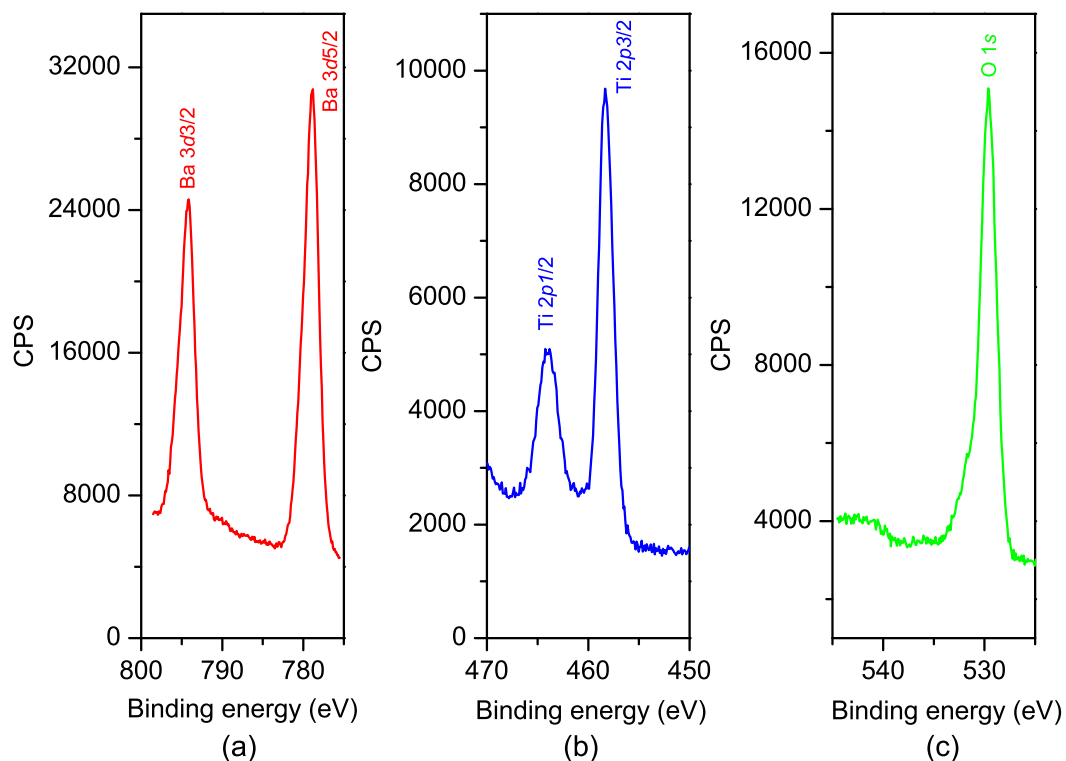


**Figure 5.2:** High resolution XPS spectra of (a) Ba  $3d$ , (b) Ti  $2p$  and (c) O  $1s$ . Binding energies of the corresponding XPS peaks indicate a stoichiometric  $\text{BaTiO}_3$  as described in the text.

Fig. 5.3 shows the AFM topography scans of  $1 \mu\text{m} \times 1 \mu\text{m}$  and  $10 \mu\text{m} \times 10 \mu\text{m}$  areas of the as-deposited  $\text{BaTiO}_3$ . The film surface is found to be smooth with an RMS roughness below 0.4 nm. A  $1 \mu\text{m} \times 1 \mu\text{m}$  scan on the surface of  $\text{BaTiO}_3$  shown in Fig. 5.3 (a) does not show any grain structure, indicating the amorphous nature of the film. Indeed, XRD spectra of the as-deposited samples did not show any peaks corresponding to  $\text{BaTiO}_3$  again confirming the amorphous nature of the film. The  $10 \mu\text{m} \times 10 \mu\text{m}$  scan shown in Fig. 5.3 (b) shows a pinhole or crack free surface. Study on the effects of a post deposition anneal on the morphology of  $\text{BaTiO}_3$  is one of the key objectives of this thesis and is discussed in detail in a later section of this chapter.

Leakage current through the ferroelectric material was also measured after depositing and fabricating  $\text{TiN}_x$  top electrodes and creating metal-insulator-metal (MIM)

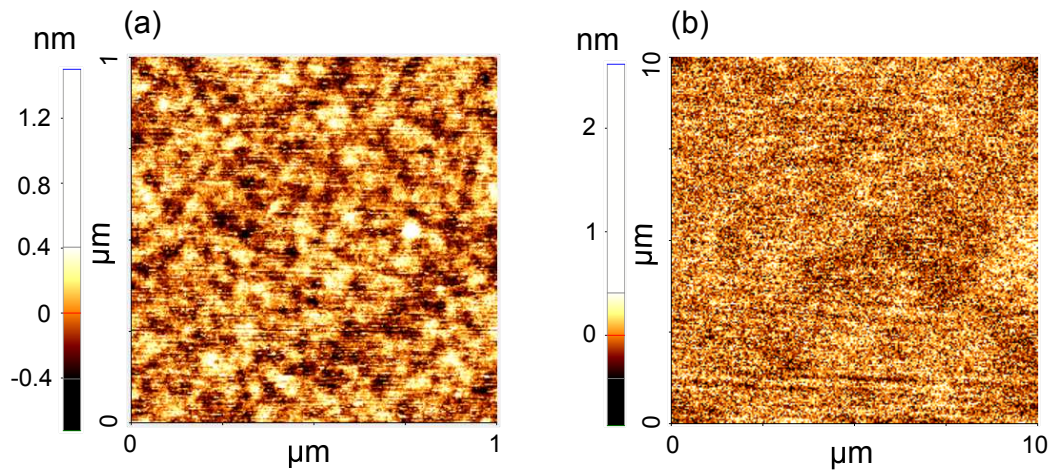


**Figure 5.3:** Showing (a)  $1\ \mu\text{m} \times 1\ \mu\text{m}$  and (b)  $10\ \mu\text{m} \times 10\ \mu\text{m}$  AFM topography scan of as-deposited  $\text{BaTiO}_3$  on  $\text{TiN}_x$ . As-deposited films are found to be smooth and without any pinholes or cracks on the surface.

structures. Amorphous films of thickness 30 nm showed a leakage current density around  $1 \times 10^{-5}\ \text{A}/\text{cm}^2$  at 500 kV/cm. However, the leakage current density (current per unit area) measured using MIM structures was found to be dependent on the electrode diameter. This is due to peripheral leakage effects, which are generally unaccounted for while representing the current density. The next section discusses the peripheral leakage effects in MIM capacitors and ways of extracting the same from leakage through the area of the electrode.

## 5.4 Peripheral Leakage Effects

Electric field lines at the edge of a parallel plate capacitor are not uniform and the field will not be contained entirely between the plates. This is called an edge or fringe effect. Fig. 5.4 is a schematic illustration of electric field lines passing through a dielectric in a MIM structure with different sized top and bottom electrodes. Electric field lines

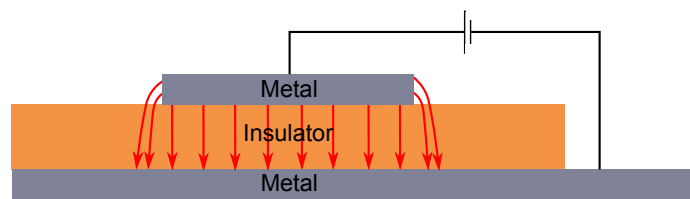


**Figure 5.4:** Schematic illustration of electric field lines passing through the insulator of a MIM capacitor.

originating from the periphery of the electrode in the figure are referred to as the fringing field. This electric field can influence the electrical properties of the MIM capacitor, especially when the area of the electrode is comparable with the fringing area. The fringing field will also contribute towards the total leakage current through the dielectric. Previous studies have found that the leakage current can be dominated by areal or peripheral current depending on the geometry of the electrode [152]. Very often leakage current density is expressed as current per unit area (in  $A/cm^2$ ) as an electrode geometry independent representation [78, 153, 154]. However, this representation completely disregards the fringing effects and counts only the leakage through the area of the electrode. Fig. 5.5 shows the leakage current per unit area for electrode diameter varying from  $50 \mu m$  to  $300 \mu m$ . Leakage current density expressed in  $A/cm^2$

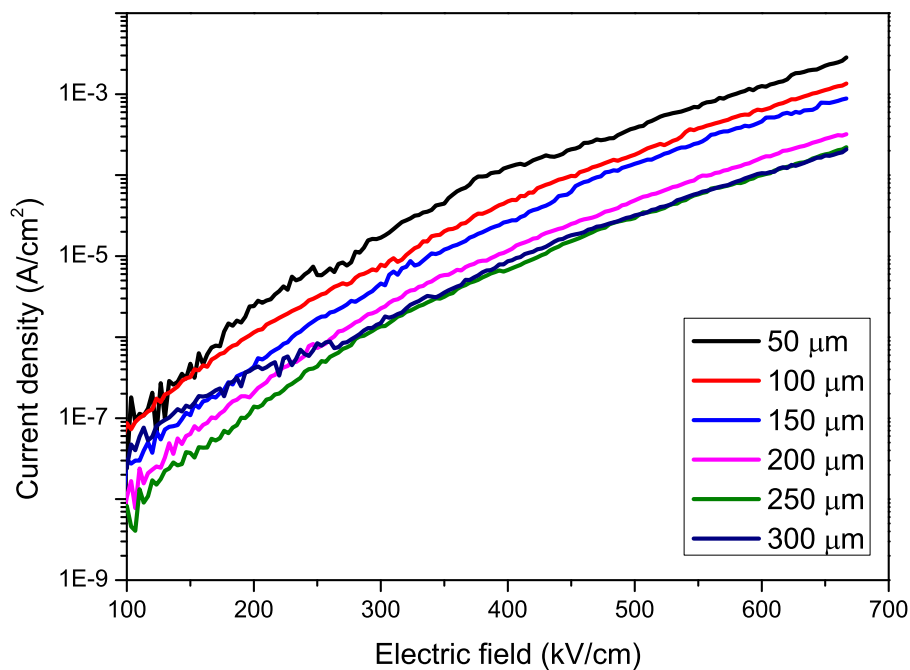


**Figure 5.5:** Leakage current per unit area for TiN/BaTiO<sub>3</sub>/TiN MIM capacitor with circular top electrodes. Leakage current density expressed in  $A/cm^2$  increases with decrease in electrode area, indicating that this form of representation still depends on the geometry of the electrodes. For electric field lower than  $100 \text{ kV/cm}$ , the leakage current is very low resulting in a very low signal to noise ratio.

increases as the diameter of the electrode decreases from  $300 \mu m$  to  $50 \mu m$ . Results imply the dependence of geometry of the electrode on the leakage current density (in  $A/cm^2$ ). As the device dimensions become smaller the ratio of perimeter to area becomes larger causing a significant contribution from the peripheral leakage towards

the total leakage. Contribution of peripheral leakage on the total leakage current is discussed in the following sections.

Leakage current in a MIM capacitor is mainly through surfaces, edges and defects. These defects include micro cracks, grain boundaries, fabrication defects or other point sources of leakage. However, leakage through grain boundaries or micro cracks will be minimal in the case of an amorphous oxide thin film and not considered as a major contribution towards the total leakage in the following approximation. A MIM capacitor will have an intrinsic part of leakage due to the electric field from the surface (area) of the electrode ( $I_a$ ) and a fringing part due to the fringing field from the periphery of the electrode ( $I_p$ ). Hence the measured leakage current ( $I_m$ ) can be written as[152, 155];

$$I_m = J_a \times Area + J_p \times Perimeter \quad (5.1)$$

where,  $J_a$  is the areal current density in A/(unit length)<sup>2</sup> and  $J_p$  is the edge current density in A/(unit length). Equation. 5.1 can be rewritten as;

$$\frac{I_m}{Area} = J_a + J_p \frac{Perimeter}{Area} \quad (5.2)$$

For a device with circular pads of diameter  $d$ , this can be rewritten as;

$$\frac{I_m}{\pi(\frac{d}{2})^2} = J_a + J_p \frac{4}{d} \quad (5.3)$$

Equation 5.3 is a linear equation of the form  $y = mx + c$  where  $m$  is the slope and  $c$  is the  $y$  intercept. Slope of  $\frac{I_m}{\pi(\frac{d}{2})^2}$  against  $\frac{4}{d}$  will give peripheral leakage density ( $J_p$ ) and the intercept will give areal leakage density ( $J_a$ ).  $J_a$  and  $J_p$  were calculated for  $d$  varying from 50  $\mu\text{m}$  to 300  $\mu\text{m}$  for a set of electric field strengths. Fig. 5.6 shows the plot of leakage current density (in A/cm<sup>2</sup>) against ratio of perimeter to area for an electric field strength of 600 kV/cm. Peripheral leakage density can be obtained from the slope of the linear fit and the intercept will give the areal density.

Plots of  $J_a$  and  $J_p$  extracted in this way, at sixteen different electric field values between 0 kV/cm to 700 kV/cm are given in Fig. 5.7. Fig. 5.7 shows that the peripheral

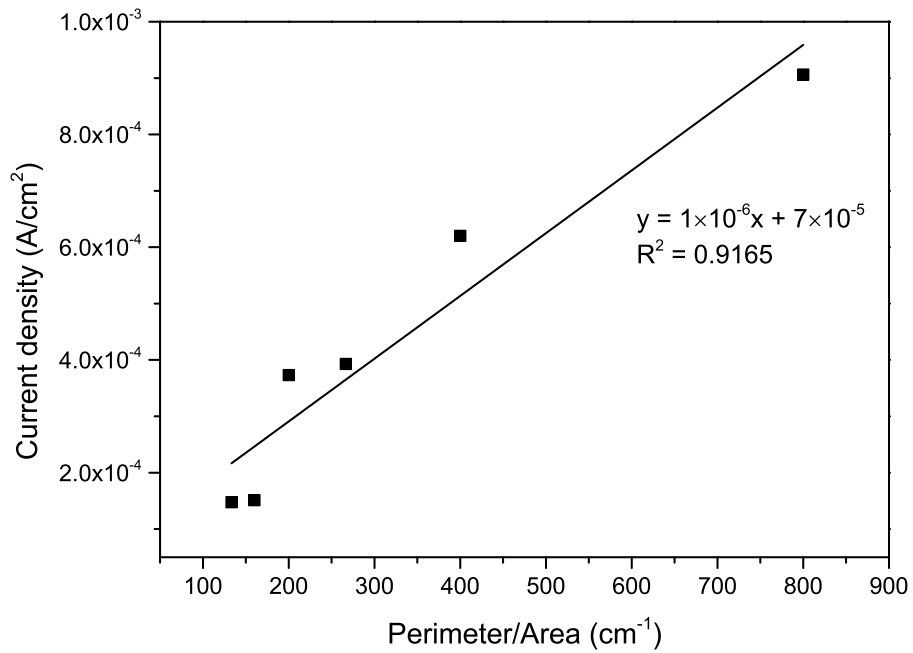


**Figure 5.6:** Plot of leakage current density (in A/cm<sup>2</sup>) against perimeter to area ratio for an electric field strength of 600 kV/cm, based on equation 5.3.

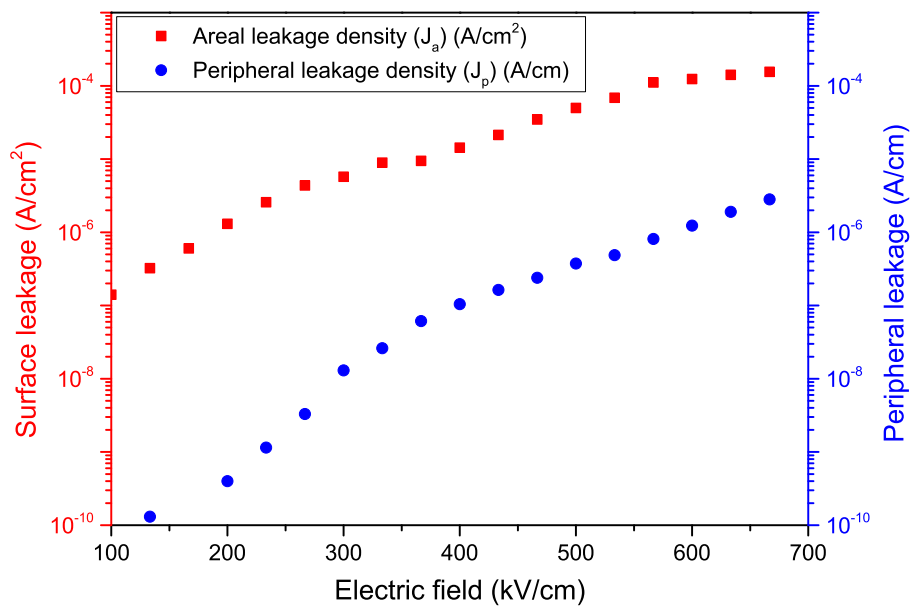


**Figure 5.7:** Areal current density and peripheral current density extracted from equation 5.3 for  $d$  ranging from 50  $\mu\text{m}$  to 300  $\mu\text{m}$  at various values of electric fields.

leakage density is nearly two orders of magnitude lower than areal leakage density. However, a direct comparison between  $J_a$  and  $J_p$  is improper as one represents current density in an area and the other one is a line current density.

The extracted current densities,  $J_a$  and  $J_p$  can be converted to corresponding current values by multiplying them with the area and perimeter of the electrode respectively for a direct comparison. Fig. 5.8 shows the peripheral leakage, areal leakage, total current and measured current for the 50  $\mu\text{m}$  electrode. Total current is the sum of the

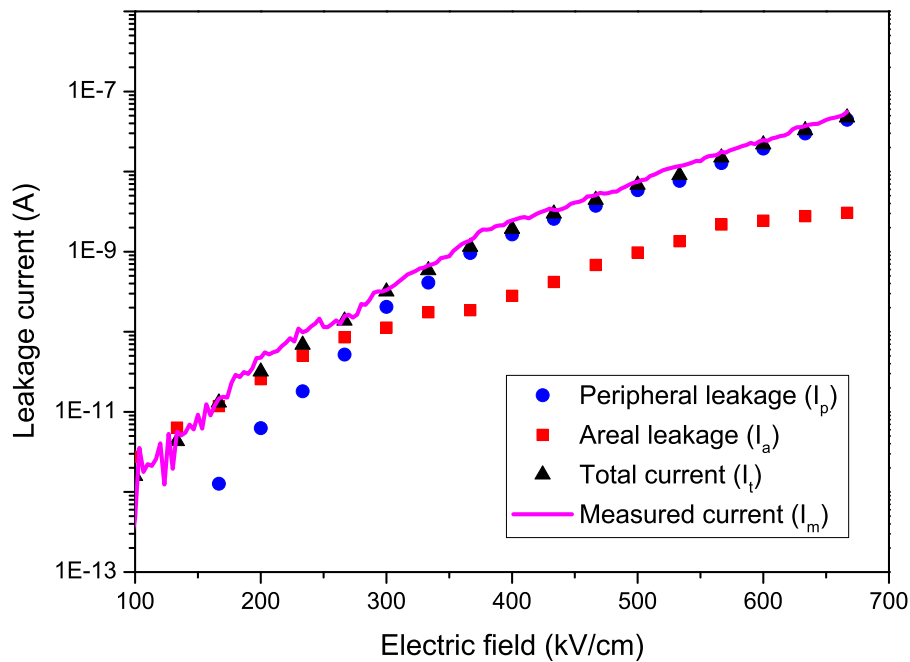


**Figure 5.8:** Showing the peripheral leakage current, areal leakage current, total current and measured current for a device with 50  $\mu\text{m}$  electrode. Results imply that the peripheral leakage is a major contribution towards the total leakage for small electrodes.

peripheral and areal leakage currents from the extracted values. Also illustrated in the figure is that the total current calculated from extracted values is in good agreement with the measured leakage current of the device. Fig. 5.8 also shows the contribution of peripheral leakage current to the total current. It can be noted that the peripheral leakage is higher than the areal leakage for a device with an electrode diameter of 50  $\mu\text{m}$ .

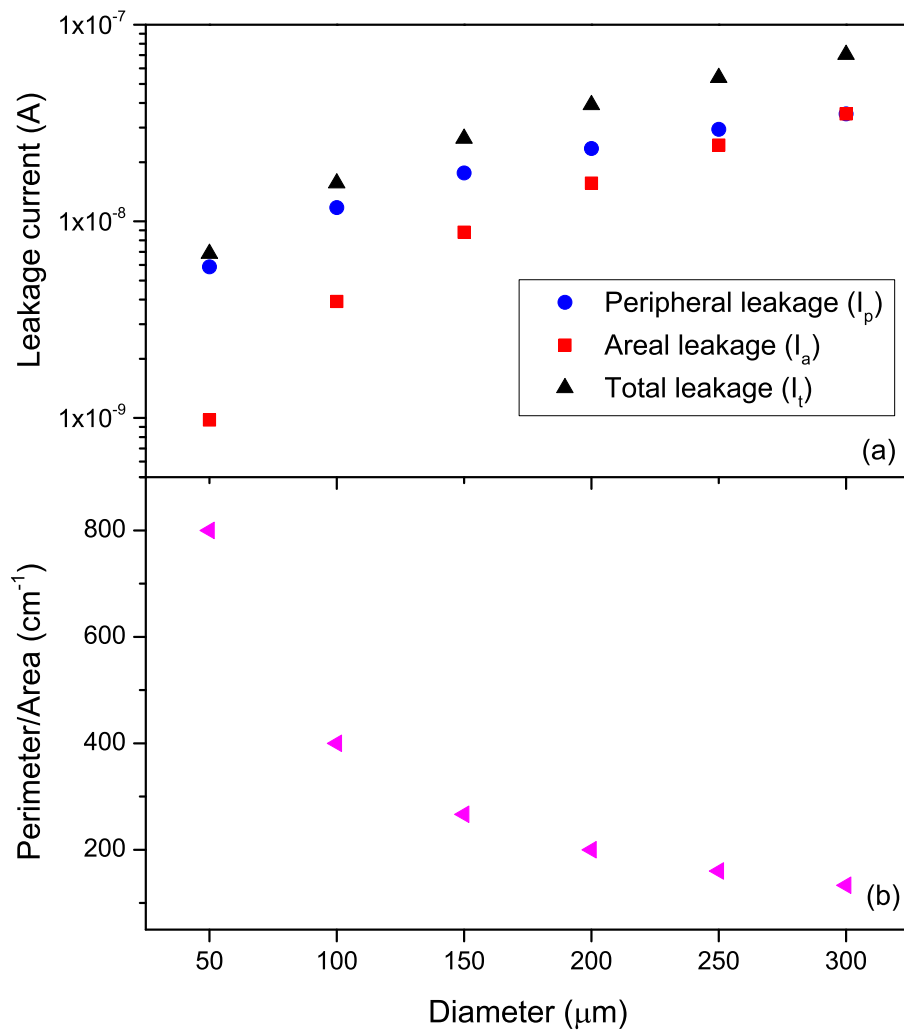
### 5.4.1 Discussion

Fig. 5.9 (a) shows the contribution of peripheral leakage current and areal leakage current towards the total current for devices with different electrode sizes for a fixed

electric field strength. In the case of a 50  $\mu\text{m}$  device, peripheral leakage is a major contribution towards the total current. With an increase in electrode size, the contribution from areal leakage increases. For a 300  $\mu\text{m}$  device, peripheral leakage and areal leakage have equal contributions towards the total leakage. Areal leakage is expected to increase further as the electrode size increases. Fig. 5.9 (b) shows the perimeter to area ratio for circular electrodes against the electrode diameter. The perimeter to area ratio decreases with the increase in the electrode diameter. The large contribution of peripheral leakage for devices with small electrodes is due to the high perimeter to area ratio for these devices. A significant contribution from the peripheral leakage is the reason for an increase in the current density (in  $\text{A}/\text{cm}^2$ ) with the decrease in electrode size which was discussed in Fig. 5.8.

The results shown above illustrate the importance of the fringing field towards the leakage current characteristics of a MIM capacitor. The electric field strength on the metal areal depends on the charge density. A charged parallel plate capacitor will have an increasing charge density as the edges of a plate are approached [156]. This high charge density increases the electric field strength at the edges of the electrode. Leakage current through an oxide depends on the electric field strength [78]. The high electric field strength at the edges results in a higher leakage current through the edges than through the rest of the electrode areal when the perimeter to areal area ratio is large. With the increase in electrode area, contribution from surface will be more significant compared to the leakage through edges.

Parasitic effects of high-k dielectrics are extensively studied for MOSFETs [157, 158] but they have been ignored in the case of MIM capacitors until recently [155]. The ever increasing demand for miniaturisation of integrated circuits has resulted in the scaling of MIM capacitors also. As the size of the electrodes become smaller, parasitic effects become more and more prominent. Here we have shown that the peripheral leakage is in fact higher than the areal leakage when the electrode diameter is smaller than 300  $\mu\text{m}$ . However, the method used to extract these values assumes that areal leakage and peripheral leakage are the main contributors towards the total leakage and



**Figure 5.9:** Showing (a) peripheral leakage current, areal leakage current and total current against electrode diameter and (b) ratio of perimeter to area against electrode diameter. Illustrates that the peripheral leakage makes a significant contribution towards the total leakage. This is down to the high perimeter to area ratio as the electrode size becomes smaller.

does not consider any defect induced leakage. Moreover, it was assumed that all the fringing field lines originate from the edges of the electrode as shown in Fig. 5.4. However, electric field lines within the periphery of the electrode will also fringe and can contribute towards the peripheral leakage current. Although the fringing effects can be calculated analytically using conformal mapping and numerical simulation techniques [159, 160], the adopted method allows an easy and quick approximation of the contribution from fringing effects on the leakage characteristics of a MIM capacitor.

## 5.5 Post Deposition Anneal of BaTiO<sub>3</sub> Thin Films

In earlier sections, it was discussed that the BaTiO<sub>3</sub> films deposited at low substrate temperatures are amorphous. It is apparent from the results that the films require a post deposition RTP in order to crystallise them. 100 nm thick BaTiO<sub>3</sub> films were deposited on silicon substrates coated with different electrode materials and were annealed. Fig. 5.10 (a) shows the optical microscopy image of as-deposited BaTiO<sub>3</sub> on platinum electrode. The film is found to be smooth when it is in an amorphous state. Fig. 5.10 (b), (c) and (d) show the optical microscopy images of BaTiO<sub>3</sub> on TiN<sub>x</sub>, nickel and platinum respectively after a post deposition anneal at 750 °C. After an anneal at

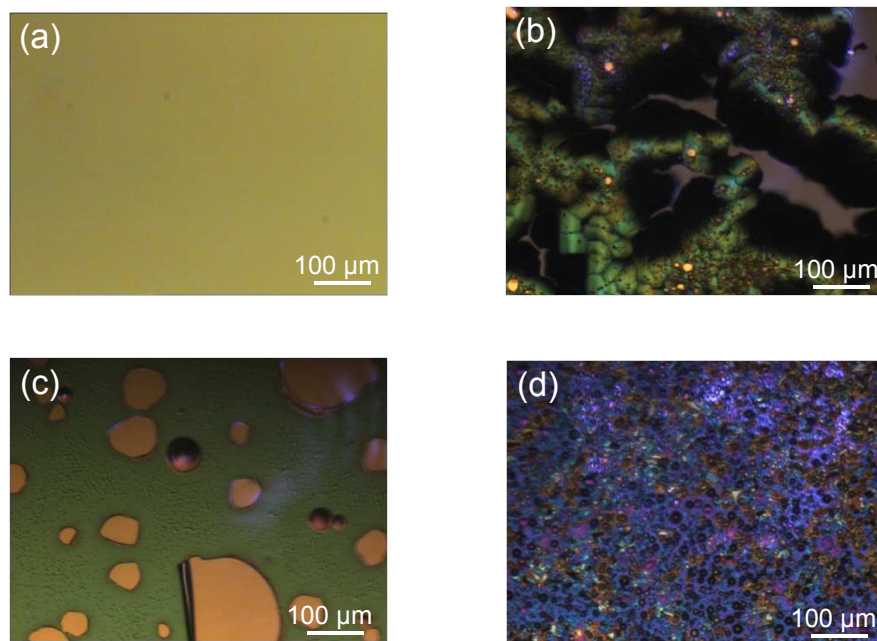


**Figure 5.10:** Optical microscopy images of 100 nm thick amorphous BaTiO<sub>3</sub> deposited on (a) platinum electrode, (b) TiN<sub>x</sub> electrode and annealed, (c) nickel electrode and annealed and (d) platinum electrode and annealed. RTP was done at 750 °C for 60 s in forming gas (N<sub>2</sub>/H<sub>2</sub>).

750 °C for 60 s in forming gas (N<sub>2</sub>/H<sub>2</sub>), films were found to either peel-off or create pinholes irrespective of the electrode material used. The peeling or pinhole effects were visible with the naked eye in most of the cases whereas the as-deposited films appeared to be very smooth. No correlation was observed between the type of instability (whether pinhole or peeling) and the type of electrode material used. However, no cracking was observed on these films. These effects have been found to be random and no conclusive

evidence was found to pinpoint the type of instability (failure modes) associated with a particular electrode material. It is believed that factors like properties of electrode material, adhesion between the electrode and insulator film, adhesion of electrode film themselves to the underlying SiO<sub>2</sub>, film thickness and annealing temperature are all contributing towards the observed random behaviour of failure modes. The instability of the film after an anneal has been represented as a variation in the surface roughness of the BaTiO<sub>3</sub> film in the following sections. Since metallic electrodes such as platinum, aluminium or nickel themselves are unstable for processing temperatures above 750 °C, TiN<sub>x</sub> electrodes were used to optimise the processing conditions in order to develop a crack free film after a post deposition anneal. TiN<sub>x</sub> also shows good adhesion properties to the underlying SiO<sub>2</sub>, avoiding chances of de-bonding from the substrate itself.

The peeling or pinhole formation is found to be due to the thermal mismatch between the substrate and the insulator film, which is discussed later. The thermal mismatch during a high temperature process generates excessive strain in the film causing it to de-laminate or create pinholes to release the strain. A commonly employed technique to avoid this issue is to reduce the temperature ramp up and ramp down rate during annealing. However, this process increases the annealing time considerably and may result in inter-diffusion of materials. It is also worth pointing out at this point that, in our experiments, BaTiO<sub>3</sub> films which underwent an anneal process at 750 °C with a ramp up rate of 75 °C/minute and a ramp down rate of 25 °C/minute had shown pinholes after an anneal as shown in Fig 5.11. It is apparent that a much lower ramp up or ramp down rate will be required to produce pinhole free BaTiO<sub>3</sub> on TiN<sub>x</sub>. However, it is anticipated that annealing parameters other than the ramp rate can be optimised to avoid the pinhole issue. In the following section, the importance of thickness of the BaTiO<sub>3</sub> film on the pinhole issue during an RTP is explored.

In order to study the effect of film thickness and RTP temperature on the pinhole formation, BaTiO<sub>3</sub> films of thicknesses ranging from 10 nm to 80 nm deposited on TiN<sub>x</sub> underwent RTP at 600 °C, 700 °C, 800 °C and 900 °C for 60 s. RMS values of surface roughness measured using AFM topography scans are given in Fig. 5.12. It can be seen

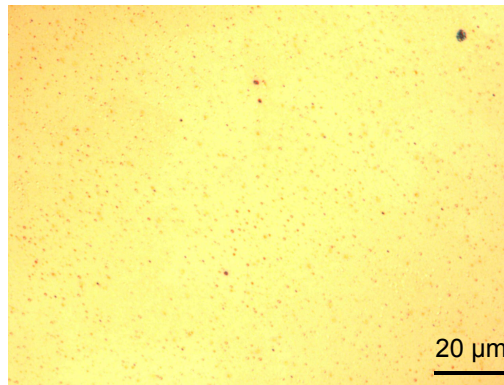


**Figure 5.11:** Showing optical microscopy image of 80 nm thick  $\text{BaTiO}_3$  deposited on  $\text{TiN}_x$  and annealed at 750 °C for 60 s, with a ramp up rate of 75 °C/minute and ramp down rate of 25 °C/minute. Numerous small dots seen on the surface are either pinholes or hillocks.

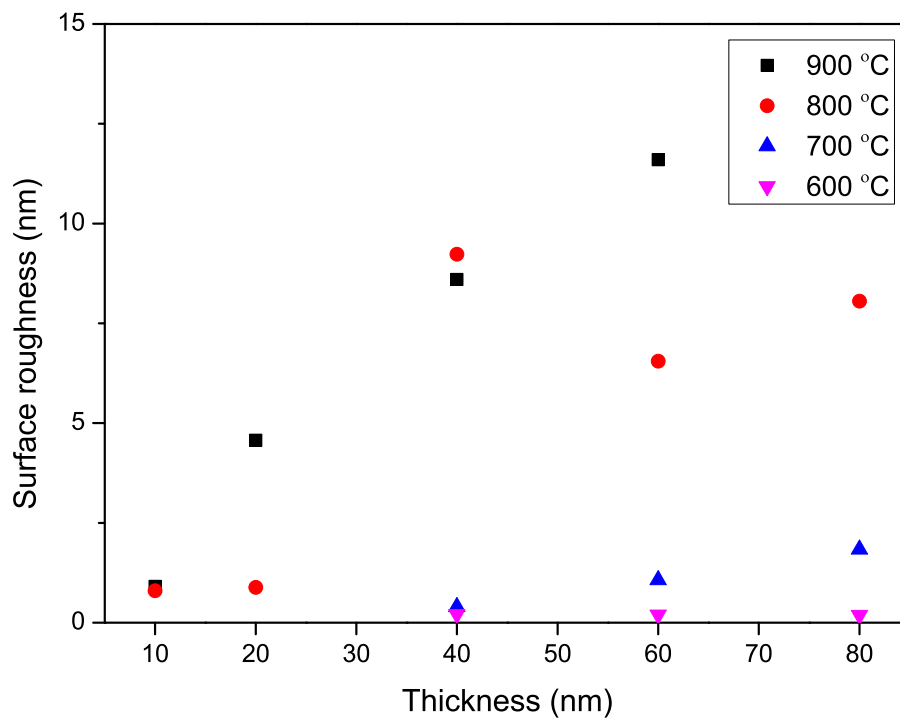


**Figure 5.12:** Surface roughness against thickness for  $\text{BaTiO}_3$  films deposited on  $\text{TiN}_x$  annealed at different temperatures and a fixed time of 60 s. A large increase in the roughness implies presence of pinholes or de-lamination. A critical roughness of 2 nm was observed for the formation of pinholes. Demonstrates that pinhole formation is dependent on both annealing temperature and film thickness.

from the figure that for a 600 °C anneal film roughness does not vary with thickness up to 80 nm. However, roughness increases with thickness when the as-deposited films were annealed at 700 °C. Furthermore, 60 nm films annealed at 700 °C showed the onset of pinhole formation. Generally, samples which showed a surface roughness above 2 nm were unstable. The critical thickness for the formation of pinholes further reduces for an 800 °C RTP.  $\text{BaTiO}_3$  films of 40 nm produce pinholes when they were annealed at 800 °C. However, 20 nm thick films had a smooth surface after an RTP at 800 °C. This trend continues for the 900 °C RTP, which showed an onset of pinhole formation for films thicker than 10 nm. The results illustrate the dependence of surface roughness or pinhole formation on the RTP temperature and film thickness.

Fig. 5.13 shows AFM topography scans of 30 nm and 50 nm thick  $\text{BaTiO}_3$  on  $\text{TiN}_x$  annealed at 750 °C in forming gas. 30 nm thick  $\text{BaTiO}_3$  (Fig. 5.13 (a)) was found to be

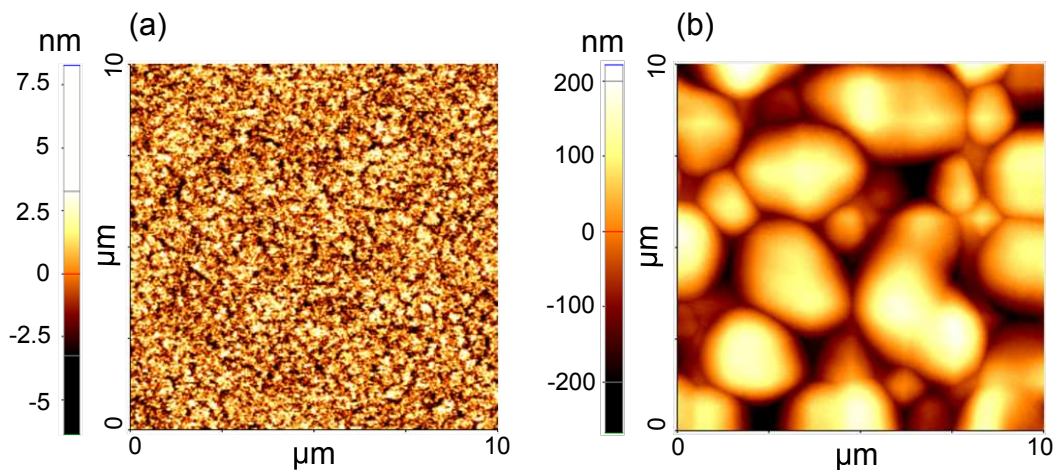


**Figure 5.13:** AFM topography scan of (a) 30 nm and (b) 50 nm thick  $\text{BaTiO}_3$  deposited on  $\text{TiN}_x$  and annealed at 750 °C in forming gas. Figures show the dependence of film stability on thickness, after annealing.

stable and smooth with an RMS surface roughness of 1.8 nm. However, the surface of the 50 nm thick film was found to be very rough as shown in Fig. 5.13 (b). The RMS surface roughness of the 50 nm film was found to be 87 nm. The film was completely de-laminated and it had agglomerated forming large heaps. The agglomeration was found to be the reason for this large increase in surface roughness after annealing. These results confirm the effect of film thickness on the pinhole formation. Film morphology completely changes upon annealing when the film thickness was increased from 30 nm

to 50 nm. These results again lead to the conclusion that there exists a critical thickness corresponding to each anneal temperature below which films are stable and pinhole free. Here the critical thickness is considered as the thickness at which films show characteristics of the onset of pinhole formation.

The above study was further extended in order to find the critical thickness for the onset of pinhole formation at various temperatures. Films with thicknesses ranging from 10 nm to 200 nm were annealed at temperatures ranging from 500 °C to 1000 °C. Hillock formation on the surface of the films for a particular RTP temperature have been identified as the onset of pinhole formation. The corresponding thickness of the film was selected as the critical thickness. As-deposited films above the critical thickness were de-laminated or found to produce pinholes after RTP. Films thinner than the critical thickness had a smooth surface after RTP. Fig. 5.14 shows the critical thickness for the formation of pinholes. The shaded region in the figure indicates the processing

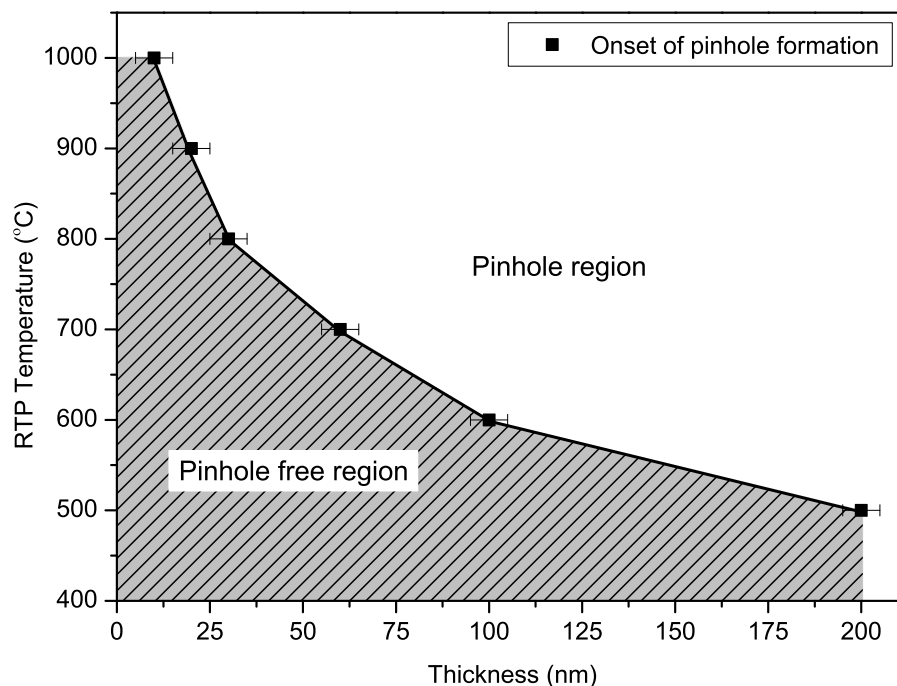


**Figure 5.14:** Effect of thickness and RTP temperature on the pinhole formation in  $\text{BaTiO}_3$  deposited on  $\text{TiN}_x$ . Maximum thickness of  $\text{BaTiO}_3$ , in order to obtain a pinhole free film after a post deposition anneal decreases with increase in RTP temperature. Data points indicate the onset of pinhole formation. Shaded region provides the parameter space for producing pinhole free films.

parameters for creating stable and pinhole free  $\text{BaTiO}_3$  on  $\text{TiN}_x$ . All samples which fall under the 'pinhole region' in Fig. 5.14 had either pinholes or were de-laminated.

Results show that the critical thickness reduces with an increase in RTP temperature. The critical thickness was around 40 nm for an 800 °C anneal and was found to be less than 25 nm for a 900 °C anneal whereas films annealed at 500 °C showed a critical thickness as high as 200 nm. It is anticipated that the critical thickness would also depend on the annealing time but this is not the focus of the present study.

It was demonstrated that the critical thickness for the formation of pinholes after an RTP reduces with increase in RTP temperature. However, ferroelectric materials such as BaTiO<sub>3</sub> have a crystallisation temperature above 750 °C. Hence, these materials will have to undergo a post deposition anneal at high temperatures in order to crystallise them if they are deposited as amorphous. The results discussed above imply that the maximum possible thickness to produce a stable and pinhole free BaTiO<sub>3</sub> on TiN<sub>x</sub> after an RTP at 800 °C is 20 nm or below. The thickness will be even lower for a further increase in the RTP temperature. This imposes a limit on the maximum possible thickness to produce a pinhole free thin film which can withstand a high temperature anneal. It is apparent from the results that a method has to be developed in order to create stable and pinhole free films having a thickness higher than the critical thickness, which can undergo RTP at 800 °C or above and crystallise them.

## 5.6 Multi-layered BaTiO<sub>3</sub>

It was shown in the last section that there is a critical thickness for the formation of pinholes after RTP. In order to deposit and anneal films thicker than the critical thickness a method was developed as follows. Initially, substrates coated with TiN<sub>x</sub> were annealed at 800 °C in forming gas for 60 s. BaTiO<sub>x</sub> films of thickness 20 nm were then deposited and underwent RTP at 800 °C in forming gas for 60 s. The resulting films were stable as their thicknesses were less than the critical thickness (Fig. 5.14) for the specified annealing conditions. Deposition of this 20 nm BaTiO<sub>3</sub> layer was repeated and annealed at the same conditions. The process of depositing and annealing films thinner than the critical thickness was followed in order to obtain films of desired thickness. Fig. 5.15 shows the process flow for developing a ‘multi-layered’ structure which was discussed

above. Sputter chamber vacuum has been broken between each deposition and RTP

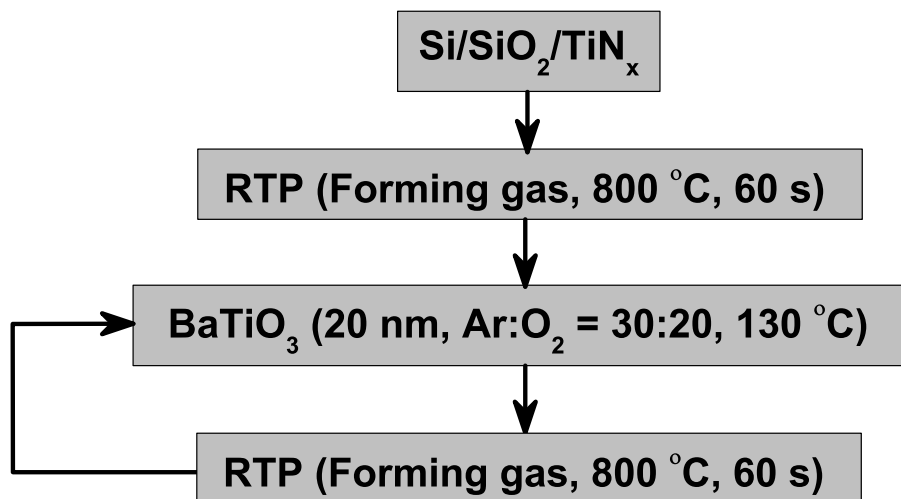


**Figure 5.15:** Process flow for the deposition and RTP of multi-layered BaTiO<sub>3</sub> on TiN<sub>x</sub>.

processes and the samples were exposed to atmosphere. An exposure to atmosphere can result in formation of carbonate phases on the surface of BaTiO<sub>3</sub> causing contamination. However, a high temperature anneal above 500 °C results in de-carbonation [161]. Moreover, the anneal process is found to inhibit further carbonation of BaTiO<sub>3</sub>. Hence, the RTP process is expected to decontaminate the BaTiO<sub>3</sub> surface.

Multi-layered films of thickness 40 nm, 60 nm and 80 nm were produced by multiple depositions and anneals of 20 nm thick films. Single layered BaTiO<sub>3</sub> of the same thicknesses were also deposited and annealed for comparison. Fig. 5.16 shows an optical microscopy image of 80 nm thick single layered and multi-layered films which were annealed at 800 °C for 60 s. The multi-layered film shown in Fig. 5.16 (a) appears

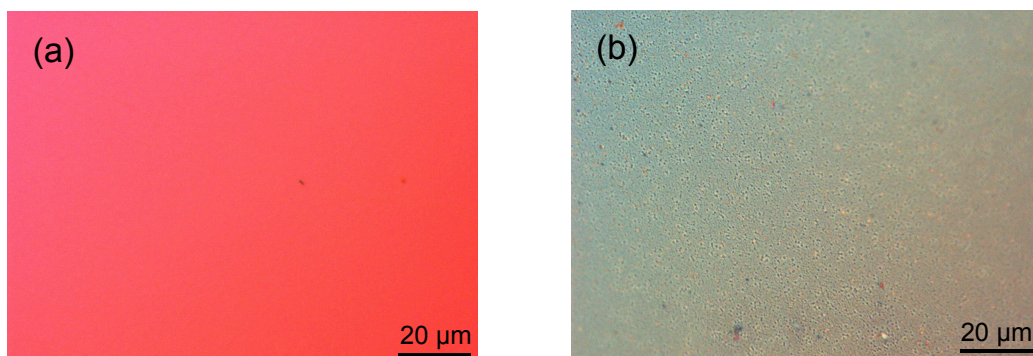


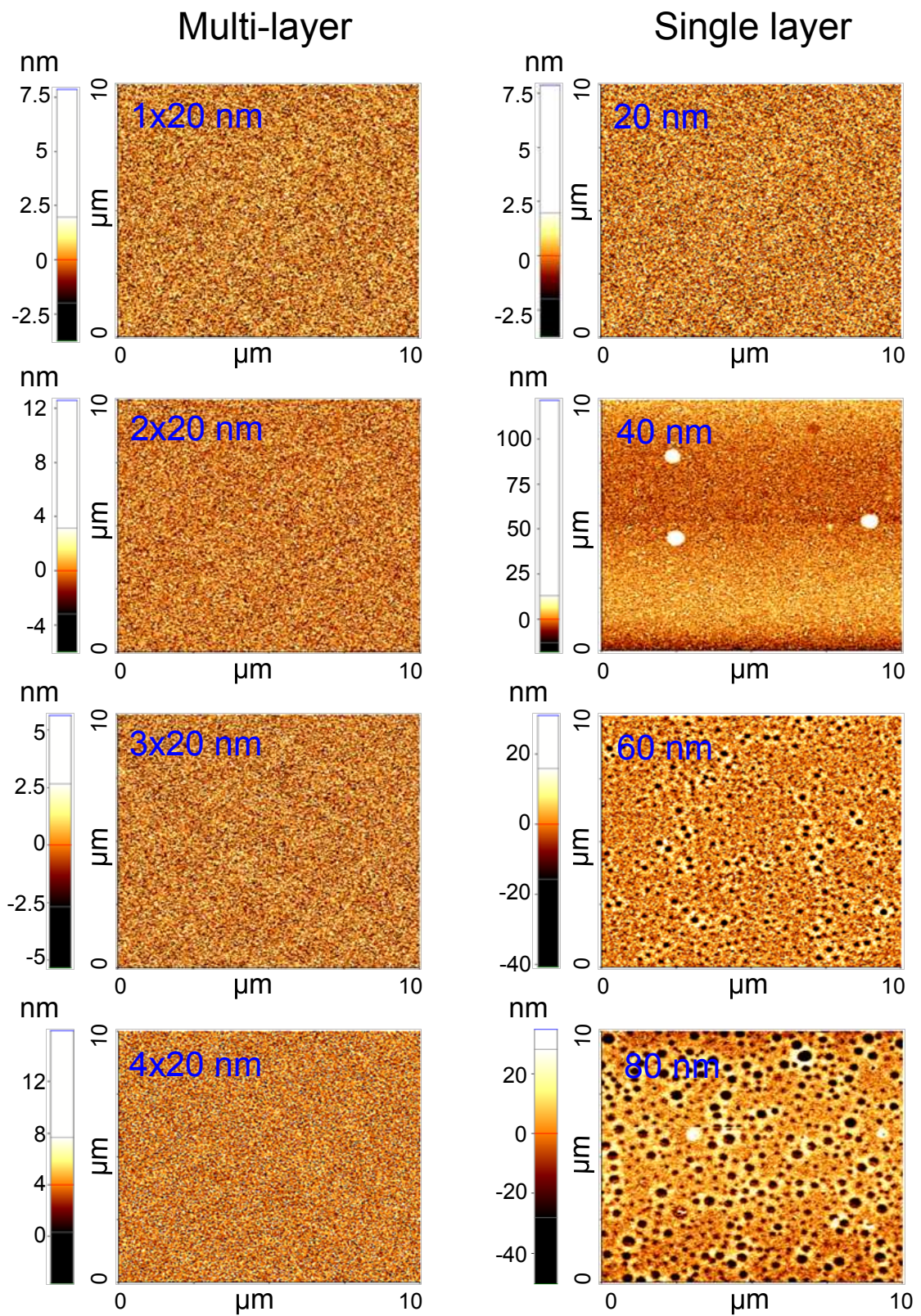
**Figure 5.16:** Optical microscopy images of (a) multi-layered and (b) single layered BaTiO<sub>3</sub> having a thickness of 80 nm. Films were deposited on TiN<sub>x</sub> and the RTP was at 800 °C in forming gas for 60 s. Multi-layered films are pinhole free compared to single layered films which shows pinholes.

to have a smooth surface compared to the single layered film of the same thickness shown in Fig. 5.16 (b). Pinholes or cracks were not observed on the multi-layered film unlike the single layered film which showed pinholes and an uneven surface even through an optical microscope.

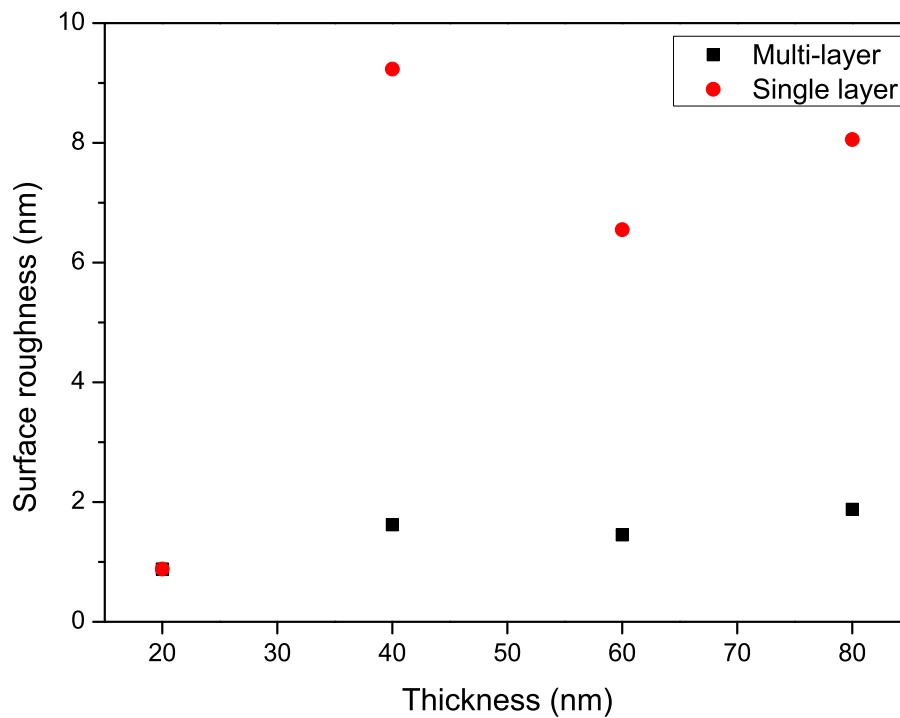
AFM topography scans were carried out to compare the morphology of multi-layered and single layered films of various thicknesses which are annealed at 800 °C. Fig. 5.17 shows the AFM images taken over a 10 μm × 10 μm area of multi-layered (left column) and single layered (right column) BaTiO<sub>3</sub> of 20 nm, 40 nm, 60 nm and 80 nm thickness. Multi-layered films of all thicknesses and single layered film of 20 nm were found to be smooth and pinhole free. Multi-layered films contained multiple layers of 20 nm thick BaTiO<sub>3</sub> as discussed previously. Irregularities were minimal on the multi-layered samples. However, single layered film of thickness 40 nm showed mounts as tall as 100 nm. Single layered films of 60 nm and 80 nm contained plenty of pinholes and films were highly unstable.

Fig. 5.18 shows the RMS surface roughness of multi-layered and single layered films of various thicknesses calculated from AFM topography scans. The surface roughness of the single layered films was found to increase with the thickness as shown in the figure. However, the surface roughness of the multi-layered films do not vary greatly with increase in thickness. The roughness of the 20 nm film was around 1 nm while the thickness of the 80 nm multi-layered films was only around 2 nm. However, the roughness of the single layered sample having a thickness of 80 nm was close to 8 nm. The large increase in the roughness for the single layered films of thicknesses 40 nm, 60 nm and 80 nm is due to mount or pinhole formation observed in these films.

The results presented above confirm that the multi-layered films produce a stable and crack free film after a post deposition anneal above the crystallisation temperature. Thicker films created by deposition and annealing of films with thickness less than the critical thickness is found to produce pinhole free films compared to the single layered films of same thickness. The next section discusses the nano-scale leakage current analysis of multi-layered and single layered films using I-AFM.



**Figure 5.17:** AFM topography of multi-layered (left column) and single layered (right column) BaTiO<sub>3</sub> on TiN<sub>x</sub> after post deposition RTP.



**Figure 5.18:** Showing the RMS surface roughness measured using AFM topography scans on multi-layered and single layered films with thicknesses varying from 20 nm to 80 nm. Demonstrates that the surface roughness of the multi-layered films do not increase with thickness compared to single layered films after the post deposition RTP at 800 °C.

### 5.6.1 Leakage current study

I-AFM (Current AFM) enables an easier and non-destructive way of measuring leakage current through a small surface area. The operation principle and setup required for measuring leakage current using I-AFM was described in section 3.2.2.1 of chapter 3. This section discusses the source of leakage current in multi-layered and single layered films measured using I-AFM. In I-AFM, the measured current is the current flowing between the AFM tip and the bottom electrode (TiN<sub>x</sub>) through thin film BaTiO<sub>3</sub>. The cantilever and the tip are conductive and are in contact with the BaTiO<sub>3</sub> surface throughout the scan.

Fig. 5.19 shows the topography and leakage current through a single layered BaTiO<sub>3</sub> of 80 nm, which was annealed at 800°C for 60 s. The topography scan shown in Fig. 5.19 (a) for a 1 μm × 1 μm area shows circular pinholes as wide as 200 nm, consistent with previous observations. The leakage current measured simultaneously on the same area given in Fig. 5.19 (b) shows regions of very high leakage. It can also

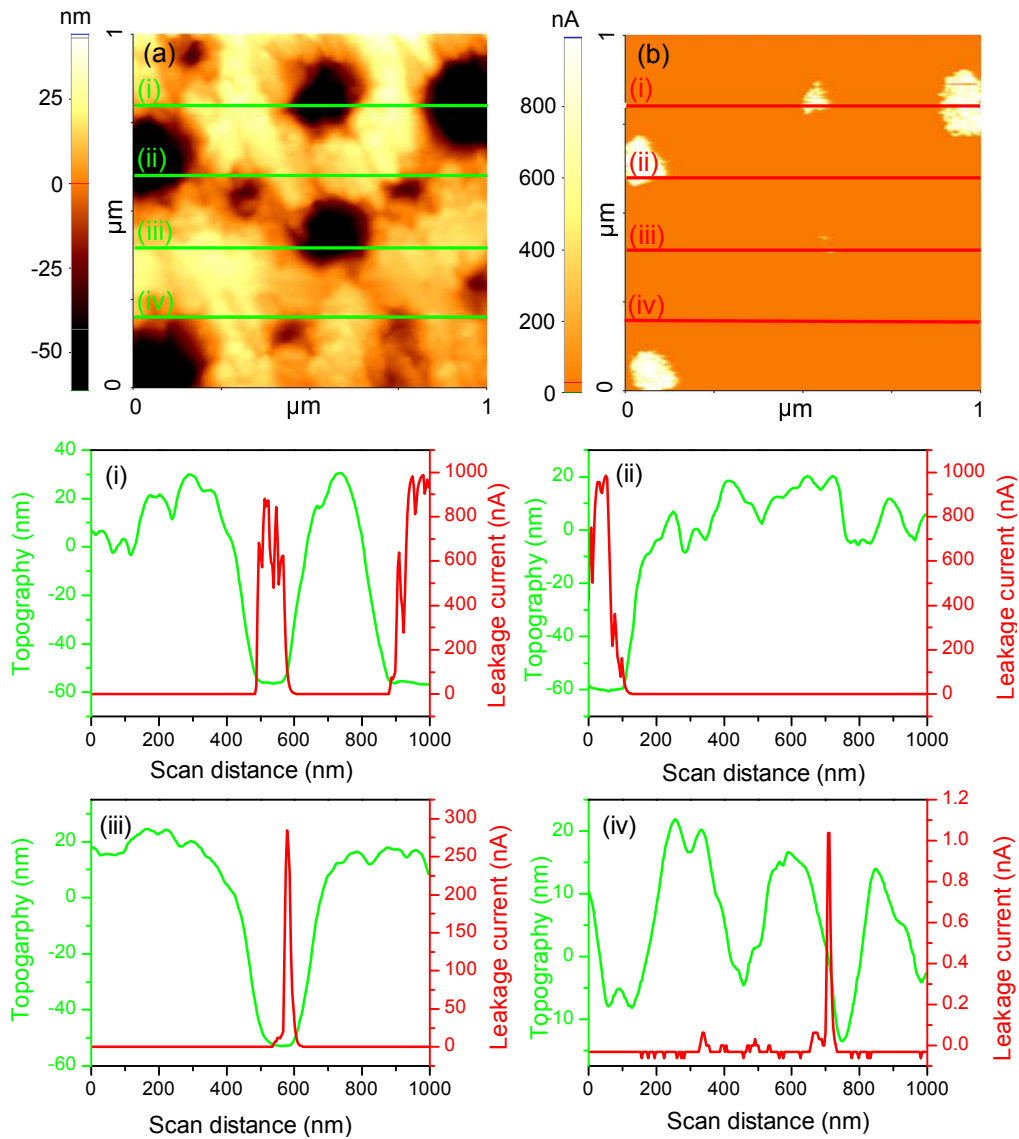


**Figure 5.19:** Shows (a) AFM topography scan and (b) I-AFM scan of 80 nm thick single layered BaTiO<sub>3</sub> on TiN<sub>x</sub> annealed at 800 °C for 60 s. Areas which showed very high leakage in (b) corresponds to pinholes in (a). (i), (ii), (iii) and (iv) show the topography variation and leakage current across a horizontal line in the AFM image. The results illustrate that the pinholes are major source of leakage in single layered films of 80 nm thickness.

be observed that these regions in the leakage current map correspond to pinholes in the topography image. An overload protection circuit in the I-AFM limits the maximum current that can be measured to 1  $\mu$ A. The leakage current reaches its maximum measurable values while scanning the pinholes in single layered films, effectively acting as a short circuit. It can be concluded that the AFM tip reaches the bottom TiN<sub>x</sub> while scanning large pinholes resulting in a very conductive circuit.

Topography and leakage current data were extracted across four distinct lines from

these images and are given in Fig. 5.19 (i), (ii), (iii) and (iv). Topography data presented in those graphs show troughs as deep as 80 nm and leakage current data shows current peaks as high as 1000 nA. The current peaks correspond to troughs in the topography data in all graphs, confirming that the pinholes are the dominant source of leakage current measured through I-AFM in single layered films. Leakage current through regions that exclude the pinholes were found to be very low.

Similar I-AFM analysis was also carried out on the multilayer  $\text{BaTiO}_3$  of thickness 80 nm which had undergone 800 °C anneals after each deposition. Fig. 5.20 (a) shows the topography and Fig. 5.20 (b) shows the leakage current map of a  $1 \mu\text{m} \times 1 \mu\text{m}$  area on the surface of the multi-layered sample. The topography scan shows a smooth surface without any pinholes consistent with the results discussed in the last section. The leakage current map shows that the leaky paths are randomly distributed. The maximum leakage current observed was 4 nA. However, the leaky paths do not correspond with any particular structure in the topography scan. Moreover, the maximum value of leakage current through the surface of the multi-layered sample is much lower compared with the single layered sample which showed a current overload and acted as a short in regions with pinholes.

Topography and leakage current data were extracted across four distinct lines from these images and are given in Fig. 5.20 (i), (ii), (iii) and (iv). The troughs in the topography scan from those graphs are less than 5 nm deep even though each layer is 20 nm thick in the multi-layered sample. Hence, it can be concluded that these troughs are not pinholes or cracks. The leakage current data across these scan lines show leaky points. However, amplitudes of the leakage current peaks are much lower than the compliance of the system ( $1 \mu\text{A}$ ), indicating that these regions are not short circuited. Moreover, peaks in the leakage current data do not correspond with troughs in the topography scan-lines. The results confirm that pinholes or cracks are not the source of leakage current in multi-layered samples whereas they were acting as a short in single layered films.

Leakage current maps were obtained on multi-layered samples with thicknesses of

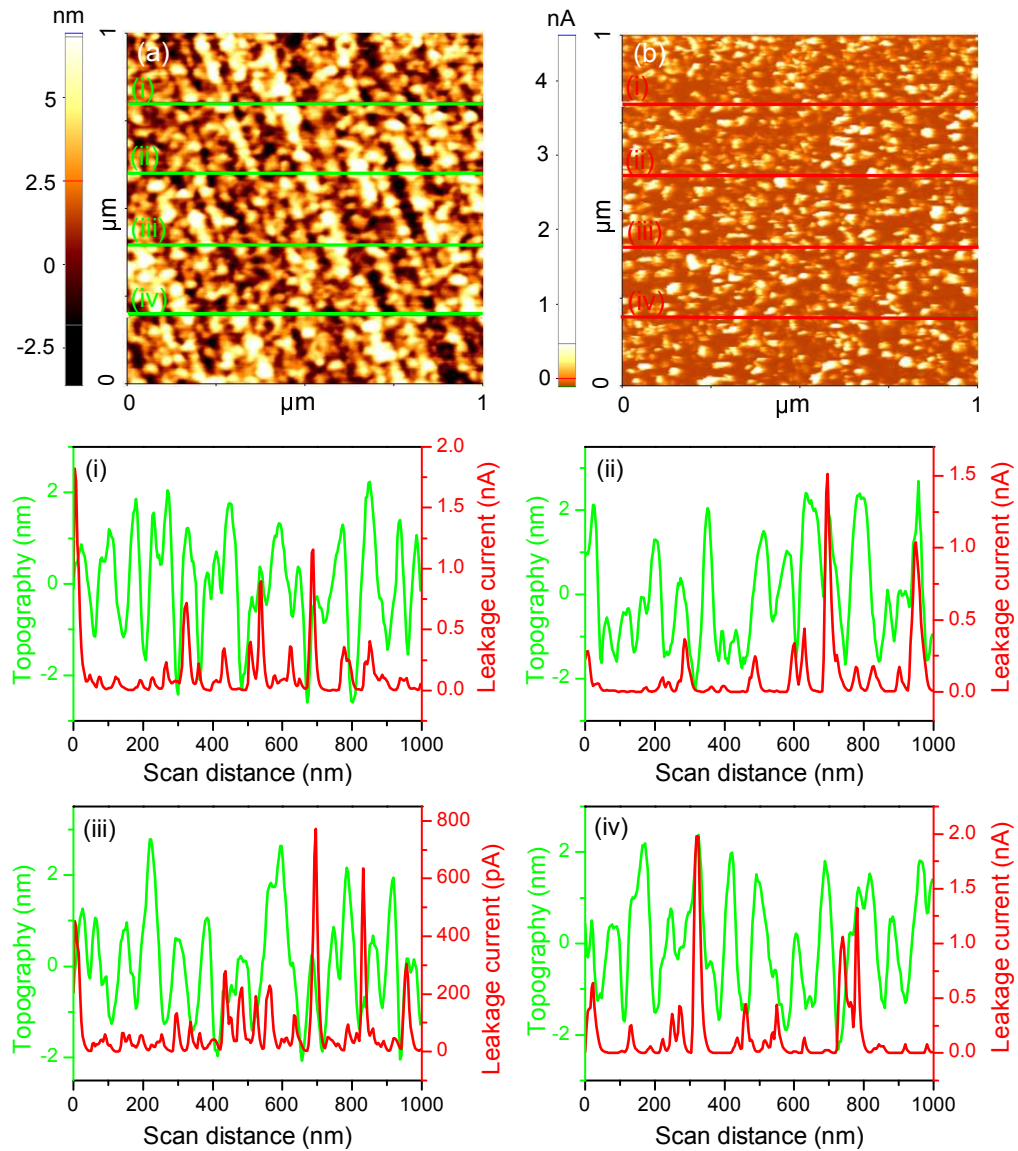


**Figure 5.20:** Shows (a) AFM topography scan and (b) I-AFM scan of 80 nm thick multi-layered BaTiO<sub>3</sub> on TiN<sub>x</sub> annealed at 800 °C for 60 s. (i), (ii), (iii) and (iv) show the topography variation and leakage current across a horizontal line in the AFM image. The results illustrate that the leakage current is not through pinholes in multi-layered films.

20 nm, 40 nm, 60 nm and 80 nm. RMS value of leakage current across a  $1 \mu\text{m} \times 1 \mu\text{m}$  area on the surface of the sample is presented in Fig. 5.21. The RMS leakage current was around 200 nA for a 20 nm film whereas it reduced to 0.2 nA for an 80 nm thick multi-layered BaTiO<sub>3</sub>. The RMS value of leakage current decreases with increasing layer thickness or, in other words, with an increase in the number of layers.

Fig. 5.22 shows the XPS survey spectrum of BaTiO<sub>3</sub> having a thickness of 20 nm after RTP at 800 °C for 60 s. Close to 10 nm was etched away from the surface in the XPS chamber to avoid the influence of any contaminant which might be present on the

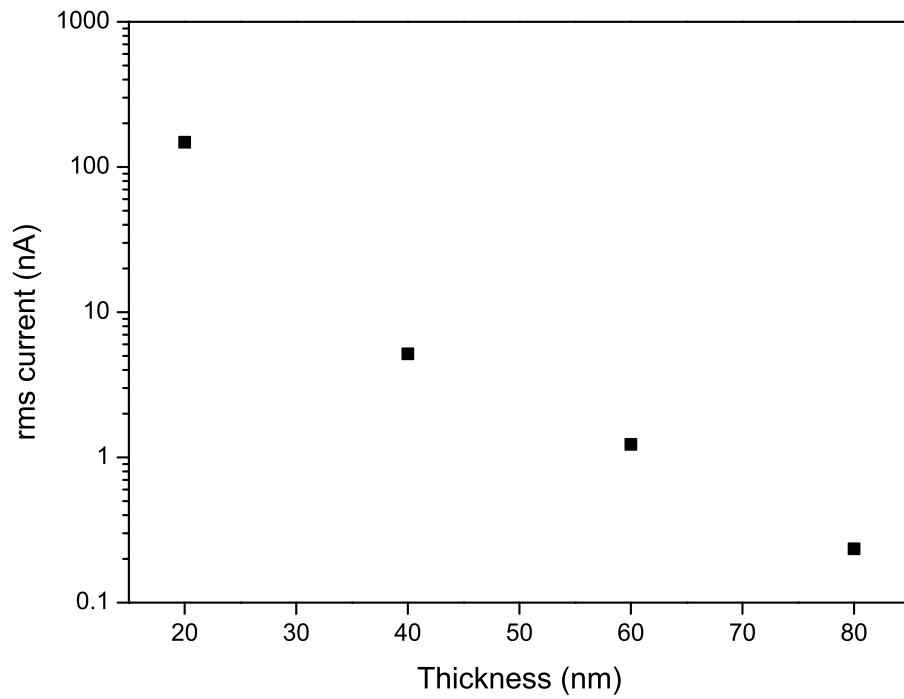


**Figure 5.21:** Shows the RMS leakage current measured from I-AFM scans on multi-layered film of various thicknesses. The RMS leakage current decreases with increase in number of layers or layer thickness.

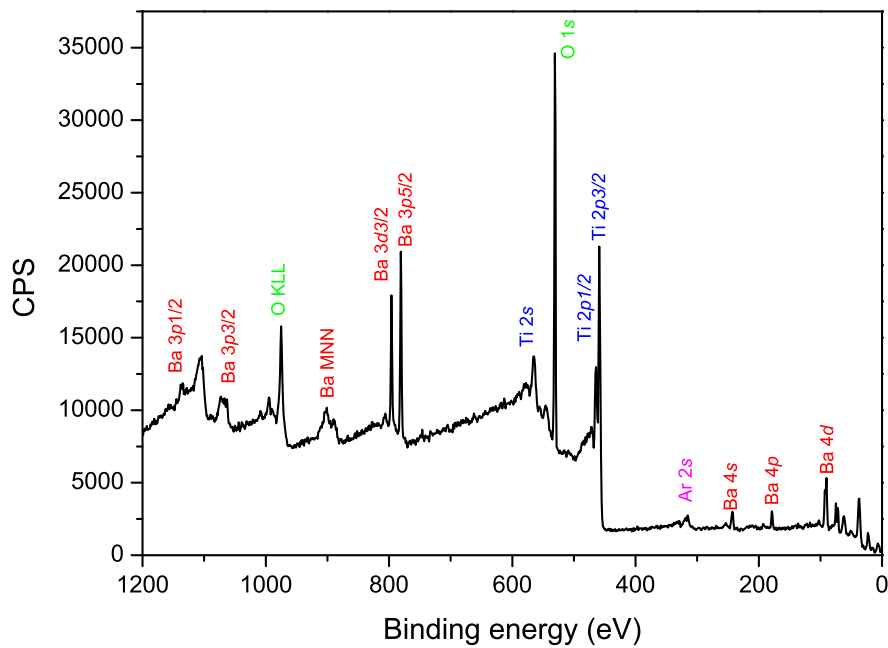


**Figure 5.22:** XPS survey spectrum of 20 nm thick  $\text{BaTiO}_3$  deposited on  $\text{TiN}_x$  and undergone an RTP at 800 °C for 60 s.

surface of the sample. The XPS spectrum shows the presence of barium, titanium and oxygen similar to that of the as-deposited film shown in Fig. 5.1 and does not show any contamination. The presence of argon is believed to be from the sputter ion source used to etch away the surface layer. The absence of a peak around 397 eV, which corresponds to N *1s*, confirms that there is no diffusion of nitrogen from the underlying TiN<sub>x</sub> into the 20 nm thick BaTiO<sub>3</sub>.

High resolution XPS spectra of barium, titanium and oxygen from the annealed sample are given in Fig. 5.23 (a), (b) and (c) respectively. The Ba *3d*<sub>5/2</sub> at 770 eV,

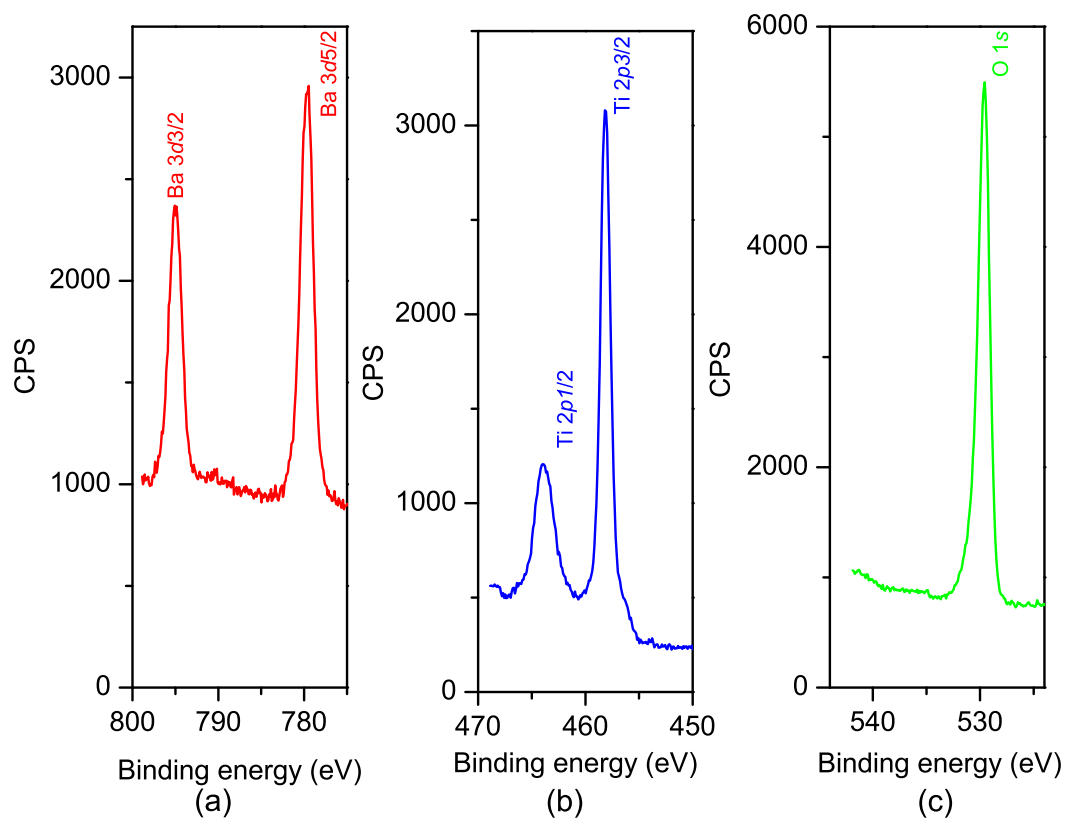


**Figure 5.23:** High resolution XPS spectra of (a) Ba *3d*, (b) Ti *2p* and (c) O *1s* of 20 nm thick BaTiO<sub>3</sub> deposited on TiN<sub>x</sub> and undergone an RTP at 800 °C for 60 s. Binding energies of the corresponding XPS peaks indicate a stoichiometric BaTiO<sub>3</sub> even after the RTP.

Ti *2p* at 458 eV and O *1s* at 529.5 eV are all indicative of a stoichiometric BaTiO<sub>3</sub> and are consistent with the spectra of as-deposited film shown in Fig. 5.2. Furthermore, the titanium spectrum in Fig. 5.23 does not show the presence of any TiN<sub>x</sub> phases which is expected at 455 eV, again confirming the absence of any diffusion from the electrode material. A low binding energy shoulder which is observed near the Ti *2p*<sub>3/2</sub> peak is

due to a reduction of Ti<sup>4+</sup> to Ti<sup>3+</sup> under the influence of ion bombardment during XPS sputter etching [151, 162]. These results confirm that the sputter deposited BaTiO<sub>3</sub> retains its stoichiometry after a post deposition anneal.

AFM topography scans of as-deposited and multi-layered BaTiO<sub>3</sub> of thickness 80 nm which underwent anneal processes at 800 °C are shown in Fig. 5.24. Grain structure was absent in the as-deposited sample shown in Fig. 5.24 (a). The surface of the as-deposited sample is found to be too smooth to detect any grain structure. However, there is a significant improvement in terms of the grain formation for the 80 nm multi-layered sample which underwent an RTP, which is shown in Fig. 5.24 (b). Grains with sizes as large as 50 nm were observed after the anneal process.

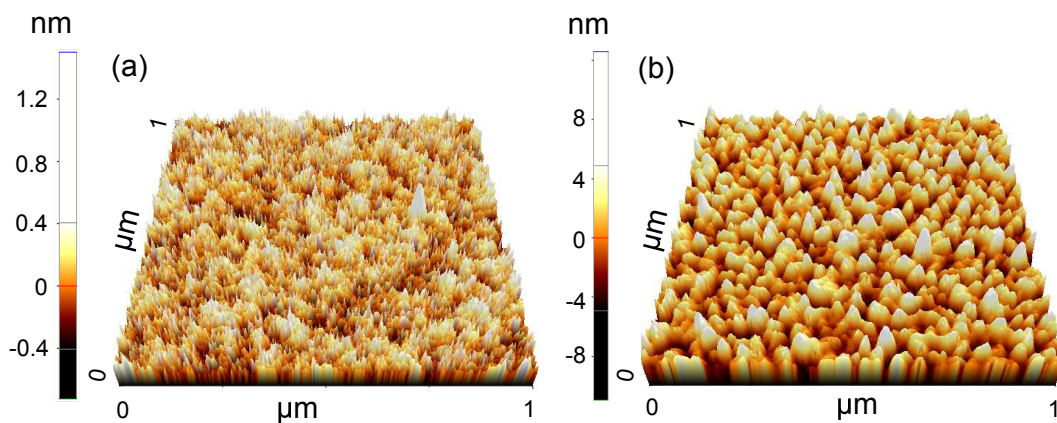


**Figure 5.24:** AFM topography of (a) as-deposited and (b) annealed multi-layer BaTiO<sub>3</sub> having a thickness of 80 nm. In the multi-layer deposition process, RTP were done at 800 °C for 60 s.

Finally, the ferroelectric properties of the multi-layered films were studied using electrostatic force microscopy (EFM). Fig. 5.25 (a) shows the EFM image of an 8  $\mu\text{m} \times 8 \mu\text{m}$  region on an 80 nm thick BaTiO<sub>3</sub> before applying an electric field. Prior to an electrical loading, polarisation is randomly oriented and hence no specific pattern can be observed in the image. A 4  $\mu\text{m} \times 4 \mu\text{m}$  region within the scan area was then polarised by applying an electric field. This was done by applying a DC bias using the same AFM tip in contact mode as discussed in the experimental section of this chapter. The polarity of the applied bias was reversed for each 1  $\mu\text{m}$  covered by the tip in the vertical direction during scanning, giving rise to a stripe pattern. Fig. 5.25 (b) shows the EFM image of the same 8  $\mu\text{m} \times 8 \mu\text{m}$  area given in Fig. 5.25 (a), which covers

the previously polarised  $4 \mu\text{m} \times 4 \mu\text{m}$  region. The polarised region can be easily distinguished by the sharp contrast. The stripe pattern is obtained by alternating the voltage polarity and shows that the film can be polarised in both directions. The EFM images confirm that the film can be polarised and they can retain the polarisation even after removal of the electric field and demonstrates the ferroelectric behaviour of the multi-layered films.

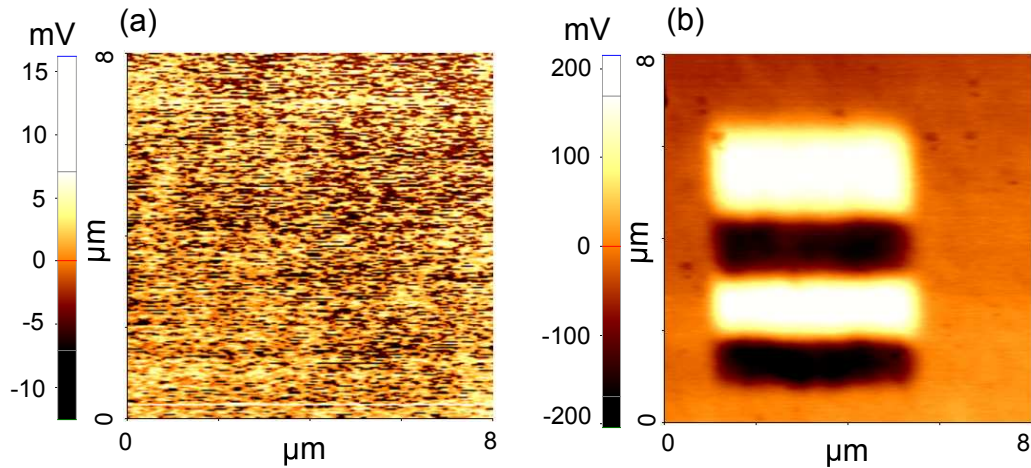


**Figure 5.25:** Showing EFM scan of  $8 \mu\text{m} \times 8 \mu\text{m}$  region on an 80 nm thick multi-layered BaTiO<sub>3</sub> (a) prior to an electrical loading and (b) after loading a  $4 \mu\text{m} \times 4 \mu\text{m}$  region inside the  $8 \mu\text{m} \times 8 \mu\text{m}$  region. Stripe pattern was obtained by reversing the polarity of applied bias while loading. Figure confirms the ferroelectric property of the multi-layered BaTiO<sub>3</sub>.

## 5.6.2 Discussion

The cracking or peeling of thin films could be influenced by factors such as surface roughness of the substrate, lattice mismatch between the film and the substrate, and the differences in coefficient of thermal expansion of the film and the substrate stack. However, it has already been shown in the previous chapter that the TiN<sub>x</sub> electrodes used for this study are smooth and the surface roughness does not increase after an anneal. BaTiO<sub>3</sub> (lattice constant  $3.99 \text{ \AA}$  [36]) deposited on TiN<sub>x</sub> (lattice constant  $4.23 \text{ \AA}$  [163]) can experience strain due to the lattice mismatch and the strain relaxation can lead to cracking of the film [164]. However, an epitaxial growth is not expected at a substrate temperature of  $130 \text{ }^\circ\text{C}$ . Moreover, it was shown that the film cracks even when annealed at  $500 \text{ }^\circ\text{C}$ , which is much lower than the crystallisation temperature of

BaTiO<sub>3</sub>. A strain generation in the film during crystallisation due to lattice mismatch is not expected as the BaTiO<sub>3</sub> film is still in the amorphous state at 500 °C. Hence, the role of lattice mismatch in the formation of pinholes can also be ruled out.

The relaxation of the strain which was generated due to the differences in the coefficient of thermal expansion during a thermal stress has been reported to be one of the main reasons for thin film cracking, mount formation, pinhole or de-lamination [58, 59, 61]. Formation of mounts and pinholes which were observed after the RTP process suggests that the film was under compressive stress during annealing [59]. The compressive stress experienced by the BaTiO<sub>3</sub> film originates mainly from the very thick silicon substrate itself [165] which has a very low coefficient of thermal expansion ( $3 \times 10^{-6} \text{ K}^{-1}$  [71]) compared to the BaTiO<sub>3</sub> film ( $10.1 \times 10^{-6} \text{ K}^{-1}$  [166]). The expansion of the BaTiO<sub>3</sub> film upon annealing is restricted by the substrate which experiences a relatively lower expansion under the same heating conditions. The BaTiO<sub>3</sub> film would experience a compressive stress due to this restriction. The resulting strain is then released through formation of mounts or pinholes.

When the film thickness is lower than the critical thickness, since the strain energy is lower, films follow different mechanisms for strain relaxation or remain in a strained state and do not de-laminate. The existence of a critical thickness has also been observed for epitaxially grown films [164, 167, 168]. Since the deposition and anneal of a subsequent layer in the multi-layered films does not result in a film with pinholes, it can be concluded that each deposited layer is in a relaxed state after RTP. The strain relaxation and thereby a low energy state could be achieved through structural deformations, phase transition, dislocation or diffusion. Ferroelectric materials also develop an internal stress by spontaneous polarisation to relax the strain generated by the thermal stress [165].

Nano-scale leakage current analysis showed that the leakage current decreases with increase in number of layers. Films with thickness less than the critical thickness are pinhole free. Subsequent layers will fill in the pinholes from previous layers if there any present and the film becomes thicker. Hence, the leakage current decreases with

an increase in the number of layers. I-AFM data of single layered films showed that pinholes form a continuous conductive channel for the AFM tip along the width of the pinhole leading to a very high leakage (Fig. 5.19). If top electrodes are deposited on these pinholes, the electrode material will reach the bottom electrode and will act as a short and this will result in device failure. The multi-layer architecture forbids the formation of a continuous conductive channel throughout the thickness of the film as they are pinhole free and through random overlapping of grains. The I-AFM scan of the multi-layer structure (Fig. 5.20) confirms that the leakage current is much lower compared to the films which showed pinholes and leakage paths are randomly distributed.

Pinhole formation and cracking are long standing problems in thin film processing. It is very common to use a reduced ramp up and ramp down rate ( 5 °C/minute) to avoid pinhole or crack formation. However, this method leaves the sample at a high temperature for a much longer time, hence lacks manufacturability, and may result in inter-diffusion of materials. However, the RTP process used in the multi-layer process is within the thermal budget of silicon technology. It was shown that a multi-layer approach can avoid the formation of pinholes when deposited on a silicon substrate, which has a large thermal expansion mismatch. The proposed method is more beneficial for ferroelectric materials such as BaTiO<sub>3</sub> which needs a very high temperature post deposition RTP for crystallisation, if they are deposited at a low substrate temperature (<500 °C).

## 5.7 Summary and Conclusions

BaTiO<sub>3</sub> thin films were deposited on a TiN<sub>x</sub> layer by RF-sputtering from a BaTiO<sub>3</sub> target at a low (130 °C) substrate temperature. As-deposited films were amorphous and showed excellent stoichiometry and very low surface roughness. MIM capacitors were also fabricated and leakage characteristics were studied. It was found that the fringing electric field causes a large peripheral leakage current. Contribution from the parasitic leakage towards the total leakage increases as the electrode size becomes smaller.

Results show that they can be as high as areal leakage current when the electrode sizes are smaller than  $300\ \mu\text{m}$ . It was demonstrated that the parasitic leakage effects cannot be ignored in micro-scale devices.

$\text{BaTiO}_3$  films also underwent post deposition RTP. RTP resulted in films that are de-laminated or with pinholes. However, a critical thickness exists below which films are pinhole free when annealed at corresponding temperatures. Multi-layered films which were created by multiple deposition-RTP cycles were found to be pinhole free, provided that each deposited layer thickness is lower than the critical thickness. Nano-scale leakage current analysis carried out using I-AFM showed that pinholes are the major sources of leakage current in single layered films. However, leakage current is not assisted through valleys in the topography in the case of multi-layered films. It was also shown that the leakage current through a multi-layered film decreases as the number of layers increases. Sputter deposited  $\text{BaTiO}_3$  processed through the multi-layer approach was found to retain the stoichiometry after the RTP process with a large increase in grain size compared to as-deposited material. Moreover, EFM scans showed that the multi-layered films can be polarised by applying an electric field, confirming the ferroelectric property of the deposited film. In this chapter, it was demonstrated that the multi-layer process is a solution for the pinhole or de-lamination problem that can occur when ferroelectric materials are deposited at a low substrate temperature as amorphous and later annealed for achieving crystallinity and grain growth.

# Polarisation Reversal Mechanisms in $\text{BaTiO}_3$

## 6.1 Introduction

Previous chapters focused mainly on deposition of  $\text{BaTiO}_3$  thin films which can withstand high temperature post deposition processing without affecting the film stability. The focus will now move towards understanding the material properties of ferroelectric films. Demonstration and exploration of new materials as well as their electrical properties is essential for the functional diversification of semiconductor-based devices. These functionalities contribute to the miniaturisation of existing electronic systems and could help realise novel systems; designated as ‘more than Moore’ in the semiconductor industry roadmap [169]. In this regard, the present chapter discusses the electric field-induced phase transition phenomenon in ferroelectric materials and its impact on the polarisation reversal mechanism in these materials.

The large piezoresponse shown by ferroelectric materials in certain directions under the application of an external electric field has been an area of some interest in recent years [42, 170, 171]. Fu and Cohen [33] showed that polarisation rotation from the tetragonal to rhombohedral phase and vice versa through an intermediate monoclinic phase is the reason for this extraordinary piezoresponse in a simple ferroelectric perovskite such as barium titanate ( $\text{BaTiO}_3$ ). The polarisation rotation with electric field, and the phase transition associated with it, causes a variation in strain in the

film and hence a difference in piezoresponse. Moreover, the rotation path depends on the orientation of the electric field with respect to crystallographic orientation of the domain. The application of an electric field which is not in alignment with the c-axis of the crystal would result in the phase transformation and leads to an extraordinary piezoresponse. The field-induced polarisation rotation has been predicted from phenomenological theories [172] as well as from first principle calculations [173].

There have been many theoretical studies to investigate the polarisation rotation mechanism due to an electric field. The existence of a monoclinic phase was confirmed by phenomenological Landau-Ginzburg-Devonshire theory, and it has been proven that eighth and twelfth order polarisation parameters are needed to explain the existence of intermediate monoclinic phases [172]. Moreover, the polarisation rotation mechanism with electric field was also established from first principles simulations of lead zirconium titanate [173]. BaTiO<sub>3</sub> is one of the simple lead-free ferroelectrics that show a similar nonlinear piezoresponse under applied DC bias [33, 170]. Franzbach *et al.* [174] were the first to compare the experimentally observed field-induced tetragonal to orthorhombic phase transition in [110]<sub>c</sub> oriented BaTiO<sub>3</sub> with theory by quantifying the polarisation and strain in the film during electric loading. They found that an increase in temperature shifts the field needed to induce this transition to a higher magnitude. In another study Paul *et al.* [32] used a first-principles-effective-Hamiltonian approach in classical molecular dynamics simulations to understand the polarisation rotation mechanism in ferroelectric BaTiO<sub>3</sub>. It was theorised that the polarisation rotation through the monoclinic phase facilitates polarisation switching at lower electric field, and causes a sharp anisotropy in polarisation switching. They also predicted that, when the polarisation ( $\vec{P}$ ) is parallel to electric field ( $\vec{E}$ ), the switching path is linear and a one-step direct switching is observed at the coercive field ( $\vec{E}_c$ ). When  $\vec{P}$  is not parallel to  $\vec{E}$  the switching is a two-step process. First the polarisation rotates from the initial crystal phase through a monoclinic phase before it switches at  $\vec{E}_c$ , causing the polarisation to switch at a lower field than when  $\vec{P} \parallel \vec{E}$ . Moreover, switching paths depend on the initial phase (tetragonal or

orthorhombic) of the domains and the angle that  $\vec{E}$  makes with the crystallographic orientation. However, demonstration of this dependence at the single domain level remains an experimental challenge.

An electric field-induced phase transition in ferroelectrics opens up a new set of potential applications. The in-plane strain in ferroelectrics has been shown to shift the Curie temperature [175], and strain induced by polarisation rotation can thus effectively be utilised to engineer the Curie temperature. Moreover, polarisation rotation can be used to tune dielectric permittivity, strain, piezoresponse and electromechanical response. Hence it is important to understand and experimentally demonstrate the underpinning mechanism of polarisation rotation.

The multitude of applications that piezoresponse force microscopy (PFM) can offer have revolutionised nano-scale domain studies of ferroelectric materials recently [73]. Tip-induced polarisation switching has greatly improved the resolution of domain imaging and spectroscopy. Piezoresponse force spectroscopy (PFS) is a simple technique that can be used to analyse the piezoresponse of materials under an applied electric field [176, 177]. A detailed description of the operation of PFS is given in section 3.2.2.3 of chapter 3. In brief, PFS uses a small alternating voltage superimposed on a pre-set direct voltage which is applied to a conductive AFM tip. When the tip is brought into contact with a ferroelectric or piezoelectric sample, due to the inverse piezoelectric effect, the sample will locally expand when  $\vec{E}$  and  $\vec{P}$  are parallel, or contract if  $\vec{E}$  is anti-parallel with  $\vec{P}$ . This piezoresponse depends on the direction of polarisation and the applied field. As the applied voltage contains an alternating component, the inverse piezoelectric effect will result in the sample surface vibrating with the frequency of the applied alternating voltage. Under this modulation, the amplitude of the piezoresponse would depend on the magnitude of the alternating voltage and the out-of-plane piezoresponse of the material. The phase of the piezoresponse will depend on the orientation of domain polarisation. This oscillation will be directly reflected on the amplitude and phase of the voltage signal of the contacting AFM tip, which can be read out using a lock-in technique.

Section 6.2 of this chapter discusses the experimental details. Material properties such as crystallinity, stoichiometry, growth mechanism *etc.* of thin film BaTiO<sub>3</sub> are shown in section 6.3, prior to investigating the polarisation reversal mechanism in these materials. Section 6.4 investigates the polarisation reversal mechanism in BaTiO<sub>3</sub>. Here we have used the PFS technique to experimentally determine the direction of polarisation vector with changing electric field, and the domain switching angle. We also show that the polarisation reversal is a two-step mechanism which includes both rotation and switching. In this study, we have also used the PFS technique to demonstrate the relation between the crystal orientation and coercive field of ferroelectric BaTiO<sub>3</sub> thin films, which is discussed in Section 6.5. Results demonstrate the role of polarisation rotation on the switching field in BaTiO<sub>3</sub>. We show that PFS is a useful technique providing sufficient resolution to determine the polarisation reversal mechanism of a single domain. It is also shown that this technique can be effectively used to predict the orientation of crystals at a domain level.

## 6.2 Experimental Details

An 80 nm thick SiO<sub>2</sub> layer was grown on a <100> oriented silicon substrate through furnace oxidation. 10 nm thick titanium and 100 nm thick platinum were evaporated to fabricate the substrate stack. BaTiO<sub>3</sub> films of thickness 160 nm were deposited on this Pt/Ti/SiO<sub>2</sub>/Si stack using pulsed laser deposition (PLD) at 740 °C with a KrF excimer laser from Lambda Physik. A reference sample, which has a single crystal orientation was also prepared by depositing 30 nm BaTiO<sub>3</sub> on an epitaxially grown SrRuO<sub>3</sub> on SrTiO<sub>3</sub> single crystal substrate at similar deposition conditions. SrRuO<sub>3</sub> was also grown using the PLD technique. Piezoresponse force spectra were acquired using a Park Systems XE 150 AFM and the cantilever used was NSC–36 Ti/Pt b. A DC bias was swept from -8 V to +8 V (corresponding to an electric field varying from -500 kV/cm to +500 kV/cm) and vice versa. The alternating voltage applied to the tip had an amplitude of 0.8 V, and a frequency of 20 kHz. The cantilever used for acquiring electrostatic force microscopy (EFM) images was NSC–14 Cu/Au. The

EFM and AFM topography scans were carried out in non contact mode. The amplitude and phase of the cantilever oscillation was read using a Stanford Research Systems DSP lock-in amplifier, model SR830. All the measurements were taken at room temperature. Prior to acquiring the EFM image, a  $4\ \mu\text{m} \times 4\ \mu\text{m}$  area was scanned in contact mode while applying a bias of -10 V to the bottom electrode. This was done in order to polarise the BaTiO<sub>3</sub> film. Crystallinity and phase composition were measured by X-ray diffraction (XRD) using PANalytical X'Pert Pro with Cu-K $\alpha$  X-ray radiation having a characteristic wavelength of 1.5418 Å. The X-rays were generated from a Cu anode supplied with 40 kV and a current of 40 mA. X-ray photo-electron spectroscopy (XPS) was performed on samples using a Thermo Scientific K-alpha instrument. Ar ions of beam current 5 mA with an acceleration of 5 kV and square raster of 1 mm were used to etch the sample for depth profiling. The X-ray spot size was 110  $\mu\text{m}$  for the XPS measurements. XPS binding energies were calibrated using the Pt 4d line of platinum achieved through depth profiling of the sample. Platinum, being a noble metal, exists in elemental form and does not make compounds with other elements under the processing conditions described above. Hence, platinum spectra provide an ideal reference line for XPS calibration in this study. Transmission electron microscopy was conducted on a JEOL 2100F microscope operating a 200 kV Schottky field emitter.

### 6.3 Material Characterisation

XRD spectrum of BaTiO<sub>3</sub> thin film is given in Fig. 6.1. XRD analysis of the film shows a polycrystalline nature and grains are oriented primarily in three preferred orientations. Peaks at 22.2°, 31.5°, 38.9° and 45.4° represents the [001], [101], [111] and [002] crystallographic orientations of BaTiO<sub>3</sub> (Inorganic Crystal Structure Database (ICSD) card: 01-074-1962). BaTiO<sub>3</sub> thin films deposited on Pt/Ti/SiO<sub>2</sub>/Si have shown polycrystalline structure in previous studies [178]. However, BaTiO<sub>3</sub> deposited on epitaxially grown SrRuO<sub>3</sub> (ICSD card: 00-025-0912) follows the [001] crystallographic orientation of the SrTiO<sub>3</sub> (ICSD card: 01-073-0661) substrate as shown in Fig. 6.2. The XRD spectrum of the reference BaTiO<sub>3</sub> sample confirms the

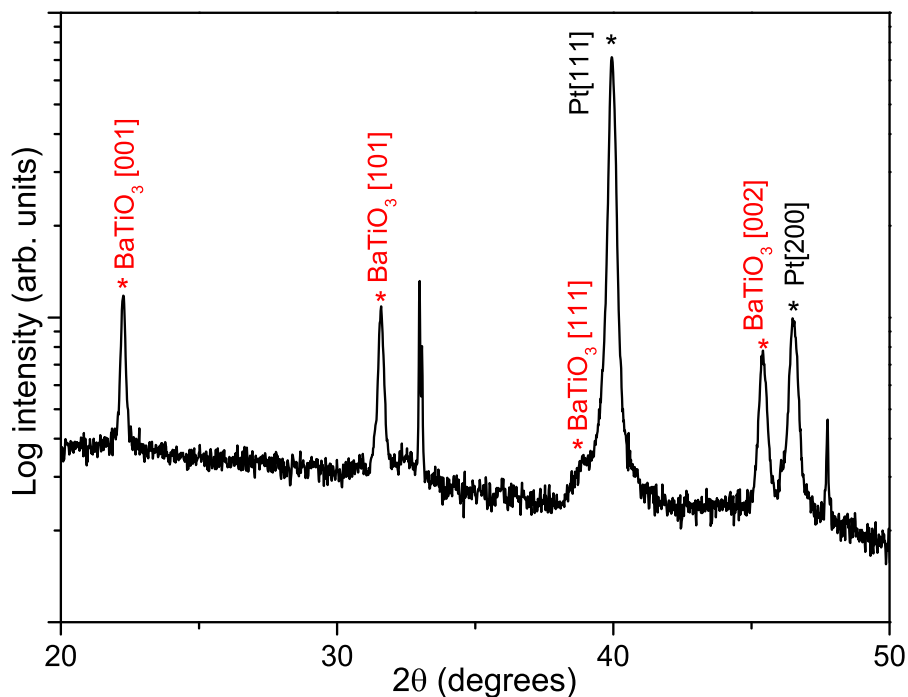


**Figure 6.1:** XRD of BaTiO<sub>3</sub> showing the polycrystalline nature of the film deposited on Pt. BaTiO<sub>3</sub> shows three preferred orientations including [001], [101] and [111].

epitaxial nature of growth on a [001] oriented single crystal substrate.

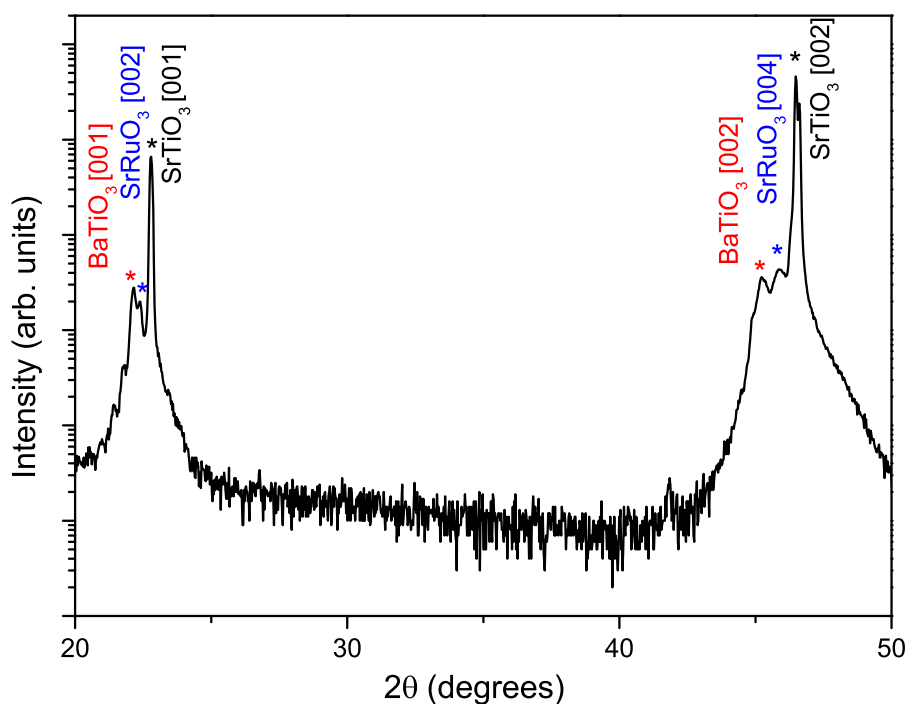


**Figure 6.2:** XRD spectrum of BaTiO<sub>3</sub> reference sample deposited on epitaxially grown SrRuO<sub>3</sub> on SrTiO<sub>3</sub> single crystal substrate. BaTiO<sub>3</sub> is grown in the same crystal orientation as that of the substrate.

An XPS survey scan of the BaTiO<sub>3</sub> film after an initial etching of the surface layer is given in Fig. 6.3. This XPS survey spectrum shows peaks corresponding to barium,

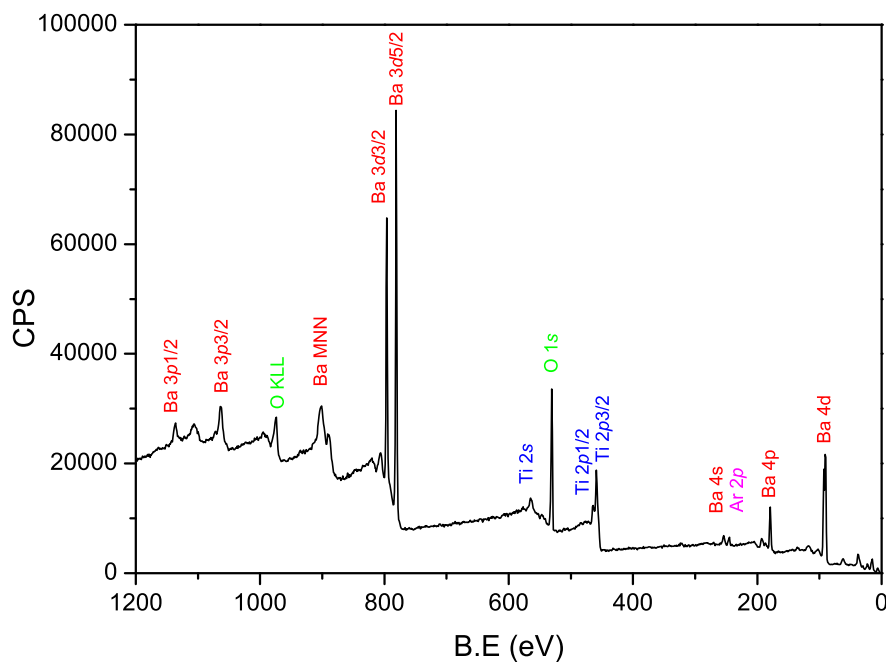


**Figure 6.3:** XPS survey scan of BaTiO<sub>3</sub> film. Measurements were taken after etching away the surface layer in the XPS chamber in order to avoid any contribution from surface contamination. Results indicate presence of barium, titanium and oxygen and do not show any contamination or diffusion. Argon is believed to have originated from the ion source during XPS etching. O KLL and Ba MNN are the Auger peaks.

titanium and oxygen. Moreover, the spectrum shows no trace of contaminants such as carbon or diffusion of platinum or silicon from the substrate. The presence of argon is believed to be from the argon ion source used to etch away the surface layer in the XPS chamber. High resolution spectra of Ba 3*d*, Ti 2*p* and O 1*s* are shown in Fig. 6.4. The

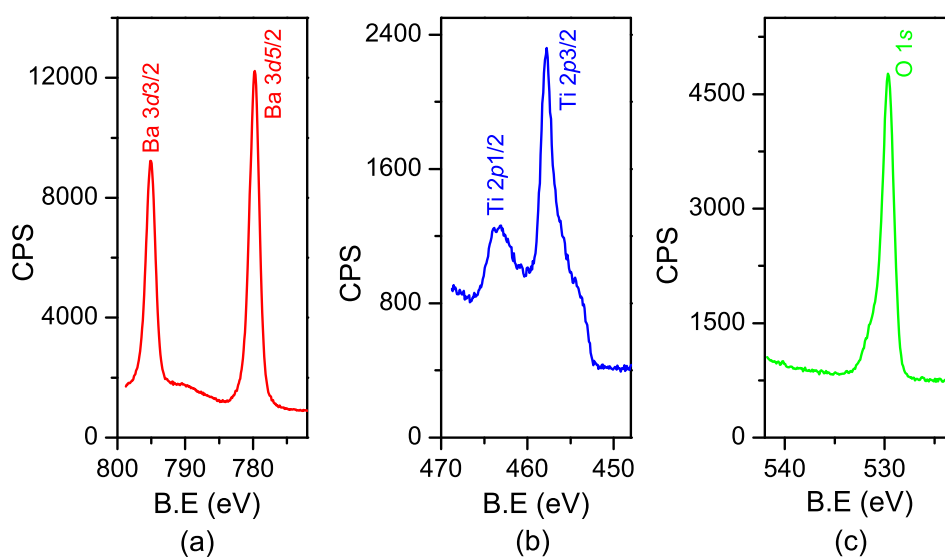


**Figure 6.4:** High resolution XPS spectra of (a) Ba 3*d*, (b) Ti 2*p* and (c) O 1*s*. Binding energies of the corresponding peaks indicate a stoichiometric BaTiO<sub>3</sub> as described in the text.

Ba  $3d_{5/2}$  peak centred on 779.3 eV (Fig. 6.4 (a)) is ascribed to the barium bound in the BaTiO<sub>3</sub> lattice [151]. The peak at 458 eV shown in Fig. 6.4 (b) is the Ti  $2p_{3/2}$  peak characteristics of stoichiometric BaTiO<sub>3</sub>. The low binding energy shoulder observed near the Ti  $2p_{3/2}$  in Fig. 6.4 (b) is due to the reduction of Ti<sup>4+</sup> to Ti<sup>3+</sup> under the influence of ion bombardment during XPS sputter etching [151, 162]. Furthermore, the peak centred on 529.5 eV is assigned to oxygen in the BaTiO<sub>3</sub> lattice in good agreement with the literature [151, 179]. XPS analysis indicates that the deposited film is stoichiometric and does not show the presence of any contamination.

An AFM topography scan of the BaTiO<sub>3</sub> thin film shown in Fig. 6.5 indicates an average diameter of 30 nm for individual grains. The diameter of the grains was also

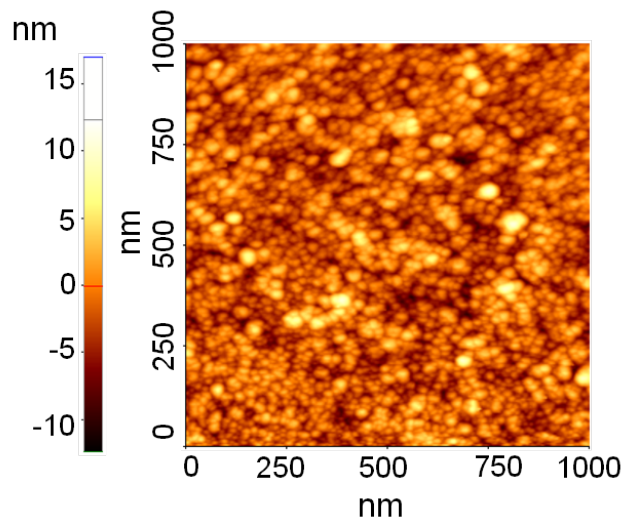


**Figure 6.5:** AFM topography of 160 nm BaTiO<sub>3</sub> deposited on Pt/Ti/SiO<sub>2</sub>/Si. AFM surface scan illustrates an average grain size of 30 nm.

confirmed by the TEM cross section shown in Fig. 6.7 (a). Fig. 6.6 shows the EFM scan of an 8  $\mu\text{m}$   $\times$  8  $\mu\text{m}$  region which overlaps with a previously polarised 4  $\mu\text{m}$   $\times$  4  $\mu\text{m}$  area. In order to polarise the film, a DC bias was applied using the same AFM tip in contact mode as discussed in the experimental section of this chapter. The polarised region can be distinguished as a bright contrasting square region in Fig. 6.6 (a). The ability of the film to retain the polarisation even close to two minutes after the removal of electric field confirms the ferroelectric nature of the deposited film. Fig. 6.6 (b) shows the PFM scan of a 1.5  $\mu\text{m}$   $\times$  1.5  $\mu\text{m}$  area within the previously polarised region (bright region in Fig. 6.6 (a)). The zoomed scan shows the presence of ferroelectric

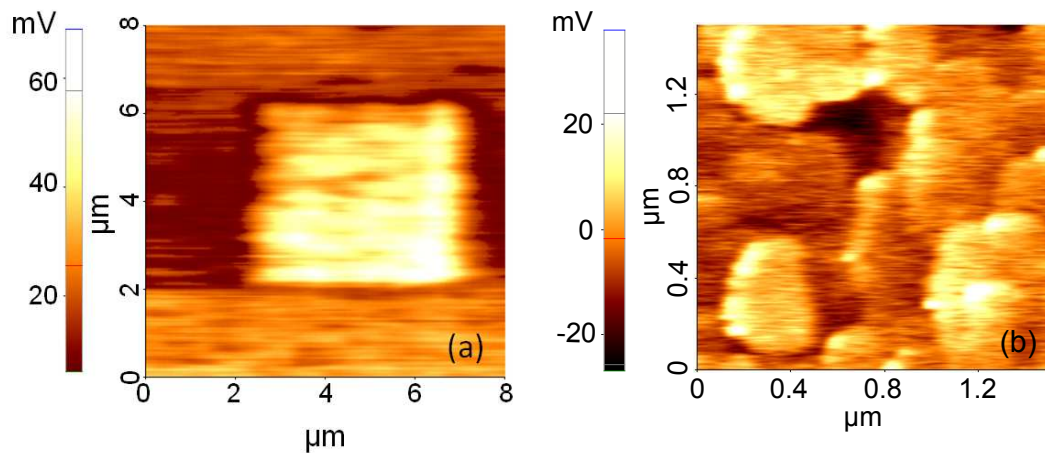


**Figure 6.6:** EFM scan of (a)  $8 \mu\text{m} \times 8 \mu\text{m}$  area which covers a previously polarised  $4 \mu\text{m} \times 4 \mu\text{m}$  area. The ability of the film to retain the polarisation after removal of electric field indicates the ferroelectric nature of the film. (b) PFM scan of  $1.5 \mu\text{m} \times 1.5 \mu\text{m}$  from the previously polarised region. Ferroelectric domains are identifiable with their contrasting colours. Ferroelectric domains are more than 200 nm in diameter and are much larger than grain sizes shown in Fig. 6.5.

domains. Moreover, these domains are at least 200 nm in diameter. The difference in the amplitude level between domains in Fig. 6.6 (b) is due to the polycrystalline nature of the film. Piezoresponse experienced by the AFM tip will change with a variation in domain orientation, hence the difference in contrast from domain to domain. Even though individual grains are 30 nm in diameter, as seen by AFM as well as TEM cross section images, Fig. 6.6 (b) shows that ferroelectric domains are much larger than this. It can be assumed that each domain is larger than a grain and consists of a large number of grains with the same crystallographic orientation [6].

Fig. 6.7 (a) shows a TEM cross section of the thin film stack illustrating the columnar growth of the  $\text{BaTiO}_3$  film used for this study. PLD-grown  $\text{BaTiO}_3$  films have demonstrated columnar growth in previous studies [180] as well. Fig. 6.7 (b) is a high resolution TEM image of the  $\text{BaTiO}_3$  film. Regions demarcated by white dotted lines contain fine fringes of a non overlapping crystal and indicate true crystal planes. Red lines in region (1) give an idea about the crystallographic orientation of the region. The same orientation runs through regions (2) and (3). This indicates that the same orientation is present throughout the thickness of the film. Coarse fringes seen nearby are Moiré fringes<sup>1</sup> formed from the fringes of overlapping crystals present within the

<sup>1</sup>Moiré fringe is an interference pattern created when two identical patterns are overlaid while slightly

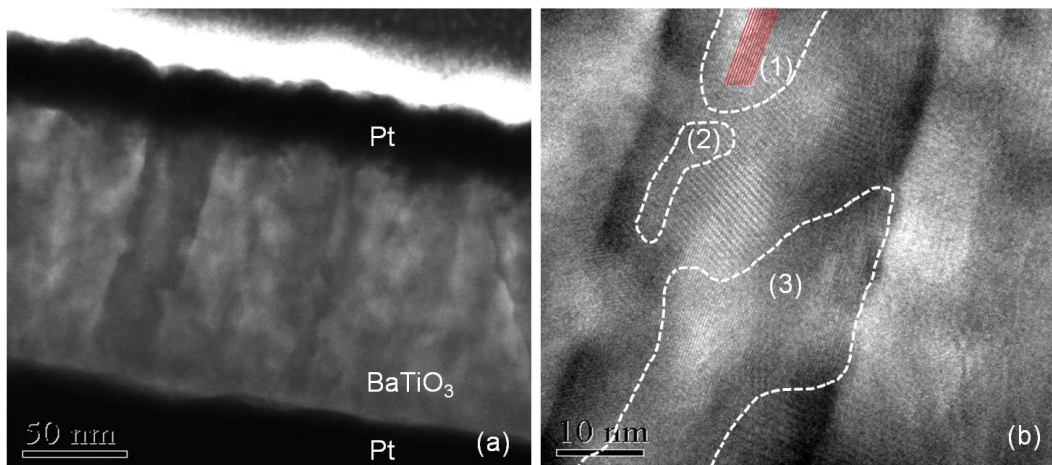


**Figure 6.7:** TEM images of (a) cross section of BaTiO<sub>3</sub> sandwiched between platinum electrodes and (b) high resolution TEM highlighting individual columns. Regions showing non overlapping crystals are demarcated by dotted lines. Orientation of the column is shown by red lines in region (1). A similar orientation runs through other regions, indicating that the same orientation is present throughout the column.

thickness of the sample [181]. The absence of fringes elsewhere could be due to the grain being oriented away from the high symmetry orientation or due to that particular region being too thick for high resolution TEM imaging.

Columnar growth of the grains and the fact that these grains follow the same crystal orientation throughout the column would result in a PFS or EFM signal which is a true characteristic of that crystal plane. Furthermore, EFM images have shown that the domains are at least 200 nm wide which is much larger than the maximum tip diameter of 80 nm. Large sizes for the domain compared to the tip diameter will eliminate the chances of any interference from nearby domains during PFS measurements. XRD spectra confirmed the polycrystalline nature of the deposited film and showed [001], [101] and [111] preferred orientations. XPS measurements demonstrated the quality and stoichiometry of the film.

## 6.4 Polarisation Reversal Mechanism

Material qualification of PLD deposited BaTiO<sub>3</sub> thin films was described in the last section. In this section, the polarisation reversal mechanism of BaTiO<sub>3</sub> is discussed. Here, by employing the PFS technique, we demonstrate experimentally that the displaced or rotated from one another.

polarisation reversal in ferroelectric materials is a two-step mechanism which includes both polarisation rotation and switching. The longitudinal piezoelectric coefficient ( $d_{zz}$ ) for materials with tetragonal symmetry, including  $\text{BaTiO}_3$ , is given by;

$$d_{zz} = (d_{31} + d_{15})\sin^2\theta\cos\theta + d_{33}\cos^3\theta. \quad (6.1)$$

where  $\theta$  is the angle between the measurement direction and the direction of spontaneous polarisation, which is the c-axis orientation for tetragonal  $\text{BaTiO}_3$  [43]. The piezoelectric tensor elements for  $\text{BaTiO}_3$  are  $d_{31} = -35$ ,  $d_{15} = 400$  and  $d_{33} = 85$  pm/V [182]. The dependence of  $d_{zz}$  on the direction of polarisation for  $\text{BaTiO}_3$  from equation 6.1 is plotted and shown in Fig. 6.8. The magnitude of  $d_{zz}$  is a maximum when the polarisation vector makes an angle around  $49^\circ$  with the longitudinal direction [43] as shown in Fig. 6.8, *i.e.* the maximum value of  $d_{zz}$  occurs when it is almost  $49^\circ$  away from polarisation direction. Here, the longitudinal piezoresponse, measurement direction and the direction of applied electric field are all referring to the out-of-plane axis.

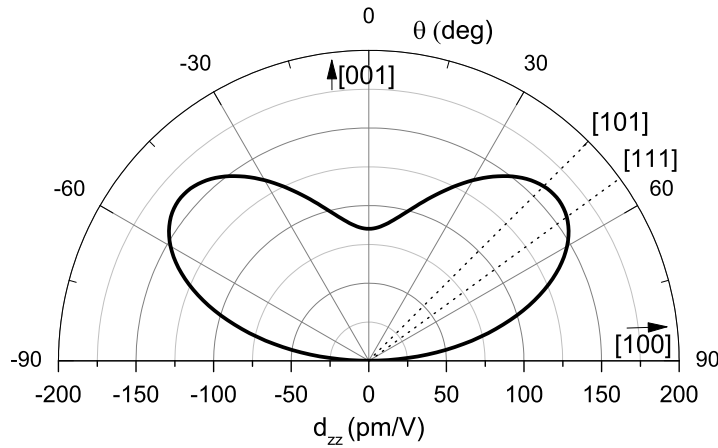


**Figure 6.8:** Dependence of longitudinal piezoelectric coefficient,  $d_{zz}$  on direction of polarisation in  $\text{BaTiO}_3$  calculated based on equation. 6.1. The maximum of piezoresponse occurs when the polarisation is oriented at  $49^\circ$  with measurement direction.

The amplitude and phase of the PFS data on the epitaxially grown [001] oriented  $\text{BaTiO}_3$  reference sample is given in Fig. 6.9. The amplitude of PFS data shown in Fig. 6.9 (a) is constant for few hundreds of kV/cm as the electric field is swept from

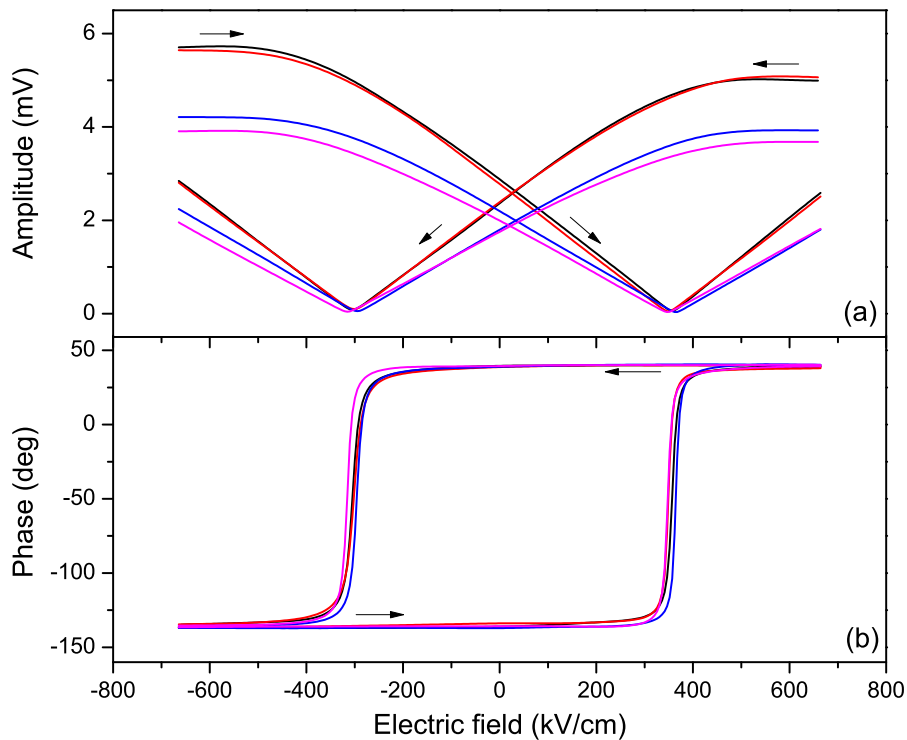


**Figure 6.9:** Amplitude (a) and phase (b) of reference BaTiO<sub>3</sub> sample epitaxially grown on [001] oriented single crystal substrate. Arrows indicate direction of electric field sweeping. There is no enhanced piezoresponse in the amplitude signal and polarisation rotation is not apparent from the phase signal implying a one-step direct switching. The forward and reverse sweeps were taken as two different measurements with a 2 s hold between the measurements resulting in a noncontinuous spectra. The DC bias was set to 0 V between measurements. This was done since a continuous sweep always resulted in a pseudo-enhanced piezoresponse between the forward and reverse seeps.

-600 kV/cm to +600 kV/cm (forward sweep). The amplitude of piezoresponse reduces upon decreasing the electric field and the ferroelectric domains switch at a coercive field of +350 kV/cm. A similar trend is followed when the electric field was swept from +600 kV/cm to -600 kV/cm (reverse sweep) and the ferroelectric domains switch at -350 kV/cm. In the case of the phase signal shown in Fig. 6.9 (b), the domain reversal appears as a large change in the phase of the piezoresponse at the coercive fields ( $\pm 350$  kV/cm). The phase signal of PFS data depend on the direction of polarisation. Hence, the switching of polarisation causes a sudden change in the phase signal. The amplitude and phase of the piezoresponse from the [001] oriented reference sample show the same characteristic as that of the ideal PFS spectra discussed in section 3.2.2.3 of chapter 3. An abrupt switch in the phase signal and the absence of an enhanced piezoresponse in the amplitude signal (as demonstrated in later sections) refers to

a direct one-step switching of ferroelectric domain. A direct switching of  $\vec{P}$  was predicted for [001] oriented BaTiO<sub>3</sub> when  $\vec{E}$  was also applied in the same direction [32]. The absence of enhanced piezoresponse in the amplitude signal (Fig. 6.9 (a)) and the absence of polarisation rotation in the phase signal (Fig. 6.9 (b)) implies the one-step switching mechanism when  $\vec{P}$  and  $\vec{E}$  are parallel.

The variation in amplitude and phase of the piezoresponse with electric field for the polycrystalline BaTiO<sub>3</sub> is shown in Fig. 6.10. When the electric field is swept from

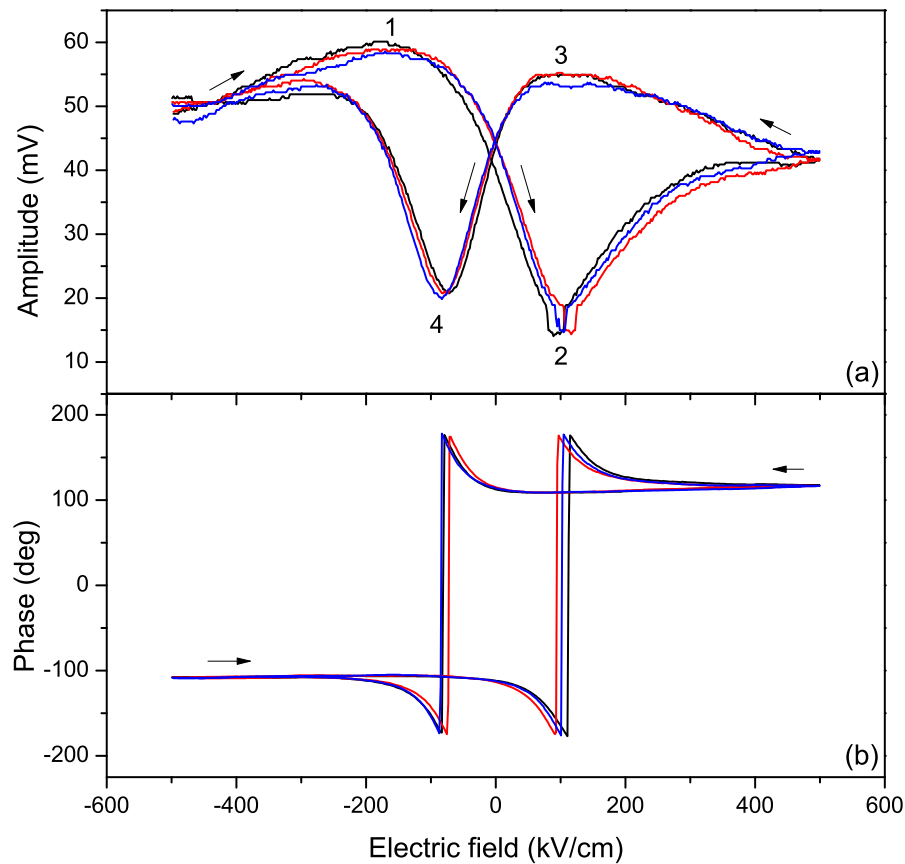


**Figure 6.10:** (a) amplitude and (b) phase of piezoresponse as a function of applied electric field. The units of amplitude and phase are arbitrary, as explained in the text. The arrows indicate the direction of electric field sweeping.

-500 kV/cm to +500 kV/cm, the amplitude of the piezoresponse first increases, reaching a maximum at around -125 kV/cm denoted as point (1) in Fig. 6.10 (a), after which it decreases. For an electric field greater than 0 kV/cm, the applied field is opposite in direction to the polarisation, which causes the domain to locally contract, leading to a reduction in signal amplitude. The amplitude reaches a minimum at 110 kV/cm, (point (2) in Fig. 6.10 (a)) representing the polarisation switching field. This switching

is also visible in the phase of the piezoresponse (Fig. 6.10 (b)) as an abrupt change in the phase signal at the switching field. Since the phase signal is dependent on the direction of polarisation, a sudden change in the direction of polarisation results in a rapid change in the phase signal. The signal amplitude increases with further increase in electric field as  $\vec{E}$  and  $\vec{P}$  are now pointing in the same direction, causing local expansion of the domain. Points (3) and (4) in Fig. 6.10(a), corresponding to the maxima and minima for the reverse sweep (+500 kV/cm to -500 kV/cm) occur around 100 kV/cm and -80 kV/cm respectively. Quantification of piezoresponse directly from the out of plane amplitude and phase is limited [183]. Moreover, these signals are produced with respect to the reference signal generated by the lock-in amplifier, introducing additional complications in quantifying the amplitude or phase of these signals.

### 6.4.1 Discussion

The large increase in the amplitude of the out-of-plane piezoresponse with decreasing electric field (Figure 6.10 (a)) on the polycrystalline sample is believed to be due to the electric field-induced phase transition through an intermediate monoclinic phase as reported previously [33]. The enhanced piezoresponse, implied from an increase in the amplitude of the out-of-plane piezoresponse with decreasing electric field was observed only when the applied electric field and the c-axis orientation of the domain are not parallel. For the [001] oriented reference sample no enhanced piezoresponse was observed as the electric field and c-axis orientations are parallel in this case. The piezoelectric coefficient of a material is proportional to its spontaneous polarisation which in turn is related to its phase. Hence a change in the phase of the material causes a variation in the piezoresponse. Since it is known that at room temperature BaTiO<sub>3</sub> is tetragonal [182] when the electric field is zero, we conclude that the phase changes from either rhombohedral or orthorhombic at high electric field to tetragonal at zero field through an intermediate monoclinic phase resulting in an enhanced piezoresponse for the polycrystalline sample. This also indicates that the  $d_{zz}$  maxima, occurring when the polarisation orientation is at 49° to the longitudinal axis, as described in the

previous section, occur at -125 kV/cm (point (1)) and 100 kV/cm (point (3)) for forward and reverse sweeps respectively in Fig. 6.10. The maxima can be used as reference points, and the orientation of the polarisation vector with varying electric field can be calculated from the change in phase with respect to these reference points. Here, it was assumed that the polarisation rotates further away from the electric field direction and towards the crystalline orientation with decreasing field. In the case of the [001] reference sample polarisation reversal is a one-step direct switching compared to the polycrystalline sample where polarisation reversal includes both rotation and switching. Hence there is no phase change and enhanced piezoresponse associated with it in the [001] oriented reference sample (Fig. 6.9).

Phase signal detected by the lock-in amplifier is given by  $\theta = \theta_{sig} - \theta_{ref}$  as described in section 3.2.2.3 of chapter 3. The variation in the phase signal with electric field is due to variation in  $\theta_{sig}$  as a result of the continuous variation of the polarisation vector. The phase signal will either increase or decrease with  $\theta_{sig}$  depending on the value of  $\theta_{ref}$ . An increase in  $\theta$  would mean that  $\theta_{sig}$  is increasing with respect to the set value of  $\theta_{ref}$ .

The orientation of the polarisation vector with respect to the out-of-plane axis for forward and reverse sweeps deduced from the phase signal is shown in Fig. 6.11. The inset figure shows the orientation of polarisation at zero field along with the phase of the crystal. BaTiO<sub>3</sub> will be in a tetragonal phase at room temperature for zero applied field [184]. While considering the forward sweep in Fig. 6.11, the polarisation vector is inclined more towards the electric field direction at very high fields. The electric field-induced phase change is the cause of this polarisation rotation. Different phases of BaTiO<sub>3</sub> will have their polarisation orientated along different axes. The tetragonal phase will have the polarisation oriented along the c-axis ([001]) whereas the polarisation will point diagonally along the face ([110]) for orthorhombic and monoclinic phases. Similarly, the polarisation vector will point diagonally across the unit cell [111] in the case of BaTiO<sub>3</sub> in its rhombohedral phase [185, 186]. At -125 kV/cm polarisation makes a 49° angle with the longitudinal axis and causes an

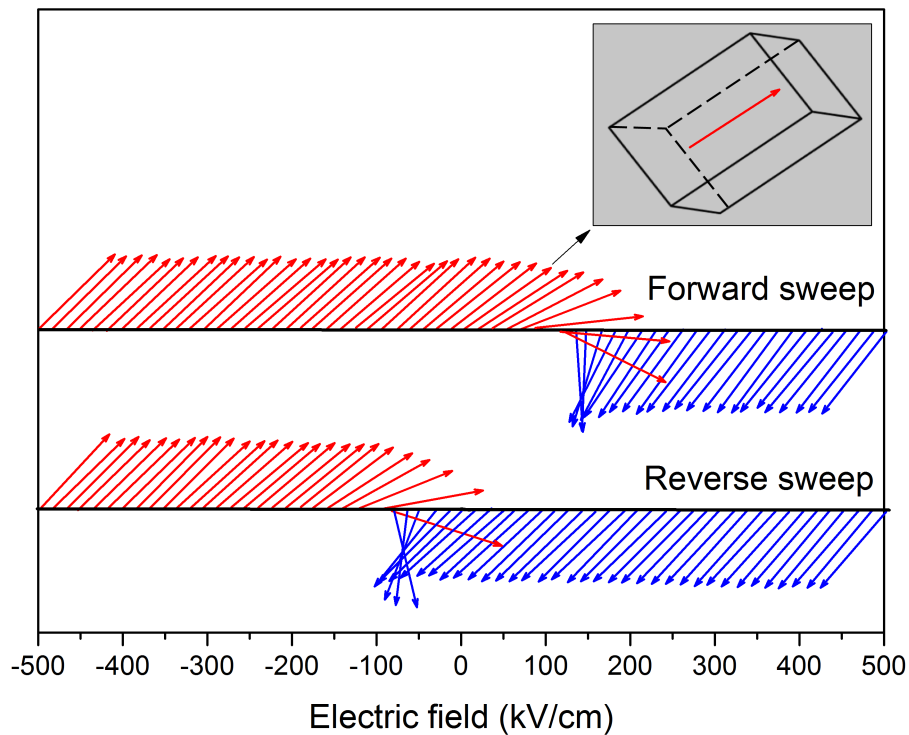


**Figure 6.11:** Direction the polarisation vector makes with longitudinal axis at different electric fields for the forward sweep (-500 kV/cm to +500 kV/cm) and reverse sweep (-500 kV/cm to +500 kV/cm). Red and blue colours indicate the up and down orientation of the polarisation respectively. Figure indicates that the polarisation reversal is a two step mechanism which includes both polarisation rotation and switching. Polarisation rotation is indicated as same coloured arrows and the switching happens when the colour of the arrows changes. Inset shows the direction of polarisation and tetragonal phase of the BaTiO<sub>3</sub> at zero field.

enhanced piezoresponse in the amplitude signal (Fig. 6.10 (a)) as described in the last paragraph. The enhanced piezoresponse would also indicate the monoclinic phase of the domain at that particular field. With decreasing applied field, the polarisation moves further away from the out-of-plane direction and moves towards the crystalline orientation. At zero applied field, the polarisation is oriented at the spontaneous polar direction (c-axis) of the tetragonal crystal lattice, which in this case is oriented at 54° with the longitudinal axis as shown in the inset. For positive values of applied electric fields the polarisation rotates further away from the spontaneous polar direction. At 110 kV/cm the polarisation switches its direction as seen in the amplitude signal and phase signal, denoted by a change in the colour of the arrow from red to blue in the case of the forward sweep in Fig. 6.11. However, the switching happens only for a small angle (about 60°) compared to the anticipated 180°. After switching, polarisation

rotates further before it aligns  $180^\circ$  opposite to its orientation at higher negative fields. For the reverse sweep, polarisation follows a similar trend. In this case, as the electric field is reduced, polarisation rotates before it actually switches, and is denoted by a change the colour of the polarisation vector from blue to red in Fig. 6.11.

$\text{BaTiO}_3$ , which is tetragonal at room temperature [184], will have spontaneous polarisation along the  $c$ -axis at zero applied field [43, 185]. For electric fields higher than  $\pm 150$  kV/cm, polarisation shows a tendency to orient towards the field direction [187]. However, the crystalline anisotropy energy, which determines the direction of spontaneous polarisation, will tend to realign the polarisation towards the crystallographic axis. As the electric field decreases, crystalline anisotropy becomes more prominent causing the polarisation to rotate towards the crystalline orientation. Results also show that at zero field the polarisation is pointed towards the spontaneous polar direction of the tetragonal lattice, as expected. When the electric field direction is anti-parallel to the polarisation, its direction changes rapidly with increasing field, and it completely switches at the critical switching field strength. We have also shown that the switching angle is around  $60^\circ$ . Polarisation further rotates with increasing field after switching, following similar behaviour at higher, negative fields, and with the direction of polarisation parallel to the electric field. These results are in contrast to the epitaxially ([001] oriented) grown sample which showed a one-step direct switching due to the alignment of its  $c$ -axis with the electric field direction. Although the upward and downward polarisations are orienting at  $180^\circ$ , the actual switching happens only for a reduced angle. Polarisation reversal in this case is assisted by polarisation rotation. The field-induced phase transition is shown to be the cause of variation in the direction of polarisation vector.

## 6.5 Impact of Polarisation Rotation on the Switching Field

In the last section it was shown that polarisation reversal is a one-step direct switching process when electric field direction and c-axis are parallel ([001] orientation). It involves both rotation and switching when the direction of electric field is not parallel to the c-axis orientation of the tetragonal BaTiO<sub>3</sub> lattice. This section focuses on the impact of polarisation rotation on the coercive field of BaTiO<sub>3</sub>. PFS data shown in Fig. 6.12 are measured at three different domains. This is deduced from the spectra

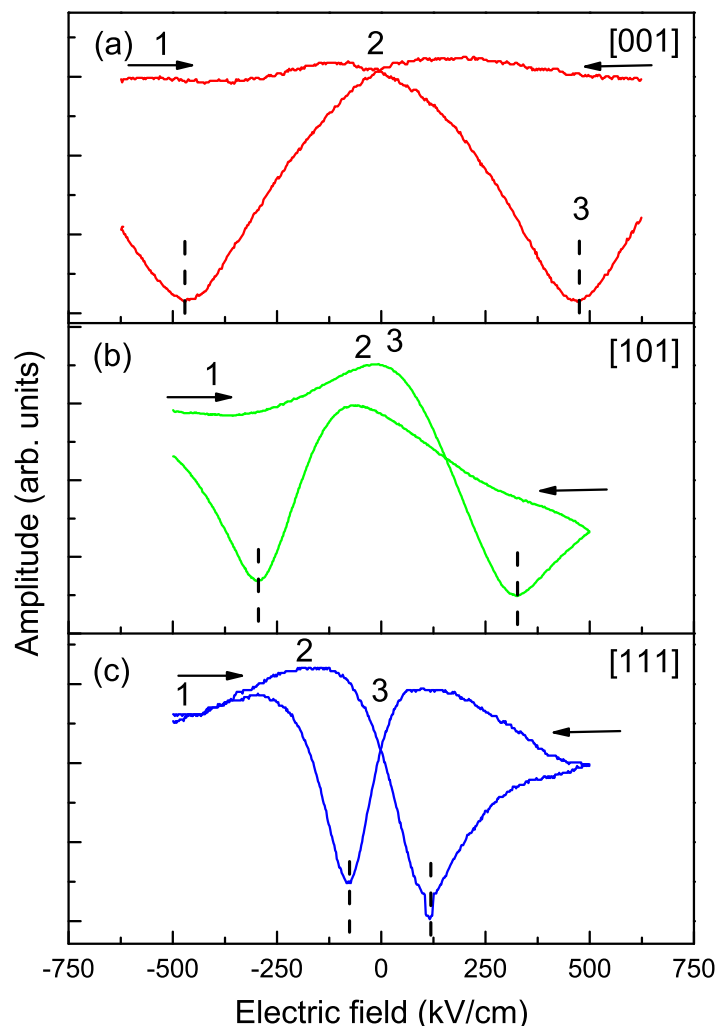


**Figure 6.12:** PFS spectra taken at three different domains. Arrows indicate the spectra for forward and reverse sweeping of the electric field. The coercive field (indicated by dotted lines) decreases as the c-axis of the tetragonal lattice moves away from the perpendicular direction. The domains are predicted as (a) [001], (b) [101] (or [011]) and (c) [111] as explained in the text.

by their different switching fields and the shapes of the piezoresponse. PFS data collected at a large number of domains fall in to one of these spectra. The following sections contain an analysis of these three types spectra based on the predictions of the dependence of crystal orientation on the polarisation reversal [32] in BaTiO<sub>3</sub> as three different scenarios (Fig. 6.13, Fig. 6.14 and Fig. 6.15). It was deduced that these three spectra represent three different ferroelectric domains; [001], [101] (or [011]) and [111]. Indeed, the XRD spectra confirm the polycrystalline nature of the BaTiO<sub>3</sub> film with [001], [101] and [111] preferred orientations as shown in Fig. 6.1, which is consistent with the PFS results. Here we have also shown that PFS can be effectively used to predict the crystal orientation at the resolution of single domain.

### ***Scenario 1: Fig. 6.12 (a)***

The PFS data in Fig. 6.12 (a) shows minimal variation in the piezoresponse with decreasing electric field in comparison to those in Fig. 6.12 (b) and (c) when the electric field was swept from -600 kV/cm to +600 kV/cm. This indicates the absence of enhanced piezoresponse and polarization rotation. The switching path in this domain exhibits the characteristics of a single-step switching mechanism, similar to the epitaxially grown reference sample, occurring when the polarisation is parallel to the electric field. As the electric field is decreased from its maximum value (denoted as point (1) in Fig.6.12 (a)) towards zero (point (2)), the piezoresponse remains same. There is no enhanced piezoresponse. For this domain, direct switching occurs at a coercive field (point (3)) when the electric field direction is opposite to the polarisation direction.

Fig. 6.13 is a schematic illustration of the polarisation reversal mechanism on [001] oriented domains for a forward sweep of electric field. Polarisation is pointed along the c-axis of the tetragonal lattice for negative fields as the electric field direction and polarisation are parallel as illustrated in Fig. 6.13 (a). At zero field polarisation is still pointing at the same direction (Fig. 6.13 (b)). When the polarisation is anti-parallel to the electric field, at the coercive field polarisation switches its direction as shown

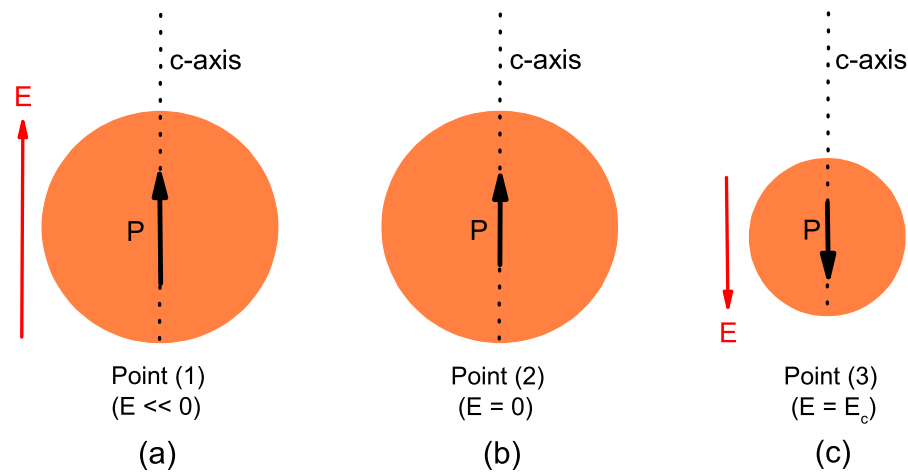


**Figure 6.13:** Schematic illustration of polarisation reversal in ferroelectric domains of spectrum in Fig. 6.12 (a) during a forward sweep showing; (a) orientation of the polarisation at high negative fields (point (1)), (b) the direction of polarisation at zero field (point (2)) and (c) the switching of direction of polarisation at coercive field (point (3)). Point (1), (2) and (3) are marked on Fig. 6.12 (a).

in Fig. 6.13 (c). Ferroelectric domains retain their tetragonal phase throughout the entire electric field sweeping as the field direction and c-axis orientation are parallel. Since there is no phase change, spectra for these domains does not exhibit enhanced piezoresponse. The absence of an enhanced piezoresponse and the existence of a single-step switching mechanism are predicted for [001] domains.

### ***Scenario 2: Fig. 6.12 (b)***

In contrast to the spectra of the domain shown in Fig. 6.12 (a), the domain in Fig. 6.12 (b) shows enhanced piezoresponse (indicated by point (3) in Fig. 6.12 (b)). The piezoresponse increases gradually as the electric field is decreased from its maximum values for forward and reverse sweeps. The presence of an enhanced piezoresponse indicates the field induced phase change and therefore a polarisation rotation. Here, the polarisation reversal mechanism involves polarisation rotation followed by switching and further rotation before the domain orientates  $180^\circ$  to its original direction during an electric field sweep as discussed in the previous section.

The correlation between the PFS data and the crystal direction of the domains shown in Fig. 6.12 (b) can be explained by the following scenario: at zero field, for a [101] or [011] oriented grain, the direction of spontaneous polarisation will be at  $45^\circ$  to the out-of-plane axis. The piezoresponse maxima occurs when the electric field makes an angle of  $49^\circ$  with the direction of polarisation as shown in Fig. 6.8 [43]. These maxima are located after the zero field for forward and reverse sweeps, which indicates that the orientation of the polarisation will be less than  $49^\circ$  at zero field, which will be the case for a [101] oriented domain.

A schematic illustration of polarisation reversal in the case of a [101] or [011] oriented ferroelectric domain for a forward sweep is shown in Fig. 6.14. The

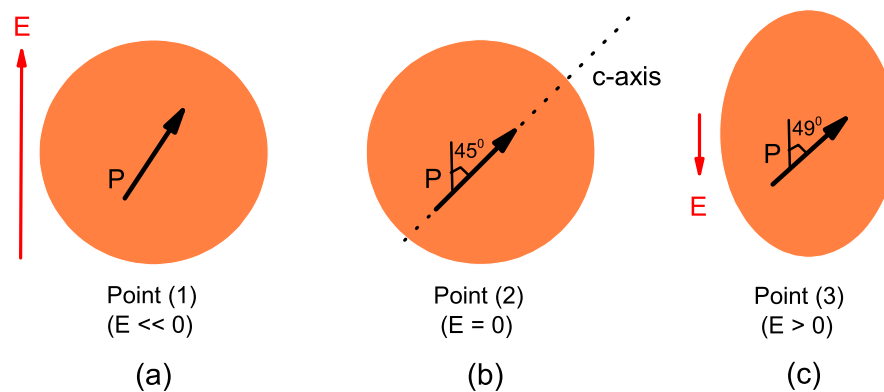


**Figure 6.14:** Schematic illustration of polarisation reversal in ferroelectric domains of spectrum shown in Fig. 6.12 (b) during a forward sweep showing; (a) approximate orientation of the polarisation at high negative fields (point (1)), (b) orientation of polarisation at zero field (point (2)); along the c-axis of the tetragonal lattice and (c) approximate orientation of the polarisation during enhanced piezoresponse (point (3)). Point (1), (2) and (3) are marked on Fig.6.12 (b).

polarisation reversal mechanism in this case for a forward sweep can be explained as follows; at high electric field, polarisation is slightly oriented towards the field direction as shown in Fig. 6.14 (a). As the electric field is reduced, the polarisation rotates. Since, at zero field, BaTiO<sub>3</sub> domains will exhibit a tetragonal lattice structure, polarisation will be oriented along the c-axis of the tetragonal crystal lattice which is pointed at  $45^\circ$  with

respect to the [001] direction as shown in Fig. 6.14 (b). As the electric field is increased in the positive direction, polarisation further rotates. When the polarisation makes an angle of  $49^\circ$  with the longitudinal axis, it passes through the monoclinic phase causing an enhanced piezoresponse. This will cause a maximum deflection to the AFM tip and is marked as point (3) in the PFS spectrum shown in Fig. 6.12 (b). The behaviour of the ferroelectric domain at this field is illustrated in Fig. 6.14 (c). An enhanced piezoresponse is illustrated as a change in the shape of the domain in the figure. For a further increase in electric field, polarisation further rotates before it actually switches at the coercive field of 325 kV/cm. It can be noted from Fig. 6.12 (b) that the switching field for a [101] (or [011]) oriented domain is lower than a [001] oriented domain shown in Fig. 6.12 (a). This indicates that the two-step mechanism involving polarisation rotation and switching allows [101] and [011] oriented ferroelectric domains to switch at a lower field compared to the [001] oriented domains, which undergo a one-step direct switching.

### ***Scenario 3: Fig. 6.12 (c)***

The PFS spectrum given in Fig. 6.12 (c) shows the smallest switching field compared to the other two spectra. This spectrum also shows an enhanced piezoresponse similar to the spectrum corresponding to [101] domain described in the last section. The presence of an enhanced piezoresponse would confirm a two-step polarisation reversal mechanism for this domain. However, the piezoresponse maximum for this spectrum occurs before the zero field for forward and reverse sweeps. A [111] oriented tetragonal BaTiO<sub>3</sub> grain will have its c-axis oriented at  $54^\circ$  with respect to the [001] direction. Since the enhanced piezoresponse happens before the sweeping field reaches zero, it can be concluded that the rotating polarisation passes through  $49^\circ$  before the field approaches zero and the polarisation aligns at  $54^\circ$  for zero field. As such, Fig. 6.12 (c), which shows a piezoresponse maximum before the sweeping field approaches zero, indicating that this particular domain is [111] oriented.

A schematic illustration of the polarisation reversal for a [111] oriented domain

during a forward sweep is given in Fig. 6.15. Similar to the [101] domain described in

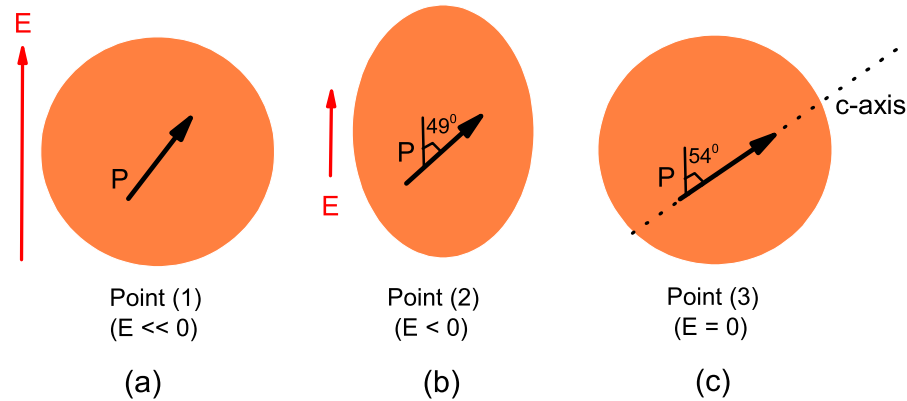


**Figure 6.15:** Schematic illustration of polarisation reversal of spectrum shown in Fig. 6.12 (c) during a forward sweep showing; (a) approximate orientation of the polarisation at high negative fields (point (1)), (b) approximate orientation of the polarisation during enhanced piezoresponse (point (2)), (c) orientation of polarisation at zero field (point (3)); along the c-axis of the tetragonal lattice. Point (1), (2) and (3) are marked on Fig.6.12 (c).

the last section; [111] domain will also have its polarisation slightly oriented towards the field direction at high electric field as shown in Fig. 6.15 (a). As the electric field is reduced, the phase of the  $\text{BaTiO}_3$  lattice changes due to the field-induced phase transition. At a particular field, the ferroelectric phase transits through its monoclinic phase and the polarisation makes an angle of  $49^\circ$  with the electric field, giving rise to an enhanced piezoresponse. This enhanced piezoresponse will cause more deflection to the AFM tip and is identifiable in the PFS data shown in Fig. 6.12 (c). An illustration of the enhanced piezoresponse and the direction of polarisation at this stage is depicted in Fig. 6.15 (b). Upon reduction of the electric field towards zero, the polarisation further rotates. At zero field,  $\text{BaTiO}_3$  transforms to its room temperature stable tetragonal lattice. Polarisation will be oriented along the c-axis at this field. For the [111] domain, polarisation will make an angle of  $54^\circ$  with the longitudinal direction as illustrated in Fig. 6.15 (c). The polarisation further rotates for further increase in the electric field in the positive direction before it finally switches at the coercive field of 125 kV/cm.

### 6.5.1 Dependence of crystalline orientation on switching field

Fig. 6.16 shows the switching field taken at five domains of each of the predicted orientations. When the polarisation reversal is a single-step switching, which is the

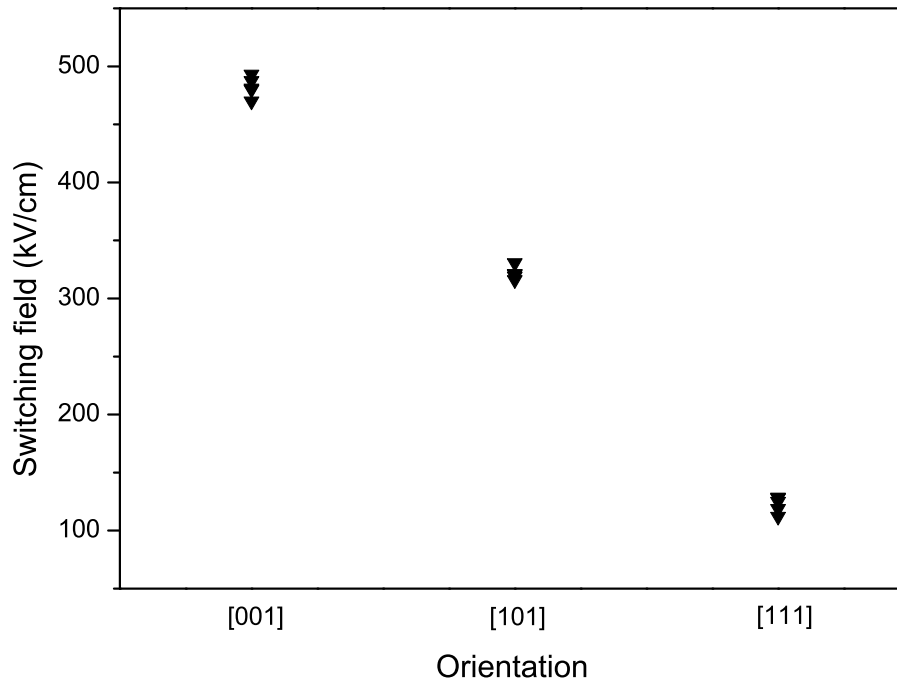


**Figure 6.16:** Variations in the switching field with variations in orientation based on five domains of each orientation for BaTiO<sub>3</sub>. Shows that polarisation rotation helps the ferroelectric domains to switch at lower fields. Coercive field reduces as the c-axis orientation of the tetragonal lattice move away from the longitudinal axis.

case for [001] domains, the coercive field is approximately 460 kV/cm. For [101] (or [011]) and [111] domains, where the polarisation reversal includes both polarisation rotation and switching, the coercive fields are 330 kV/cm and 120 kV/cm respectively. Different crystal orientations show a different coercive field and its strength depends on the direction of the applied field with respect to crystal orientation. The rotation of the polarisation is found to enable the domains to switch at lower fields compared to the scenario where the electric field and polarisation direction are parallel. Moreover, the electric field strength required to switch the polarisation reduces as the c-axis of the tetragonal lattice moves away from the applied field direction. In the case of [001] oriented domains, the c-axis and field direction are parallel and those domains require the highest field strength to switch the polarisation. However, when the field direction makes 45° with the c-axis of the crystal, which is the case for [101] and [011]

oriented domains; the field required to switch the polarisation was lower than that for [001] domains. Furthermore, field required for [111] oriented domains was the lowest, as the c-axis is further away from the longitudinal axis in this case. Here we have demonstrated experimentally that the electric field required to switch the polarisation of BaTiO<sub>3</sub> decreases as the c-axis of the tetragonal lattice moves away from the electric field direction. Results presented in this work are in good agreement with the first principles simulations in [32].

PFS is a technique which is commonly used to study the properties of ferroelectric materials [73]. Here, we have used PFS technique to predict the crystalline orientation at domain level in a ferroelectric material, with the aid of another commonly used micro-scale measurement technique such as XRD. It was demonstrated how analysis and interpretation of the spectra can be effectively used to improve a state of the art technique such as PFS. The fact that BaTiO<sub>3</sub> has its longitudinal piezoelectric coefficient maxima ( $d_{zz}$ ) far away, almost 49° from the longitudinal axis, makes such an analysis easy. This causes significant differences in the shapes of the spectra of domains with different crystallographic orientations making them easily distinguishable. However, such a prediction of crystal orientation would be challenging for materials such as Pb<sub>x</sub>Zr<sub>1-x</sub>TiO<sub>3</sub>, which have a  $d_{zz}$  maximum closer to the longitudinal axis.

## 6.6 Summary and Conclusions

In conclusion, the results presented in this work have shown experimentally that the polarisation reversal in BaTiO<sub>3</sub> is a two-step process, including both polarisation rotation and switching when electric field and spontaneous polarisation are not parallel. However, it was found to be a single-step process when the c-axis of the tetragonal lattice and electric field are parallel. Experimental results discussed here are directly comparable with first principle simulation results [32]. It was also found that the domain switching angle is lower than the anticipated values due to polarisation rotation.

PFS data were also used to study the switching response of BaTiO<sub>3</sub> films at

the resolution of individual domains. It was shown that spectra obtained from three different domains can be interpreted by the polarisation switching mechanism associated with the field-induced phase transition as predicted by theory. Based on this analysis, the PFS data were exploited to predict the crystal orientation of the domains, which were confirmed by XRD measurements. The electric field required to switch the ferroelectric polarisation was found to decrease as the c-axis of the tetragonal lattice moves away from the field direction. A [001] oriented domain required the highest field to switch the polarisation compared to a [101] or [111] oriented domain due to the one-step direct switching phenomenon shown by them. Polarisation rotation was found to aid the [101] and [111] domains to switch at a lower field; with the latter requiring the lowest field among them. Field-induced phase transition and the polarisation rotation associated with it enables these domains to switch at a lower field compared to the [001] domain.

This experimental evidence highlights the impact of a field-induced phase transition on the polarisation reversal mechanism in ferroelectric materials. Results shown here confirm the importance of crystalline orientation on the ferroelectric switching field. The understanding and experimental demonstration of these key material properties are hoped to aid in the functional diversification of semiconductor devices. The fact that crystalline orientation directly affects the coercive field, a key property of any ferroelectric material, is important for the design and engineering of future ferroelectric based devices. It was also demonstrated that PFS provides a significant understanding of the relation between crystallographic orientation and switching mechanism in ferroelectric materials. PFS will be a valuable technique in characterisation of future ferroelectric devices with a key outcome of the analysis being that the switching fields can be reduced by careful design of the film orientation, a critical factor in low power nano-ferroelectric devices.

## Summary and Conclusions

This research was focused both on the fabrication and nano-scale characterisation of BaTiO<sub>3</sub> thin films. In chapter 4 of this thesis, deposition of TiN<sub>x</sub> which can withstand a high temperature anneal was developed, and was later used as an electrode for BaTiO<sub>x</sub>. TiN<sub>x</sub> was deposited by reactive sputtering using a titanium target in a nitrogen ambient. Initially, deposition parameters such as power, substrate temperature and chamber pressure were optimised to develop a TiN<sub>x</sub> recipe. Nitrogen flow rate during deposition was then varied in order to investigate its effect on film resistivity. Conductivity is found to improve with increasing nitrogen content. Films were then annealed, varying the time and temperature of the anneal. Resistivity was found to decrease with longer annealing time and higher temperature during post deposition annealing. TiN<sub>x</sub> films showed good thermal and electrical stability upon annealing and did not show any silicon diffusion.

It was found that film orientation can influence resistivity, with [111] oriented films more resistive than [200] oriented films. Higher surface roughness and thereby larger numbers of electron scattering sites for the [111] oriented film compared to the [200] oriented film is found to be the reason for this variation in resistivity. Moreover, re-crystallization effects brought on by post deposition annealing also cause the resistivity to decrease for all films. Films deposited above 20% nitrogen flow rates during deposition were all stoichiometric TiN. However, TiN<sub>x</sub> deposited at a very high nitrogen flow rate was found to be electrically, thermally and morphologically more stable than the ones deposited at low nitrogen flow rates. Due to its stability against

a high temperature process in an oxygen free ambient,  $\text{TiN}_x$  deposited on a silicon substrate was used to deposit  $\text{BaTiO}_3$  which would undergo a post deposition anneal.

Sputter deposition and post deposition anneal of  $\text{BaTiO}_3$  films were discussed in chapter 5.  $\text{BaTiO}_3$  films were sputtered on a  $\text{TiN}_x/\text{SiO}_2/\text{Si}$  stack. MIM capacitors were also fabricated by depositing  $\text{TiN}_x$  top electrodes of various sizes. Leakage current density (current/area) was found to increase with decrease in electrode size. Peripheral leakage due to fringing electric field was found to be the reason for this anomaly. Leakage current due to the fringing field and field originating from electrode surface area were extracted for MIM capacitors with electrode sizes ranging from  $50\ \mu\text{m}$  to  $300\ \mu\text{m}$ . Peripheral leakage increased with an increase in perimeter to surface area ratio. Peripheral leakage current was found to be as high as areal leakage current for electrode sizes smaller than  $300\ \mu\text{m}$ . These results showed the importance of fringing electric field in the electrical properties of MIM capacitors. This signifies that contributions from parasitic effects cannot be neglected for micro-scale devices.

Results in chapter 5 showed that a post deposition anneal of  $\text{BaTiO}_3$  films on  $\text{TiN}_x$  resulted in hillock or pinhole formation. The pinhole/hillock formation is the result of a compressive stress developed during the annealing process which is exerted by the underlying silicon substrate. The stress is developed due to a lower value of thermal coefficient of expansion in silicon compared to that for the  $\text{BaTiO}_3$ . However, a critical thickness existed for each temperature below which films are stable. Based on these results, a multi-layer approach was developed by depositing multiple layers of films thinner than critical thickness, where deposition of each layer was followed by a 'high temperature' RTP. Results discussed in chapter 5 demonstrated that films of various thicknesses thus produced are morphologically stable with least variation in surface roughness in comparison to their single layered counterparts which showed pinholes or hillocks.

Nano-scale leakage current analysis showed a reduced leakage current through multi-layered films whereas the bottom electrodes were directly exposed through pinholes, acting as leakage paths in single layered films. Leakage hot-spots in the

I-AFM scan of the single layered sample matched the pinholes in the AFM topography scan which was simultaneously acquired. Absence of pinholes in multi-layered samples results in a reduced leakage current. Leakage current was not mediated through troughs in the sample surface in the case of multi-layered samples. This hypothesis was proven by the random distribution of leakage hot-spots in the I-AFM scan when compared with the surface morphology of the simultaneously acquired AFM topography. Results demonstrated that multi-layered films can withstand a high temperature post deposition anneal which is necessary for crystallisation of these films without causing any de-lamination effects. Furthermore, EFM scans confirmed the ferroelectric properties of the multi-layered films.

In chapter 6, the impact of an electric field induced phase transition on the polarisation switching mechanism in ferroelectric materials was demonstrated experimentally using PFS. It was shown that the giant piezoresponse shown by ferroelectric materials, due to polarisation rotation, can be used to predict the direction of the polarisation vector using PFS. When the direction of applied field is different to the crystal orientation, the polarisation reversal is found to be a two-step process which includes both polarisation rotation and switching, consistent with first principle calculations. Results show that the direction of polarisation varies with applied electric field before it actually switches. An electric field induced phase transition is the reason for this variation in direction of polarisation with electric field.

PFS was also used to identify domain orientation, and to experimentally demonstrate the impact of crystalline orientation on the switching field of ferroelectric  $\text{BaTiO}_3$  at a spatial resolution better than 100 nm. The enhanced piezoresponse due to the field induced phase transition shown by ferroelectric materials was detected through PFS spectra and was used to identify the crystallographic orientation of ferroelectric domains in a polycrystalline film by analysing the shape of the spectra.  $\text{BaTiO}_3$  thin films deposited through the pulsed laser deposition technique showed [001], [101] and [111] preferential orientations when measured by XRD. PFS spectra taken at three sets of locations showed different switching fields of 460 kV/cm, 330 kV/cm and

120 kV/cm when the electric field was swept from -600 kV/cm to 600 kV/cm. The spectra also varied from each other in terms of the position at which the enhanced piezoresponse occurs due to phase change. These results were analysed based on first principle calculations which showed that when the direction of spontaneous polarisation and applied electric field are parallel, the polarisation reversal is a one step mechanism which includes only switching. However, when the applied electric field and direction of spontaneous polarisation are not parallel, polarisation reversal is a two step mechanism which includes both rotation and switching.

The PFS spectra of domains that showed no enhanced piezoresponse were identified as having [001] orientation. In these cases, the direction of applied field and direction of spontaneous polarisation are parallel, giving a one-step polarisation reversal and no phase change. By contrast, for the two other types of spectra, there were variations of field at which enhanced piezoresponse occurred. These were identified as [101] and [111] by analysing the field at which this enhanced piezoresponse occurs. The results demonstrated that electric field induced phase change causes the [101] and [111] domains to reverse polarisation at a low field. A key outcome of the analysis was that switching fields can be reduced by careful design of the film orientation, a critical factor in low power ferroelectric memory devices. This work also demonstrated the application of the PFS technique in understanding the crystallographic orientation and switching response in ferroelectric materials by virtue of the field induced phase transition shown in these materials.

Key objectives of this thesis were to address the fabrication issues and to experimentally demonstrate ferroelectric switching mechanism of BaTiO<sub>3</sub> at domain level. These findings would facilitate achieving 'more Moore' and 'more than Moore' objectives in semiconductor processing technology. In this study it has been shown that a multi-layer approach can be employed for depositing BaTiO<sub>3</sub> on a silicon substrate at process temperatures relevant for silicon technology. We propose that the multi-layered technique is an appropriate solution for integrating BaTiO<sub>3</sub> with existing silicon technology. It was also shown that sputter deposited TiN<sub>x</sub> can be used

in processes which require high process temperatures without deteriorating electrical properties, a key issue in device fabrication. It is also hoped that the electric field induced phase transition and the polarisation rotation associated with it would enable achieving 'more than Moore' concepts in nanoelectronics. Finally, this thesis also demonstrated the important role of a nano-scale characterisation technique such as SPM in understanding electrical, material as well as electromechanical properties of ferroelectric materials.

## 7.1 Future Work

This thesis mainly focused on depositing high quality ferroelectric thin films. Most of the characterisation and analysis were centred on understanding various mechanisms at a nano-scale. A next step will be to fabricate devices with these films and study the characteristics at a macro-scale. Properties such as leakage current, break-down field, dielectric constant and dielectric loss should be optimised before these films are used in various applications. However, it is anticipated that this can be achieved through careful selection of deposition parameters and post deposition anneal conditions. Preliminary results showed that leakage current through MIM capacitors having a BaTiO<sub>3</sub> thickness of 80 nm, fabricated by multi-layer approach is around  $1 \times 10^{-2}$  A/cm<sup>2</sup> at an electric field of 50 kV/cm. This level of leakage is undesirable for a device point of view. It is suggested that an improvement in leakage current can be achieved through increasing the number of layers in the multi-layered structure. An enhancement in the device break-down field is also expected by increasing the number of layers. Once the macro-scale leakage current is under control, ferroelectric properties can be studied and optimised at a device level. The ferroelectric properties of these films can be optimised through careful improvement of RTP conditions. It had been shown that a cubic phase and tetragonal phase can co-exist in BaTiO<sub>3</sub> thin films that are not grown epitaxial [188]. Existence of a mixed phase is found to reduce the ferroelectric properties. The phase of the ferroelectric materials is known to show a dependence on the grain size. A critical grain size (few tens of nanometres) is required for these materials to exist in

a tetragonal phase and to show ferroelectricity, a property known as size driven phase transition [189]. A progressively lesser tetragonal phase is observed with decreasing grain size. Thin films with grain sizes less than the critical grain size will be cubic in phase and will show paraelectric properties. Hence, by varying the RTP conditions and thereby optimising the grain growth, one can control the ferroelectric - paraelectric behaviour in these materials. For instance, an increased grain size and therefore an improvement in the ferroelectric properties can be achieved by increasing the RTP temperature or time.

A further development for this research will be to integrate the multi-layered BaTiO<sub>3</sub> into the gate stack of a MOSFET in order to achieve a steep sub-threshold slope. Results shown by Appleby et al [18] suggest that BaTiO<sub>3</sub> can show a negative capacitance at room temperature. In this research it was demonstrated that thin film BaTiO<sub>3</sub> can be deposited on a silicon substrate within the constraints of the semiconductor manufacturing. Hence, a next step will be the combination of these two results, which is the integration of BaTiO<sub>3</sub> into the gate stack of a silicon MOSFET. Fig. 7.1 shows a schematic illustration of a MOSFET which has ferroelectric material integrated into the gate stack. Another approach at an application level will be to deposit BaTiO<sub>3</sub> in a

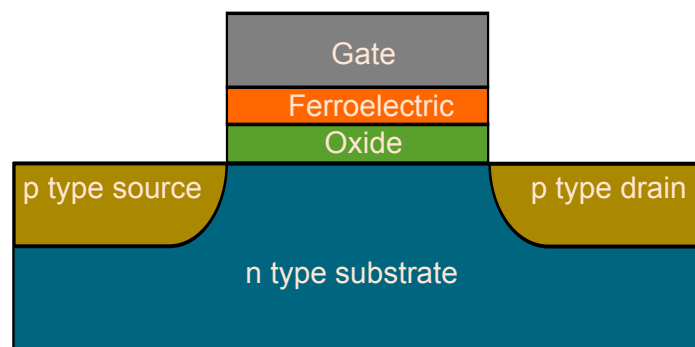


**Figure 7.1:** Schematic illustration of ferroelectric integration into the gate stack of a MOSFET in order to achieve a steep sub-threshold slope.

paraelectric phase. A paraelectric BaTiO<sub>3</sub> can be used to fabricate tuneable capacitor or a DRAM capacitor cell for increased capacitance density. Here, the RTP temperature should be decreased to obtain BaTiO<sub>3</sub> with a grain size below critical values so that they are in the cubic phase. In an FeRAM or for use in the gate stack of a MOSFET in

order to achieve a steep subthreshold slope, a ferroelectric BaTiO<sub>3</sub> is required. Hence, the RTP temperature/time can be increased to obtain films with grains that are larger than the critical grain size. The fact that the coercive field of BaTiO<sub>3</sub> depends on crystallisation orientation also allows one to design ferroelectric based devices that require less power to switch polarisation states.

## References

- [1] G. Moore, “Cramming More Components Onto Integrated Circuits,” *Electronics*, vol. 38, 1965.
- [2] J. F. Scott, “Applications of Modern Ferroelectrics,” *Science*, vol. 315, no. 5814, pp. 954–959, 2007.
- [3] K. Rabe, M. Dawber, C. Lichtensteiger, C. Ahn, and J.-M. Triscone, “Modern physics of ferroelectrics: Essential background,” in *Physics of Ferroelectrics*, vol. 105 of *Topics in Applied Physics*, pp. 1–30, Springer Berlin, Heidelberg, 2007.
- [4] N. Setter, D. Damjanovic, L. Eng, G. Fox, S. Gevorgian, S. Hong, A. Kingon, H. Kohlstedt, N. Y. Park, G. B. Stephenson, I. Stolitchnov, A. K. Taganstev, D. V. Taylor, T. Yamada, and S. Streiffer, “Ferroelectric thin films: Review of materials, properties, and applications,” *Journal of Applied Physics*, vol. 100, no. 5, 2006.
- [5] J. Valasek, “Piezo-Electric and Allied Phenomena in Rochelle Salt,” *Physical Review*, vol. 17, pp. 475–481, apr. 1921.
- [6] J. F. Scott, *Ferroelectric Memories*, vol. 3. Berlin Heidelberg, Germany: Springer-Verlag, 2000.
- [7] D. W. Chapman, “Some Thin-Film Properties of a New Ferroelectric Composition,” *Journal of Applied Physics*, vol. 40, no. 6, pp. 2381–2385, 1969.

- [8] M. Francombe, "Ferroelectric films and their device applications," *Thin Solid Films*, vol. 13, no. 2, pp. 413–433, 1972.
- [9] S. Eaton, D. Butler, M. Parris, D. Wilson, and H. McNeillie, "A Ferroelectric Nonvolatile Memory," in *Solid-State Circuits Conference, 1988. Digest of Technical Papers. ISSCC. 1988 IEEE International*, p. 130, feb. 1988.
- [10] M. Dawber, K. M. Rabe, and J. F. Scott, "Physics of thin-film ferroelectric oxides," *Review of Modern Physics*, vol. 77, pp. 1083–1130, oct. 2005.
- [11] V. Garcia, M. Bibes, L. Bocher, S. Valencia, F. Kronast, A. Crassous, X. Moya, S. Enouz-Vedrenne, A. Gloter, D. Imhoff, C. Deranlot, N. D. Mathur, S. Fusil, K. Bouzehouane, and A. Barthélemy, "Ferroelectric Control of Spin Polarization," *Science*, vol. 327, no. 5969, pp. 1106–1110, 2010.
- [12] A. S. Mischenko, Q. Zhang, J. F. Scott, R. W. Whatmore, and N. D. Mathur, "Giant Electrocaloric Effect in Thin-Film  $\text{PbZr}_{0.95}\text{Ti}_{0.05}\text{O}_3$ ," *Science*, vol. 311, no. 5765, pp. 1270–1271, 2006.
- [13] D. S. Jeong, R. Thomas, R. S. Katiyar, J. F. Scott, H. Kohlstedt, A. Petraru, and C. S. Hwang, "Emerging memories: resistive switching mechanisms and current status," *Reports on Progress in Physics*, vol. 75, no. 7, p. 076502, 2012.
- [14] D. Daranciang, M. J. Highland, H. Wen, S. M. Young, N. C. Brandt, H. Y. Hwang, M. Vattilana, M. Nicoul, F. Quirin, J. Goodfellow, T. Qi, I. Grinberg, D. M. Fritz, M. Cammarata, D. Zhu, H. T. Lemke, D. A. Walko, E. M. Dufresne, Y. Li, J. Larsson, D. A. Reis, K. Sokolowski-Tinten, K. A. Nelson, A. M. Rappe, P. H. Fuoss, G. B. Stephenson, and A. M. Lindenberg, "Ultrafast Photovoltaic Response in Ferroelectric Nanolayers," *Physical Review Letters*, vol. 108, p. 087601, feb. 2012.
- [15] V. V. Lemanov, E. P. Smirnova, P. P. Syrnikov, and E. A. Tarakanov, "Phase transitions and glasslike behavior in  $\text{Sr}_{1-x}\text{Ba}_x\text{TiO}_3$ ," *Physical Review B*, vol. 54, pp. 3151–3157, aug. 1996.

- [16] G. Salvatore, D. Bouvet, and A.-M. Ionescu, "Demonstration of subthreshold swing smaller than 60mV/decade in Fe-FET with P(VDF-TrFE)/SiO<sub>2</sub> gate stack," in *Electron Devices Meeting, 2008. IEDM 2008. IEEE International*, pp. 1–4, dec. 2008.
- [17] A. Islam Khan, D. Bhowmik, P. Yu, S. Joo Kim, X. Pan, R. Ramesh, and S. Salahuddin, "Experimental evidence of ferroelectric negative capacitance in nanoscale heterostructures," *Applied Physics Letters*, vol. 99, no. 11, 2011.
- [18] D. J. R. Appleby, N. K. Ponon, K. S. K. Kwa, B. Zou, P. K. Petrov, T. Wang, N. M. Alford, and A. O'Neill, "Experimental observation of negative capacitance in ferroelectrics at room temperature," *Nano Letters -Article ASAP*.
- [19] S. Salahuddin and S. Datta, "Use of Negative Capacitance to Provide Voltage Amplification for Low Power Nanoscale Devices," *Nano Letters*, vol. 8, no. 2, pp. 405–410, 2008.
- [20] S. Salahuddin and S. Datta, "Can the subthreshold swing in a classical FET be lowered below 60 mV/decade?," in *Electron Devices Meeting, 2008. IEDM 2008. IEEE International*, pp. 1–4, dec. 2008.
- [21] S. M. Sze and K. K. NG, *Physics of Semiconductor Devices -Third edition*. Hoboken, New Jersey, USA: John Wiley & Sons INC., 2007.
- [22] R. Feynman, R. B. Leighton, and M. Sands, *The Feynman Lectures on Physics*, vol. 2. Adison-Wesley, 1964.
- [23] R. Cohen, "Nanocapacitors: Undead layers breathe new life," *Nature Materials*, vol. 8, pp. 366–368, 2009.
- [24] J. W. Reiner, A. M. Kolpak, Y. Segal, K. F. Garrity, S. Ismail-Beigi, C. H. Ahn, and F. J. Walker, "Crystalline Oxides on Silicon," *Advanced Materials*, vol. 22, no. 26-27, pp. 2919–2938, 2010.

- [25] “International Technology Roadmap for Semiconductors: Emerging Research Devices.” <http://www.itrs.net/Links/2011ITRS/2011Chapters/2011ERD.pdf>. Available online, Accessed: 06-05-2014.
- [26] G. H. Jonker and J. H. van Santen, “Properties of Barium Titanate in Connection with Its Crystal Structure,” *Science*, vol. 109, pp. 632–635, 1949.
- [27] J. Y. Jo, Y. S. Kim, T. W. Noh, J.-G. Yoon, and T. K. Song, “Coercive fields in ultrathin BaTiO<sub>3</sub> capacitors,” *Applied Physics Letters*, vol. 89, no. 23, 2006.
- [28] V. K. Wadhawan, *Introduction to ferroic materials*. Amsterdam, Netherlands: Gordon and Breach Science Publishers, 2000.
- [29] A. M. Bratkovsky and A. P. Levanyuk, “Depolarizing field and “real” hysteresis loops in nanometer-scale ferroelectric films,” *Applied Physics Letters*, vol. 89, no. 25, 2006.
- [30] R.-H. Horng, D.-S. Wu, S.-H. Chan, M.-C. Chiang, T.-Y. Huang, and S. Sze, “Rapid-Thermal-Processed BaTiO<sub>3</sub> Thin Films Deposited by Liquid-Source Misted Chemical Deposition,” *Japanese Journal of Applied Physics*, vol. 37, no. 3R, p. 885, 1998.
- [31] G. Yuan, J. Chen, H. Xia, J. Liu, J. Yin, and Z. Liu, “Ferroelectric domain evolution with temperature in BaTiO<sub>3</sub> film on [001] SrTiO<sub>3</sub> substrate,” *Applied Physics Letters*, vol. 103, no. 6, 2013.
- [32] J. Paul, T. Nishimatsu, Y. Kawazoe, and U. V. Waghmare, “Polarization rotation, switching, and electric-field-temperature phase diagrams of ferroelectric BaTiO<sub>3</sub>: A molecular dynamics study,” *Physical Review B*, vol. 80, p. 024107, jul. 2009.
- [33] H. Fu and R. Cohen, “Polarization rotation mechanism for ultrahigh electromechanical response in single-crystal piezoelectrics,” *Nature*, vol. 403, no. 6767, pp. 281–3, 2000.

- [34] M. E. Lines and A. M. Glass, *Principles and Applications of Ferroelectrics and Related Materials*. Oxford, UK: Clarendon Press, 1977.
- [35] E. Fatuzzo and W. J. Merz, *Ferroelectricity*. Amsterdam, North-Holland, 1967.
- [36] S. G. Jona Franco, *Ferroelectric crystals*. New York, USA: Dover Publications INC, 1993.
- [37] B. A. Strukov and A. P. Levanyuk, *Ferroelectric Phenomena in Crystals*. Berlin Heidelberg, Germany: Springer-Verlag, 1998.
- [38] R. Waser, *Nanoelectronics and Information Technology*. -Second, corrected edition. Weinheim, Germany: WILEY-VCH Verlag GmbH & Co.KGaA, 2005.
- [39] Frazer, B. C. and Danner, H. R. and Pepinsky, R., "Single-Crystal Neutron Analysis of Tetragonal BaTiO<sub>3</sub>," *Physical Review*, vol. 100, pp. 745–746, 1955.
- [40] P. Chandra and P. Littlewood, "A Landau Primer for Ferroelectrics," in *Physics of Ferroelectrics*, vol. 105 of *Topics in Applied Physics*, pp. 69–116, Springer Berlin, Heidelberg, 2007.
- [41] W. J. Merz, "Domain Properties in BaTiO<sub>3</sub>," *Physical Review*, vol. 88, pp. 421–422, oct. 1952.
- [42] S.-E. Park and T. R. ShROUT, "Ultrahigh strain and piezoelectric behavior in relaxor based ferroelectric single crystals," *Journal of Applied Physics*, vol. 82, no. 4, pp. 1804–1811, 1997.
- [43] X.-h. Du, Q.-M. Wang, U. Belegundu, A. Bhalla, and K. Uchino, "Crystal orientation dependence of piezoelectric properties of single crystal barium titanate," *Materials Letters*, vol. 40, no. 3, pp. 109–113, 1999.
- [44] D. Damjanovic, F. Brem, and N. Setter, "Crystal orientation dependence of the piezoelectric d<sub>33</sub> coefficient in tetragonal BaTiO<sub>3</sub> as a function of temperature," *Applied Physics Letters*, vol. 80, no. 4, pp. 652–654, 2002.

- [45] S. Wada, S. Suzuki, T. Noma, T. Suzuki, M. Osada, M. Kakihana, S.-E. Park, L. E. Cross, and T. R. Shrout, "Enhanced Piezoelectric Property of Barium Titanate Single Crystals with Engineered Domain Configurations," *Japanese Journal of Applied Physics*, vol. 38, no. 9S, p. 5505, 1999.
- [46] B. D. Fahlman, *Materials Chemistry -Second Edition*. New York, USA: Springer, 2011.
- [47] R. Zallen, *The Formation of Amorphous Solids*, pp. 1–32. Weinheim, Germany: Wiley-VCH Verlag GmbH, 2007.
- [48] M. Avrami, "Kinetics of Phase Change. I General Theory," *The Journal of Chemical Physics*, vol. 7, pp. 1103–1112, 1939.
- [49] M. Avrami, "Kinetics of Phase Change. II Transformation-Time Relations for Random Distribution of Nuclei," *The Journal of Chemical Physics*, vol. 8, no. 2, pp. 212–224, 1940.
- [50] M. Avrami, "Granulation, Phase Change, and Microstructure Kinetics of Phase Change. III," *The Journal of Chemical Physics*, vol. 9, no. 2, pp. 177–184, 1941.
- [51] *BEOL Wiring Process for CMOS Logic*, vol. 220102025. San Jose , California, USA: VLSI Research INC., 1995.
- [52] D. E. Mercer, A. Jain, and S. W. Butler, "Will thermal budget really matter in the future?," *Rapid Thermal and Other Short-Time Processing Technologies II, Electrochemical Society*, vol. 140, no. 3, p. 247, 2001.
- [53] R. Doering and Y. Nishi, *Handbook of Semiconductor Manufacturing technology -Second edition* . Boca Raton, Florida, USA: CRC Press, 2008.
- [54] G. Eftekhari, "Characterization of Thin SiO<sub>2</sub> Grown by Rapid Thermal Processing as Influenced by Processing Parameters," *Journal of The Electrochemical Society*, vol. 140, no. 3, pp. 787–789, 1993.

- [55] O'Sullivan, B. J. and Hurley, P. K. and Leveugle, C. and Das, J. H., "Si(100) - SiO<sub>2</sub> interface properties following rapid thermal processing," *Journal of Applied Physics*, vol. 89, no. 7, pp. 3811–3820, 2001.
- [56] C. Lavoie, F. d'Heurle, C. Detavernier, and C. C. Jr., "Towards implementation of a nickel silicide process for CMOS technologies," *Microelectronic Engineering*, vol. 70, no. 2-4, pp. 144–157, 2003.
- [57] J. Niess, S. Paul, S. Buschbaum, P. Schmid, and W. Lerch, "Mainstream rapid thermal processing for source - drain engineering from first applications to latest results," *Materials Science and Engineering: B*, vol. 114-115, pp. 141–150, 2004.
- [58] A. Evans and J. Hutchinson, "The thermomechanical integrity of thin films and multilayers," *Acta Metallurgica et Materialia*, vol. 43, no. 7, pp. 2507–2530, 1995.
- [59] A. G. Evans, M. D. Drory, and M. S. Hu, "The cracking and decohesion of thin films," *Journal of Materials Research*, vol. 3, pp. 1043–1049, oct. 1988.
- [60] S. S. Sengupta, S. M. Park, D. A. Payne, and L. H. Allen, "Origins and evolution of stress development in sol-gel derived thin layers and multideposited coatings of lead titanate," *Journal of Applied Physics*, vol. 83, no. 4, pp. 2291–2296, 1998.
- [61] S. J. Skrzypek, A. Baczmanski, W. Ratuszek, and E. Kusior, "New approach to stress analysis based on grazing-incidence X-ray diffraction," *Journal of Applied Crystallography*, vol. 34, no. 4, pp. 427–435, 2001.
- [62] A. Evans and J. Hutchinson, "On the mechanics of delamination and spalling in compressed films," *International Journal of Solids and Structures*, vol. 20, no. 5, pp. 455–466, 1984.
- [63] S. T. Oyama, *The Chemistry of Transition Metal Carbides and Nitrides*. New York, USA: Blackie Academic and Professional, 1996.

- [64] K. Wasa, M. Kitabatake, and H. Adachi, *Thin Films Materials Technology: Sputtering of Compound Materials*. Norwich, New York, USA: William Andrew, INC, 2004.
- [65] D. Depla, S. Heirwegh, S. Mahieu, and R. D. Gryse, "Towards a more complete model for reactive magnetron sputtering," *Journal of Physics D: Applied Physics*, vol. 40, no. 7, p. 1957, 2007.
- [66] M. Audronis, G. Abrasonis, F. Munnik, R. Heller, P. Chapon, and V. Bellido-Gonzalez, "Diffusive racetrack oxidation in a Ti sputter target by reactive high power impulse magnetron sputtering," *Journal of Physics D: Applied Physics*, vol. 45, no. 37, p. 375203, 2012.
- [67] T. M. Tritt, *Thermal Conductivity: Theory, Properties and Applications*. New York, USA: Kluwar Academic/Plenum Publishers, 2004.
- [68] R. A. Powell and S. Rossnagel, *PVD for Microelectronics: Sputter Deposition Applied to Semiconductor Manufacturing (Thin Films)*. California, USA: Academic Press, 1999.
- [69] J. A. Thornton, "Influence of apparatus geometry and deposition conditions on the structure and topography of thick sputtered coatings," *Journal of Vacuum Science & Technology*, vol. 11, no. 4, pp. 666–670, 1974.
- [70] M. Orita, H. Ohta, H. Hiramatsu, M. Hirano, S. Den, M. Sasaki, T. Katagiri, H. Mimura, and H. Hosono, "Pulsed laser deposition system for producing oxide thin films at high temperature," *Review of Scientific Instruments*, vol. 72, no. 8, pp. 3340–3343, 2001.
- [71] S. Fransilla, *Introduction to micro fabrication*. West Sussex, England: John Wiley & Sons , Ltd., 2004.
- [72] A. Gruverman and S. V. Kalinin, "Piezoresponse force microscopy and recent

- advances in nanoscale studies of ferroelectrics,” *Journal of Materials Science*, vol. 41, no. 1, pp. 107–116, 2006.
- [73] S. V. Kalinin, A. N. Morozovska, L. Q. Chen, and B. J. Rodriguez, “Local polarization dynamics in ferroelectric materials,” *Reports on Progress in Physics*, vol. 73, p. 056502, 2010.
- [74] G. Binnig, H. Rohrer, C. Gerber, and E. Weibel, “Surface Studies by Scanning Tunneling Microscopy,” *Physical Review Letters*, vol. 49, pp. 57–61, jul. 1982.
- [75] G. Binnig, C. F. Quate, and C. Gerber, “Atomic Force Microscope,” *Physical Review Letters*, vol. 56, pp. 930–933, mar. 1986.
- [76] Y. Martin, C. C. Williams, and H. K. Wickramasinghe, “Atomic force microscope-force mapping and profiling on a sub 100-Å scale,” *Journal of Applied Physics*, vol. 61, no. 10, pp. 4723–4729, 1987.
- [77] R. A. Oliver, “Advances in AFM for the electrical characterization of semiconductors,” *Reports on Progress in Physics*, vol. 71, no. 7, p. 076501, 2008.
- [78] S. A. Mojarad, K. S. K. Kwa, J. P. Goss, Z. Zhou, N. K. Ponon, D. J. R. Appleby, R. A. S. Al-Hamadany, and A. O’Neill, “A comprehensive study on the leakage current mechanisms of Pt/SrTiO<sub>3</sub>/Pt capacitor,” *Journal of Applied Physics*, vol. 111, no. 1, p. 014503, 2012.
- [79] R. Kapoor, *Nanoscale characterisation of dielectrics for advanced materials and electronic devices*. Phd thesis, Newcastle University, jan. 2013.
- [80] Y. Katano, T. Doi, H. Ohno, and K. Yoh, “Surface potential analysis on doping superlattice by electrostatic force microscope,” *Applied Surface Science*, vol. 188, no. 3-4, pp. 399–402, 2002. Proceedings of the 4th International Conference on Noncontact Atomic Microscopy.
- [81] S. V. Kalinin, E. Karapetian, and M. Kachanov, “Nanoelectromechanics of

- piezoresponse force microscopy,” *Physical Review B*, vol. 70, p. 184101, nov. 2004.
- [82] R. Proksh and S. V. Kalinin, “Piezoresponse Force Microscopy with Asylum Research AFMs.” <http://http://www.asylumresearch.com/Applications/PFMAppNote/PFM-ANHR.pdf>. Available online, Accessed: 06-03-2014.
- [83] S. Dieter K, *Semiconductor material and device characterization -Third edition*. New York, USA: John Wiley & Sons INC., 2006.
- [84] R. Rymaszewski, “Relationship between the correction factor of the four-point probe value and the selection of potential and current electrodes,” *Journal of Physics E: Scientific Instruments*, vol. 2, no. 2, p. 170, 1969.
- [85] L. J. V. Pauw, “A method of measuring the resistivity and hall coefficient on lamellae of arbitrary shape,” *Philips technical review*, vol. 20, p. 220, 1958.
- [86] D. H. Petersen, O. Hansen, T. M. Hansen, P. Bøggild, R. Lin, D. Kjær, P. F. Nielsen, T. Clarysse, W. Vandervorst, E. Rosseel, N. S. Bennett, and N. E. B. Cowern, “Review of electrical characterization of ultra-shallow junctions with micro four-point probes,” *Journal of Vacuum Science & Technology B*, vol. 28, no. 1, pp. C1C27–C1C33, 2010.
- [87] N. F. Za’bah, *Top-Down fabrication of silicon nanowires using optical lithography*. Phd thesis, Newcastle University, jan. 2012.
- [88] Y. Abe, E. Watanabe, K. Sasaki, and S. Iura, “Effects of thermal treatment on structural and electrical properties of sputtered Ir-W alloy thin films,” *Surface and Coatings Technology*, vol. 198, no. 1-3, pp. 148–151, 2005.
- [89] K. Takemura, S. Yamamichi, P.-Y. Lesaichere, K. Tokashiki, H. Miyamoto, H. Ono, Y. Miyasaka, and M. Yoshida, “RuO<sub>2</sub>/TiN-Based Storage Electrodes for

- (Ba, Sr)TiO<sub>3</sub> Dynamic Random Access Memory Capacitors,” *Japanese Journal of Applied Physics*, vol. 34, no. Part 1, No. 9B, pp. 5224–5229, 1995.
- [90] T. Nakamura, Y. Fujimori, N. Izumi, and A. Kamisawa, “Fabrication Technology of Ferroelectric Memories,” *Japanese Journal of Applied Physics*, vol. 37, no. Part 1, No. 3B, pp. 1325–1327, 1998.
- [91] Y. J. Song, H. H. Kim, S. Y. Lee, D. J. Jung, B. J. Koo, J. K. Lee, Y. S. Park, H. J. Cho, S. O. Park, and K. Kim, “Integration and electrical properties of diffusion barrier for high density ferroelectric memory,” *Applied Physics Letters*, vol. 76, no. 4, pp. 451–453, 2000.
- [92] R. Horng, D. Wu, L. Wu, S. Wei, S. Chan, C. Leu, T. Huang, S. Sze, and M. Lee, “Co-sputtered Ru-Ti alloy electrodes for DRAM applications,” *Thin Solid Films*, vol. 343-344, pp. 598–601, 1999.
- [93] J.-E. Sundgren, “Structure and properties of TiN coatings,” *Thin Solid Films*, vol. 128, no. 1-2, pp. 21–44, 1985.
- [94] N. Yokoyama, K. Hinode, and Y. Homma, “LPCVD Titanium Nitride for ULSIs,” *Journal of The Electrochemical Society*, vol. 138, no. 1, pp. 190–195, 1991.
- [95] M. C. Lemme, J. K. Efavi, T. Mollenhauer, M. Schmidt, H. D. B. Gottlob, T. Wahlbrink, and H. Kurz, “Nanoscale TiN metal gate technology for CMOS integration,” *Microelectronic Engineering*, vol. 83, p. 1551, 2006.
- [96] C. A. Dimitriadis, S. Logothetidis, and I. Alexandrou, “Schottky barrier contacts of titanium nitride on n-type silicon,” *Applied Physics Letters*, vol. 66, no. 4, pp. 502–504, 1995.
- [97] R. Dauskardt, M. Lane, Q. Ma, and N. Krishna, “Adhesion and debonding of multi-layer thin film structures,” *Engineering Fracture Mechanics*, vol. 61, no. 1, pp. 141–162, 1998.

- [98] M. Lukosius, C. Walczyk, M. Fraschke, D. Wolansky, H. Richter, and C. Wenger, "High performance metal-insulator-metal capacitors with atomic vapor deposited HfO<sub>2</sub> dielectrics," *Thin Solid Films*, vol. 518, no. 15, pp. 4380–4384, 2010.
- [99] V. Talyansky, R. Vispute, R. Ramesh, R. Sharma, T. Venkatesan, Y. Li, L. Salamanca-Riba, M. Wood, R. Lareau, K. Jones, and A. Iliadis, "Fabrication and characterization of epitaxial AlN/TiN bilayers on sapphire," *Thin Solid Films*, vol. 323, no. 1-2, pp. 37–41, 1998.
- [100] J. Westlinder, T. Schram, L. Pantisano, E. Cartier, A. Kerber, G. S. Lujan, J. Olsson, and G. Groeseneken, "On the thermal stability of atomic layer deposited TiN as gate electrode in MOS devices," *Electron Device Letters, IEEE*, vol. 24, pp. 550–552, sept. 2003.
- [101] N. Mustapha and R. Howson, "Optical TiN films by filtered arc evaporation," *Surface and Coatings Technology*, vol. 92, p. 29, 1997.
- [102] K. Lal, A. Meikap, S. Chattopadhyay, S. Chatterjee, M. Ghosh, K. Baba, and R. Hatada, "Electrical resistivity of titanium nitride thin films prepared by ion beam-assisted deposition," *Physica B: Condensed Matter*, vol. 307, no. 1-4, pp. 150–157, 2001.
- [103] Y. Jeyachandran, S. Narayandass, D. Mangalaraj, S. Areva, and J. Mielczarski, "Properties of titanium nitride films prepared by direct current magnetron sputtering," *Materials Science and Engineering: A*, vol. 445-446, pp. 223–236, 2007.
- [104] P. Roquiny, F. Bodart, and G. Terwagne, "Colour control of titanium nitride coatings produced by reactive magnetron sputtering at temperature less than 100 °C," *Surface and Coatings Technology*, vol. 116-119, pp. 278–283, 1999.
- [105] H. O. Pierson, "The refractory nitrides," in *Handbook of Refractory Carbides and Nitrides* (H. O. Pierson, ed.), pp. 156–162, Westwood, NJ: William Andrew Publishing, 1996.

- [106] S. T. Oyama, *The Chemistry of Transition Metal Carbides and Nitrides*. Netherlands: Springer, 1996.
- [107] K.-C. Park and K.-B. Kim, "Effect of Annealing of Titanium Nitride on the Diffusion Barrier Property in Cu Metallization," *Journal of The Electrochemical Society*, vol. 142, no. 9, pp. 3109–3115, 1995.
- [108] G. Sjoblom, J. Westlinder, and J. Olsson, "Investigation of the thermal stability of reactively sputter-deposited TiN gate electrodes," *Electron Devices, IEEE Transactions on*, vol. 52, p. 2349, oct. 2005.
- [109] J.-P. Ao, Y. Naoi, and Y. Ohno, "Thermally stable TiN Schottky contact on AlGaN/GaN heterostructure," *Vacuum*, vol. 87, p. 150, 2013.
- [110] F.-H. L. Lu and J.-L. Lo, "The influences of oxygen impurity contained in nitrogen gas on the annealing of titanium nitride," *Journal of the European Ceramic Society*, vol. 22, no. 8, pp. 1367–1374, 2002.
- [111] H. Park, M. Chang, M. Jo, R. Choi, B. H. Lee, and H. Hwang, "Device Performance and Reliability Characteristics of Tantalum-Silicon-Nitride Electrode/Hafnium Oxide n-Type Metal-Oxide-Semiconductor Field-Effect Transistor Depending on Composition," *Japanese Journal of Applied Physics*, vol. 48, p. 116506, 2009.
- [112] Y. Liu, T. Kamei, K. Endo, S. Oúchi, J. Tsukada, H. Yamauchi, T. Hayashida, Y. Ishikawa, T. Matsukawa, K. Sakamoto, A. Ogura, and M. Masahara, "Nanoscale Wet Etching of Physical-Vapor-Deposited Titanium Nitride and Its Application to Sub-30-nm-Gate-Length Fin-Type Double-Gate Metal-Oxide-Semiconductor Field-Effect Transistor Fabrication," *Japanese Journal of Applied Physics*, vol. 49, no. 6, p. 06GH18, 2010.
- [113] F. Fracassi, R. dAgostino, R. Lamendola, and I. Mangieri, "Dry etching of titanium nitride thin films in CF<sub>4</sub>-O<sub>2</sub> plasmas," *Journal of Vacuum Science Technology A: Vacuum, Surfaces, and Films*, vol. 13, no. 2, pp. 335–342, 1995.

- [114] T. Easwarakhanthan, M. B. Assouar, P. Pigeat, and P. Alnot, "Optical models for radio-frequency-magnetron reactively sputtered AlN films," *Journal of Applied Physics*, vol. 98, no. 7, p. 073531, 2005.
- [115] M. Vila, E. Román, and C. Prieto, "Electrical conduction mechanism in silicon nitride and oxy-nitride-sputtered thin films," *Journal of Applied Physics*, vol. 97, no. 11, p. 113710, 2005.
- [116] T. Brat, N. Parikh, N. S. Tsai, A. K. Sinha, J. Poole, and C. Wickersham, "Characterization of titanium nitride films sputter deposited from a high-purity titanium nitride target," *Journal of Vacuum Science & Technology B: Microelectronics and Nanometer Structures*, vol. 5, no. 6, pp. 1741–1747, 1987.
- [117] F.-H. Lu and H.-Y. Chen, "XPS analyses of TiN films on Cu substrates after annealing in the controlled atmosphere," *Thin Solid Films*, vol. 355-356, pp. 374–379, 1999.
- [118] J. Wang, W. Liu, and T. Mei, "The effect of thermal treatment on the electrical properties of titanium nitride thin films by filtered arc plasma method," *Ceramics International*, vol. 30, no. 7, pp. 1921–1924, 2004.
- [119] H. G. Tompkins, "Oxidation of titanium nitride in room air and in dry O<sub>2</sub>," *Journal of Applied Physics*, vol. 70, no. 7, pp. 3876–3880, 1991.
- [120] F. Vaz, J. Ferreira, E. Ribeiro, L. Rebouta, S. Lanceros-Méndez, J. Mendes, E. Alves, P. Goudeau, J. Rivière, F. Ribeiro, I. Moutinho, K. Pischow, and J. de Rijk, "Influence of nitrogen content on the structural, mechanical and electrical properties of TiN thin films," *Surface and Coatings Technology*, vol. 191, pp. 317–323, 2005.
- [121] A. L. Patterson, "The Scherrer Formula for X-Ray Particle Size Determination," *Physical Review*, vol. 56, pp. 978–982, 1939.

- [122] W. Spengler, R. Kaiser, A. N. Christensen, and G. Müller-Vogt, "Raman scattering, superconductivity, and phonon density of states of stoichiometric and nonstoichiometric TiN," *Physical Review B*, vol. 17, pp. 1095–1101, feb. 1978.
- [123] W. Spengler, R. Kaiser, and H. Bilz, "Resonant Raman scattering in a superconducting transition metal compound, TiN," *Solid State Communications*, vol. 17, no. 1, pp. 19–22, 1975.
- [124] H. C. Barshilia and K. Rajam, "Raman spectroscopy studies on the thermal stability of TiN, CrN, TiAlN coatings and nanolayered TiN/CrN, TiAlN/CrN multilayer coatings," *Journal of Materials Research*, vol. 19, no. 11, pp. 3196–3205, 2004.
- [125] R. Chowdhury, R. D. Vispute, K. Jagannadham, and J. Narayan, "Characteristics of titanium nitride films grown by pulsed laser deposition," *Journal of Materials Research*, 1996.
- [126] M. J. Vasile, A. B. Emerson, and F. A. Baiocchi, "The characterization of titanium nitride by x-ray photoelectron spectroscopy and Rutherford backscattering," *Journal of Vacuum Science & Technology A: Vacuum, Surfaces, and Films*, vol. 8, no. 1, pp. 99–105, 1990.
- [127] C. Nunes Kirchner, K. H. Hallmeier, R. Szargan, T. Raschke, C. Radehaus, and G. Wittstock, "Evaluation of Thin Film Titanium Nitride Electrodes for Electroanalytical Applications," *Electroanalysis*, vol. 19, no. 10, pp. 1023–1031, 2007.
- [128] L. Hultman, J.-E. Sundgren, L. C. Markert, and J. E. Greene, "Ar and excess N incorporation in epitaxial TiN films grown by reactive bias sputtering in mixed Ar/N<sub>2</sub> and pure N<sub>2</sub> discharges," *Journal of Vacuum Science & Technology A: Vacuum, Surfaces, and Films*, vol. 7, no. 3, pp. 1187–1193, 1989.
- [129] K. G. Grigorov, G. I. Grigorov, M. Stoyanova, J. Vignes, J. Langeron, P. Denjean,

- and J. Perriere, "Diffusion of Si in titanium nitride films. Efficiency of TiN barrier layers," *Applied Physics A*, vol. 55, p. 502, 1992.
- [130] T. Nakano, K. Hoshi, and S. Baba, "Effect of background gas environment on oxygen incorporation in TiN films deposited using UHV reactive magnetron sputtering," *Vacuum*, vol. 83, no. 3, pp. 467–469, 2008.
- [131] N. D. Cuong, D.-J. Kim, B.-D. Kang, and S.-G. Yoon, "Effects of Nitrogen Concentration on Structural and Electrical Properties of Titanium Nitride for Thin-Film Resistor Applications," *Electrochemical and Solid-State Letters*, vol. 9, no. 9, pp. G279–G281, 2006.
- [132] L.-J. Meng and M. D. Santos, "Characterization of titanium nitride films prepared by d.c. reactive magnetron sputtering at different nitrogen pressures," *Surface and Coatings Technology*, vol. 90, no. 1-2, pp. 64–70, 1997.
- [133] B. Hahn, J. Jun, and J. Joo, "Plasma conditions for the deposition of TiN by biased activated reactive evaporation and dependence of the resistivity on preferred orientation," *Thin Solid Films*, vol. 153, no. 1-3, pp. 115–122, 1987.
- [134] S. Zerkout, S. Achour, A. Mosser, and N. Tabet, "On the existence of superstructure in  $\text{TiN}_x$  thin films," *Thin Solid Films*, vol. 441, no. 1-2, pp. 135–139, 2003.
- [135] S. Kim and O.-Y. Kwon, "BaTiO<sub>3</sub> thin film prepared by coating-pyrolysis process on Nb-doped SrTiO<sub>3</sub> substrate," *Journal of Materials Science*, vol. 34, no. 4, pp. 707–709, 1999.
- [136] M.-B. Lee, M. Kawasaki, M. Yoshimoto, and H. Koinuma, "Heteroepitaxial growth of BaTiO<sub>3</sub> films on Si by pulsed laser deposition," *Applied Physics Letters*, vol. 66, no. 11, pp. 1331–1333, 1995.
- [137] O. Trithaveesak, J. Schubert, and C. Buchal, "Ferroelectric properties of epitaxial

- BaTiO<sub>3</sub> thin films and heterostructures on different substrates,” *Journal of Applied Physics*, vol. 98, no. 11, 2005.
- [138] L. Qiao and X. Bi, “Domain configuration and phase transition for BaTiO<sub>3</sub> thin films on tensile Si substrates,” *Journal of Crystal Growth*, vol. 310, no. 24, pp. 5327–5330, 2008.
- [139] D. K. Fork, F. A. Ponce, J. C. Tramontana, and T. H. Geballe, “Epitaxial MgO on Si[001] for Y-Ba-Cu-O thin-film growth by pulsed laser deposition,” *Applied Physics Letters*, vol. 58, no. 20, pp. 2294–2296, 1991.
- [140] T. Inoue, Y. Yamamoto, S. Koyama, S. Suzuki, and Y. Ueda, “Epitaxial growth of CeO<sub>2</sub> layers on silicon,” *Applied Physics Letters*, vol. 56, no. 14, pp. 1332–1333, 1990.
- [141] T.-U. Kim, B. R. Kim, W.-J. Lee, J. H. Moon, B.-T. Lee, and J. H. Kim, “Integration of artificial SrTiO<sub>3</sub>/BaTiO<sub>3</sub> superlattices on Si substrates using a TiN buffer layer by pulsed laser deposition method,” *Journal of Crystal Growth*, vol. 289, no. 2, pp. 540–546, 2006.
- [142] E. M. Kim, J.-Y. Cho, J. H. Moon, W.-J. Lee, H. S. Kim, and J. H. Kim, “Effects of deposition temperature on the crystallinity of Ba<sub>0.5</sub>Sr<sub>0.5</sub>TiO<sub>3</sub> epitaxial thin films integrated on Si substrates by pulsed laser deposition method,” *Ceramics International*, vol. 34, no. 4, pp. 1017–1021, 2008.
- [143] W.-T. Liu, S. Cochrane, S. T. Lakshmikummar, D. Knorr, E. J. Rymaszewski, J. Borrego, and T.-M. Lu, “Low-temperature fabrication of amorphous BaTiO<sub>3</sub> thin-film bypass capacitors,” *Electron Device Letters, IEEE*, vol. 14, pp. 320–322, July 1993.
- [144] P. Li, T.-M. Lu, and H. Bakhru, “High charge storage in amorphous BaTiO<sub>3</sub> thin films,” *Applied Physics Letters*, vol. 58, pp. 2639–2641, Jun. 1991.

- [145] D. Berry and J. Santiago-Aviles, “*Organometallic precursors in conjunction with rapid thermal annealing for synthesis of thin film ceramics,*” 1993. US Patent 5,217,754.
- [146] F. Haskins and A. Balmer, “*Method of forming thin films for ferroelectric devices,*” 1970. US Patent 3,496,008.
- [147] K. Kageyama, T. Hosokura, T. Nakaiso, and H. Takagi, “Dielectric properties of (Ba,Sr)TiO<sub>3</sub> thin films with varied microstructures prepared by the chemical solution deposition method for thin-film capacitors and ferroelectric varactors.,” *IEEE transactions on ultrasonics, ferroelectrics, and frequency control*, vol. 57, no. 10, pp. 2198–2204, 2010.
- [148] F. M. Pontes, M. T. Escote, C. C. Escudeiro, E. R. Leite, E. Longo, A. J. Chiquito, P. S. Pizani, and J. A. Varela, “Characterization of BaTi<sub>1-x</sub>Zr<sub>x</sub>O<sub>3</sub> thin films obtained by a soft chemical spin-coating technique,” *Journal of Applied Physics*, vol. 96, no. 8, pp. 4386–4391, 2004.
- [149] G. W. Scherer, “Sintering of sol-gel films,” *Journal of Sol-Gel Science and Technology*, vol. 8, no. 1-3, pp. 353–363, 1997.
- [150] F. Jomni, P. Gonon, F. El Kamel, and B. Yangui, “Effect of the oxygen addition in the sputtering gas on the dielectric properties of a-BaTiO<sub>3</sub> films,” *Integrated Ferroelectrics*, vol. 97, no. 1, pp. 121–128, 2008.
- [151] M. Wegmann, “XPS Analysis of Submicrometer Barium Titanate Powder,” *Journal of American Ceramic Society*, vol. 87, no. 3, pp. 371–377, 2004.
- [152] V. Martinez, C. Besset, F. Monsieur, L. Montes, and G. Ghibaudo, “Impact of Oxygen Vacancies Profile and Fringe Effect on Leakage Current Instability of Tantalum Pentoxide Metal-Insulator-Metal (MIM) Capacitors,” in *Integrated Reliability Workshop Final Report, 2008. IRW 2008. IEEE International*, pp. 21–24, 2008.

- [153] S. Ezhilvalavan and T.-Y. Tseng, "Conduction mechanisms in amorphous and crystalline Ta<sub>2</sub>O<sub>5</sub> thin films," *Journal of Applied Physics*, vol. 83, no. 9, pp. 4797–4801, 1998.
- [154] J. Sun, X. J. Zheng, W. Yin, M. H. Tang, and W. Li, "Space-charge-limited leakage current in high dielectric constant and ferroelectric thin films considering the field-dependent permittivity," *Applied Physics Letters*, vol. 97, no. 24, 2010.
- [155] V. Martinez, C. Besset, F. Monsieur, D. Ney, L. Montes, and G. Ghibaudo, "New insight into tantalum pentoxide Metal-Insulator-Metal (MIM) capacitors: Leakage current modeling, self-heating, reliability assessment and industrial applications," in *Reliability Physics Symposium, 2008. IRPS 2008. IEEE International*, pp. 225–229, may 2008.
- [156] G. W. Parker, "Electric field outside a parallel plate capacitor," *American Journal of Physics*, vol. 70, no. 5, pp. 502–507, 2002.
- [157] N. Mohapatra, M. Desai, S. Narendra, and V. Rao, "The effect of high-K gate dielectrics on deep sub-micrometer CMOS device and circuit performance," *Electron Devices, IEEE Transactions on*, vol. 49, pp. 826–831, may 2002.
- [158] S.-H. Kim, J. Fossum, and J.-W. Yang, "Modeling and Significance of Fringe Capacitance in Nonclassical CMOS Devices With Gate-Source/Drain Underlap," *Electron Devices, IEEE Transactions on*, vol. 53, pp. 2143–2150, sept. 2006.
- [159] M. Hegg and A. Mamishev, "Influence of variable plate separation on fringing electric fields in parallel-plate capacitors," in *Electrical Insulation, 2004. Conference Record of the 2004 IEEE International Symposium on*, pp. 384–387, 2004.
- [160] J.-Z. Bao and C. C. Davis, "Study of fringing-field effects on the capacitance of a dielectric disk with a circular conducting hole," *Physical Review E*, vol. 47, pp. 3670–3676, may 1993.

- [161] C. Hérard, A. Faivre, and J. Lemaître, “Surface decontamination treatments of undoped BaTiO<sub>3</sub> part I: Powder and green body properties,” *Journal of the European Ceramic Society*, vol. 15, no. 2, pp. 135–143, 1995.
- [162] J. Sullivan, S. Saied, and I. Bertoti, “Effect of ion and neutral sputtering on single crystal TiO<sub>2</sub>,” *Vacuum*, vol. 42, no. 18, pp. 1203–1208, 1991.
- [163] M. Straumanis, C. Faunce, and W. James, “Bonding, lattice parameter, density and defect structure of TiN containing an excess of N,” *Acta Metallurgica*, vol. 15, no. 1, pp. 65–71, 1967.
- [164] J. Matthews and A. Blakeslee, “Defects in epitaxial multilayers: II. Dislocation pile-ups, threading dislocations, slip lines and cracks,” *Journal of Crystal Growth*, vol. 29, no. 3, pp. 273–280, 1975.
- [165] M.-H. Zhao, R. Fu, D. Lu, and T.-Y. Zhang, “Critical thickness for cracking of Pb(Zr<sub>0.53</sub>Ti<sub>0.47</sub>)O<sub>3</sub> thin films deposited on Pt/Ti/Si[100] substrates,” *Acta Materialia*, vol. 50, no. 17, pp. 4241–4254, 2002.
- [166] J. Schubert, O. Trithaveesak, A. Petraru, C. L. Jia, R. Uecker, P. Reiche, and D. G. Schlom, “Structural and optical properties of epitaxial BaTiO<sub>3</sub> thin films grown on GdScO<sub>3</sub>[110],” *Applied Physics Letters*, vol. 82, no. 20, pp. 3460–3462, 2003.
- [167] J. Matthews and A. Blakeslee, “Defects in epitaxial multilayers: I. Misfit dislocations,” *Journal of Crystal Growth*, vol. 27, pp. 118–125, 1974.
- [168] J. Matthews and A. Blakeslee, “Defects in epitaxial multilayers: III. Preparation of almost perfect multilayers,” *Journal of Crystal Growth*, vol. 32, no. 2, pp. 265–273, 1976.
- [169] W. Arden, M. Brillouet, P. Copez, M. Graef, B. Huizing, and R. Mahnkopf, “More-than-Moore White Paper.” <http://www.itrs.net/Links/2010ITRS/IRC-ITRS-MtM-v2%203.pdf>. Available online, Accessed: 13-12-2013.

- [170] B. Noheda, D. E. Cox, G. Shirane, S.-E. Park, L. E. Cross, and Z. Zhong, "Polarization Rotation via a Monoclinic Phase in the Piezoelectric 92%  $\text{PbZn}_{1/3}\text{Nb}_{2/3}\text{O}_3$ -8%  $\text{PbTiO}_3$ ," *Physical Review Letters*, vol. 86, pp. 3891–3894, 2001.
- [171] S. K. Mishra, D. Pandey, and A. P. Singh, "Effect of phase coexistence at morphotropic phase boundary on the properties of  $\text{Pb}(\text{Zr}_x\text{Ti}_{1-x})\text{O}_3$  ceramics," *Applied Physics Letters*, vol. 69, no. 12, pp. 1707–1709, 1996.
- [172] D. Vanderbilt and M. H. Cohen, "Monoclinic and triclinic phases in higher-order Devonshire theory," *Physical Review B*, vol. 63, p. 094108, jan. 2001.
- [173] L. Bellaiche, A. García, and D. Vanderbilt, "Electric-field induced polarization paths in  $\text{Pb}(\text{Zr}_{1-x}\text{Ti}_x)\text{O}_3$  alloys," *Physical Review B*, vol. 64, no. 6, p. 060103, 2001.
- [174] D. J. Franzbach, Y. J. Gu, L. Q. Chen, and K. G. Webber, "Electric field-induced tetragonal to orthorhombic phase transitions in  $[110]_c$ -oriented  $\text{BaTiO}_3$  single crystals," *Applied Physics Letters*, vol. 101, no. 23, p. 232904, 2012.
- [175] J. H. Haeni, P. Irvin, W. Chang, R. Uecker, P. Reiche, and Y. L. Li, "Room-temperature ferroelectricity in strained  $\text{SrTiO}_3$ ," *Nature*, vol. 430, no. August, pp. 583–586, 2004.
- [176] S. Jesse, A. P. Baddorf, and S. V. Kalinin, "Dynamic behaviour in piezoresponse force microscopy," *Nanotechnology*, vol. 17, no. 6, p. 1615, 2006.
- [177] B. J. Rodriguez, A. Gruverman, A. I. Kingon, R. J. Nemanich, and J. S. Cross, "Three-dimensional high-resolution reconstruction of polarization in ferroelectric capacitors by piezoresponse force microscopy," *Journal of Applied Physics*, vol. 95, no. 4, pp. 1958–1962, 2004.
- [178] Z. Hu, G. Wang, Z. Huang, X. Meng, and J. Chu, "Investigations on the infrared optical properties of  $\text{BaTiO}_3$  ferroelectric thin films by spectroscopic

- ellipsometry,” *Semiconductor Science and Technology*, vol. 18, no. 6, p. 449, 2003.
- [179] M. López, G. Fourlaris, and F. Riley, “Interaction of barium titanate powders with an aqueous suspending medium,” *Journal of the European Ceramic Society*, vol. 18, no. 14, pp. 2183–2192, 1998.
- [180] Y. Zhou, C.-S. Park, C.-H. Wu, D. Maurya, M. Murayama, A. Kumar, R. S. Katiyar, and S. Priya, “Microstructure and surface morphology evolution of pulsed laser deposited piezoelectric BaTiO<sub>3</sub> films,” *Journal of Materials Chemistry C*, vol. 1, pp. 6308–6315, 2013.
- [181] D. Williams and B. Carter, *Transmission electron microscopy: A textbook for materials science*. New York, USA: Springer Science+ Media LLC., 2009.
- [182] C. Harnagea, A. Pignolet, M. Alexe, and D. Hesse, “Piezoresponse scanning force microscopy: What quantitative information can we really get out of piezoresponse measurements on ferroelectric thin films,” *Integrated Ferroelectrics*, vol. 38, no. 1-4, pp. 23–29, 2001.
- [183] S. V. Kalinin, B. J. Rodriguez, S. Jesse, J. Shin, A. P. Baddorf, P. Gupta, H. Jain, D. B. Williams, and A. Gruverman, “Vector Piezoresponse Force Microscopy,” *Microscopy and Microanalysis*, vol. 12, pp. 206–220, may 2006.
- [184] R. Clarke, “Phase transition studies of pure and flux-grown barium titanate crystals,” *Journal of Applied Crystallography*, vol. 9, pp. 335–338, aug. 1976.
- [185] G. H. Kwei, A. C. Lawson, S. J. L. Billinge, and S. W. Cheong, “Structures of the ferroelectric phases of barium titanate,” *The Journal of Physical Chemistry*, vol. 97, no. 10, pp. 2368–2377, 1993.
- [186] L. Kim, J. Kim, D. Jung, J. Lee, and U. V. Waghmare, “Polarization of strained BaTiO<sub>3</sub>/SrTiO<sub>3</sub> artificial superlattice: First-principles study,” *Applied Physics Letters*, vol. 87, no. 5, 2005.

- [187] H. Zhang, "Polarization rotation theory for field-induced-phase transitions in BaTiO<sub>3</sub> single crystal," *Journal of Applied Physics*, vol. 113, no. 18, pp. 184111–9, 2013.
- [188] D. J. R. Appleby, N. K. Ponon, K. S. K. Kwa, U. Hannemann, P. K. Petrov, N. M. Alford, and A. O'Neill, "Ferroelectric properties in thin film barium titanate grown using pulsed laser deposition," *Journal of Applied Physics -Submitted*.
- [189] Z. Zhao, V. Buscaglia, M. Viviani, M. T. Buscaglia, L. Mitoseriu, A. Testino, M. Nygren, M. Johnsson, and P. Nanni, "Grain-size effects on the ferroelectric behavior of dense nanocrystalline BaTiO<sub>3</sub> ceramics," *Physical Review B*, vol. 70, p. 024107, jul. 2004.